THE UNIVERSITY OF
SYDNEY

Engineering Culture Conditions of Human Stem Cell-Derived Organoids

Queenie Yip

A thesis submitted in fulfilment of the requirements for the degree of
Doctor of Philosophy

Faculty of Engineering

School of Biomedical Engineering

The University of Sydney

2025

Authorship Attribution Statement

This thesis contains published material in: Peter LH Newman, **Queenie Yip,** Pierre Osteil, Tim A. Anderson, Jane QJ Sun, Daryan Kempe, Maté Biro, Jae-Won Shin, Patrick PL Tam, and Hala Zreiqat; "Programming of Multicellular Patterning with Mechano-Chemically Microstructured Cell Niches." *Advanced Science* 10, no. 15 (2023): 2204741. This publication forms a portion of the methods section of "Chapter 3: Micropatterning and modulation of human pluripotent stem cell cultures to characterise early neural differentiation". Relevant to this thesis, I wrote the Supporting Information regarding the extended methods of the developed printing technology.

In addition to the statement above, permission to include the published material has been granted by the corresponding author.

Student Name: Queenie Yip Date: 30.09.2024

As supervisor for the candidature upon which this thesis is based, I can confirm that the authorship attribution statement above is correct.

Supervisor Name: Hala Zreiqat Date: 24.09.2024

Statement of Originality

I hereby declare that the work contained in this thesis has not been previously submitted to any other institution for a degree or as part of requirements for a degree. This thesis has been written and prepared solely by the author, and all projects and studies were designed and analysed by the author. The same applies to the original manuscripts which have been published in peer-reviewed journals and form parts of this thesis.

I declare that the work in this thesis is original, and all external information sources and literature used have been acknowledged and indicated in this thesis.

Acknowledgements

Given the (*geographical*) space and (*psychological*) time it has taken to complete this thesis, I have an insurmountable number of people I want and need to thank.

To my supervisors. Thank you for believing in me and giving me the grace to make mistakes and learn from them. Hala, thank you for seeing potential in me from before I even started. I'm not sure I'll ever achieve that Nobel prize, but your belief was enough. Anai, thank you for taking me in as one of your own and continually believing I could find a way even, after many failed attempts. I could not have finished this journey without your support. Patrick, thank you for the ongoing advice, time, and resources you have offered – I appreciate your wisdom and experience. Lastly, Pete, I cannot thank you enough for teaching me how to learn and grow inside and outside the lab. I will always appreciate the conversations, experiments, and experiences we shared.

To all past and current members of the Tissue Engineering and Biomaterials lab. It has been an absolute pleasure and honour to share a lab and office space with you. You have no idea how much fun it has been to discuss research, life, and life beyond research with you all. I will dearly miss our daily 11 am walks across campus.

To all past and current members of the Stem Cell Medicine group. As a bioengineer, I'd like to thank all of you for welcoming me. I have cherished the time we spent together in both TC and the T-room. What an absolute joy it has been to have the opportunity to meet all of you.

To our small Gels and Cells sub-group in the 424 lab. You all made the start of my PhD and learning cell culture a joy. Gels & Cells will hold a special place in my heart for always plus 90 days of previous messages.

To my brothers, Ricky and William. Thank you for the random adventures and conversations, and for feeding the cats when I'm away at conferences.

To my cats, Bijoux and Rocky. Thank you for being such cutie pies and never having done anything wrong in your life ever. I've learnt much about patience, boundaries, and unconditional conditional love from you. William's cats, Xyla and Mewy, also get a special mention for convincing me to adopt my own.

To my mum. I know it's hard to tell, but I appreciate everything you do for me and I hope to gradually give back everything and more.

To my best friends, Jisu, Myra, Mendy, and Maab. Thank you for always being there for me throughout the awful schedules and stressful times. I am forever indebted to you all for showing me what love and community can and should be. We were kids together, and now we are grown and still growing together.

By the time this thesis is finished, it will have been 15 years since we met. So, I dedicate this one to you.

I would like to acknowledge support from Milan Fernando in performing the first preliminary long-term iPSC culture experiments in Chapter 3

The research reported in this thesis was supported by the award of a Research Training Program scholarship to the PhD Candidate

Table of Contents

List of Figures xii

List of Tables xxiv

List of Abbreviations xxv

Thesis Abstract xxvii

Chapter 1: Introduction 1

1.1 Significance of stem cell-derived organoids 2

1.2 Overview of the thesis 3

1.3 Hypothesis and aims 4

1.3.1 Hypothesis 4

1.3.2 Aims 4

Chapter 2: Manipulating culture conditions for organoid applications 5

2.1 Introduction 6

2.2 Creating *in vitro* human models using stem cells 6

2.3 Retinal tissues and organoids for clinical applications 12

2.3.1 Retinal anatomy 13

2.3.2 Retinal development 15

2.3.3 Retinal organoid generation 19

2.3.4 Retinal cell transplantation 20

2.3.5 Remaining hurdles to clinical translation....23
2.4 Methods to enhance the generation of retinal organoids....25
2.4.1 Modulation of known signalling pathways and gas concentrations....25
2.4.2 Bioengineered devices for improved retinal tissue growth....27
2.4.3 Bioengineered methods for improved scalability....32
2.5 Micropatterning cells to induce spatial confinement in stem cells....36
2.5.1 Micropatterning to enhance tissue culture....36
2.5.2 Methods of micropatterning....38
2.5.3 Effect of micropattern geometry....40
2.5.4 Micropatterning for clinical applications....42
2.6 Micropatterning of tissue and organoid cultures....43
2.6.1 Micropatterning of embryonic tissues....43
2.6.2 Micropatterning of mesoderm- and endoderm-derived tissues....45
2.6.3 Micropatterning of ectoderm tissues....46
2.7 Motivation of this thesis....49
Chapter 3: Micropatterning and modulation of human pluripotent stem cell cultures to characterise early neural differentiation....51
3.1 Introduction....52
3.2 Experimental Section....55
3.2.1 Materials and procedures....55
3.2.2 Functionalisation of glass coverslips....55

3.2.3 Preparation of pre-polymer printing solution....56

3.2.4 Fabrication of micropatterned glass substrates....57

3.2.5 Sterilisation and preparation of printed substrates....61

3.2.6 Maintenance of iPSC lines and neural differentiation....61

3.2.7 Immunohistochemistry....63

3.2.8 Imaging of patterned glass substrates....63

3.2.9 Quantification of patterned cultures....64

3.2.10 Statistical analysis....64

3.3 Results and Discussion....65

3.3.1 Design and optimisation of technique to fabricate micropatterned glass substrates through 3D printing....65

3.3.2 Cell behaviour and viability on micropatterned glass substrates....70

3.3.3 Effect of dimension and biochemical modulation in early micropatterned cell cultures....77

3.3.4 Effect of dimension and biochemical modulation in intermediate stages of neural differentiation....84

3.3.5 Development of a scalable method for micropatterning glass substrates....90

3.3.6 Evaluation of long-term differentiation and viability on micropatterned glass substrates....97

3.4 Conclusion....103

Chapter 4: Micropatterning the self-organisation of pluripotent stem cells to generate neuroretinal vesicles....104

4.1 Introduction....105

4.2 Experimental Section....107

4.2.1 Materials and procedures....107

4.2.2 Fabrication of micropatterned plastic substrates using PEG hydrogels....107

4.2.3 Fabrication of micropatterned plastic substrates directly with UV light....107

4.2.4 Maintenance of iPSC lines and neural differentiation....108

4.2.5 Immunohistochemistry....108

4.2.6 Imaging of micropatterned cultures....108

4.2.7 Quantification of micropatterned cultures....109

4.2.8 Statistical analysis....109

4.3 Results and Discussion....110

4.3.1 Characterisation of a SIX6-GFP reporter cell line in a 2D/3D retinal organoid protocol....110

4.3.2 Design and validation of a technique to micropattern tissue culture plastic using PEG polymers....117

4.3.3 Design and validation of a technique to micropattern tissue culture plastic directly using UV light....123

4.3.4 Optimisation of cell behaviour on micropatterned tissue culture plastic....131

4.3.5 Long-term culture and evaluation of retinal differentiation on micropatterned tissue culture plastic....140

4.3.6 Validation and quantification of retinal organoids grown on micropatterned tissue culture plastic....155

4.4 Conclusion....167

Chapter 5: Biochemical modulation of pluripotent stem cell cultures to enhance the formation of neuroretinal vesicles 168

5.1 Introduction 169

5.2 Experimental Section 172

5.2.1 Materials and procedures 172

5.2.2 Maintenance of iPSC lines and neural differentiation 172

5.2.3 Imaging and quantification of culture plates 173

5.2.4 Statistical Analysis 173

5.3 Results and Discussion 175

5.3.1 Preconditioning of 2D confluent cultures through modulation of TGF-β/Nodal and SHH pathways 175

5.3.2 Long-term treatment of cultures through timed WNT inhibition and SHH activation 185

5.3.3 Modulation of 2D confluent cultures through retinoic acid signalling prior to the onset of SIX6-GFP expression 192

5.3.4 Modulation of 2D confluent cultures through the late and early supplementation of retinoic acid 199

5.3.5 Initialising 2D confluent cultures through an early transient pulse of FGF2 and TGF-β using E8 media 207

5.3.6 Characterisation of the endogenous signalling levels of key signalling pathways across different stages of passage numbers of three iPS cell lines 213

5.3.7 Evaluating the combined treatment of micropatterned substrates and preconditioning on retinal differentiation 220

5.3.8 Evaluating the combined treatment of micropatterned substrates and RA treatment on retinal differentiation 228

5.4 Conclusion 239

Chapter 6: Conclusions and Recommendations 241

6.1 Conclusions 242

6.2 Limitations of the current work 245

6.3 Future recommendations 251

List of References 257

Thesis Appendix 271

List of Figures

Figure 2.1 Overview of organoid research, including examples of organoid generation methods, tissue types, and downstream applications. Adapted from Hofer & Lutolf[4].....8

Figure 2.2 Number of publications relating to organoids of different tissue types and cell replacement therapies; relative to the number of publications produced in the given year. Data sourced from Pubmed (https://pubmed.ncbi.nlm.nih.gov/). 10

Figure 2.3 Considerations for generating organoids from different embryoid body-derived germ layers, including cell source, matrix, physical cues, soluble factors, and integrating cues. Adapted from Zhao et al[8].....11

Figure 2.4 Cellular architecture and layers of the adult human retina, including key cell layers and cell types.....14

Figure 2.5 Development of the human eye, including the key markers involved and approximate time points in days from conception.....16

Figure 2.6 Development of the human brain as related to Carnegie stages. The development of the retina from the neural ectoderm occurs starting from approximately stage 8 at Day 21 to 28 post-fertilisation. Adapted from O'Rahilly & Fabiola[44]. 18

Figure 2.7 Common methods to generate retinal tissues and organoids. Adapted from Oswald, et al.[56].....20

Figure 2.8 Overview of the approaches to deliver retinal cells to the subretinal space via bioengineered and traditional methods. 22

Figure 2.9 Common signalling pathways modulated during the process of retinal differentiation, including the molecular mechanisms and commonly used agonists and antagonists. Adapted from Wagstaff et al.[93] 26

Figure 2.10 Schematic showing the different types of protocols used to generate retinal organoids, showing the stepwise processes involved. Adapted from Kim et al[53]. 27

Figure 2.11 Engineering methods to control stem cell self-organisation through biophysical and biochemical cues. Adapted from Brassard & Lutolf[106].....28

Figure 2.12 High-throughput biomaterial-based arrays for the scaled generation of retinal organoids using 3D suspension methods. 33

Figure 2.13 Methods to control initial conditions of stem cell cultures. Adapted from Brassard & Lutolf[106].....35

Figure 2.14 Differences in the analysis and applications of conventional and micropatterned cultures. Adapted from Blin[163].....37

Figure 2.15 Micropatterning to enhance the control over initial conditions of self-organisation and morphogenesis. Stimulation with low concentrations of Matrigel induces the formation of neural tube-like structures in these platforms. Adapted from Karzbrun[154].....44

Figure 3.1 Application of custom-built printer to fabricate custom micropatterns on glass substrates using laser-based UV polymerisation. 66

Figure 3.2 Optimisation of printing speed to fabricate custom micropattern designs.....68

Figure 3.3 Different micropattern geometries fabricated using the custom-built printer..69

Figure 3.4 iPSCs (HOIK1) were seeded at standard cell density on micropatterned substrates and differentiated for 4 weeks using proneural induction media. 71

Figure 3.5 Poor capacity for vesicle formation was observed in certain cell lines (149BR) after 3 weeks of differentiation in proneural induction media, despite vesicle formation in glass and plastic control substrates (n = 2 wells, N = 1 differentiation; Scale bar = 1050 μm). 74

Figure 3.6 Representative images of high initial seeding density of iPSC (HOIK1) cultures differentiated for up to 3 weeks in proneural induction media. 75

Figure 3.7 Representative images of iPSCs seeded onto micropatterned cultures, differentiated for 72 hours in proneural induction media, and treated with Matrigel through media dilution of direct embedding. 79

Figure 3.8 Matrigel (MG) treatments caused an increase in the average colony height, though reduced the proportion of intact colonies after 72 hours. 80

Figure 3.9 Representative images of SOX1 and PAX6 immunofluorescent stained micropatterned colonies treated with 4% Matrigel showed that decreased pattern diameter is correlated with increasing colony height. 85

Figure 3.10 Proportion of intact colonies on different pattern sizes after one week of differentiation in proneural induction media, with and without Matrigel treatment. 87

Figure 3.11 Micropatterned colonies (1 mm diameter) treated with 4% Matrigel showed complex and uncontrolled tissue organisation with high variability in colony height after 14 days of differentiation. 89

Figure 3.12 A patterned photomask was designed using computer-aided design software (SolidWorks, Dassault Systèmes) and fabricated by the Research and Prototype Foundry at the University of Sydney. 91

Figure 3.13 (a) Schematic of the sandwich technique for UV polymerisation of a PEG polymer solution. (b) Setup using a UV lamp, retort stand, and clamps. Created with BioRender.com. 92

Figure 3.14 Circular micropatterns (1 mm diameter) fabricated using the newly developed method of micropatterning PEG polymers onto glass substrates. 93

Figure 3.15 Circular micropatterns with 2 mm diameters could be fabricated at high resolution through UV polymerisation of PEG polymers onto glass substrates.....95

Figure 3.16 Macroscopic image of micropatterned cell cultures of different geometries on glass substrates within a 6-well plate.....96

Figure 3.17 Poor viability of micropatterned cell cultures was observed on 1 mm-diameter patterns after 3 weeks of neural differentiation. 4x objective scale bar = 1050 µm; 10x objective scale bar = 400 µm.....98

Figure 3.18 High expression of SIX6-GFP was observed in cells on tissue culture plastic regions adjacent to the edge of the glass coverslip and culture well after 3 weeks of neural differentiation. 4x objective scale bar = 1050 µm; 10x objective scale bar = 400 µm.....101

Figure 4.1 Brightfield and GFP imaging of 2D-induced confluent monolayer cultures from week 1 to 4 (top) and 3D suspension cultures of collected retinal vesicles at week 5 (bottom) using the EP1.SIX6-GFP reporter cell line.....111

Figure 4.2 Different morphological features observed in brightfield imaging at day 37 corresponds to varied GFP regionalisation in SIX6-GFP reporter cell lines.....113

Figure 4.3 Representative immunofluorescent staining of retinal organoids at week 5, 7, and 9 using eye field markers PAX6 and LHX2, and SIX6-GFP.....114

Figure 4.4 Immunofluorescent staining of connected retinal-brain structures confirms specificity of the SIX6-GFP reporter for retinal tissues. 116

Figure 4.5 Micropatterning of PEG hydrogels on tissue culture plastic was achieved using photopolymerisation of a PEG prepolymer solution.....118

Figure 4.6 A cut out sheet of parafilm was used as a mask to define the region of polymerisation and break the surface tension of liquids on tissue culture plastic. 119

Figure 4.7 Tissue-culture treated plastic coverslips can support the attachment of PEG polymers and subsequent cell seeding. 121

Figure 4.8 Schematic representation of the UV lamp-based micropatterning set-up (top) and successful implementation in two separate laboratories (bottom). 124

Figure 4.9 Cells seeded onto UV-micropatterned tissue culture surfaces selectively attached and proliferated on regions not exposed to UV light.....126

Figure 4.10 Alterations in UV exposure time resulted in distinct cell morphologies upon cell attachment and differentiation (Scale bar = 1050 μm). 129

Figure 4.11 Representative images of distinct macroscopic patterning of tissue culture wells within 1 week of differentiation across the HOIK1, IMR90, and EP1 cell lines.....130

Figure 4.12 A high number of cell aggregates were produced in the un-optimised UV patterning protocol and could be collected for further culture.....133

Figure 4.13 Optimisation and characterisation of the effect of distance from the centre of the well on subsequent colony morphology.....135

Figure 4.14 Representative images of cell colonies on UV patterned tissue culture plate following the optimisation of the protocol.....136

Figure 4.15 Fabrication of micropatterned tissue culture plastic using different dimensions of patterns shows the adaptability of the developed technique.....138

Figure 4.16 Differentiation of cells on UV-micropatterned tissue culture plastic prior to optimisation of protocols reveal high levels of disorganisation by week 4.....142

Figure 4.17 Optimised micropatterning of tissue culture plastic retained the flat morphology of cell colonies at the onset of differentiation and enabled the formation of a neat cell monolayer between patterned colonies at week 2 of differentiation.....144

Figure 4.18 UV-treated micropatterned tissue culture plastic successfully supported the self-organisation of retinal vesicles by week 3 of differentiation.....147

Figure 4.19 Representative image of a micropatterned culture at week 4, showing a mass loss of vesicle structures over time due to the highly budded 3D structures detaching following shear forces induced during cell media changes.....148

Figure 4.20 UV micropatterned cultures are visibly distinct from control cultures both macroscopically and microscopically (Scale bar = 1050 μm).....149

Figure 4.21 Representative images of an entire well of the micropatterned culture showing the distribution and distinct patterning of GFP+ vesicles. 149

Figure 4.22 3D vesicles collected from 2D UV micropatterned cultures after 4 weeks of differentiation show clear (a) retinal and (b) brain morphologies, with no unusual features (Scale bar = 500 µm) 150

Figure 4.23 Cortical brain vesicles spontaneously formed in one independent batch of micropatterned cultures by week 4. 152

Figure 4.24 Collected brain organoids possess clear typical neural rosette morphology and no expression of SIX6-GFP (Scale bar = 1050 µm). 153

Figure 4.25 Preliminary schematic of the proposed effect of micropatterning-induced spatial confinement on the differential specification of forebrain and retinal fates. 154

Figure 4.26 Representative images showcasing machine learning-based segmentation of 3D vesicle structures and SIX6-GFP+ regions on 2D substrates in merged brightfield and GFP image channels 156

Figure 4.27 The accuracy of segmentation performed by the machine learning model is dependent on the location of the well plate 157

Figure 4.28 Representative images of micropatterned culture over time (top) and the plotted location of identified vesicle structures through the trained model (bottom). 158

Figure 4.29 Quantification of GFP+ areas within micropatterned cultures in the SIX6-GFP reporter cell lines after 4 weeks of differentiation. 159

Figure 4.30 Quantification of the fold-change in GFP+ areas within paired samples of micropatterned and non-micropatterned cultures in the SIX6-GFP reporter cell lines after 4 weeks of differentiation. 161

Figure 4.31 Quantification of the number of vesicles produced within micropatterned cultures across three cell lines after 4 weeks of differentiation. 163

Figure 4.32 Quantification of the fold-change in the number of vesicles produced within paired samples of micropatterned and non-micropatterned cultures across three cell lines after 4 weeks of differentiation. 165

Figure 5.1 Schematic overview of the timeline of trialled biochemical modulation treatments relative to Differentiations days. 173

Figure 5.2 Representative images of the capacity of preconditioning treatment to improve retinal differentiation across three cell lines after 4 weeks of differentiation.....177

Figure 5.3 Quantification of the average number of vesicles produced (left) and the fold-change within paired samples (right) of preconditioning treated cultures and non-treated controls across three cell lines after 4 weeks of differentiation. 180

Figure 5.4 Quantification of the average number of GFP+ regions produced (left) and the fold-change within paired samples (right) of preconditioning treated cultures in SIX6-GFP reporter cell lines after 4 weeks of differentiation. 183

Figure 5.5 Representative images of the capacity of IWR and SAG timed media treatment to improve retinal differentiation across three cell lines after 4 weeks of differentiation. 186

Figure 5.6 Quantification of the average number of vesicles produced (left) and the fold-change within paired samples (right) of cultures with IWR and SAG media treatments and non-treated controls across two cell lines after 4 weeks of differentiation.....188

Figure 5.7 Quantification of the average number of GFP+ regions produced (left) and the fold-change within paired samples (right) of cultures with IWR and SAG media treatments and non-treated controls in a SIX6-GFP reporter cell line after 4 weeks of differentiation.....190

Figure 5.8 Representative images of the capacity of RA treatment from day 10 – 16 to improve retinal differentiation across three cell lines after 4 weeks of differentiation. 193

Figure 5.9 Quantification of the average number of vesicles produced (left) and the fold-change within paired samples (right) of Day 10 – 16 RA treated cultures and non-treated controls across three cell lines after 4 weeks of differentiation.....195

Figure 5.10 Quantification of the average number of GFP+ regions produced (left) and the fold-change within paired samples (right) of Day 10 – 16 RA treated cultures and non-treated controls in SIX6-GFP reporter cell lines after 4 weeks of differentiation.....197

Figure 5.11 Representative images of the capacity of late RA treatment (Day 14 – 20) to improve retinal differentiation across three cell lines after 4 weeks of differentiation. 200

Figure 5.12 Quantification of the average number of vesicles produced (left) and the fold-change within paired samples (right) of late RA treated cultures (Day 14 – 20) and non-treated controls across three cell lines after 4 weeks of differentiation.....201

Figure 5.13 Quantification of the average number of GFP+ regions produced (left) and the fold-change within paired samples (right) of late RA treated cultures (Day 14 – 20) and non-treated controls in SIX6-GFP reporter cell lines after 4 weeks of differentiation.....202

Figure 5.14 Representative images of the capacity of early RA treatment (Day 6 – 12) to improve retinal differentiation across three cell lines after 4 weeks of differentiation. 204

Figure 5.15 Quantification of the average number of vesicles produced (left) and the fold-change within paired samples (right) of early RA treated cultures (Day 6 – 12) and non-treated controls after 4 weeks of differentiation (N = 3 independent batches).....205

Figure 5.16 Representative images of the capacity of E8 pulse treatment across three cell lines after 4 weeks of differentiation, and quantification of the number of vesicles produced in the HOIK1 cell line.....209

Figure 5.17 Quantification of the average number of vesicles and GFP+ regions produced within paired samples of E8 pulse treated cultures and non-treated controls in SIX6-GFP reporter cell lines after 4 weeks of differentiation (N = 3 independent batches).....211

Figure 5.18 Quantitative analysis of TGF-β expression across early, intermediate, and late passage number groups across three iPSC lines at the pluripotent stage prior to differentiation (N = 4 independent batches).....214

Figure 5.19 Quantitative analysis of Nodal expression across early, intermediate, and late passage number groups across three iPSC lines at the pluripotent stage prior to differentiation (N = 4 independent batches).....216

Figure 5.20 Quantitative analysis of SHH expression across early, intermediate, and late passage number groups across three iPSC lines at the pluripotent stage prior to differentiation (N = 5 independent batches).....217

Figure 5.21 Quantitative analysis of WNT3A expression across early, intermediate, and late passage number groups across three iPSC lines at the pluripotent stage prior to differentiation (N = 4 independent batches). 218

Figure 5.22 Representative images of the capability of combined UV micropatterning and preconditioning treatments to improve or alter retinal differentiation across three cell lines after 4 weeks of differentiation. 221

Figure 5.23 Quantification of the average number of vesicles produced (left) and the fold-change within paired samples (right) of combined micropatterning and preconditioning (PC) treatments, non-treated micropatterned controls, and non-treated, non-micropatterned controls across three cell lines after 4 weeks of differentiation..... 223

Figure 5.24 Quantification of the average number of GFP+ regions produced (left) and the fold-change within paired samples (right) of combined micropatterning and preconditioning treatments, non-treated micropatterned controls, and non-treated, non-micropatterned controls in SIX6-GFP reporter cell lines after 4 weeks of differentiation..... 225

Figure 5.25 Representative images of the capacity of combined micropatterning and early RA treatments (Day 6 – 12) to improve retinal differentiation across three cell lines after 4 weeks of differentiation. 229

Figure 5.26 Quantification of the average number of vesicles produced (left) and the fold-change within paired samples (right) of combined micropatterning and RA treatments (Day 6 – 12), non-treated micropatterned controls, and non-treated, non-micropatterned controls across three cell lines after 4 weeks of differentiation..... 232

Figure 5.27 Quantification of the average number of GFP+ regions produced (left) and the fold-change within paired samples (right) of combined micropatterning and RA treatments (Day 6 – 12), non-treated micropatterned controls, and non-treated, non-micropatterned controls in SIX6-GFP reporter cell lines after 4 weeks of differentiation.....236

List of Tables

Table 3.1 Prepolymer formula for PEG-based hydrogels.....57

Table 5.1 Treatments applied to retinal differentiation protocol 172

Table 5.2 Primer designs for qPCR experiments.....174

List of Abbreviations

ESC	embryonic stem cell
E6	essential 6 cell culture media
E8	essential 8 cell culture media
DMEM	Dulbecco's modified eagle's medium
GMP	Good manufacturing practice
hESC	human embryonic stem cell
hiPSC	human induced pluripotent stem cell
hPSC	human pluripotent stem cell
iPSC	induced pluripotent stem cell
PBS	phosphate-buffered saline
PDMS	polydimethylsiloxane
PEG	polyethylene glycol
PIM	proneural induction media
PSC	pluripotent stem cell
RDM	retinal differentiation media
RPE	retinal pigment epithelium

TCP	tissue culture plastic
UV	ultraviolet
Vis	visible
2D	2-dimensional
3D	3-dimensional

Thesis Abstract

This thesis aimed to develop and characterise novel biophysical and biochemical approaches to influence the self-organisation of retinal vesicles from two-dimensional (2D) confluent stem cell cultures. This work addresses a critical need in the field of regenerative medicine for retinal diseases, which affect millions worldwide and often lead to irreversible vision loss. Current treatments for retinal degenerative diseases, while beneficial, are limited in their ability to restore vision once photoreceptors are lost. As such, cell replacement therapy using photoreceptors derived from stem cell-derived retinal tissues, known as retinal organoids, has emerged as a promising avenue for vision restoration, showing encouraging results in preclinical studies. However, the translation of this technology to clinical applications faces significant hurdles, primarily due to challenges in scalability, reproducibility, and automation capacity of current organoid production methods. These limitations stem from the inherent variability and labour-intensive nature of traditional organoid culture techniques. To address these challenges, we hypothesise that bioengineering-based methods, with a focus on micropatterning techniques, can be leveraged to exert greater control over the formation of retinal vesicles—the initial stage of retinal organoids. Specifically, we investigate whether these approaches can spatially define vesicle formation, a crucial step towards enabling automation and increasing the throughput of retinal organoid generation.

Our study employs a multifaceted approach, combining biophysical manipulation through micropatterning with biochemical modulation of signalling pathways known to be crucial in retinal development. Using novel methods developed in this thesis, we demonstrate that retinal vesicle formation can be spatially patterned in a defined and predictable manner. This finding represents a significant advance in controlling the complex process of self-organisation in stem cell cultures, potentially paving the way for more standardised and efficient organoid

generation protocols. Furthermore, we show that biochemical modulation strategies, previously established in three-dimensional (3D) aggregate-based cultures, can be translated to our 2D confluent monolayer-based culture system. This finding bridges the gap between different culture paradigms and suggests that insights from 3D systems can inform the optimisation of 2D-to-3D transition cultures. Additionally, we develop and characterise new biochemical modulation regimens that have not been previously studied in the generation of retinal vesicles. These novel approaches expand the tools available for directing retinal tissue development *in vitro* and may offer new insights into the molecular mechanisms governing retinal development.

A key strength of our study lies in its comprehensive approach, utilising three different cell lines and parallel non-treated control cultures. This study design allows us to demonstrate how the success of biophysical or biochemical modulation may be intricately linked to the initial state of the cell culture and its inherent propensity to self-organise into vesicles. By elucidating these relationships, we provide crucial insights into the parameters required for successful retinal vesicle formation, potentially enabling more targeted and efficient protocols tailored to specific cell lines or culture conditions.

The significance of this thesis extends beyond its immediate findings. By informing our understanding of the parameters required to induce and spatially define 3D vesicle growth from 2D cultures *in vitro*, we lay the groundwork for more controlled and predictable organoid production. Moreover, our exploration of the biochemical support necessary for this process, both with and without spatial patterning, offers a nuanced view of the interplay between physical and chemical cues in directing stem cell fate and tissue morphogenesis. Crucially, all methods developed in this work are compliant with current Good Manufacturing Practice (cGMP) protocols, a vital consideration for potential clinical translation.

The work in this thesis represents an advancement towards potentiating the clinical translation of retinal organoid cultures for high-throughput applications. By addressing key challenges in organoid production, including spatial control, reproducibility, and scalability, our findings have broad implications for disease modelling, drug development, and cell replacement therapies that can be translated towards other tissue types. As future research continues to refine these techniques and elucidate the complex processes governing organogenesis, we move closer to realising the full potential of stem cell-derived therapies for treating degenerative diseases and restoring vision to millions worldwide.

Chapter 1:
Introduction

1.1 Significance of stem cell-derived organoids

Cell culture plays a key role in modern biological research and medical applications. It provides a controlled and consistent environment for studying cellular behaviour, testing pharmaceutical compounds, and developing therapeutic interventions. Particularly, complex tissues that resemble the host species' organs can be grown *in vitro* through modern techniques such as stem cell and organoid technology. Human stem cell-derived organoids are imperative as human models for testing new compounds and/or gene therapies, improving our understanding of developmental biology, and providing a source of functional cells for cell replacement therapies. Despite its importance, without introducing complicated devices or materials, traditional cell culture methods often suffer from low throughput and poor reproducibility, limiting their utility in large-scale, high-precision applications.

High-throughput cell culture methods are needed to enhance the consistency and production efficiency of *in vitro* models such as organoids. However, ensuring these high-throughput methods can successfully and effectively generate the desired tissues in a reproducible and scalable manner is a critical challenge. As such, new methods to improve the generation of consistent and high-quality organoids are required. Importantly, to potentiate the development of clinically relevant therapeutic products, these methods should comply with current Good Manufacturing Practice.

1.2 Overview of the thesis

Chapter 2 reviews the literature regarding the generation of retinal tissues *in vitro*, focussing on applications for cell replacement therapies. Here, the current shortcomings of scalable retinal organoid formation and the potential of micropatterning techniques to address these limitations are discussed.

Chapter 3 describes the fabrication of micropatterned glass substrates using PEG-based polymer and two different methods of UV photo-polymerisation. The first method comprises a custom-built laser-based printing system while the second method explores a newly developed lamp-based method.

Chapter 4 explores new methods of micropatterning, focussing on tissue culture plastic surfaces. Here, we develop a unique method to pattern cell culture wells to better control cell attachment and enable the self-organisation of retinal vesicles from 2D confluent monolayer cultures.

Chapter 5 analyses different pathways of biochemical modulation to improve the generation of retinal vesicles from 2D confluent monolayer cultures. Various regimens are tested and evaluated using three different iPSC lines, including two fluorescent reporter cell lines. Select treatments are subsequently combined with our developed micropatterning method, integrating both biochemical and biophysical cues to enhance retinal vesicle formation.

Chapter 6 presents the conclusions from this thesis, acknowledges the limitations of the research performed, and makes recommendations for future work.

1.3 Hypothesis and aims

1.3.1 Hypothesis

The development of techniques to better control the initial state of pluripotent stem cell cultures, such as methods of micropattern-induced spatial confinement and early biochemical modulation, will enable the spatially defined generation of retinal vesicles from 2D confluent monolayer cultures for clinical applications.

1.3.2 Aims

The specific aims of this thesis are:

1. To develop a method that controls the initial spatial distribution of pluripotent stem cell colonies on 2D surfaces and supports the long-term differentiation and self-organisation of retinal vesicles from confluent monolayer cultures.
2. To evaluate the effect of biochemical modulation of various signalling pathways in enhancing the generation of retinal vesicles from confluent monolayer cultures.

Chapter 2: Manipulating culture conditions for organoid applications

2.1 Introduction

Scalable and reproducible cell culture methods are essential for accurate human models *in vitro* and for generating therapeutic cell products in sufficient quantities while maintaining their quality and safety. These therapies hold promise for treating a variety of diseases, from cancer to degenerative disorders. However, their widespread adoption hinges on the ability to reliably produce healthy and/or therapeutic cells on a large scale with minimal human intervention while complying with GMP (Good Manufacturing Practice) procedures. Importantly, stem cell and organoid technologies offer a means to conduct studies without the need for animal models or invasive procedures on humans. This not only addresses ethical concerns associated with animal and human experimentation but also circumvents some limitations of these models, such as species differences and individual variability. In light of the above, there is a pressing need for high-throughput, reproducible cell culture methods.

2.2 Creating *in vitro* human models using stem cells

Advancements in tissue engineering and regenerative medicine are pivotal in the repair and/or regeneration of tissues and organs. These fields utilise biological techniques, such as cell culture, to grow tissues *in vitro*, providing potential solutions to the limitations of traditional transplantation methods. Moreover, the innovative application of biocompatible materials and devices has prolonged the lifespan of countless individuals. As cells are the building blocks of tissues and organs, their role in these fields can be imperative for the regeneration or replacement of human tissues that resemble the native architecture and function as closely as possible. The emergence of stem cell technology[1-3] has been instrumental in this area. Pluripotent stem cells (PSCs), encompassing both embryonic stem cells (ESCs) and induced pluripotent stem cells (iPSCs), offer a renewable source of cells that can be manipulated

towards almost every tissue type in the human body. PSCs have the potential for indefinite self-renewal, representing valuable cell sources to replace diseased or injured tissues. Interest in stem cell therapeutics has evolved tremendously in the last decade with the advent of iPSCs, attained from somatic cell sources rather than early-stage embryos as required with ESCs.

Furthermore, the development of organoids, miniaturised tissues that replicate the architecture and functionality of organs, has expanded the complexity and functionality of stem cell technologies. These three-dimensional structures, derived from pluripotent stem cells such as iPSCs, mimic the architecture and functionality of organs. This ability to replicate the complex structure of organs sets organoids apart from traditional two-dimensional cell cultures and offers a renewable source of cells and tissues.

The importance of organoids lies in their potential to more closely resemble human tissues compared to animal models and their relative ease of accessibility compared to human tissue explants. Organoids can serve as accurate models for studying organ development, disease progression, and drug response (Figure 2.1). For instance, organoids can be used to model diseases at the cellular level, providing insights into the mechanisms of various conditions, including inherited or acquired disorders. Moreover, these tissues hold promise for personalised medicine. By creating organoids from a patient's own cells, clinicians can test the effectiveness and safety of drugs, reducing the risk of adverse reactions, and increasing the potential likelihood of successful treatment. These approaches may revolutionise how we treat diseases, moving away from current universal and broad-acting approaches towards more individualised and targeted therapeutics.

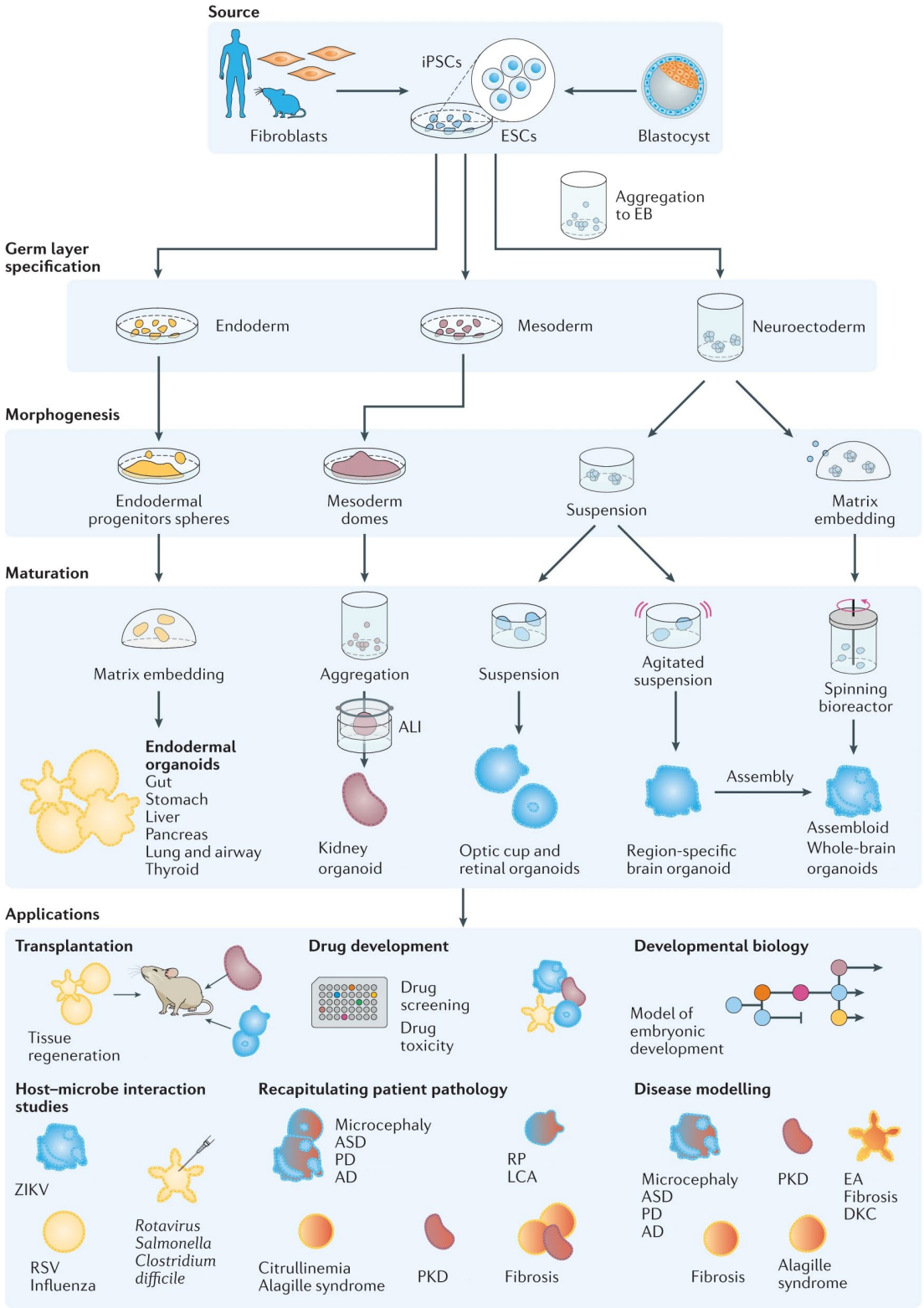

Figure 2.1 Overview of organoid research, including examples of organoid generation methods, tissue types, and downstream applications. Adapted from Hofer & Lutolf[4].

Beyond the modelling of tissue interactions, organoids show potential as a cell source to replace damaged tissue in patients. For example, current research has explored the use of intestinal organoids to as methods to treat conditions such as inflammatory bowel disease[5], brain organoids for poststroke repair[6], and retinal organoids to treat inherited blindness[7]. In particular, the development of retinal organoids has seen significant progress over the past decade, particularly in terms of differentiation efficiency and degree of developmental maturity. The advanced nature of retinal organoids lies in their ability to closely mimic the structure and function of the human retina and recapitulate early events in embryology, such as optic vesicle evagination and invagination. As such, these tissues have broad application prospects in disease modelling and drug development. Importantly, the eye is considered an immune-privileged tissue to a certain degree, with specialised insulation of the visual system from local and systemic immune provocation to preserve the homeostatic functions of the highly specialised neural retinal cells. This favourable immune privilege and the relatively ease of access of the site of transplantation has further encouraged research in cell therapies derived from stem cell and organoid sources. However, retinal organoid protocols can be lengthy and resource-heavy compared to other organoid systems due to the time required for retinal cell differentiation and maturation. These features collectively position retinal organoids amongst the intermediate of research in cell replacement therapies, after lung, brain, gut, kidney, and liver organoids (Figure 2.2).

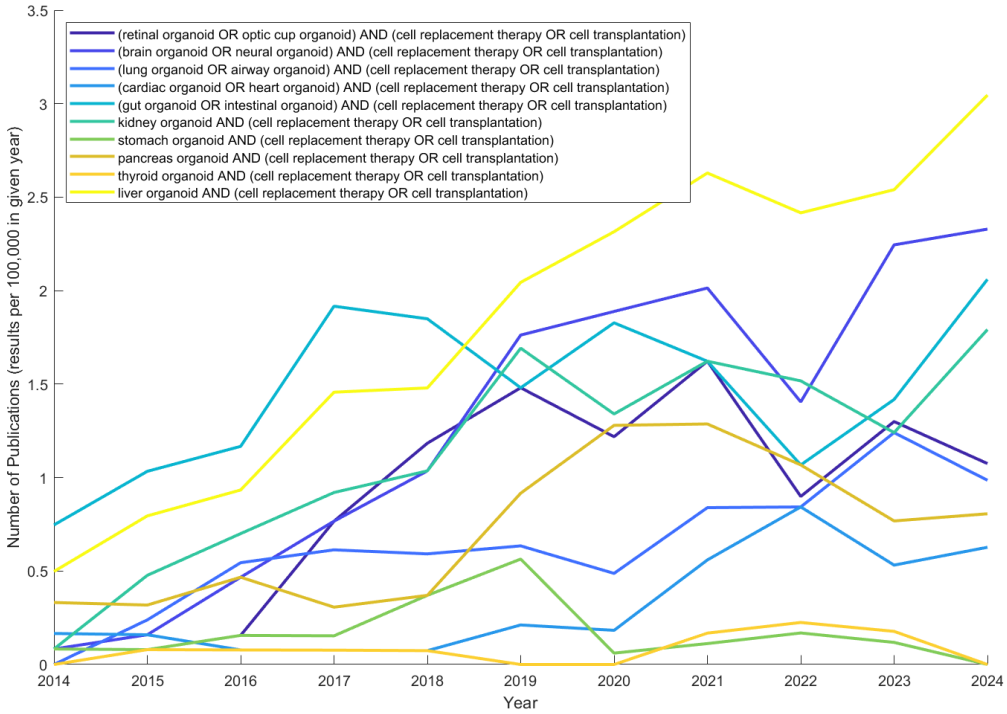

Figure 2.2 Number of publications relating to organoids of different tissue types and cell replacement therapies; relative to the number of publications produced in the given year. Data sourced from Pubmed (https://pubmed.ncbi.nlm.nih.gov/).

Retinal organoids mimic the formation of the retina from neuro-ectoderm, the outermost embryonic germ layer. The ectoderm forms two optic vesicles, the distal portion of which folds inward to form the optic cups. This process occurs during the third to eighth weeks following fertilisation, a critical period when most organs start to develop. The ability of retinal organoids to recapitulate these intricate developmental events further highlights their utility in understanding human development. Retinal organoids closely resemble the retinal structure and can include all cell types of the human retina. This allows for the potential for sorting of desirable cell types from the cultured organoids for transplantation or further studies.

Overall, organoids represent a significant step forward in our ability to study and treat diseases. As organoid techniques are continually refined, their importance in medicine and research is likely to grow. However, significant challenges still remain, such as ensuring the survival and

integration of these organoid-derived cells and tissues post-transplantation. Moreover, the scalability and reproducibility of these tissues *in vitro* are significant obstacles to clinical translation. To overcome these challenges, many engineering approaches are being investigated to enhance cell culture consistency, throughput, and complexity (Figure 2.3).

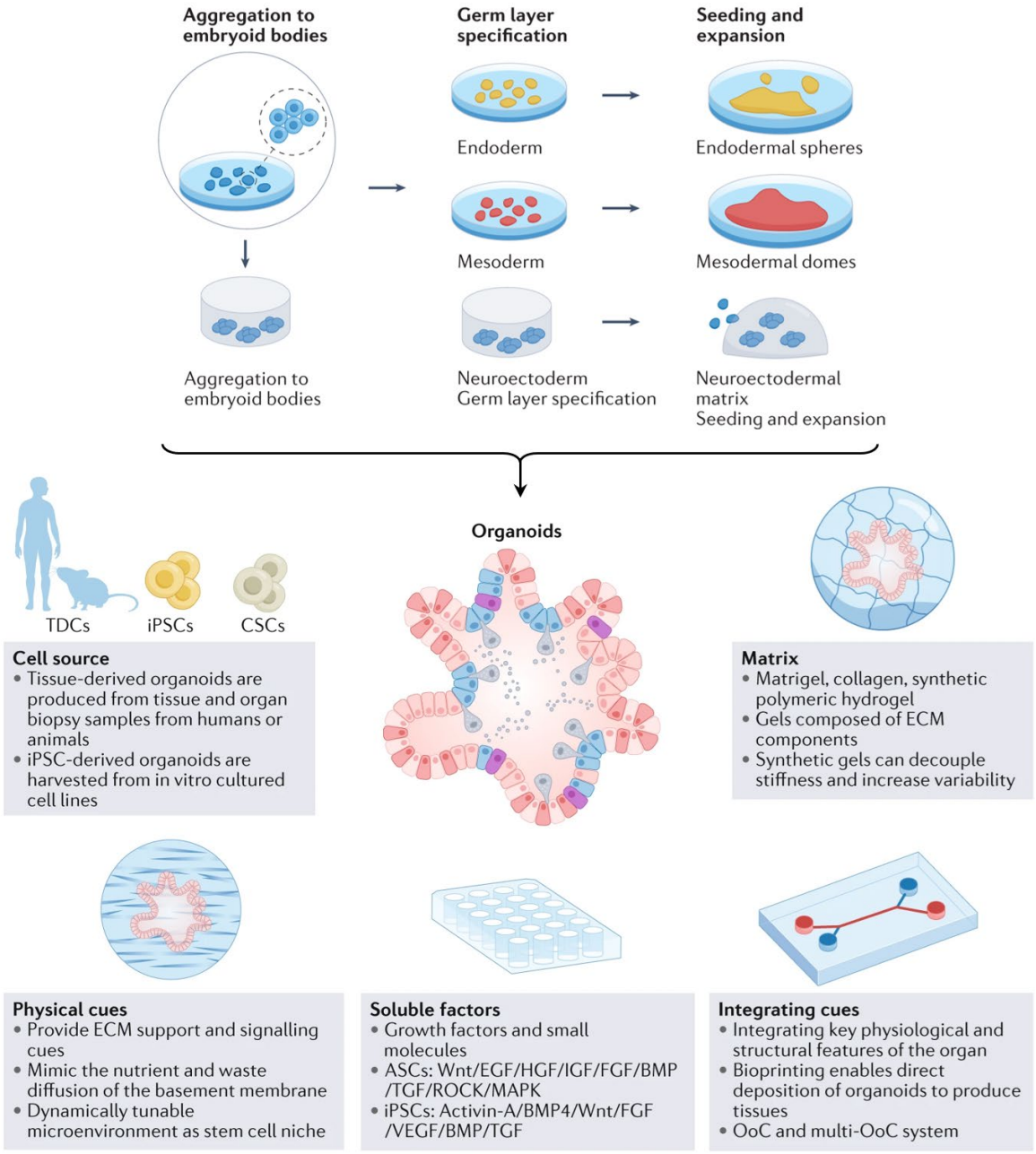

Figure 2.3 Considerations for generating organoids from different embryoid body-derived germ layers, including cell source, matrix, physical cues, soluble factors, and integrating cues. Adapted from Zhao et al[8].

2.3 Retinal tissues and organoids for clinical applications

Retinal degenerative disorders represent a group of diseases characterised by vision loss affecting the retina, the light-sensing tissue at the back of the eye containing photoreceptor cells and other interneurons. Moreover, diseases affecting the centrally located macula substructure, which contains a high density of colour-sensitive cone photoreceptors responsible for high visual acuity, are also usually associated with damage to the supporting retinal pigment epithelium (RPE) layer. Retinal degenerative diseases cause progressive blindness, commonly through injury and atrophy of photoreceptors, and available treatments are currently limited in their capacity to restore tissue loss. Inherited retinal diseases can potentially benefit from gene therapies and pharmacological interventions if treatment is delivered at early to mid-stages of disease. However, at advanced stages this would be ineffectual due to their inability to restore the significant retinal cell loss which occurs in late-stage disease. Treatments for acquired multifactorial diseases, such as age-related macular degeneration (AMD), which alone affects 1 in 10 people over the age of 60[9], are also dependent on the stage and status of the condition, with challenges in the pharmaceutical treatment of the more prevalent non-neovascular subtype[10].

Cell replacement therapy, particularly the transplantation of RPE and PR cells, is a promising approach to treating retinal degenerative disorders[11,12]. By mimicking natural eye development *in vitro*, retinal tissues can be derived from PSCs in the form of cell sheets or retinal organoids (ROs), providing a renewable source of healthy retinal and RPE cells. These functional tissues, which can comprise diverse neuroretinal cell types[13], can be used in cell therapy approaches by transplanting mixed or isolated cell populations[14]. Already, the transplantation of RPE cells has demonstrated visual improvements in clinical trials involving patients with severe AMD[15,16]. However, despite favourable outcomes in preclinical models, the transplantation of

PR cells remains a challenge[7,17]. Recently, the first clinical trial focusing on the safety of transplanting iPSC-derived tissues comprising PR cells has commenced[18,19].

Protocols harnessing PSCs to generate multicellular retinal tissues similar to that of the natural retina have advanced prospects of photoreceptor replacement therapies, however, they remain limited in their scalability and reproducibility—a prerequisite for clinical translation. Improved control over the development, survival, and morphological integrity of stem cell-derived tissues is critical in generating functional stem cell products that better mimic *in vivo* retinal development. Engineering approaches to enhance cell culture consistency, throughput, and complexity have been proposed to address these challenges[20]. These principles usually employ biomaterial or device-based technical innovations to control processes or environments beyond what traditional methods can offer. Moreover, this expands to automated cell culture systems, such as robotics and artificial intelligence, that offer enhanced control over the maintenance, differentiation, and maturity of stem cell cultures; attributes that are necessary to develop better *in vitro* models and will be critical in generating clinical-grade stem cell products that mimic *in vivo* retinal development and cellular functionality. As such, there is an evident gap in reproducible and scalable organoid protocols that can be easily automated, warranting further work in this field.

2.3.1 Retinal anatomy

The mature retina has an intricate cellular composition with functional diversity specified by numerous genes. The neural retina is a stratified structure of seven layers, organised in the following order from the inner to outer eye: 1) nerve fibre layer, 2) ganglion cell layer, 3) inner plexiform layer, 4) inner nuclear layer (INL), 5) outer plexiform layer, 6) outer nuclear layer (ONL), and 7) photoreceptor outer segment layer (Figure 2.4). The ONL contains photoreceptor cell bodies while the INL contains cell bodies of interneurons: amacrine, bipolar,

and horizontal cells. The ganglion cell layer comprises the cell bodies of retinal ganglion cells (RGC), which couple the retina to the central nervous system via axonal projections originating from the nerve fibre layer which then converge along the optic nerve. Interneurons synapse with the photoreceptors and RGCs in the outer and inner plexiform layers, respectively. The cone-dense fovea centralis, the central region of the macula, possesses a specialised architecture with fewer interneurons to enable direct stimulation and less obstruction for sharp visual acuity[21].

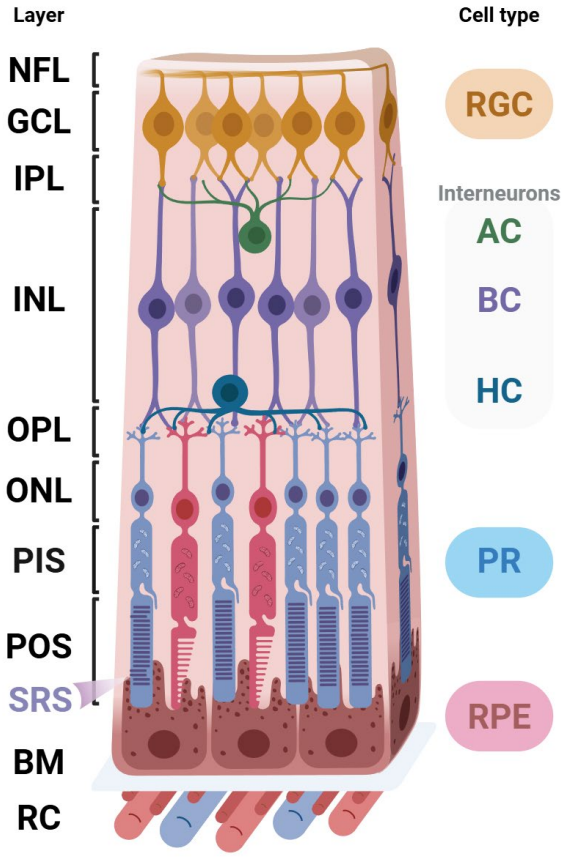

Figure 2.4 Cellular architecture and layers of the adult human retina, including key cell layers and cell types.

Cellular architecture and layers of the mature retina; RGC, retinal ganglion cells; AC, amacrine cells; BC, bipolar cells; HC, horizontal cells; PR, photoreceptors; NFL, nerve fibre layer; GCL, ganglion cell layer; IPL, inner plexiform layer; INL, inner nuclear layer; OPL, outer plexiform layer; ONL, outer nuclear layer; PIS, photoreceptor inner segments; POS, photoreceptor outer segments; BM, Bruch's membrane; RC, retinal choroid. Created with BioRender.com.

Although the neural retina and the RPE layer are anatomically in close apposition, a pseudo region can be created when these two structures separate due to damage or direct injection of products, creating the subretinal space (SRS). The SRS is recognised as the ideal position to deliver therapeutics such as gene therapies or grafts of photoreceptor and RPE cells. In the SRS, transplanted photoreceptors can connect with the host's existing interneurons while RPE cells can restore the endogenous epithelial monolayer, establishing a process known as cellular integration. The RPE monolayer has a distinct pigmented, hexagonal morphology, forming tight junctions which comprise the outer blood-retina barrier and regulate the movement of nutrients to and from the neural retina and the vascularised choroid[22]. RPE cells support healthy visual function through secretions such as pigment epithelium-derived factor (PEDF) and vascular endothelial growth factor (VEGF)[23]. The apical microvilli of RPE functions in the maintenance of photoreceptor outer segments and chemical scrubbing of free radicals, whereby RPE dysregulation is associated with oxidative stress and visual disorders[24,25]. The underlying retinal choroid is essential for the flow of nutrients and oxygen and is separated from the RPE via Bruch's membrane, a dynamic semi-permeable collagenous layer continuous with the RPE basement membrane[26]. The Bruch's membrane serves to passively regulate biomolecule exchange between the retina and the vascularised retinal choroid.

2.3.2 Retinal development

Human eye development is a process tightly regulated by key genes, driving essential morphological changes that play a pivotal role in the formation of the eye field in the neural plate and the emerging bilateral optic vesicles and optic cups, which eventually form the neural retina and supporting RPE (Figure 2.5). Understanding retinal development is fundamental to the effective generation of stem cell-derived tissues. Early structures that form the retina are present at week two of development in the neural tube (12-20 days). The downstream

development of these early retinal structures is partly mediated by crosstalk with cells of the neural crest and surface ectoderm[27] (Figure 2.6).

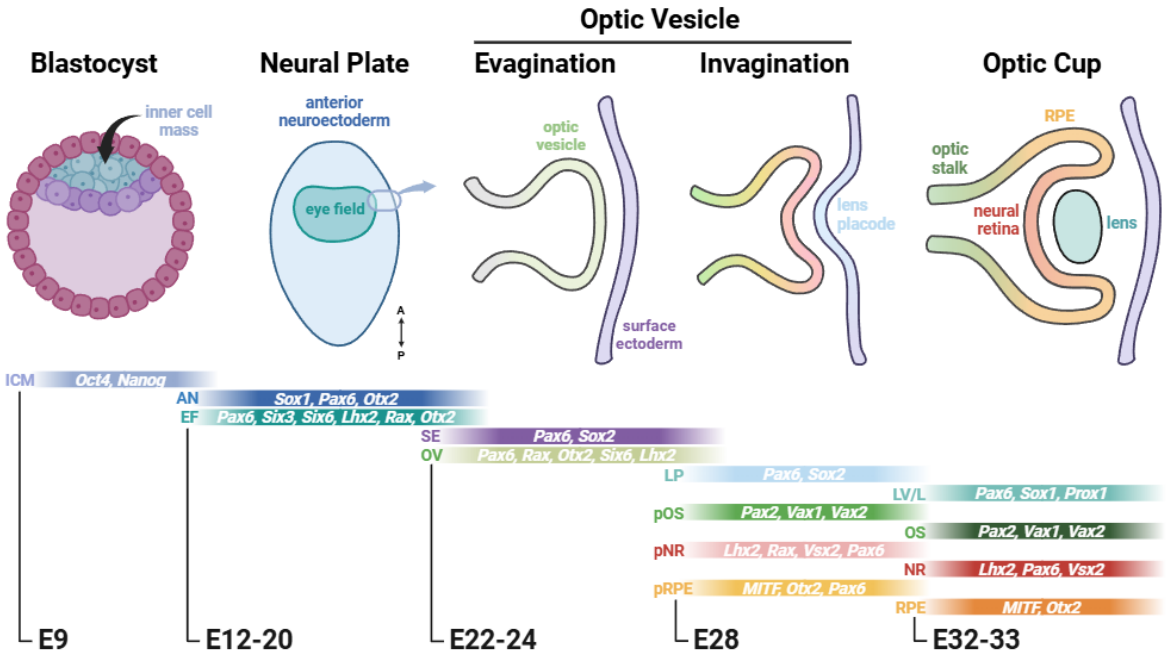

Figure 2.5 Development of the human eye, including the key markers involved and approximate time points in days from conception.

The eye field forms from the neural plate (E12-20), progressing to bilateral optic vesicles (E22-24), where retinal progenitor cells polarise towards neural retina or RPE (E28). The optic stalk develops from the pinching of the ventral optic cup, providing passage for retinal ganglion cell axons to connect to the optic nerve (E32-33); ICM, inner cell mass; AN, anterior neuroectoderm; EF, eye field; SE, surface ectoderm; OV, optic vesicle; pOS, presumptive optic stalk; pRPE, presumptive retinal pigment epithelium; pNR, presumptive neural retina; LP, lens placode; OS, optic stalk; RPE, retinal pigment epithelium; NR, neural retina; LV/L, lens vesicle/lens. Created with BioRender.com.

In humans, retinogenesis begins at the late gastrula stages from the anterior region of the neural plate, with the specification of a region known as the eye field. After approximately three weeks of gestation, bilateral expansion of the eye field generates symmetric indentations known as optic sulci, establishing the optic vesicles (22-24 days)[28]. The optic vesicles evaginate towards the surface ectoderm to form the characteristic spherical structure of the eye, thereby initiating

the polarisation of retinal progenitor cells (RPCs) of the presumptive neural retina and neighbouring presumptive RPE. The subsequent invagination of the optic vesicle forms the optic cup, comprising the neural retina in the inner layer and the RPE in the outer layer (28 days). During this process, the optic stalk develops from the pinching of the ventral optic cup (32-33 days), providing passage for RGC axons to project via the optic nerve. The RPCs of the neural retina then stratify into the layers of the retina, with cells differentiating in the following order: RGCs, horizontal cells, cone photoreceptors, amacrine cells, rod photoreceptors, bipolar cells, and Müller glia cells.

Identifying the role of key genes instructs our understanding of retinal development. The retina is derived from the neuroectodermal lineage, with the SOX gene family playing broad roles in regulating neural differentiation and progenitor maintenance[29,30]. SOX1 plays a central role in neural determination[31,32], with early expression in the anterior neural plate and later downregulation during eye field and optic vesicle formation[33], where SOX2 plays a wider role[34].

The key transcription factors involved in eye field specification have been well-characterised, including PAX6, RAX, SIX3, LHX2, OTX2, and SIX6. The regulation of PAX6 is critical in eye development, whereby PAX6 null mice have a complete lack of eyes[35] and PAX6-deficient mice develop with dosage-dependent eye abnormalities[36]. Similarly, the optic cup and lens placode fail to form in LHX2 knockout mice, while the optic nerve and optic tract fail to form in RAX knockout mice; both resulting in anophthalmia, a birth defect resulting in the absence of one or both eyes[37,38]. SIX3 and SIX6 are closely related genes that share similar expression patterns specific to the early onset of the developing vertebrate eye field, where SIX6 expression can be observed as early as the gastrula stages[39,40]. In mice studies, the ectopic expression of SIX6 in RPE cells has the potential to induce the activation of neural retina-

associated genes, highlighting its functions in promoting retinal development[39]. MITF and VSX2 serve reciprocal roles in the specification of RPE and the neural retina, respectively, whereby the loss of MITF can be induced by the ectopic expression of VSX2 and result in the absence of pigmentation[41]. During the stage of photoreceptor development, RAX inactivation in postnatal mouse retinas demonstrated reduced expression of rod- and cone-specific genes, reduced number of cone cells, and impaired phototransduction of photoreceptor cells[42].

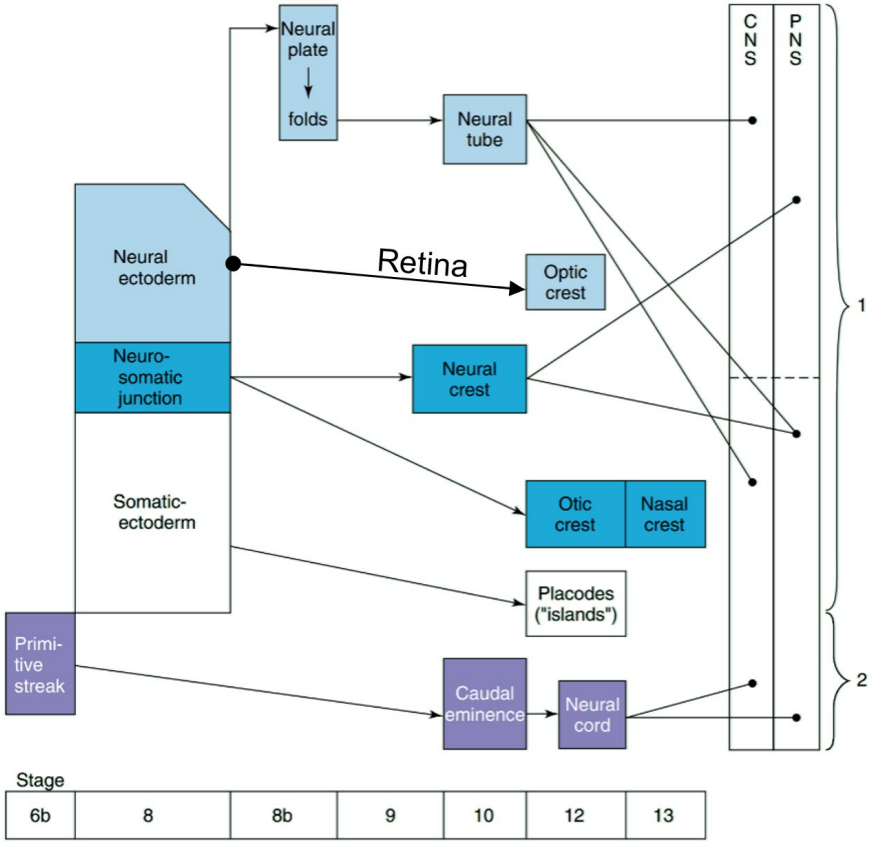

Figure 2.6 Development of the human brain as related to Carnegie stages. The development of the retina from the neural ectoderm occurs starting from approximately stage 8 at Day 21 to 28 post-fertilisation. Adapted from O'Rahilly & Fabiola[44].

Accordingly, the successful development of the retina's stratified structure and proper connections between different neuronal cell types, crucial for retinal function, rely heavily on the coordinated action of multiple transcription factors[43]. Our understanding of developmental

biology has instructed many of the current advances in the stem cell field and the differentiation of various cells and tissues, particularly the generation of organoids.

2.3.3 Retinal organoid generation

Retinal organoids mimic the retinal niche and generate more mature and functional cells compared to standard 2D monolayer cultures. These tissues can mature in suspension with stratified neural retinal layers forming via stochastic self-organising multicellular interactions using guided or non-guided differentiation protocols. Protocols for deriving retinal organoids from PSCs commonly involve initiating the differentiation of 2D adherent cultures[45,46], 3D embryoid body (EB) suspensions[47,48], or combinations of both (e.g. 3D-2D-3D culture)[49-52] using a neural or retinal differentiation media (Figure 2.7). Subsequently, tissues resembling optic vesicles are commonly manually dissected and placed into low-attachment plates for long-term culture, where precursors of retinal cells, including RPE and photoreceptors, emerge to then be matured in a retinal maturation medium.

Characterisation of various protocols elucidates that retinal organoids can recapitulate the development and proportion of cell types of the foetal and adult retina to a certain degree[53]. Importantly, retinal organoid-derived photoreceptors exhibit both morphological and functional attributes, including photoreceptor outer segment structures[54] and wavelength-specific light responses[55]. However, retinal organoids still lack architectural attributes, including vascularisation and a complete RPE monolayer in close apposition to photoreceptors. RPE cells are either absent from retinal organoids or distributed in asymmetric clusters, leaving photoreceptor outer segments—the most exterior layer of mature retinal organoids—directly facing culture media[13]. Despite these limitations, the functional and structural features of retinal organoids have proved invaluable as reliable *in vitro* tools for disease modelling and drug development and as a scalable source of transplantable photoreceptor cells. In comparison, the

relatively straightforward induction of hPSCs into RPE monolayers has enabled the commencement of multiple clinical studies[12].

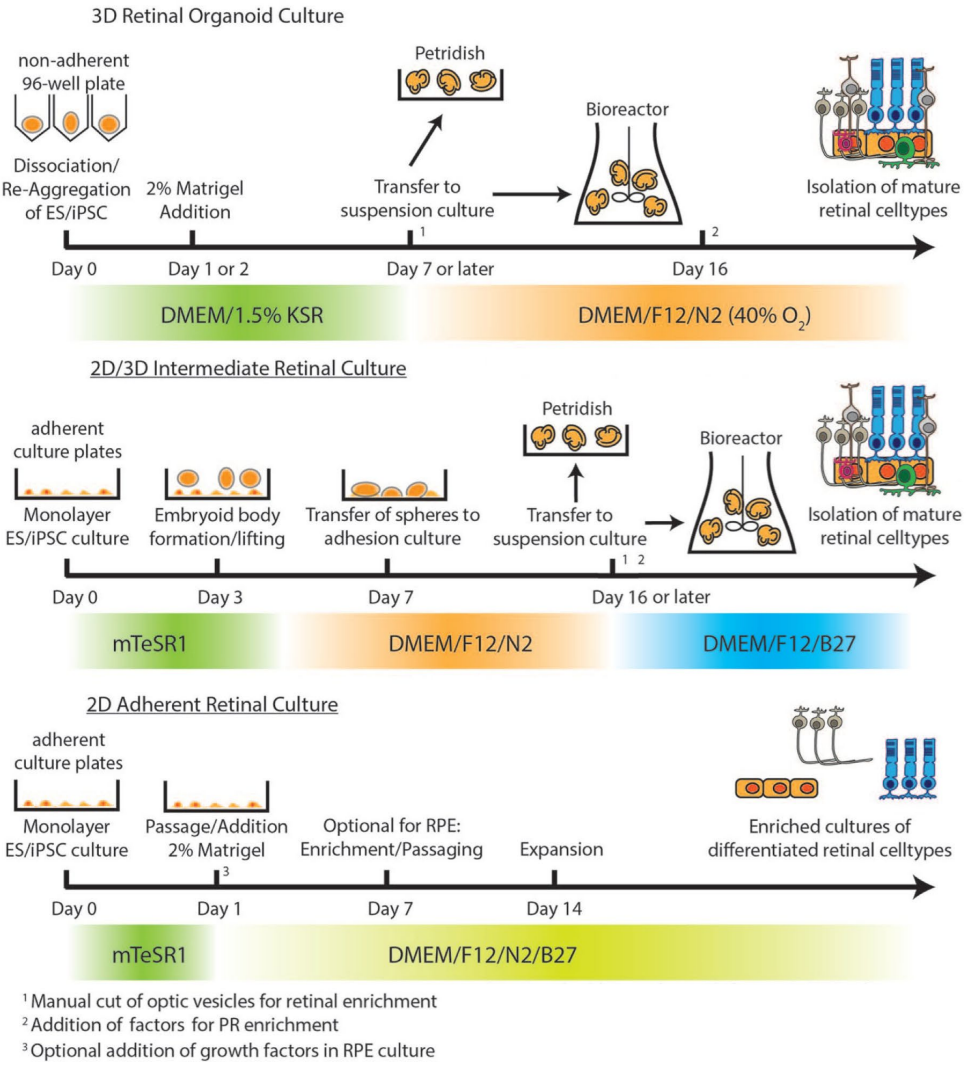

Figure 2.7 Common methods to generate retinal tissues and organoids. Adapted from Oswald, et al.[56]

2.3.4 Retinal cell transplantation

Transplantation studies of neural retinal cells in preclinical models, including rodents[57-61] and non-human primates[62-64], have demonstrated encouraging evidence for the potential of cell therapies in treating retinal degeneration. Early studies in the 1990s to early 2000s reported the safety of foetal- and cadaveric-derived retinal cell injections in patients with retinal

degeneration[65-68], albeit with mixed outcomes of visual maintenance and/or restoration[69]. Encouragingly, numerous clinical trials involving transplanting hPSC-derived RPE have recently progressed[15,16,70,71], and safety evaluations of hPSC-derived retinal cell sheet transplantation are underway[18].

Retinal cell replacement therapies can be delivered either as an intact cell sheet or as suspended cells in a bolus injection, both presenting benefits and drawbacks (Figure 2.8). Cell suspensions offer surgical simplicity and ease of processing, though they do not maintain the native 3D architecture of the RPE monolayer or stratified retina, resulting in a disorganised cell mass lacking polarity[72]. Cell sheets may be transplanted with or without supporting materials, where the latter may result in the formation of rosette-like structures[73]—a phenomenon commonly associated with suboptimal cell integration. Biomaterial scaffolds can offer a dual role in retinal tissue engineering, acting both to deliver cells and to facilitate functional integration with the existing or residual retinal circuits.

Given that degenerative retinal diseases often lead to cell loss, particularly of the light-sensitive photoreceptors and supporting RPE, scaffolds must facilitate comparable cell densities to the healthy retina. Likewise, long-term cell survival following transplantation is crucial[74]. At the macula, cone photoreceptors, rod photoreceptors, and RPE cells have physiological densities of 160,000, 110,000, and 4,200 cells per mm^2, respectively. These densities decrease at the peripheral retina to 4,200, 35,000, and 1,600 cells per mm^2, respectively[75,76]. Achieving the delicate balance between mechanical properties, surgical handling, and cell density is critical for successful retinal tissue engineering and transplantation.

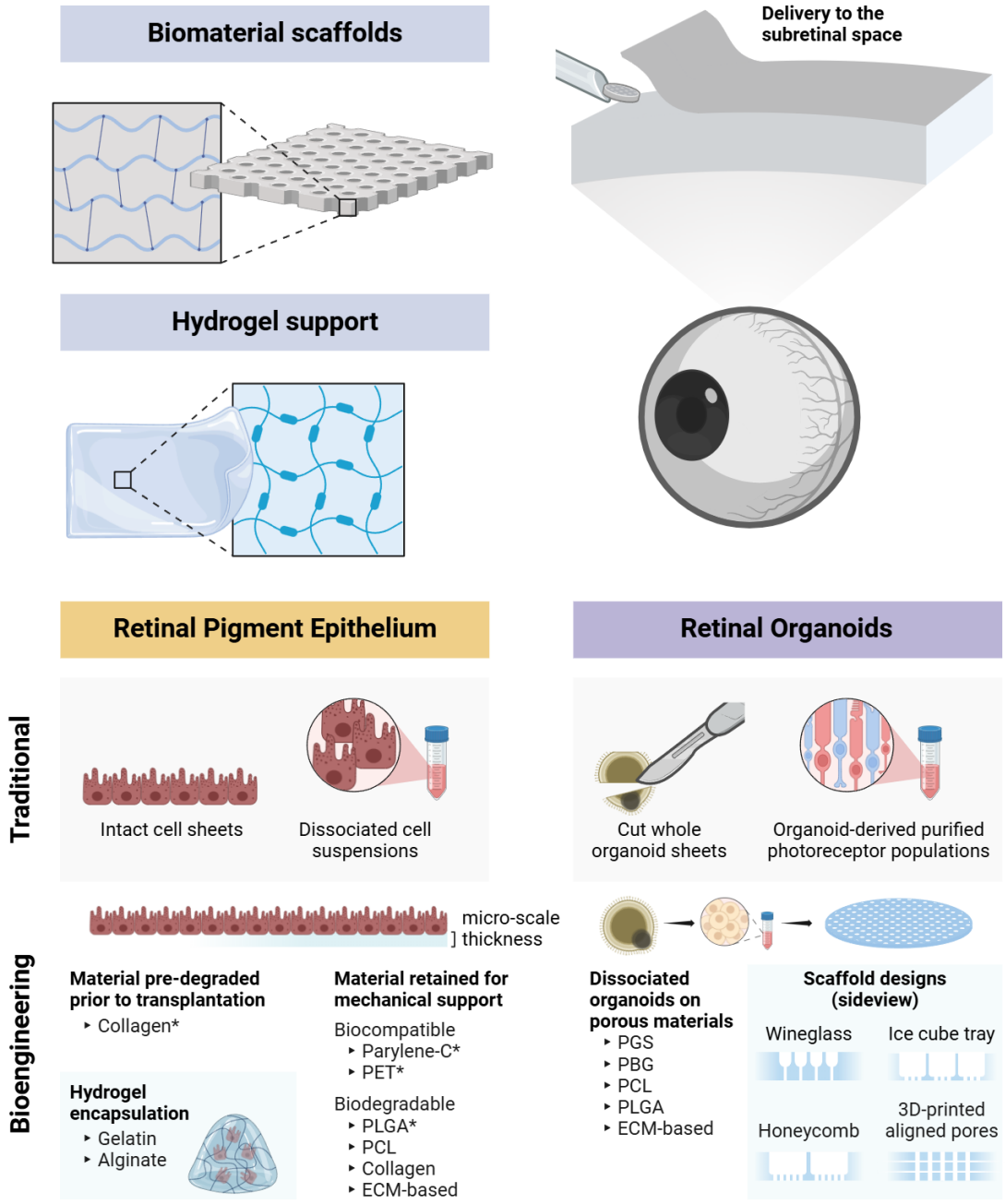

Figure 2.8 Overview of the approaches to deliver retinal cells to the subretinal space via bioengineered and traditional methods.

Compared to traditional methods, which may not use biomaterials, scaffolds offer a way to support retinal cell growth and/or transplantation through thin polymer layers or hydrogel encapsulation[80,81]. Depending on the method of delivery, biomaterials may be degraded prior to transplantation[54] or maintained for longer-term mechanical support. Retinal pigment epithelium has been cultured on biocompatible materials such as Parylene-C, polyethylene terephthalate (PET), poly(lactic-co-glycolic acid) (PLGA), poly(caprolactone) (PCL),

collagen, and other extracellular matrix (ECM)-based polymers. Similarly, retinal organoid-derived cells have been dissociated and seeded onto porous biomaterials fabricated from poly(glycerol-sebacate) (PGS), polybenzyl glutamate (PBG), PCL, PLGA, and ECM-based materials. Complex scaffold designs aim to guide cell organisation reflecting that of the native retina, such as through micropatterned pores for cell alignment. Asterisks indicate materials currently or previously in clinical trials. Created with BioRender.com.

Clinical trials involving biomaterial scaffolds for RPE have demonstrated promising outcomes, including a two-year survival of functional donor hESC-derived RPE cells[77] and a certain degree of enhanced visual acuity[78]. However, most reported clinical studies employ inert, non-biodegradable porous scaffolds for cell delivery[15,16], albeit with thin membranous architectures ($\leq$ 10 μm thicknesses). The effect of long-term retention of these foreign materials currently remains unclear. Biodegradable materials may offer an alternative approach, facilitating gradual material degradation over time and minimising the risk of obstruction due to cellular debris accumulation in scaffold pores over time[79]. Regardless of the material choice, rigorous quality control remains essential to mitigate risks and maintain consistent scaffold performance.

2.3.5 Remaining hurdles to clinical translation

The stratified architecture of the neural retina presents a persistent challenge in the design of mimetic scaffolds. Historically, research has focussed on cultivating RPC populations within such scaffolds, a task complicated by the prior limited availability of RPCs, which were primarily obtained from foetal sources. Contemporary efforts have shifted towards utilising stem cell-derived RPCs, particularly from retinal organoids, and providing an engineered environment for cells to organise, differentiate, and mature. Stem cell-derived retinal tissues can develop native-like functions and maturity *in vitro*, offering scalability and accessibility that their foetal- or cadaver-derived counterparts lack. In particular, retinal organoid-derived

RPCs (retinal organoid-RPCs)[82-86] may possess advantageous functional attributes due to their capacity for self-organisation compared to RPCs grown using other methods; for instance, directly from hESCs (hESC-RPCs)[87] or iPSCs (iPSC-RPCs)[88]. Following the differentiation of retinal organoids, retinal organoid-RPC populations can be obtained through organoid dissociation or dissection.

Although stem cell-derived retinal tissues are a favourable source of transplantable cells, the consistency of generation and differentiation still requires improvement. Further research on parameters such as the optimal retinal organoid stage and maturity for populating scaffolds, particularly to facilitate easily transplantable architectures, may improve outcomes of donor-host integration. Moreover, the presence of appositional RPE could be critical in supporting neural retinal cell organisation pre-transplantation and survival post-transplantation. Methods to develop stratified retinal tissue sheets that have consistency across the plane of the scaffold and include a supporting RPE monolayer could provide an ideal graft for transplantation, particularly for patients affected by the loss of multiple cell types.

Importantly, clinical translation of photoreceptor transplantation is hindered by the suboptimal reproducibility and scalability of retinal organoid generation, further compounded by the inclusion of manual dissection steps in some protocols[89]. Heterogeneity in individual retinal organoids is observed within and between laboratories[89], highly implicated by the inherent stochasticity of PSCs as well as variability between cell lines[90]. As such, retinal organoids of the same age may exhibit variations in cellular composition and maturity, which can pose challenges for their clinical application. Although manual dissection at flexible time points (assessed through morphological features) may partially overcome this issue, it may further introduce human error and bias and risk of contamination. Moreover, the need to manually isolate retinal tissues from other cell types relies highly on researcher competency and

technique. Thus, methods to improve and automate the generation and isolation of these tissues are critical.

2.4 Methods to enhance the generation of retinal organoids

Considerable research on the optimal conditions for PSC-derived retinal organoids has informed our understanding of the environmental cues necessary for enhanced cell function and maturity[13,91,92]. As such, there have been significant efforts in refining retinal organoid protocols to improve differentiation and generation efficiency. Moreover, bioengineering methods to improve control of the culture environment and spatiotemporal parameters are currently emerging.

2.4.1 Modulation of known signalling pathways and gas concentrations

Methods to improve retinal differentiation generally involve the activation or inhibition of signalling pathways involved in retinal development. Retinal organoid protocols can be classified as unguided or guided, where the main difference is the amount of growth factors involved. Briefly, guided retinal differentiation involves the supplementation of culture media with growth factors or small molecules to regulate one or more signalling pathways, including WNT, SHH, FGF, NODAL, TGF-β, NOTCH, IGF-1, and BMP4[92,93] (Figure 2.9). Other supplemented factors that act on several pathways and improve tissue structure or distinct cell functions include taurine[49], retinoic acid[94], and foetal bovine serum[95] (Figure 2.10). Further specification or maturation of retinal cell types can be regulated through thyroid hormone signalling[96], neurotrophins[97], and antioxidant and lipid supplementation[54]. However, the response to biochemical modulation can vary based on the cell line and protocol used[98]. Moreover, the inclusion of various biologics may lead to higher costs and a more elaborate regulatory assessment. For these reasons, some approaches aim to harness the capacity of PSCs

to self-organise into 3D retinal tissues with minimal or short-term manipulation[45,99], or to utilise less expensive alternatives such as small molecules[93].

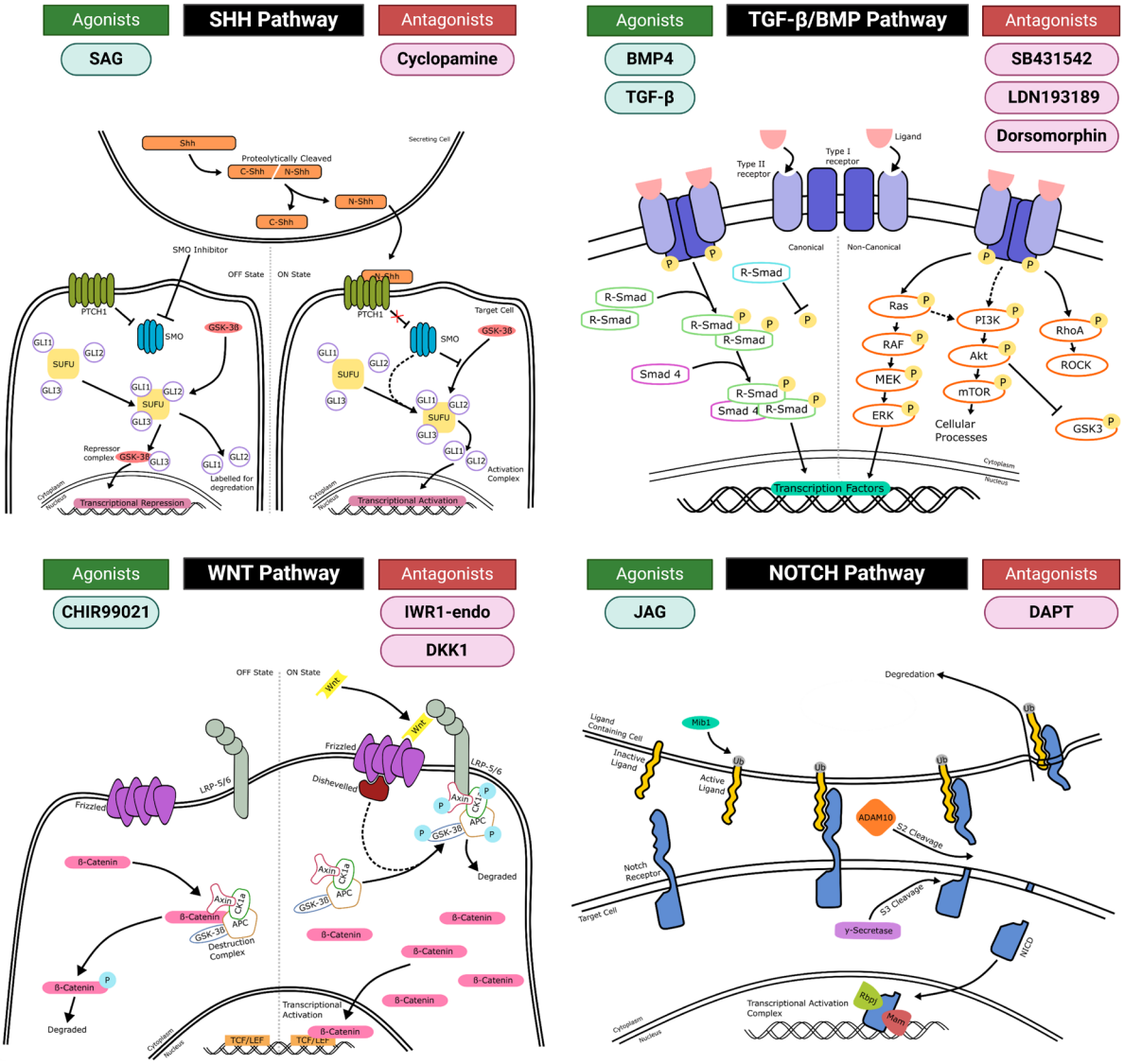

Figure 2.9 Common signalling pathways modulated during the process of retinal differentiation, including the molecular mechanisms and commonly used agonists and antagonists. Adapted from Wagstaff et al.[93]

Simple alterations to improve the culture niche have effectively guided retinal cell differentiation. For instance, hypoxic conditions (1% O_2) enhanced pro-angiogenic factors in retinal progenitor cells (RPCs)[100], while 3% O_2 increased RPC proliferation[101]. Manipulating gas concentrations (10% CO_2/5% O_2) during early differentiation stages can similarly improve

organoid viability, size, and vesicle quantity[102]. Prolonged hypoxia upon differentiation induced up to a three-fold increase in SIX6 positive RPCs at day 15; however, excessive hypoxia was associated with necrosis and reduced organoid size[103], indicating the time-dependent nature of such alterations. Alternatively, hyperoxic cultures of 40% O_2 improved retinal ganglion cell (RGC) survival in late RO cultures[48], revealing the potential role of dynamic or graded environments for optimal differentiation. Although established differentiation methods have successfully generated mature retinal tissues predominantly through standardised static culture conditions[54,94], technologies that offer higher control over culture parameters and dynamics may further improve functional outcomes[4,104].

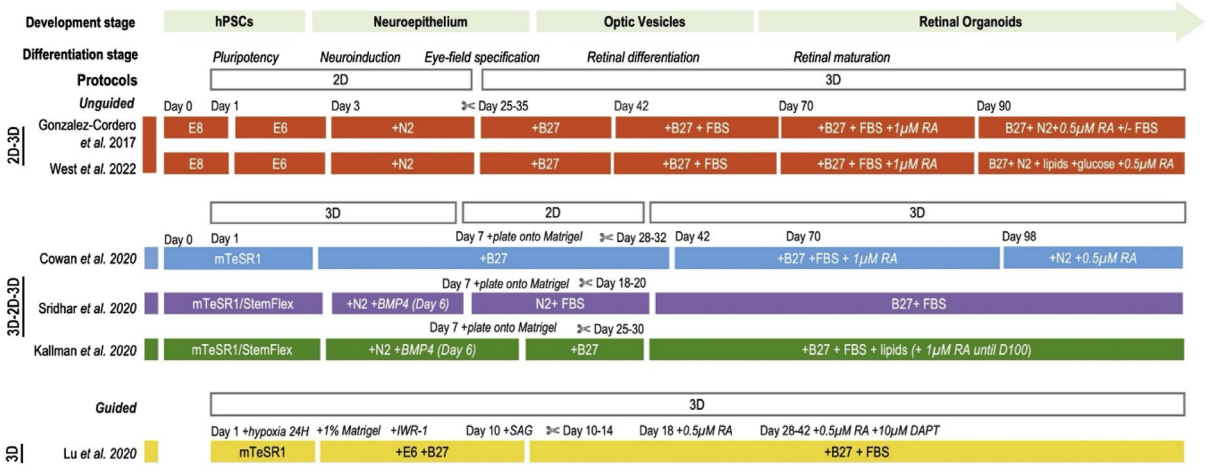

Figure 2.10 Schematic showing the different types of protocols used to generate retinal organoids, showing the stepwise processes involved. Adapted from Kim et al[53].

Most protocols require manual dissection at some point, as indicated by the scissor symbol. hPSCs, human pluripotent stem cells; E8, Essential 8; E6, Essential 6; RA, retinoic acid; H, hour; DAPT, N-[N-(3,5-difluorophenacetyl)-l-alanyl]-S-phenyl glycine t-butyl ester) γ-secretase inhibitor; ✂, dissection/dislodgment.

2.4.2 Bioengineered devices for improved retinal tissue growth

While established methods predominantly rely on exploiting matrices and delivering external growth factors to guide retinal development, bioengineered approaches offer another dimension to cultures. Bioengineering approaches aim to enhance the generation and

specification of retinal cells, with multiple approaches applied throughout the past decades. Moreover, engineering methods promise to control retinal organoid development and enhance multicellular architectures to better recapitulate physiology[105] (Figure 2.11). This includes dynamic microenvironments, precise controls over spatiotemporal parameters, biomimetic materials to facilitate retinal cell growth, and automated systems to improve the reproducibility, efficiency, and scalability of retinal cell generation for transplantation.

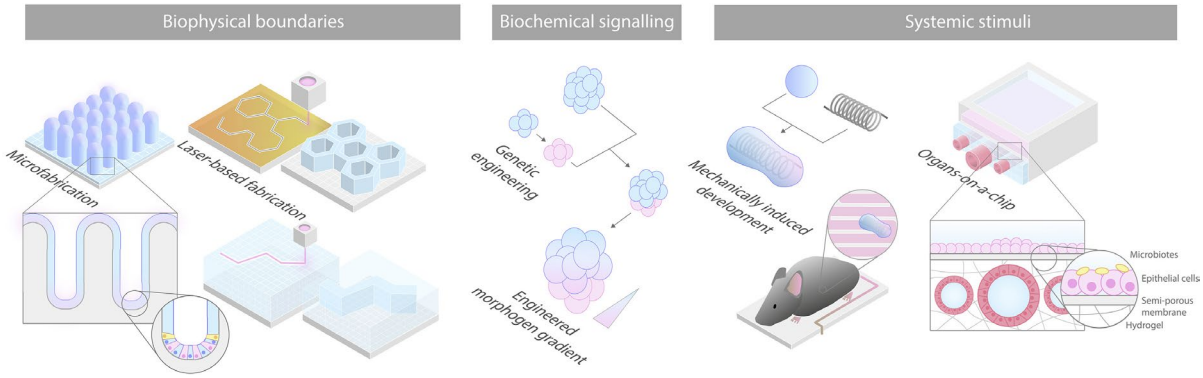

Figure 2.11 Engineering methods to control stem cell self-organisation through biophysical and biochemical cues. Adapted from Brassard & Lutolf[106].

As human development occurs within a dynamic, vascularised environment, technologies to mimic the gas, nutrient, and signalling gradients have been employed, such as bioreactors. Bioreactors are specialised culture environments that enable the mass transport of nutrients and oxygen via mechanical forces such as rotation or propulsion. Through integrated sensors, bioreactors allow for higher control over parameters such as temperature, gas, and pH, with automated feedback systems now under investigation[107]. This level of control, paired with the provision of *in vivo*-like biophysical stimuli such as fluid flow and shear, may enable the generation of tissues with improved maturity and cellular yields. As such, bioreactors are pivotal for standardising bio-production and provide an optimal method for scaling up cell cultures while meeting Good Manufacturing Practice (GMP) standards, as they can be readily utilised as a closed system. While bioreactor-based retinal cultures have been limited to bench-

scale systems with working volumes of up to 100 mL[108-112], studies showing enhanced retinal organoid differentiation[113] and photoreceptor yields have validated their utility[114]. When moving toward clinical applications, large-scale systems such as industrial stirred tank bioreactors may prove to be crucial.

Dynamic environments provided by bioreactors may enhance the structure and maturation of cultured tissues. Spinner flask bioreactors (SFBs) employ internal impellor-driven agitation to promote improved nutrient and oxygen diffusion, facilitating improved maturity and yields of RO-derived PRs[114] and retinal stem cells[115]. Rotating wall bioreactors (RWBs) use externally actuated rotation to distribute shear forces over the vessel wall, providing favourable low-shear culture environments potentially ideal for long-term tissue culture[108]. Other rotational systems, such as rotary shakers, have similarly supported the culture of RPC-derived PRs, RGCs, bipolar cells, and amacrine cells[111], encouraging the application of such environments to improve tissue growth. However, the high operational costs and resource needs associated with large bioreactor systems, such as greater culture media volumes, limit current investigations of potential scale-up applications.

As a result, small-scale technologies to induce dynamic microenvironments may be favourable, such as devices which use microfluidics. Microfluidic devices fine-tune the spatial and temporal dynamics of the cell environment[116], demonstrating utility in enhancing retinal tissue function and structure[117-119]. These devices range from retina-on-a-chip platforms[117] and whole mice retinal explant cultures[120], to systems for drug response studies[118,121,122]. Through microfluidic platforms, complex multicellular cultures can be achieved, often as adjacent compartmentalised cultures with shared media for paracrine signalling.

Microfluidic systems have offered enhanced retinal organoid development by enabling RPE co-cultures[117] or offering compartmentalised sites while maintaining the paracrine effects of shared cell media[119]. A study incorporating retinal organoids with retina-on-a-chip technology could simulate retinal choroid dynamics by seeding RPE on a porous membrane adjacent to an underlying microfluidic perfusion channel[117]. Subsequently, retinal organoids were loaded onto the RPE and embedded in a hyaluronic acid (HA)-based hydrogel, modelling the close apposition of the RPE-photoreceptor interface and mimicking interactions such as outer segment phagocytosis. Using microfluidics to harness paracrine effects, a similar study cultured a series of 70-day-old retinal organoids for up to five weeks in compartmentalised chambers interconnected by perfusion channels[119]. Interestingly, these microfluidic-cultured retinal organoids exhibited reduced oxidative stress[119], which may benefit long-term tissue survival.

Microfluidic systems that mimic complex retinal interactions, such as retinal organoid-RPE co-cultures, offer insights beyond what organoids alone can provide. Given the potential to define complex multicellular interactions, promising avenues for future work include leveraging microfluidics to achieve cellular compositions that are currently unattainable; for example, by assembling tissues one cell type at a time[123]. The addition of diverse cell types or structures such as vascularisation in these platforms could further enhance retinal organoid fidelity and is currently being explored in other neural organoids[124,125]. Although these techniques can assemble complex tissues and organoid interactions, their current limitations include time-intensive fabrication and set-up, the need for auxiliary equipment and infrastructure, and challenges in the replicability of complex designs. Moreover, there remains little evidence that these devices can enhance the generation of retinal organoids beyond co-culture applications.

Techniques that aim to alter the spatial properties of cell culture without altering the culturing environment provide an alternative method to create complex tissues and signalling gradients. Bioprinting offers a precise method for depositing biological materials, such as cells and growth factors, into programmed spatial arrangements. Various bio-inks may be utilised in bioprinting, readily switched via multiple printheads or fluidic systems to create multi-material constructs. For instance, inkjet bioprinting has been employed to pattern the deposition of rat RGCs[126-128], and assemble RGC co-cultures with retinal glial cells[129]. Another study inkjet-printed porcine photoreceptors over a human RPE layer, achieving a layered organisation that enhanced RPE function, including VEGF secretion and photoreceptor outer segment phagocytosis[128]. However, despite technological progress, bioprinting strategies generally struggle to achieve both high viability and cell density[130] for physiologically relevant models. In more advanced bioprinting efforts, fibroblasts, endothelial cells, and pericytes were co-cultured to model the capillary bed present at the retinal choroid[131]. Bioprinting of the three cell types facilitated enhanced formation of vascular networks compared to cell dispensing methods without printing. The addition of RPE to the platform proved critical in producing barrier functions, generating a Bruch's-membrane-like structure, and inducing capillary fenestration, effectively generating a model of the outer blood-retinal barrier[131].

3D printing is another promising technique to control spatial parameters. 3D-printed materials with complex multimodal cues for cellular control, such as chemically[132], mechanically[133], and mechano-chemically[134,135] micro-structured materials may provide ideal environments for retinal organoids or organoid-derived cells. Two-photon polymerisation (TPP) is an innovative 3D-printing method offering nanoscale resolution[136]. Scaffolds produced using TPP can support the alignment of RPC neuronal processes while also optimising for high cell densities in both non-degradable[137] or biodegradable[138] materials. As such, 3D-printed scaffolds are a

valuable tool for high consistency and enhanced cell organisation. However, although this technique provides an ideal material for the transplantation of dissociated cells, 3D printing applications for generating organoids are currently limited. As such, methods that utilise printing techniques for the generation of high-throughput retinal organoids may improve current outcomes.

2.4.3 Bioengineered methods for improved scalability

High throughput and automated bioengineering strategies aim to improve the reproducibility, efficiency, and maturity of retinal cell cultures. These approaches include custom high-throughput arrays[139-141], liquid-handling robotics[142-146], and artificial intelligence (AI) for culture optimisation[146,147].

High-throughput cell culture arrays offer efficient generation of isolated retinal vesicles through optimised materials and designs, potentially reducing labour-intensive and bias-inducing protocol steps (Figure 2.12). These culture arrays typically first induce the formation of EBs in 3D suspension, somewhat mimicking the cell aggregation process *in vivo*. Following this, these aggregates can be further maintained in the same culture vessel for long-term growth, or plated on 2D tissue culture plates for adherent growth. In the latter approach, retinal tissues are then dissected after one month for 3D suspension culture. As such, the majority of organoid protocols will mature tissues within 3D suspension cultures.

Retinal organoids can be successfully generated in 96-well V-bottom[148] or U-bottom culture plates[149], facilitating straightforward applications such as drug testing of individual organoids, compared to protocols where numerous organoids are grown in the same well—for example, 6-well plates. These array-based protocols may also reduce the number of transfer and dissection steps, enabling high-throughput workflows adaptable to imaging, robotic cultures,

and GMP-compliant conditions. In one study, retinal organoid protocols were translated from 6-well plate cultures to 96-well setups, introducing altered cell environments. The relatively higher nutrient availability in 96-well setups enhanced RPE generation, RGC differentiation, and cGMP response, with changes in cell seeding density causing higher expression of markers for different retinal cells at each extreme[149]. However, across five iPSC lines, there was apparent variability in organoid size, generation efficiency, and the presence or absence of RPE cells, an ongoing challenge in the field.

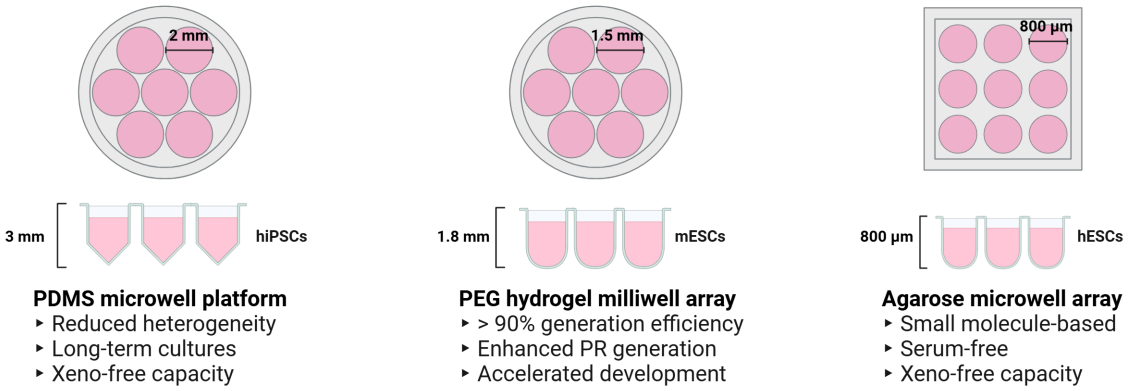

Figure 2.12 High-throughput biomaterial-based arrays for the scaled generation of retinal organoids using 3D suspension methods.

Biomaterials-based culture arrays have been developed from materials such as polydimethylsiloxane (PDMS)[141], poly(ethylene glycol) (PEG)[139], and agarose[140]. These protocols have demonstrated the capacity for xenogeneic-free conditions in compliance with current Good Manufacturing Practice regulations. Created with BioRender.com.

Biomaterial-based array platforms and protocols that start from EB generation can improve retinal organoid generation and differentiation efficiency[139], and can be further translated to GMP-friendly xeno-free culture workflows[140,141]. Round-bottomed PEG-based milliwell arrays demonstrated a 93% generation efficiency of mouse PSC-derived retinal organoids, with accelerated cone photoreceptor maturity and increased photoreceptor proportions compared to mature mouse retinas[139]. Similarly, agarose-based microwell platforms have facilitated the formation of EBs for subsequent retinal organoid differentiation in 6-well plates[50] and the

complete generation and culture of retinal organoids without transfer steps[140]. Microwell arrays that enable the generation and culture of retinal organoids in a single platform may be ideal for reducing the potential for contamination and errors caused by transfer steps. For instance, a micromoulded agarose-based microwell platform effectively generated and supported the culture of hESC-derived OV structures for up to 40 weeks[140]. Interestingly, changing to larger suspension cultures at the 6-week timepoint enhanced photoreceptor morphology and retinal organoid size, potentially highlighting limitations caused by microwell size constraints over time.

Polydimethylsiloxane (PDMS), a material widely used for its hydrophobic properties, interestingly facilitates the growth of RPE monolayers[150-152]. Through partial adherence to the culture vessel sidewalls, 3D-printed PDMS microwells supported the generation of retinal organoids possessing adjacent RPE, a feature that could not be achieved in plastic control cultures unless supplemented with exogenous BMP4 stimulation[141]. As such, milli- and microwell arrays can support long-term retinal organoid generation and differentiation in single platforms, though functional outcomes and transplantation studies of these retinal organoids will provide further insights into the utility of these platforms in clinical applications. Nevertheless, the facile translation of such platforms to automated cell culture systems presents a significant benefit for clinical translation.

Methods to improve throughput and reproducibility of 3D tissues often focus on applying multi-well tissue culture plates, such as 96-well or 364-well platforms. Due to the requirement of 3D aggregates for growth within these high-throughput arrays, the potential for protocols that have a 2D-based component, such as 2D-3D or 3D-2D-3D protocols, to be scaled or automated is relatively more difficult. For example, retinal tissues that can be grown from

confluent 2D cell layers cannot be adapted to these platforms. As such, techniques to improve the high-throughput capacity of 2D-based steps are critical to clinical translation.

The capacity for stem cells to self-organise from monolayers into the laminated structure of retinal organoids is undoubtedly complex and a significant challenge to completely control. It is evident that a fine balance between intrinsic signalling gradients and extrinsic engineered patterning must be achieved. Numerous strategies have been implemented to control the initial conditions of stem cell cultures (Figure 2.13).

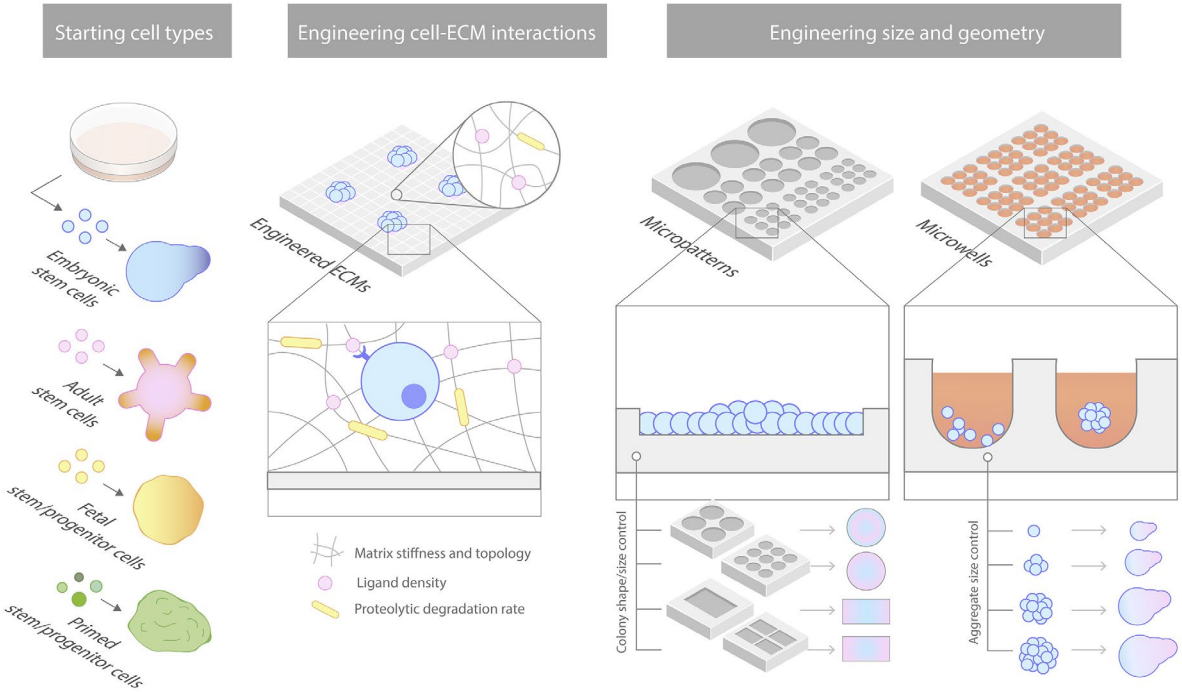

Figure 2.13 Methods to control initial conditions of stem cell cultures. Adapted from Brassard & Lutolf[106].

Interestingly, micropatterns to confine cell populations within a 2D region have shown high control over the precise phenotypic profile of the cultured tissues[106]. Moreover, micropatterned arrays of stem-cell-derived tissues have demonstrated improved phenotypic consistency[259-261] and the emergence of cell types that are not present in traditional cultures[262]. However, the application of micropatterns for the growth of retinal tissues is currently underutilised. Such

methods may be amenable to the automation of vesicle dissection or may support the growth of relatively pure retinal populations and are potentially critical in the pathway towards the clinic, particularly when integrated with GMP-compliant protocols.

2.5 Micropatterning cells to induce spatial confinement in stem cells

Variability in retinal tissue differentiation exists between laboratories due to differences in cell lines and protocols used. Batch-to-batch variations in tissue size, morphology, and maturity are an ongoing challenge due to the stochasticity of stem cells, in addition to human errors and bias in culturing practices. Achieving consistency remains a challenge, necessitating robust protocols and quality control measures[148]. Integrating high-throughput and automated processes offers higher control over culture conditions while removing human-related errors during seeding, media changes, or mixing processes. While traditional biological approaches focus on the exogeneous delivery of biologics regulating retinogenesis, bioengineering approaches offer systematic controls in order to enhance the scalability and reproducibility of tissues for therapeutic applications. Micropatterned arrays are a promising high-throughput approach that can enhance the reproducibility of 2D or 3D cultures. Such methods have been shown to improve the phenotypic consistency of self-organising tissues and organoids[153-155].

2.5.1 Micropatterning to enhance tissue culture

Micropatterning techniques generally aim to spatially confine cells within a 2D area to create signalling gradients and/or to promote perpendicular growth. Cells can sense and respond to mechanical forces and biophysical cues from their environment, which influence their fate and lineage through various signalling pathways. Moreover, micropatterned culture can enable facile downstream analysis of high-throughput cell cultures (Figure 2.14). Initial studies on bovine and rat cells showed that spatial confinement of cell populations influences patterns of

proliferation depending on the tissue geometry (shape and size) and mechanical stress gradients[156]. Moreover, subsequent studies in ESCs demonstrated that manipulating the properties of the stem cell niche on circular micropatterned cultures, such as the size and cellular composition, can regulate differentiation and self-renewal[157,158]. Importantly, geometric confinement on circular micropatterns was able to reproducibly recapitulate the spatial patterning observed in early gastrulation[153,159], highlighting the importance of cell colony size in controlling the self-organisation of stem cells. This approach provides a sensible approximation to the self-organisation of the early gastrula, offering enhanced models compared to 3D embryoid bodies.

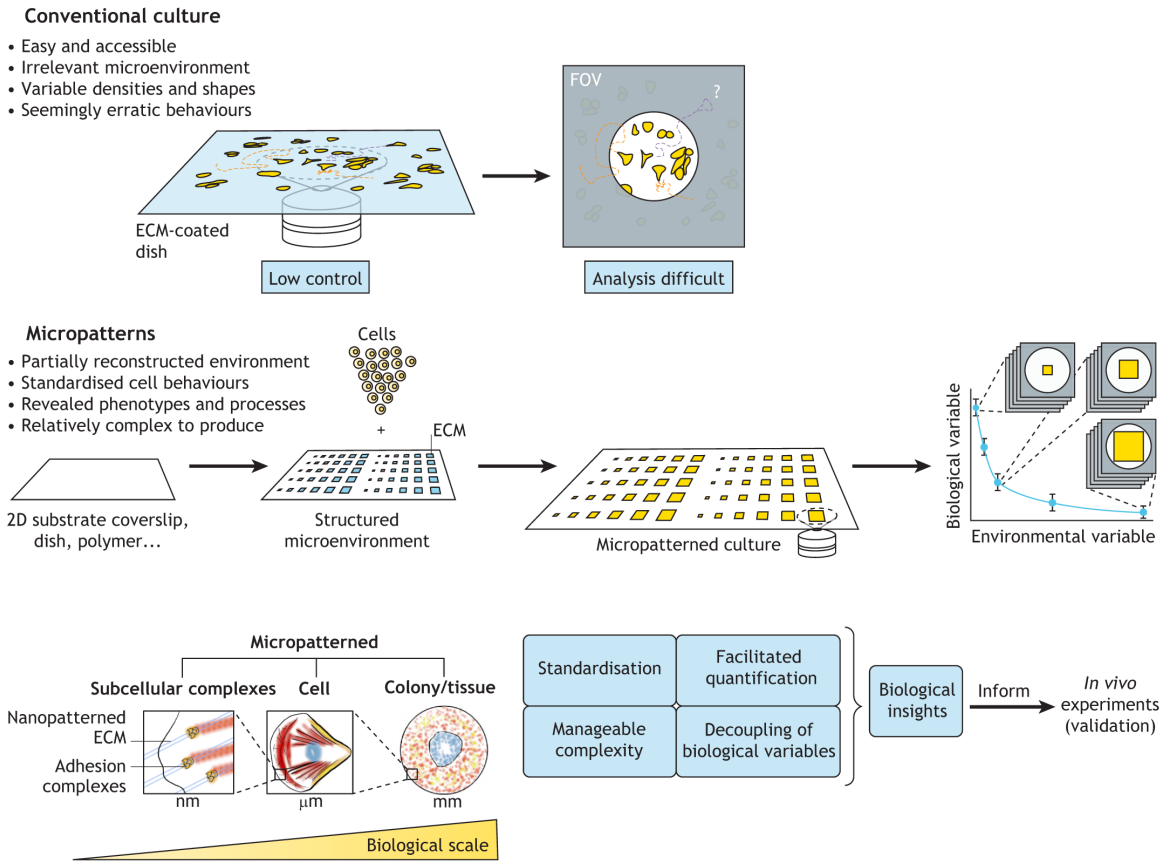

Figure 2.14 Differences in the analysis and applications of conventional and micropatterned cultures. Adapted from Blin[163].

In a study comparing 3D microwells to 2D micropatterns, embryoid bodies derived mouse ESCs showed enhanced proliferation and differentiation on the micropatterned surfaces[160]. As previously discussed, retinal organoids grown in microwell platforms with partial adherence to the vessel wall similarly demonstrated enhanced differentiation when compared to organoids grown in non-adherent microwells[141]. These studies highlight the potentially significant role of cell adherence in proliferation and differentiation. Moreover, the enhanced reproducibility and scalability[161,162] in cell cultures as reported across micropatterning studies warrants further research in the application of such techniques to improve retinal organoid cultures.

2.5.2 Methods of micropatterning

Micropatterning techniques commonly involve fabrication via lithography, microcontact printing (stamping), or chemical or topological modification to substrate surfaces[164]. These techniques generally define areas in which cell attachment is supported or inhibited, or a combination of both. To support cell attachment, adhesive proteins or ECM extracts can be used, including Matrigel/Geltrex, collagen, vitronectin, or Arg-Gly-Asp (RGD) peptide motifs. Alternatively, to prevent cell attachment, non-fouling biomaterials or coatings to decrease surface tension can be utilised, such as polyethylene glycol (PEG) [160], polyvinyl alcohol[165], and polyacrylamide-based[166] polymers, and surfactant solutions.

In lithography techniques, a photomask and UV light are commonly used to 1) bond adhesion peptides or proteins to support the attachment of cells on a non-adherent substrate and/or 2) polymerise and attach a non-adherent polymer to a tissue culture substrate. In the latter approach, a subsequent surface coating of adhesive proteins—such as Matrigel or collagen—is generally necessary for ideal stem cell attachment, as in the regular practice of stem cell culture. In microcontact printing, a patterned polymeric stamp is fabricated (conventionally through lithography techniques) to transfer attachment ligands in the desired micropattern or

to prevent non-adhesive coatings from affecting desired regions[156]. In this approach, it is similarly possible to transfer non-adhesive polymers to pattern a surface. Chemical or topological modifications to substrate surfaces can similarly be performed through lithography, microcontact, or laser-guided processes. Alternatively, tissue culture plastic surfaces can be directly patterned through a photomask and deep UV lithography techniques to photodegrade the polymer surface[167,168]. Although these direct patterning techniques require subsequent development using chemical solvents to remove polymer regions of irradiation, their minimal use of polymeric stamps or biomaterials may be favourable for easily generating reproducible patterns in a straightforward manner.

Micropatterned substrates that use stamps or biomaterials inherently require the introduction of foreign substances into the culturing vessel. Thus, sterility and purity are critical to ensuring the quality of subsequent stem cell culture. Moreover, many micropatterning techniques may require auxiliary equipment—such as tools for scribing or micromachining—or the addition of exogenous substrates or materials—such as pre-polymer solutions, chemical developers, or glass coverslips—to tissue culture platforms. High expertise can be required to develop polymeric stamps and or complex biomaterials. Further, such procedures may create complex workflows requiring multiple washing or polymerisation steps, reducing the accessibility of easily customisable micropatterned substrates. Depending on the substrate material, surfaces that are overly stiff, such as glass, may not be ideal for long-term cultures (> 28 days) of neural tissue subtypes, which have been shown to have enhanced differentiation on softer substrates[169]. As such, micropatterned cultures on tissues culture plastic surfaces may be ideal for the long-term growth required for retinal organoid differentiation.

Interestingly, depending on the technique used, cells may be confined for the duration of tissue culture or have the potential to migrate within or away from the initial patterned area[170].

However, cell migration beyond the patterned area is generally considered unfavourable and undesired and, as a result, research on the effect of temporary or changing spatial confinement remains limited. As such, biological processes in embryo- and organogenesis, which experience dynamic changes in physical properties such as spatial confinement and cell density, may not be fully represented in environments with static levels of geometric confinement. Moreover, morphological processes that rely on cell-cell interactions and other extrinsic instructive cues, such as that influencing optic cup morphogenesis[171], may be better realised in dynamic microenvironments. Thus, further research in the micropatterning of retinal tissues may elucidate the mechanisms of optic cup development.

2.5.3 Effect of micropattern geometry

The role of micropattern shape and size in stem cell cultures can be crucial in controlling cell differentiation and tissue morphogenesis[153]. As previously explored, hPSCs cultivated on micropatterns can be utilised to observe the effects of colony size and geometry on cell fate. In such studies, a correlation between colony diameter and gene expression have been observed, revealing a spatial ordering in hESC colonies[153]. Interestingly, small colonies were observed to be somewhat equivalent to the edges of large colonies, with respect to signalling pathway activity and expression of pluripotency factors. Another study reported the effect of colony size on the morphology of a neural plate-like tissue structure. It was found that the width of the neural plate structure scaled linearly with micropattern size, while non-neural ectoderm was confined to a fixed region[154]. Interestingly, neural folding morphology did not simply scale with size, indicating that geometry plays a significant role in determining the final shape of the neural tube.

In other stem cell-derived tissue models, pattern size has demonstrated an impact on differentiation efficiency and cellular compositions. For instance, iPSCs cultured on varying

pattern dimensions showed size-dependent capacities to differentiate towards endothelial cell linages. In particular, smaller sizes promoted higher differentiation efficiency as assessed by the fraction of expressed vascular endothelial cadherin[172]. Interestingly, studies in hESCs have shown that larger micropattern sizes support the enrichment of cells towards neural fates compared to smaller sizes[158]. Moreover, the homogeneity of differentiation of stem cells within micropatterns has been shown to depend on the size of confinement, where cells on larger patterns (225 – 500 μm diameter) tended to be highly influenced by local cell-cell interactions as opposed to global mechanics as observed in cells within smaller patterns[173]. Cells in smaller patterns also tended to collectively differentiate or remain in a stem cell state, revealing the impact of localised signalling on neighbouring cells. A similar trend is observed in non-micropatterned cells with varied cell densities[157], highlighting the effect of the local microenvironment in modulating and instructing cell signalling.

The geometry of micropatterns has similarly been shown to affect stem cell fate decisions[174]. hPSCs seeded within different micropatterned shapes, such as circles, squares, rectangles, and arcs, demonstrated varied capacities for mesoendoderm differentiation[174]. Anisotropic shapes, mainly geometries with sharp corners or convex curvatures, induced higher levels of Brachyuary, correlated with increased integrin-mediated traction forces within these regions. Similarly, cells on isotropic shapes, namely circular geometries, showed relatively uniform and lower Brachyuary expression across the colony borders compared to anisotropic shapes, due to the absence of sharp or convex edges.

In organoid models, morphological symmetry-breaking mechanisms have been identified through the application of guided microenvironments achieved via patterning techniques[175]. For instance, elongated rod or cross-shaped patterns were able to induce symmetry-breaking and the patterning of intestinal epithelial cells that varied between the tips, sides, and centre of

the patterns. Similarly, by altering the width of elongated rectangular micropatterns, tissues were able to undergo folding mimicking that of the neural tube[154]. Interestingly, wide and narrow patterns were able to recapitulate the morphological features observed along the anterior-posterior axis of the neural plate and developing neural tube. Deep learning models to characterise and predict the effects of geometry-guided morphogenesis[176]. Through the developed model, morphology could be blindly predicted with an accuracy ranging from 61% to 68%, where some geometries being predicted with better precision than others.

Such studies inform the significance of micropattern size and geometry on the resulting tissue, highlighting potential considerations required when designing experiments for different tissue types. Importantly, many of these studies are performed in conjunction with supplementary biochemical signalling and induction towards certain tissue fates. As such, understanding cell and tissue behaviours within the complex interactions of biochemical gradients and biophysical forces is crucial in advancing our understanding of stem cell biology and tissue morphogenesis.

2.5.4 Micropatterning for clinical applications

The enhanced reproducibility and scalability offered by micropatterned cultures garnered much interest in high-throughput screening of therapeutics for clinical applications. In one study, the development of a micropatterned drug screening platform demonstrated utility in assessing the teratogenic potential of various compounds[177]. By inducing mesoendoderm fate in micropatterned cultures, the degree to which compounds were able to disrupt morphological events, such as the formation of an annular tissue pattern, could be quantified against dose-dependent treatments. Importantly, the use of various hPSC lines minimised the effects caused by inter-species variation. Another study utilised deep learning to analyse the effect of various compounds on micropatterned self-organised models of early human neurulation[178]. A high-throughput screen of drug candidates was performed, using convolutional neural networks to

assess their capacity to reverse a complex phenotype associated with Huntington's disease. However, applications have been currently limited to disease modelling and drug discovery. As such, further work on the utility of micropatterning in improving the scalability of cell therapies is warranted.

2.6 Micropatterning of tissue and organoid cultures

Researchers have leveraged micropatterning techniques to develop tissues such as those modelling embryogenesis and organogenesis. Such studies inform the application of micropatterning in generating self-organising tissues. Moreover, since these processes arise by harnessing the self-organising capacity of stem cells, geometrically controlled cell cultures offer reproducibility and control beyond that of traditional methods.

2.6.1 Micropatterning of embryonic tissues

As previously discussed, recent advancements have shown that micropatterning can be used to develop embryo-like structures, or gastruloids, from hESCs. When hESCs are grown on geometrically confined disks and exposed to BMP4, they can differentiate and self-organise into concentric rings of embryonic germ layers[153]. This process was demonstrated to be robust and amenable to analysis at a subcellular resolution. During mouse gastrulation, BMP4 signalling activates the WNT pathway, in turn activating the ACTIVIN/NODAL pathway. This hierarchy of signalling activity could be modelled in human stem cell-derived gastruloids, where all three germ layers—and a trophectoderm-like layer—could be induced in the same tissue. Moreover, further studies using similar micropatterned platforms identified a previously unknown human organiser subpopulation, able to be induced via WNT and ACTIVIN treatment[179]. The applications of such models in inducing neural tube morphogenesis[154] are

similarly significant in elucidating the morphological events of embryogenesis without requiring the use of human embryos (Figure 2.15).

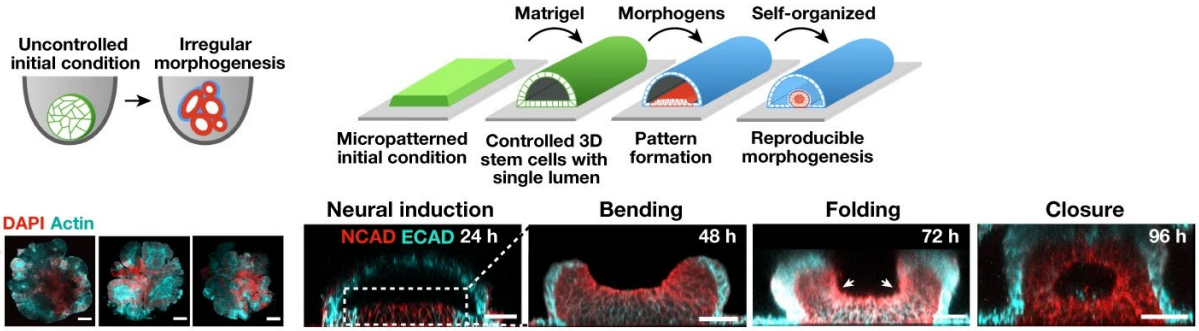

Figure 2.15 Micropatterning to enhance the control over initial conditions of self-organisation and morphogenesis. Stimulation with low concentrations of Matrigel induces the formation of neural tube-like structures in these platforms. Adapted from Karzbrun[154].

These landmark studies have paved the way for further investigations of *in vitro* models of gastrulation. However, these studies are commonly performed on glass substrates, which may not be conducive to optimised levels of cell proliferation and differentiation, as previously discussed. Interestingly, one recent study investigated the effect of substrate alone on inducing stem cell differentiation, in the absence of solution factors such as BMP4, WNT, and ACTIVIN treatment[180]. It was observed that, compared to cells on glass substrates, cells on softer hydrogel substrates (10 to 100 kPa) demonstrated higher degrees of proliferation and differentiation. More importantly, the material-guided onset of gastrulation was observed in the absence of exogenous biochemical induction. In accordance with this, circular micropatterns on soft hydrogel substrates (2.7 kPa) have demonstrated altered morphological features, primarily the generation of multiple peripheral regions of gastrulation-like subpopulations[181], as opposed to the concentric ring structures found in glass-cultured micropatterns[153]. Such studies highlight

the equally important role of the biophysical microenvironment in instructing morphogenesis and differentiation.

As highlighted through previous literature, micropatterning offers a promising avenue for the development of embryo-like tissues and models, providing valuable insights into human development and offering potential improvements to other related differentiation protocols.

2.6.2 Micropatterning of mesoderm- and endoderm-derived tissues

Micropatterning of other tissue types are similarly informative in the generation and long-term culture of organoids. In mesoderm tissues, micropatterned cultures were able to promote self-organising cardiac tissues resembling the early stages of cardiac development[182,183]. Interestingly, the presence of cell-free regions within the well-defined microchambers in the tissue mimicked chambers found in cardiac tissues. These tissues could be cultured for up to 20 days, with larger diameter patterns (400 μm and 600 μm) successfully generating cardiac tissues that were unable to be generated in smaller patterns (200 μm). Moreover, the generation of cardiac organoids resembling embryonic cardiogenesis using such platforms can provide robust platforms for drug screening and understanding early developmental processes[184].

In endoderm tissues, micropatterned cultures could successfully induce the self-organisation of lung buds resembling fetal lung tissues, comprising alveolar and airway proximodistal tissue patterning[185]. The high-throughput platformed enabled the study of SARS-CoV-2 infections, identifying the role of the BMP signalling pathway in increasing infection susceptibility. Interestingly, smaller diameters (225-μm) were found to be more conducive to the formation of buds with appropriate tissue patterning.

Multilineage tissues, such as those of the gastrointestinal system, offer further insights into the effects of micropatterning to induce robust self-organisation. One micropatterned system could

generate intestinal organoids and maintain them in culture for up to 40 days before transfer to suspension cultures[186]. These stem cell–derived gut organoids, produced in xeno-free conditions, showed a well-organised morphology, comprised the major intestinal cell lineages, and demonstrated functional attributes alike that of mature intestinal tissues. However, the proportion of organoids with contractile movements—also the only tissues that were responsive to drugs that modulate intestinal contractile activity—was only 4%, highlighting challenges with controlling the origins of cell types in such multicellular tissues.

2.6.3 Micropatterning of ectoderm tissues

Micropatterned methods can enable the generation of ectoderm-derived tissues of consistent size, geometries, and cell compositions compared to traditional methods. Though SB431542 and LDN 193189 treatment, the use of circular micropattern substrates enabled the generation of tissues expressing PAX6+ neuronal progenitors on patterns ranging 80-500 μm in diameter[155]. However, a minimum diameter size of 200 μm was required in order to induce self-organised structures possessing radial organisation and cell polarisation towards a central lumen. Interestingly, larger diameters (500 μm) demonstrated lower consistency in complete lumen closure, compared to smaller diameters (200 μm), further highlighting the size-dependency of self-organisation and localised cell signalling in larger patterns. Moreover, in contrast to non-geometrically confined monolayer cultures, micropatterned cultures exhibited accelerated self-organisation into characteristic neural rosette structures. These structures were observable by day 5 on micropatterns, whereas they remained absent even by day 7 in non-micropatterned cultures—even though both cultures had acquired neural fates at comparable time points, as indicated by NCAD expression. Importantly, upon replacement of LDN with BMP4 treatment, these micropatterned neuruloids expressed markers of all the neurulation-associated ectodermal fates (neural, neural crest, sensory placodes, and epidermis) at day 7. As

such, the robust model of neurulation generated through micropatterning techniques proved critical in high-throughput screening of potential therapeutics[178].

Interestingly, robust neuroepithelial structures can be derived from 1000-μm diameter micropatterned cultures through the induced patterning of mesoendoderm tissues to guide the self-organisation of primitive ectoderm, as opposed to direct induction towards neuroepithelial fate—which generated less ordered tissues[187]. These structures, termed mesoendoderm-primed tissues, could induce regionalised tissue folding of primitive ectoderm epithelium adjacent to the mesoendoderm cells at the colony edges. By day 5, these tissues expressed PAX6 and OTX2 in the non-folded central region, away from the mesoendoderm cell populations. Tissues that were not mesoendoderm-primed demonstrated a less organised tortuous structure andexpressed higher levels of anterior neural markers PAX6 and OTX2. Interestingly, when the mesoendoderm-primed tissues were treated with a neural induction medium rather than a mesoendoderm medium, the micropatterned colonies retain their capacity to fold and expressed neural and early eye field marker PAX6 by day 5, highlighting the plasticity and adaptability of the system. These results highlight the significance of temporal parameters in generating highly structured and robust neuroepithlial tissues. Moreover, similar to previous studies, a size-dependent effect on differentiation was observed, where the smaller colonies demonstrated stronger mesoendoderm identities, leading to increased folding. Collectively, these results may be indicative of the importance of multi-step or long-term protocols in enabling self-organised morphogenesis rather than relying solely on biochemically guided differentiation protocols. Furthermore, larger micropattern sizes may be more conducive towards less tissue bending and, thus, higher proportions of primitive ectoderm tissues in such protocols. Interestingly, micropatterning in non-neural ectoderm tissues, such as amniotic

ectoderm[188], have similarly shown the size-dependent effect of spatial confinement and the generation of tissues with folding or luminal cavities.

An alternative micropatterning study has observed the effects of non-adherent initial geometric confinement on long-term differentiation of cerebral organoids[189]. By initially confining hESCs within flat microwells of various geometries—including triangles, stars, arcs, and more complex butterfly and peanut shapes —for five days prior to subsequent suspension culture, the study showed that by day 40 the cell aggregates were able to eventually adopt a spherical shape similar to controls generated in 96-well round-bottomed plates. Further analysis revealed that there was no significant difference between transcriptional dynamics and differentiation between microwell and 96-well plate aggregates between day 10 and day 40, however, transcriptomic differences were observed. Clear contrasts in differentially expressed genes were observed in day 40 aggregates derived from flat microwells, such as the downregulation of retina-associated genes and the upregulation of markers associated with cortical, forebrain, and ganglionic eminence structures when compared to 96-well plate aggregates. However, due to the non-adherent nature of the microwell cultures, these results could highlight the synergistic effect of confinement and cell-substrate attachment in self-organising micropatterned cultures that is absent in this case.

The widespread application of micropatterning to generate tissues that mimic gastrulation and organogenesis underscores its potential as a cell culture tool. However, the limited use of these techniques in retinal tissues reveals a gap in this field. Challenges associated with generating retinal tissues in micropatterns remain unclear, though may be related to the long-term nature of such protocols and difficulties in controlling morphogenesis well past initial seeding. This effect may be further exacerbated when working with neural cell types, which tend to preferentially proliferate on softer substrates. As such, developing softer materials for the

generation and long-term culture of neural retinal cells may require innovative methods and/or designs. Retinal cultures initiated from self-organizing confluent monolayer cultures may be particularly amenable to micropatterning. Translating existing retinal organoid protocols, which rely on precise morphogen fields for 3D bud formation, to micropatterned cultures could streamline workflows. These cultures facilitate the subsequent excision of budded 3D vesicles from batched tissue cultures—a process currently difficult to adapt for automated systems and GMP manufacturing. Further research is needed to establish a scalable method for generating high-throughput retinal tissues, valuable for drug discovery, disease modelling, and a reliable source of transplantable retinal cells.

2.7 Motivation of this thesis

Micropatterning methods are an invaluable tool to generate highly consistent tissues *in vitro* for diseases modelling[155,185] and drug development[177,178,184]. However, their applications in enhancing the scalability and reproducibility of retinal organoids are currently underutilised. Controlling the initial culture conditions of 3D aggregates is extremely challenging due to the 3D cell-cell interactions that can occur, thus leading to irregular morphogenesis for each experiment[154]. Thus, initiating cultures from 2D substrates may enable higher control. Further, considering that many ongoing pre-clinical studies utilise a variation of adherent retinal cell culture to successfully generate retinal organoids through stem cell self-organisation[46,74,190], it is imperative that methods to control the region and efficiency of organoid growth are established. To be compliant with current Good Manufacturing Practice protocols, such techniques should utilise biocompatible, sterilisable, and physico-chemically stable methods and materials. Furthermore, minimal manipulation to current retinal organoid protocols is ideal in order to prevent external factors or complexities from influencing the differentiation and self-organisation of tissues. As such, micropatterning of 2D surfaces, particularly those already

implemented for tissue growth, is a great platform for achieving scalable and consistent organoid cultures. The goals of this thesis were firstly focused on developing a method to culture early neural cell populations to characterise cell behaviours and ensure correct morphological features and expression of transcription factors. These initial methods focussed on using micropatterned biocompatible materials via novel printing techniques on glass substrates, which is widely used in cell culture and ideal for its optical and surface properties—that is, facile for immunostaining, imaging, and surface functionalisation. To prolong these cultures towards the month-long timescale required for ideal retinal vesicle growth, we pivoted towards micropatterning tissue culture plastic—a ubiquitous surface in all tissue culture laboratories. In addition, we studied the effect of biochemical modulation of both well-characterised and less well-described signalling pathways on retinal vesicle growth. Finally, we combine the knowledge gained in both biophysical and biochemical modulation to propose an integrated platform to facilitate the efficient generation of retinal vesicles.

Chapter 3: Micropatterning and modulation of human pluripotent stem cell cultures to characterise early neural differentiation

3.1 Introduction

Complex regulatory interactions occur in the development of the human eye, including the neurogenesis of the retinal cell types[191]. Understanding early neural development is critical for advancing the role of diverse cell types in coordinating retinal specification. It provides insights into the complex processes that guide the formation of the nervous system, from the proliferation of neural progenitor cells to their differentiation into specialised neurons such as those found in the retina. However, studying these mechanisms *in vivo* presents significant challenges due to the early nature of these developmental processes, their complexity, and the potential ethical considerations involved; for instance, when using animal models. For these reasons, iPSCs and suitable differentiation protocols offer a promising avenue to overcome such challenges. They provide a platform for modelling early neurogenesis *in vitro*, enabling the observation and manipulation of neural development in a controlled environment[192]. In particular, micropatterning techniques have shown promise in guiding *in vitro* tissue growth in a relatively structured and predictable manner[154,155], potentially enabling the enhanced reproducibility and precision of iPSC-based neural tissue models. This chapter explores the potential of micropatterning to mimic the *in vivo* environment of early neural development, thus providing accessible and accurate human models *in vitro*.

Micropatterning techniques have evolved significantly over the years, with numerous methods being developed to create precise and reproducible patterns. These commonly involve multiple material and/or solution deposition steps, or curing, polymerisation, and heating steps[164]. Furthermore, these methods generally require a photomask for defined patterns, which may not be easily changed without manufacturing an entirely new photomask. As such, depending on the pattern shape or photomask material used, costs can be high during the prototyping stage when optimising for the ideal shape and size of patterns.

One such method that has gained considerable attention is for manufacturing customisable patterns for cell culture is 3D printing. This technology allows for the creation of intricate micropatterns that can guide the growth of iPSC-derived tissues. Specifically, 3D printing through a laser-based UV method allows for simple alterations for micropatterns simply by changing the preset design via software[135]. This enables facile and customisable high-resolution polymerisation of pre-polymer solutions via optimised laser power, position, and time. Thus, a pattern of any shape or size can be easily generated without requiring the manufacture of numerous photomasks, a resource that can be costly if high resolution is required.

When employing such printing methods, the selection of appropriate materials is critical in controlling cell behaviour. It is possible to choose a biomaterial that either supports or inhibits the growth of iPSCs in a printed area, or a combination of both. For instance, ECM extracts like Matrigel, which support iPSC growth, can be incorporated into printing solutions[135], ensuring optimal iPSC attachment and proliferation of cells only within polymerised areas. Alternatively, polymers with natural attachment peptides, such as collagen, can be utilised. Conversely, materials like poly(vinyl alcohol)[193,194] or polyethylene glycol (PEG)[195] can be used to prevent protein adsorption and cell attachment, thereby confining cells to non-polymerised spaces. By restricting cells to these printed areas, controlled environments can be established. In such systems, the cells generally remain confined throughout the entire growth and differentiation period. In addition to physical confinement, biochemical factors can be introduced to induce differentiation towards desired tissue fates. Furthermore, the use of ECM extracts, such as Matrigel, as media supplements can promote 3-dimensional growth, enabling the formation of complex structures[196].

In this study, we leverage these PEG-based techniques to test the hypothesis that micropatterns can confine iPSCs and enhance their neural differentiation, forming 3D neural and retinal vesicles. We focus on the early stages of cell behaviour, up to 14 days, and characterise the gene expression of early neural markers. To further enhance the 3-dimensional aspect of our cultures, we incorporate Matrigel and examine its effects on tissue formation. Following these preliminary experiments, we evaluate the influence of substrate material on neural differentiation towards retinal fate for up to four weeks. To efficiently evaluate retinal differentiation in real-time, we harness a GFP reporter cell line driven by the expression of SIX6, one of the earliest genes involved in eye field specification. Our findings are crucial to inform further understanding of the isolated generation and differentiation of tissues in 2D cultures. Through this research, we hope to pave the way for more sophisticated and robust methods of tissue growth and differentiation.

3.2 Experimental Section

3.2.1 Materials and procedures

Micropatterns on glass substrates were prepared via two UV light-based methods: 1. A laser-directed method that locally polymerises a pre-polymer solution, and 2. A lamp-based method that bulk polymerises a pre-polymer solution. PEG-based polymers were used as the primary printing solution, chosen for their biocompatibility, inert properties, and versatility. Part of this work was performed at the Research and Prototype Foundry Core Research Facility at the University of Sydney (part of the Australian National Fabrication Facility), where a custom-made chrome photomask was fabricated. This part of the study used three hiPSC lines: HOIK-1 iPSCs (HPSI0314i-hoik_1, Wellcome Trust Sanger Institute, United Kingdom)[197], 149BR iPSC line, and EP1.SIX6-GFP reporter iPSC line[103]. The SIX6-GFP reporter iPSC line was generously donated by A/Prof Karl Wahlin.

3.2.2 Functionalisation of glass coverslips

Glass coverslips (borosilicate) were treated with a silanisation solution to improve the attachment of printed structures and prevent PEG polymer swelling delamination during cell culture[198]. Glass silanisation covalently binds siloxane functional groups[199], allowing the acrylate functional group of PEG to bind upon UV-activated polymerisation[200]. Thus, the silane couples the PEG hydrogel to the glass for long-term stability.

Coverslips were washed with MilliQ H_2O to remove impurities such as dirt and dust. These were then washed 3 times with methanol to clean the glass and remove excess water. The coverslips were then immersed in methanol, taking care not to be left for an unnecessarily long period of time (e.g., several hours) as impurities in methanol may adsorb to the surface.

To prepare the silanisation solution, a Pyrex flask was thoroughly rinsed with methanol and sonicated. Methanol was added to the flask, followed by glacial acetic acid (Sigma A6283) and 3-(trimethoxysilyl)propyl acrylate (TCI A1597) in a 100:5:3 ratio. For instance, a 108 mL silanisation was created using 100mL methanol, 5 mL acetic acid, and 3 mL 3-(trimethoxysilyl)propyl acrylate). The methanol in the dishes containing the coverslips was replaced with the silanisation reaction mixture and left in a fume hood for 45 minutes to allow for the silanisation reaction to occur. Following this, the silanisation reaction mixture was removed and the coverslips were rinsed three times with ethanol. The flask was covered in cling wrap and the coverslips were dried using a small gas flow of N_2 within covered flask inside a fume hood. Slides were washed with isopropyl alcohol (IPA) and wiped with KimWipes prior to use. The silanised coverslips could be used immediately or stored at 4°C for later application.

3.2.3 Preparation of pre-polymer printing solution

Poly(ethylene glycol) diacrylate (PEGDA) (M_n 700; Sigma-Aldrich 455008), a derivative of PEG, was used to create a prepolymer printing solution. A cytocompatible photoinitiator, lithium phenyl-2,4,6-trimethylbenzoylphosphinate (Sigma-Aldrich 900889), was incorporated to facilitate the photo-polymerisation of the PEG-based hydrogels. MilliQ water was used as the base solvent for the prepolymer solution. The composition of the PEG-based prepolymer solution is listed in Table 3.1. For experiments incorporating Matrigel into the printing solution, a 50:50 ratio of Matrigel to the prepolymer solution was prepared in an ice bath. Printing was performed in a 4°C cold room to prevent premature gelation.

Table 3.1 Prepolymer formula for PEG-based hydrogels.

Solution	Volume (v/v%)
PEGDA	12.5
Photoinitiator	5
Water	82.5

3.2.4 Fabrication of micropatterned glass substrates

Upon UV initiation, free-radical polymerisation of the acrylate end groups[201] generates a stiff and inert hydrogel that attaches to the silanised glass surface. Two methods were used to create micropatterned glass substrates using UV photo-polymerisation of the prepolymer solution.

Method 1: Laser-based printing technique

The 3D printer was calibrated and operated under controlled conditions to print the desired structures onto glass coverslips. The precision of the 3D printer allowed for the creation of intricate and uniform structures, providing an optimal environment for cell adhesion and growth.

Fabrication of print chamber and sample coverslips. A photoresist was injected onto glass coverslip(s) sandwiched by two hydrophobic PDMS-coated glass slides during printing. For 48-well plate experiments and 6-well plate experiments, 10 mm diameter circular coverslips and 24 x 24 mm square coverslips were used, respectively. This setup formed the print chamber, which was then clamped into the printer stage. PDMS-coated 50x75x1 mm glass slides (Corning CLS294775X50) were prepared using PDMS (Corning Sylgard 184) ten-part base to one-part curing agent. The solution was mixed with a metal spatula and briefly centrifuged to remove bubbles. Glass slides were spin-coated with PDMS on a Laurell EDC

650 series spin coater. PDMS was poured onto the centre of the glass slides at a volume approximately the size of an Australian 50 cent coin. The glass slide was loaded onto the spin coater and the spin coater was ramped to 1600 rpm for 10 seconds and stopped. The glass slides were then placed onto a hot plate at 200 ˚C for 1 min before being transferred to a 37 ˚C oven overnight.

Printing was completed on an acrylate-functionalised coverslip base that forms a stable substrate for transport and culture of the printed materials, including the prevention of sample delamination, sample-folding, or strain deformation due to hydrogel swelling. As well, the covalent attachment assists sample handling for downstream cell culture.

The print chamber is assembled by suctioning the acrylated coverslips onto the PDMS-coated glass slide. A single print may consist of four 10-mm diameter circular coverslips or one 24x24 mm square coverslip positioned in the middle of the slide. Suction force holds sample coverslips to the PDMS coating. Plain square glass coverslips (24 mm x 24 mm) are positioned adjacent to each short edge of the PDMS slide to ensure the correct elevation of the chamber's top (Figure 3.1b). The top chamber comprised an opposing PDMS glass slide and effectively sandwiched the acrylated substrate coverslips within a hydrophobic glass chamber when positioned on top. The printer setup was housed within a dark 4°C cold room to limit photoactivation of the resist, as well as damage, misfolding, and gelling of sensitive biochemical reagents. All printer components and reagents were stored in the cold room to acclimatize before printing to prevent condensation. The base PDMS slide was inserted into the printing stage and secured into position through bolts at the bottom of each corner. The chamber's top slied was then positioned on top to ensure correct calibration of the coverslips and chamber height. The printer stage was then mounted onto the main body of the printer via machine bolts.

Calibration of printer laser with sample coverslips and stage. A camera assembly was mounted below the printing stage to monitor laser alignment and focus. The printer's laser was first calibrated to the camera assembly using the custom printer software. The distance between the laser and camera assembly was altered for parfocality. The camera was focused on the stage by changing the stage height. To calibrate the laser focus, the laser was moved to a position that passed the acrylated coverslip by navigation using the GUI stage map within the printer control panel. Focusing the laser at this position ensured an accurate focal length of the light path that includes the refractive differences of all materials and prevents aberrations caused by coverslip edges. During this step, focal asymmetry and astigmatisms could be reduced by carefully calibrating machine thumbscrews on the mechano-optical components housing the laser fiber unit, collimator, beam expander, and focal objective.

The stage height was adjusted to focus on the print sample during laser calibration, ensuring calibration between the laser, camera, and stage/samples. Camera parameters such as exposure, gain, binning, frames per second, and gamma could be adjusted in the GUI to visualise the live image better.

Injection of photoresist into glass print chamber. Following calibration of the printer, a photoresist was injected within the print chamber onto the acrylated coverslips. Accurate assembly of the print chamber resulted in a 50 μm void between the PDMS top slide and sample for photoresist injection.

gcode upload and print initiation. The software interpreted and translated gcode commands, sending these to the PI controllers (V-528.1AA /V-528.1AB and M-406 including corresponding controllers C-413 and C863 from Physik Instrumente (PI) GmbH & Co. KG).

An inspection of the printing area was performed to ensure no objects were obstructing printer movement. Printing was initiated and confirmed for correct laser movement.

Removal of samples from the printer. The top slide was carefully removed after printing termination to ensure that the printed substrate was not damaged or attached to the chamber. The stage was then unfastened from the printer and removed. The printing chamber was unclamped and taken out of the stage, revealing the samples. For each coverslip, a well of either a 48-well plate or 6-well plate was prepared with PBS supplemented with penicillin and streptomycin. Coverslips were removed from the base PDMS-coated glass using a scalpel blade to gently disturb the suction forces between the sample base and the PDMS. Care was taken not to damage the printed substrate or glass coverslip. The coverslips were then moved to the well plate, ensuring that the printed substrate faced the correct side upwards. Well plates containing samples were then parafilmed and left to wash on a plate rocker at 4˚C for 48 hours before use. Samples have been stored for up to 1 week without observing any changes to their function.

Method 2: Lamp-based printing technique

A custom-made chrome photomask with circular patterns was fabricated at the Research and Prototype Foundry Core Research Facility at the University of Sydney (part of the Australian National Fabrication Facility). Photopolymerisation was performed using a collimated light source (OmniCure S1500). The printing chamber was slightly modified from the previously described chamber used in the laser-based micropatterning method. A glass slide coated with Sigmacote (Sigma SL2) instead of PDMS was used as the base of the chamber. A droplet of the PEG pre-polymer solution (10 µL for 10 mm circular coverslips, 25 µL for 24 mm square coverslips) was placed onto the coated glass slide and a silanised coverslip was gently placed

on top, allowing the liquid to spread evenly between both glass surfaces. The surface of the coverslip was gently tapped with forceps if the liquid could not reach areas from surface forces alone. The photomask was placed superior to the coverslip and the UV lamp was applied from above for 1 minute at 100% power. The micropatterned coverslips were then gently lifted using a scalpel blade and placed into a culture vessel containing PBS supplemented with penicillin and streptomycin. Culture well plates containing samples were then sealed with parafilm and left to wash on a plate rocker at 4˚C for 48 hours before use.

3.2.5 Sterilisation and preparation of printed substrates.

The printed patterns are washed two times with sterile PBS prior to cell seeding. While submerged in PBS, samples are UV-sterilised in a biosafety cabinet for 15 minutes, with the plate lid removed. Coverslips were further sterilised by washing two times with 70% ethanol. Prior to seeding, micropatterned coverslips are incubated with Matrigel or Geltrex for 1 hour to support cell attachment.

3.2.6 Maintenance of iPSC lines and neural differentiation

hPSCs were cultured under standard conditions using Essential 8 media (E8; Thermo Fisher) on Geltrex-coated 6-well plates. For neural differentiation of hPSCs on one month-long cultures, we used our established protocol[46]. When 80% confluent, hPSCs were dissociated using Versene solution for approx. 5 minutes. hPSCs were collected and resuspended in E8 media for further maintenance culture on micropatterned substrates in 6 well plates. Small clumps were resuspended for standard seeding densities, while single-cell solutions of approx. 2 million cells/well were resuspended for high seeding densities. For retinal neuroepithelial differentiation hPSCs were maintained as described above until 90-95% confluent, then media without FGF (E6, Thermo Fisher) was added to the cultures for two days (D0 and 1 of differentiation) followed by a neural induction period (up to 4 weeks) in proneural induction

media (PIM; Advanced DMEM/F12, 1× N2 supplement, 1.9 mM L-glutamine, 1× MEM-NEAA, 10% antibiotic-antimycotic [All Life Technologies]).

For cultures lasting less than one month, neural differentiation was performed as above except with altered seeding density on 48 multi-well plates. Following dissociation, hPSCs were collected in a single-cell solution and resuspended at approx. 0.4 million cells/well in E8 media with 10 μM of a Rock inhibitor (Y-27632). E8 media was replaced after 2 hours, without Rock inhibitor. After 24 hours, E8 media was replaced with E6 media (Day 1 and 0) and then PIM (Day 2) for the remainder of the differentiation period. PIM was changed daily for 72-hour-long experiments and every second day for 1- or 2-week-long experiments unless replenishing media for specific treatments. Matrigel treatments were performed for 24 hours on Day 0 for 72-hour-long experiments and on Day 4 for 1- or 2-week-long experiments.

For Matrigel treatments of 2%, 4%, 10%, and 33%, cold Matrigel solution was diluted into pre-cooled PIM and mixed up and down with a P1000 pipette to ensure a homogenous solution. Cells were immediately placed into the incubator following treatment with Matrigel solutions and media was replaced without Matrigel after 24 hours. For Matrigel treatments of 66% and 100%, a droplet of cold Matrigel solution (diluted or pure) was placed onto a sterilised pre-cooled PDMS-coated glass slide and the micropatterned glass coverslip was gently placed cell-side down onto the droplet using sterilised tweezers, ensuring homogenous distribution of the Matrigel. After 30 minutes, 250 mL of PBS was gently added to the top side of the coverslip and the tweezers were used to gently dislodge and place the coverslip into a 48-well plate containing PIM.

3.2.7 Immunohistochemistry

Micropatterned samples were washed three times with PBS and fixed with 4% paraformaldehyde (PFA) in PBS for 15 minutes directly within the tissue culture plate. Cells were then permeabilised for 15 minutes at room temperature with 0.1 w v^{-1}% Triton X-100 in PBS, followed by incubation in a blocking buffer (3% BSA, 3.75 mg mL^{-1} glycine, and 0.05% w v^{-1} Tween 20) for 1 hour. Primary antibodies were diluted in solution containing 1% BSA and 0.05% w v^{-1} Tween 20 in PBS and incubated for 2 hours (SOX1, 1:500, ab109290, abcam; PAX6, 1:500, ab78545, abcam). The solution was removed and washed 3 times with PBS. Secondary antibodies were diluted in the same solution as previously and incubated for 1 hour (α-mouse. 488, 1:500, ab150077, abcam; α-rabbit. 647, 1:500, ab150075, abcam). Nuclear counterstains were performed using Hoechst 33342 at 0.1 µg mL^{-1} (Sigma 14533) diluted in ×1 PBS and incubated for 30 min. Samples were then washed 3 times with PBS prior to mounting. Micropatterned coverslips were mounted on 50x75x1 mm glass slides by placing a droplet of ProLong™ Gold (Thermo Fisher) and gently dropping the coverslips cell-side down, ensuring optimal preservation and visualization of the samples.

3.2.8 Imaging of patterned glass substrates

Live imaging of the micropatterned substrates was performed using an EVOS FL microscope for brightfield monitoring. Confocal imaging was performed using a Zeiss LSM 800 confocal microscope (Zeiss, Germany). For fluorescently stained substrates, images were collected using Z-stacks of 1 µm. Whole coverslips were imaged through multi-position image tiles that were stitched together to create montages of the entire patterned coverslip. Images of single colonies were utilised for representative imaging and quantification.

3.2.9 Quantification of patterned cultures

Images were quantified manually (e.g. counting the percentage of intact colonies) or using custom MATLAB scripts (Appendix). To quantify the average height of the micropatterned colonies, the average of the x and y projections of individually imaged colonies was used. Segmentation of the individual colonies was performed using Otsu's method of thresholding to minimise variations between samples caused by background fluorescence. Region properties of the segmented colonies were extracted from the TIFF image scaled from pixels to actual values.

3.2.10 Statistical analysis

For each of the 72-hour, 7-day, and 4-week experimental time points, a minimum of 3 independent experimental replicates were performed. Experiments were performed in duplicate or triplicate for each independent replicate. For the 14-day experimental time point, only one independent replicate was performed, in duplicate. Welch's t-test was performed for samples with one independent variable, and two-way ANOVA with Tukey's method for multiple comparisons was performed for samples with two independent variables (not significant "n.s." $p > 0.05$, or significant: $*p < 0.05$, $**p < 0.01$, $***p < 0.001$).

3.3 Results and Discussion

3.3.1 Design and optimisation of technique to fabricate micropatterned glass substrates through 3D printing

Micropatterns of various geometries and dimensions could be fabricated from the laser-based UV photopolymerisation method (Figure 3.1). This technique demonstrated a high degree of customisability, enabling the creation of 2D patterns through programming of the x-y stage (Figure 3.1a). Glass substrates were selected as the material surface due to the ease with which polymer materials can be attached through covalent bonding[195]. To avoid concentrated points of mechanical stress associated with corners, such as those in polygons, patterns with curved geometries were selected.

The adherence of the printed patterns to the glass substrate was robust, attributed to the functionalisation of the glass surface via silanisation prior to printing. This preparation minimised the potential for patterns to detach or delaminate after multiple washes with PBS, as well as during media changes. The patterns remained physically intact for a one-week testing period under storage conditions of PBS submersion in a 4°C cold room. Furthermore, the patterned substrates could withstand sterilisation procedures involving 70% ethanol and UV exposure in a biosafety cabinet without apparent signs of damage or physicochemical changes.

One limitation of the method was noted in the attachment of the glass substrate to the printing platform (Figure 3.1b). The glass was held in place by being suctioned to a polydimethylsiloxane (PDMS)-coated chamber, utilising glass-silicone suction forces. However, in some instances, the glass substrate broke when being removed from the PDMS coating for placement into 48-well plates. These occurrences were infrequent, and the affected substrates were discarded. Additionally, occasional calibration issues with the laser resulted in slight inaccuracies in the printed diameters.

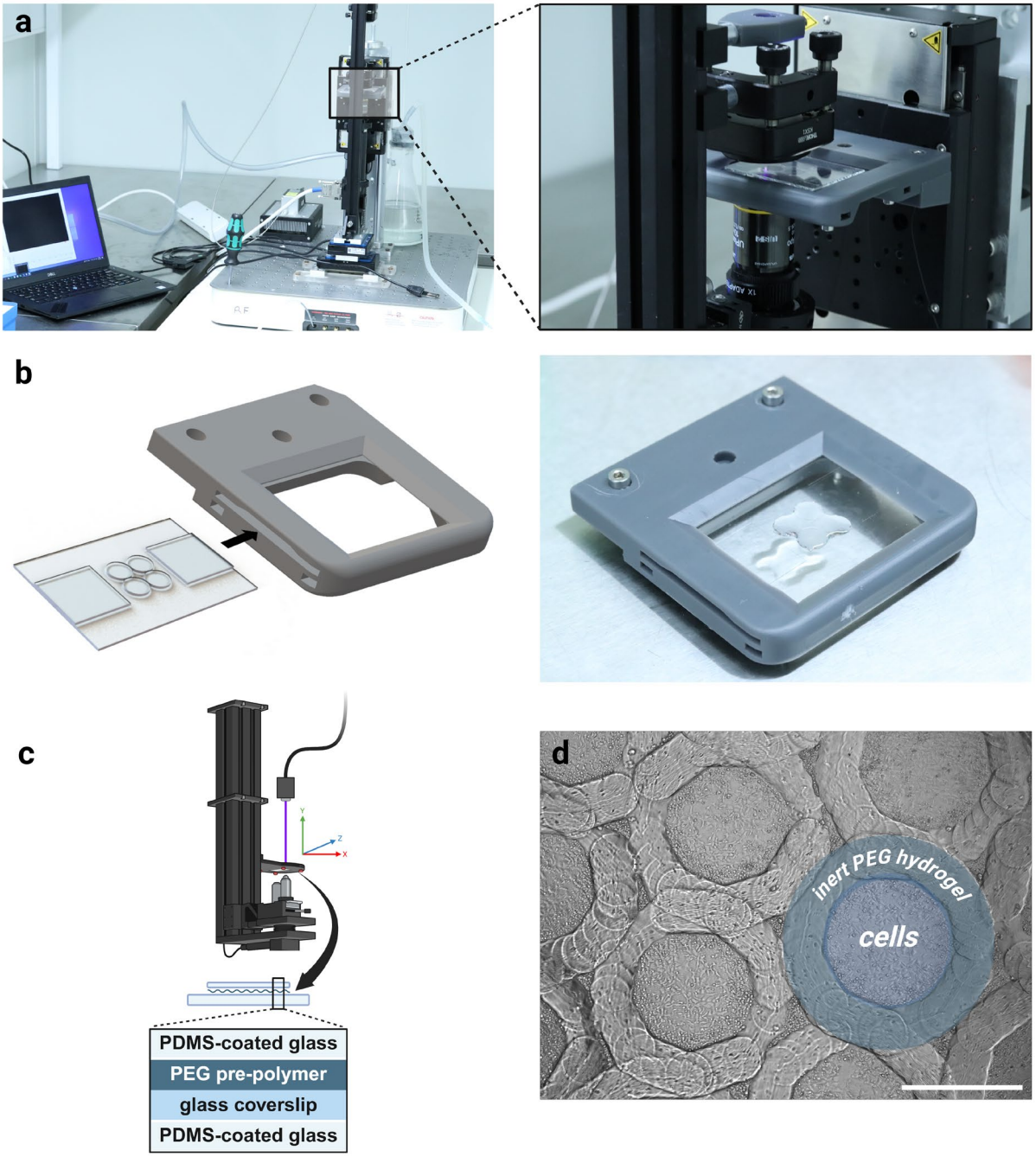

Figure 3.1 Application of custom-built printer to fabricate custom micropatterns on glass substrates using laser-based UV polymerisation.

(a) Setup with connected computer and GUI. (b) Chamber slide holder design (left) and 3D printed (right). (c) Schematic of the sandwiched layers within the glass chamber. (d) Brightfield image of an example printed pattern with cells residing on areas without the printed PEG hydrogel. Scale bar = 1000 µm.

Another limitation was the time required for printing—approximately 30 minutes to complete four 10 mm circular coverslips—which may not be inducive for high-throughput applications.

Laser printing speeds varying from 55 – 80 mm min^{-1} were tested while keeping a constant laser power. To avoid excessive polymerisation or the potential for undesired light refraction or reflections, a relatively low laser power of 30% PWM was selected. The slower speed (55 mm min^{-1}) resulted in more consistent, smooth, and complete patterns (Figure 3.2). In contrast, intermediate speeds of 65 mm min^{-1} and fast speeds of 80 mm min^{-1} led to imperfections such as incomplete polymerisation of patterns or disjoined features (Figure 3.2). These imperfections were characterised by irregular, fragmented features, which could compromise the structural integrity and functionality of the printed patterns.

As such, we selected the optimised speed of 55 mm min^{-1} while keeping all other parameters constant, including laser power, to ensure uniform polymerisation and feature continuity. By optimising the printing speed for laser power, the method facilitated the printing of circles with different diameters on the same glass substrate, enabling facile downstream characterisation of the effect of dimension on cell cultures.

The patterning of other shapes, such as sinusoids, was also tested. These shapes were successfully produced, with angles, offsets, and spaces being customisable according to desired design specifications, and the successful attachment of cells on the glass substrates (Figure 3.3). Promisingly, selective adhesion and survival of cells were observed in regions devoid of the printed PEG polymer. This observation confirmed that the printed regions could inhibit cell attachment, enabling the precise patterning of cells in confined areas. No unusual cell morphology or cell detachment was observed after 48 hours of culture (Figure 3.3), suggesting

that the patterned substrates could provide a conducive environment for cell growth and maintenance.

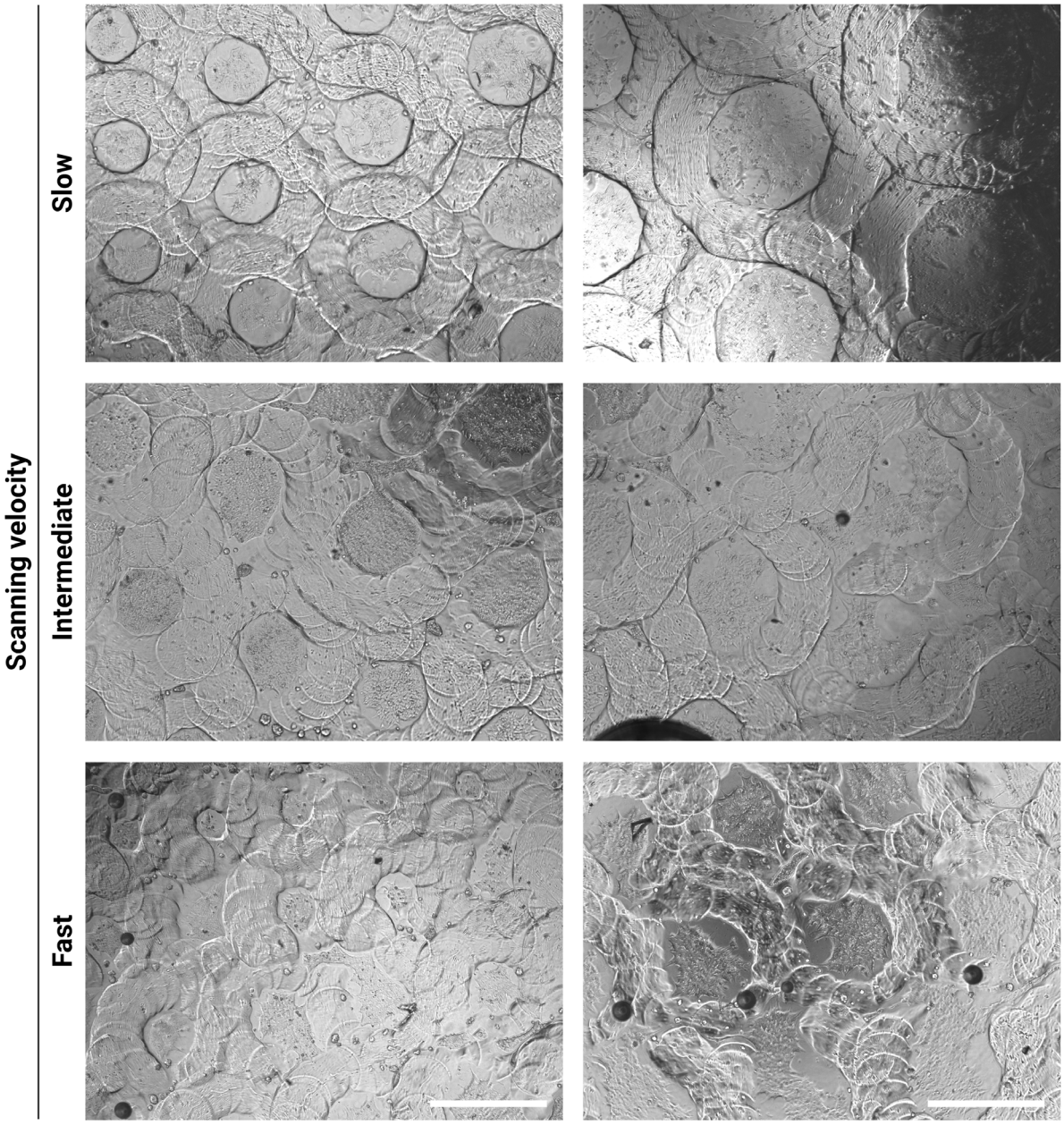

Figure 3.2 Optimisation of printing speed to fabricate custom micropattern designs. Slow speeds (55 mm min^{-1}) demonstrated improved hydrogel resolution and integrity compared to intermediate (65 mm min^{-1}) and fast (80 mm min^{-1}) speeds. Laser power was kept constant during optimisation. Scale bar = 1000 µm.

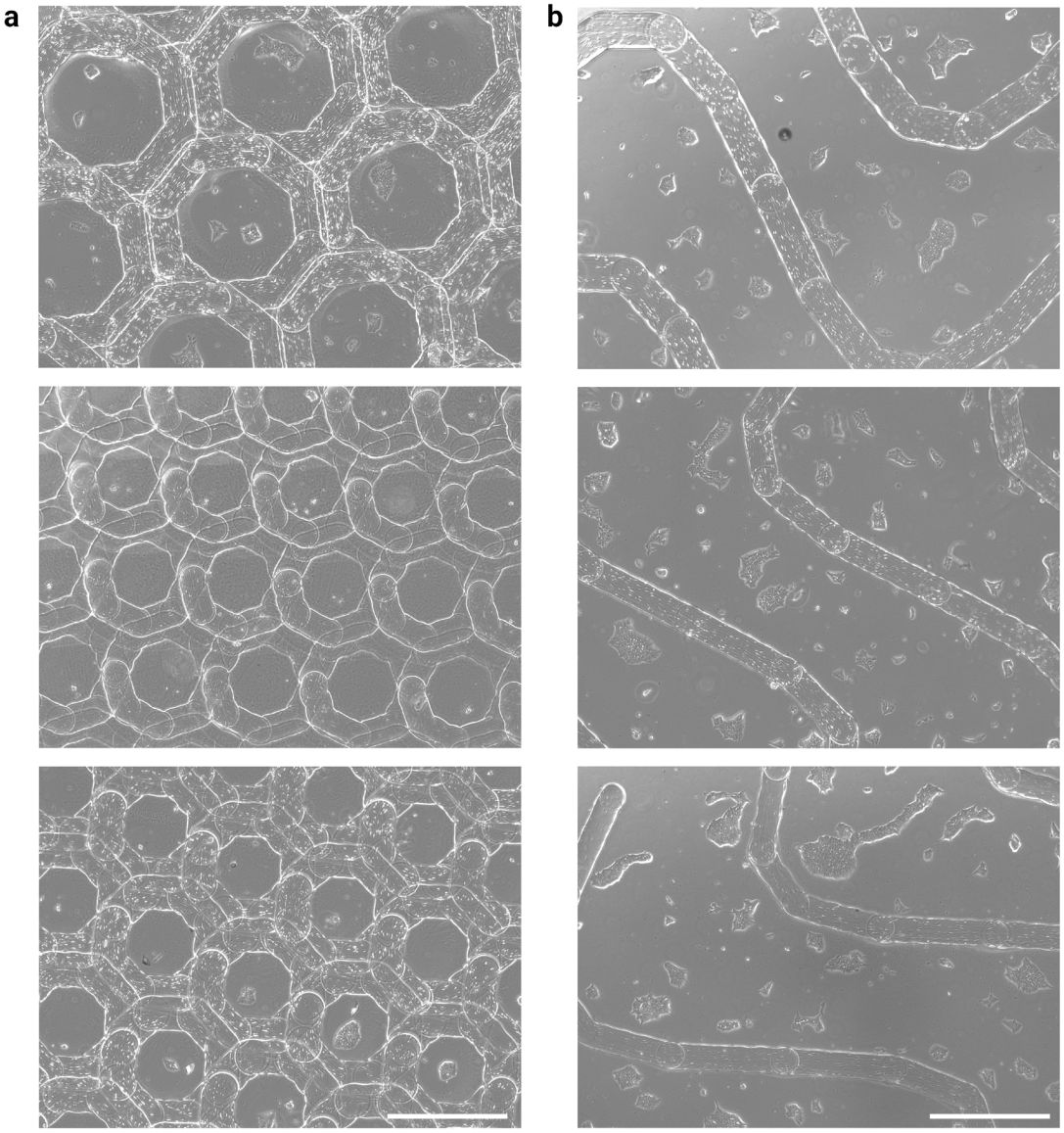

Figure 3.3 Different micropattern geometries fabricated using the custom-built printer. (a) Circular patterns of different diameters and (b) sinusoid geometries were fabricated. Cells were seeded on these patterns, showing regular attachment and morphology post-seeding. Scale bar = 1000 μm.

Since cells were seeded in a homogenised media solution, the distribution of cells could not be inherently controlled. The low seeding density utilised in the initial tests resulted in the absence of cells in some of the individual circular micropatterns (Figure 3.3a). Due to the complete isolation of the individual circular patterns due to the printed PEG boundaries, the initial

absence of cells in a particular region meant the absence of cells throughout the remainder of the culture period. This issue was less concerning in the sinusoid pattern, due to the large space offered for cells to proliferate and eventually for individual colonies to contact each other (Figure 3.3b). As such, higher seeding densities may be required to ensure the complete occupation of cells within each individual circular pattern. Nevertheless, we observe that PEG-based micropatterning techniques can be used to fabricate patterns of various dimensions and geometries. Importantly, the polymer remained stable after cell seeding and no attachment of cells to the polymer was observed.

3.3.2 Cell behaviour and viability on micropatterned glass substrates

As our standard differentiation protocol involves the self-organisation of 3D tissues from confluent monolayer cultures over a one-month long period, we next aimed to assess the long-term behaviour of cells on our micropatterned substrates. The long-term viability (up to 4 weeks) of three different iPS cell lines was assessed using glass coverslips printed with circular and sinusoidal micropatterns. It was hypothesised that the curved geometry of these shapes could induce the formation of optic cup-like structures.

To characterise the capacity of neural and retinal organoid formation, neural induction started when iPSCs reached 90-100% confluency. To minimise further variations from standard protocol, cells were seeded at standard density as previously established[46]. In all independent replicate cultures, we observed cell attachment to specified regions of the micropatterned substrates for the duration of the 4-week differentiation period (Figure 3.4). However, proliferation and long-term attachment of cells were highly dependent on pattern geometry and the location within a well.

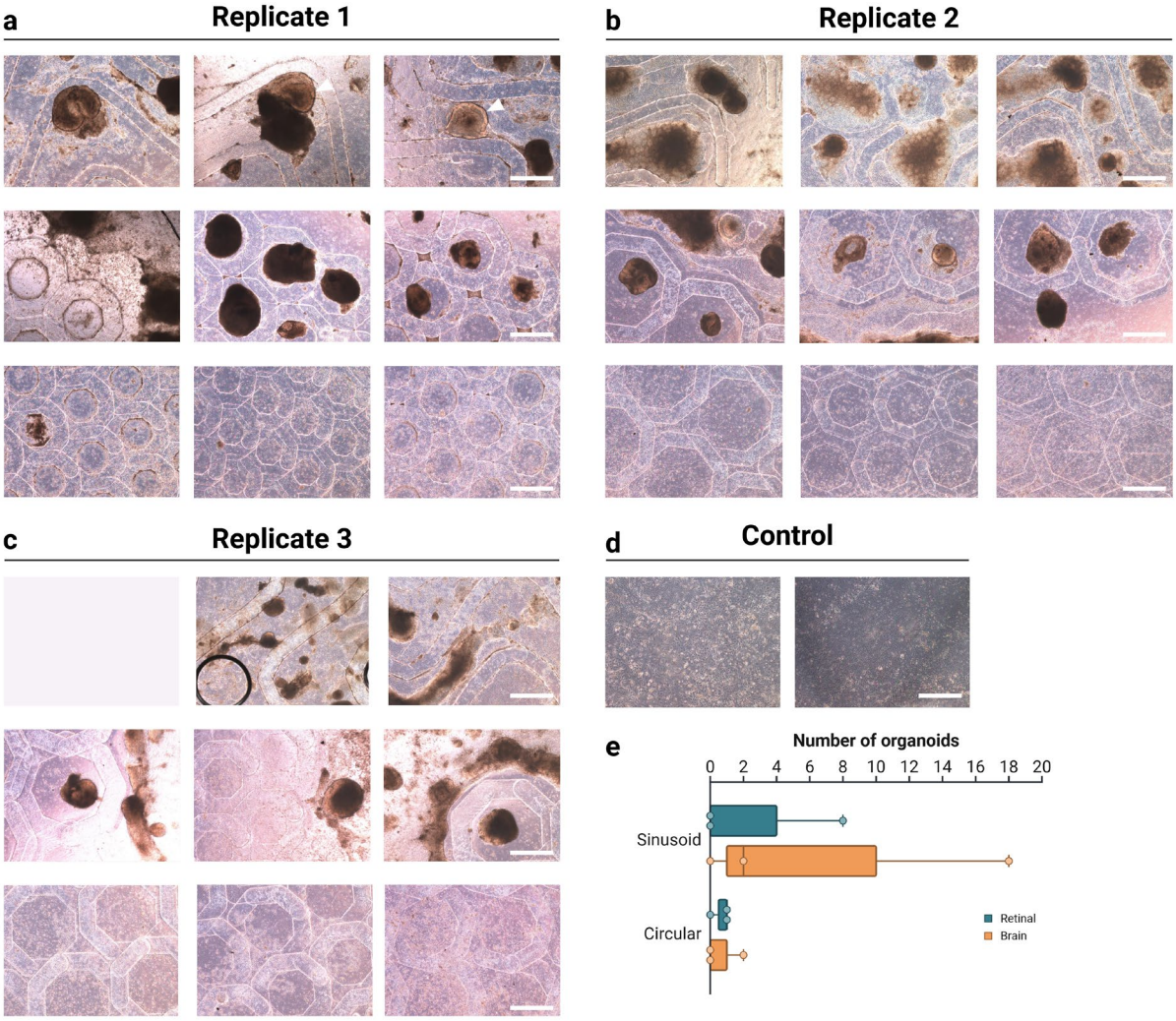

Figure 3.4 iPSCs (HOIK1) were seeded at standard cell density on micropatterned substrates and differentiated for 4 weeks using proneural induction media.

(a) Replicate 1 showed the formation of retinal vesicles within the sinusoid pattern, indicated by the shiny neuroepithelial border of the rounded tissues (white arrowhead). Cells in the circular micropatterns had the capacity to form dark neural tissue structures, though only near the edges of the coverslip. (b) Replicate 2 showed the formation of neural rosette structures on the sinusoid patterns. Poorly formed vesicle structures were observed in few of the circular patterns. (c) Replicate 3 demonstrated some neuroepithelial structures growing on the sinusoid pattern, though these tissues were poorly organised. Few vesicles, which lacked proper neuroepithelial tissues, grew within the circular patterns. (d) Control cultures differentiated poorly, with no vesicles forming. (e) Quantification of the micropatterned substrates showed that the sinusoid pattern had a higher capacity for retinal organoid generation (n = 2 wells, N = 3 independent batches). Scale bar = 1000 μm.

Interestingly, in circular micropatterns, regions of the glass substrate not covered by micropatterns showed high cell densities after 4 weeks, while cell attachment within the confined patterns was relatively poor (Figure 3.4a-c). This may suggest that complete confinement may not be conducive to the long-term survival of cell colonies. In some cases, vesicle tissue structures, characterised by a rounded 3D appearance, were observed within both the circular and sinusoid geometries. We observed the scarce formation of tissues with retinal vesicle-like features such as the characteristic bright and well-defined neuroepithelial border. These tissues were observed within the sinusoid pattern both at the curved and straight boundaries (Figure 3.4a).

In one independent replicate, dark rounded tissues with a neural rosette appearance formed within the circular patterns at the edge of the coverslip (Figure 3.4a). These structures have been previously characterised as cortical brain-like tissues[202] that spontaneously appear under our established protocol. As such, it is plausible that the complete confinement of cells may have the potential to generate individual cortical-like tissues, though this result was inconsistent across other replicates performed. The particular location of this observation, at the edges of the well plate, may be correlated with potential edge effects associated with the multi-well plate. Previous work has highlighted the uneven distribution of cells within multi-well plates, particularly at the edges, due to thermal gradients[203], potentially contributing to our observed results.

Across the three independent experiments, high variability was observed, with half of the cultures failing to generate either retinal or brain vesicles (Figure 3.4e). In total, the sinusoid patterns had the potential to produce a greater number of retinal vesicles than the circular patterns (an 8-fold increase). However, the nominal difference was relatively low (n = 7 retinal vesicles). Interestingly, the control cultures on glass substrates failed to form any well-defined

vesicles (Figure 3.4d). This may indicate that, in the absence of spatial confinement, the glass substrate may not be conducive to neural or retinal differentiation.

To test whether a different cell line may be more amenable to glass substrates, a single independent replicate was performed on a different iPSC line (149BR). The same conditions and seeding densities were used; however, due to the higher number of retinal tissues formed on the sinusoid pattern, only the sinusoid patterns were used for this experiment. Moreover, we added a tissue culture plastic control culture to observe the differences between glass and plastic substrates. Interestingly, on sinusoid micropatterns, the second cell line showed high cell detachment at Day 25 of differentiation, with no clear formation of retinal or brain tissues (Figure 3.5). In contrast, the control glass and tissue culture plastic substrates supported the formation of retinal vesicles with clear neuroepithelial borders. We unexpectedly observed higher cell detachment on the tissue culture plastic surfaces compared to the non-patterned glass substrates. As we are not particularly interested in the generation of vesicles without the use of micropatterning, these cultures were not quantified. From this preliminary study, we postulate that some cell lines may have a higher capacity for survival and differentiation on micropatterned substrates than others. Moreover, these cell lines may also have differential responses to the stiffness of the substrate, particularly that between glass and plastic. However, due to constraints in resources, the experiment was not replicated. As such, future work to reproduce this study may improve the reliability of these findings.

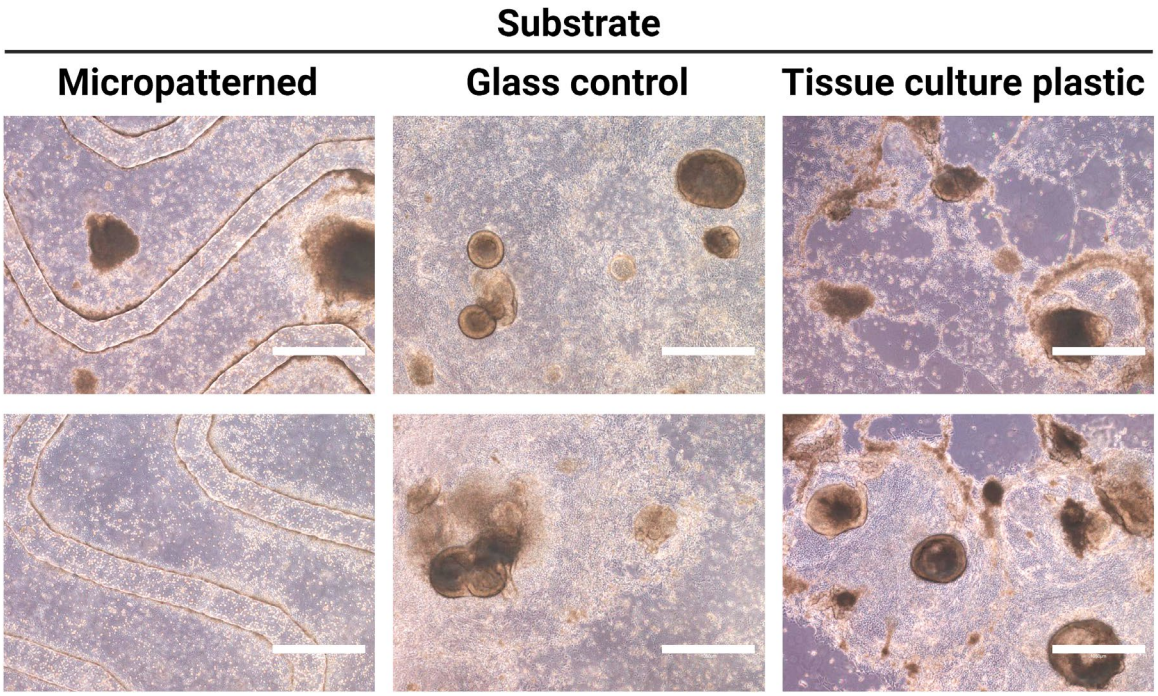

Figure 3.5 Poor capacity for vesicle formation was observed in certain cell lines (149BR) after 3 weeks of differentiation in proneural induction media, despite vesicle formation in glass and plastic control substrates (n = 2 wells, N = 1 differentiation; Scale bar = 1050 µm).

Having previously observed that low cell seeding leads to a lack of iPSCs forming a confluent monolayer of cells and thus poor differentiation outcomes, we similarly performed a preliminary singular study on the seeding of cells at high density using our originally tested cell line. However, as we were more interested in the generation of spatially defined tissues, we chose to only move forward with circular micropatterns. High-density seeding (2×10^6 cells per well) on the circular micropatterns resulted in complete cell confluency within 48 – 72 hours (Figure 3.6). Following the start of differentiation, confined cells survived up to one month on the circular patterns. However, the cells had a high tendency to detach or form aggregated structures resembling those of embryoid bodies. These structures did not possess well-defined borders, potentially indicating poor differentiation and a lack of tissue self-organisation. Due to the lack of any well-formed vesicles, these results could not be quantified.

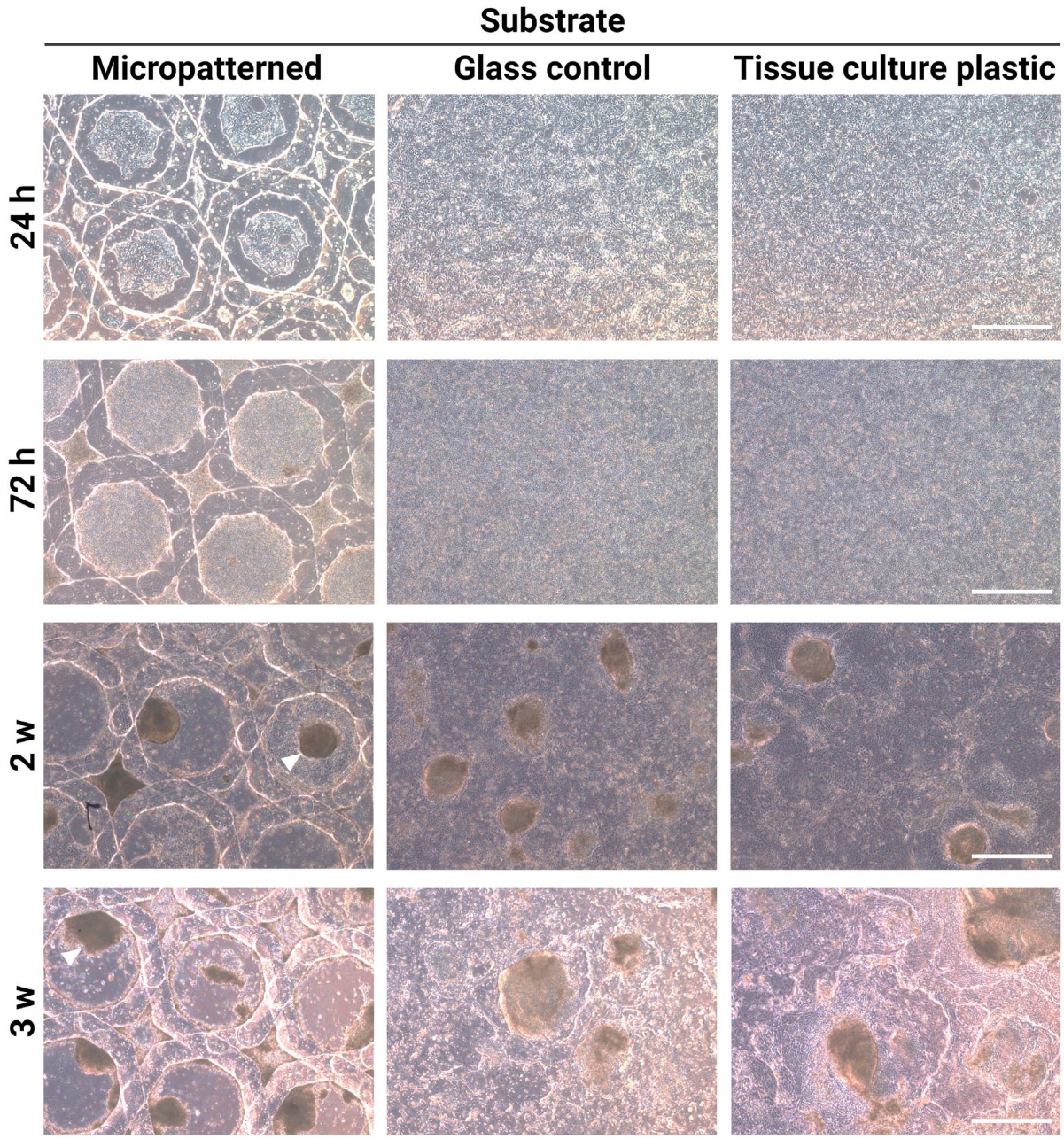

Figure 3.6 Representative images of high initial seeding density of iPSC (HOIK1) cultures differentiated for up to 3 weeks in proneural induction media.

Higher initial seeding density improved the formation of immature vesicle structures on glass and tissue culture plastic surfaces but not micropatterned cultures (n = 2 wells, N = 1 differentiation batch). On micropatterned cultures, poorly structured cell aggregates formed within some circular patterns (white arrowheads). Scale bar = 1000 µm.

Interestingly, on non-micropatterned glass and plastic, we observed that the tested cell line could form structures that resembled immature retinal vesicles, characterised by bright rounded

neuroepithelial-like tissue. Although these structures lacked clear tissue organisation, the differential behaviour of cells upon lower and higher seeding densities may indicate that higher cell densities affect the long-term survival of the cell line utilised. This may suggest that higher seeding densities to reach confluency sooner may improve outcomes on glass substrates, and potentially on micropatterned substrates. Indeed, it has previously been reported that higher cell densities can outweigh effects caused by high substrate stiffnesses[204], such as those of glass surfaces. As such, we moved forward with higher seeding densities for future experiments to ensure all circular patterns reach confluence at similar time points. However, it is evident that further optimisation of either physical or biochemical parameters may be required for optimal self-organisation, regardless of initial seeding density.

Our initial studies show evidence that micropatterns have the potential to support cell viability and self-organisation of cells in the short and long term. Nonetheless, high variability was observed within and between cell lines and at different seeding densities. The first cell line demonstrated superior growth compared to the second cell line in patterning conditions. However, these cultures tended towards cortical brain fates rather than retinal differentiation, possibly indicating the absence of the correct stimuli to induce retinal differentiation. In contrast, the second cell line only formed organoids on non-micropatterned glass or tissue culture plastic controls. Although the sinusoid patterns were relatively more conducive to organoid self-organisation than circular micropatterns, their geometry was not favourable as the appearance of organoids was stochastic. Alternatively, under optimised conditions, circular micropatterns can potentially enable the isolated and predictable generation of numerous organoid structures within a single patterned substrate. As such, circular micropatterns were selected for further optimisation.

3.3.3 Effect of dimension and biochemical modulation in early micropatterned cell cultures

To optimise the scalable generation of 3D tissues within circular micropatterns, the initial 72 hours of neural differentiation were characterised in a scaled-down 48-well plate setting. This approach was designed to systematically explore the effects of ECM components on the early stages of neural differentiation, with a specific focus on delivery of Matrigel, an ECM extract known to induce the formation of complex 3D structures[154]. By evaluating colony integrity and viability under various Matrigel concentrations, we aimed to refine our protocol to reliably induce early neural-retinal structures, thereby enhancing the physiological relevance of the tissue model.

Two methods of Matrigel stimulation were utilised, the dilution of Matrigel in media (2-33%) or the direct embedding of coverslips in Matrigel (66-100%) at the onset of neural differentiation. Brightfield imaging revealed that colonies treated with higher concentrations of Matrigel (33-100%) exhibited increasingly complex morphological features by the 72-hour time point (Figure 3.7). This included the formation of dark folded structures indicative of early tissue folding and invagination processes[154]. Interestingly, no differences between 33% Matrigel dilution and 100% Matrigel embedding were evident, indicating there may be a threshold in which maximal tissue folding occurs. The relatively lower tissue folding observed in 66% Matrigel embedded treatments may be the result of poor stimulation due to the dilution of Matrigel upon embedding. As such, effective stimulation via the Matrigel may have been hindered due to poor contact with cells during the short incubation period of 30 minutes. In contrast, the 24-hour treatment period in the Matrigel dilution protocol potentially offered higher levels of stimulation.

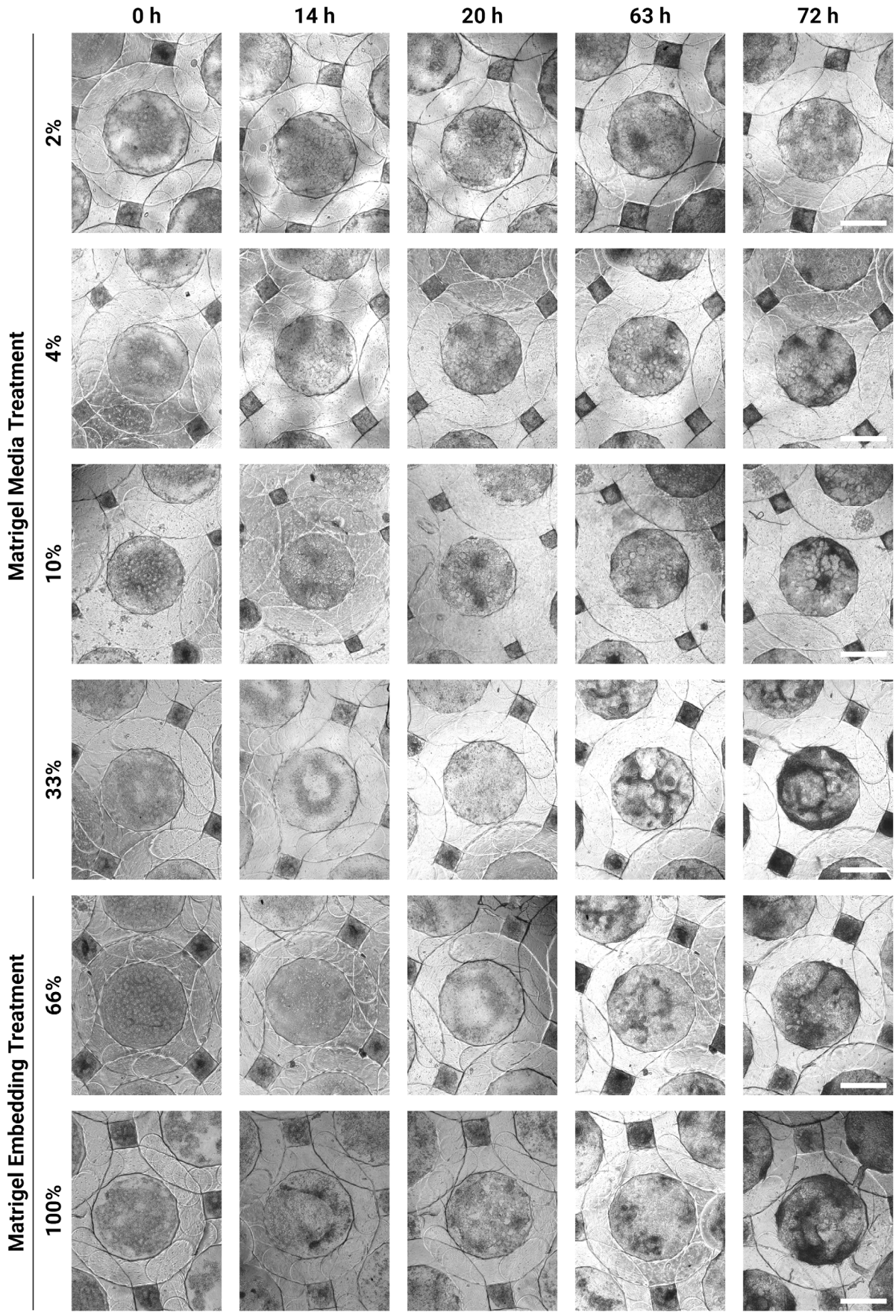
0 h
14 h
20 h
63 h
72 h
Matrigel Media Treatment
2%
4%
10%
33%
Matrigel Embedding Treatment
66%
100%

Figure 3.7 Representative images of iPSCs seeded onto micropatterned cultures, differentiated for 72 hours in proneural induction media, and treated with Matrigel through media dilution of direct embedding.

Micropatterned cultures treated with 33% Matrigel diluted in the media or embedded directly in 100% Matrigel showed the highest observable level of tissue folding, as indicated by dark neural structures forming in the centre of the colony. Scale bar = 400 µm.

In lower concentrations of Matrigel dilution, neuralisation was still evident, with the formation of neural rosette structures in the centre of tissues given the 10% treatment and, to a lesser extent, the 4% treatment (Figure 3.7). However, no evident 3D structures were observed in these lower concentrations. As such, a clear correlation between Matrigel concentration and morphological complexity can observed within the first 72 hours of stimulation, depending on the method of treatment. This is consistent with previous literature using Matrigel to induce tissue folding[154], suggesting that ECM proteins and/or gel structures can promote the mechanical and biochemical environment necessary for cells to engage in more complex morphogenetic movements, akin to those observed during early neural development.

To better understand the formation of 3D structures, the height of individual micropatterns was quantified in large micropatterns (1000-µm diameter). Consistent with observations in gross morphology, increasing concentrations of Matrigel were correlated with increasing colony height (Figure 3.8a). A significant increase in height was observed within patterns embedded with 100% Matrigel concentration (48.2 µm ± 8.0) when compared to all other conditions, with the largest difference observed of 15.8 µm compared to the 2% Matrigel treatment (32.5 µm ± 2.33). These results suggest that the ECM hydrogel environment provided by high concentrations of Matrigel is critical for promoting vertical growth, a key aspect of 3D tissue formation. However, higher variability was also correlated with increasing Matrigel concentrations (Figure 3.8a).

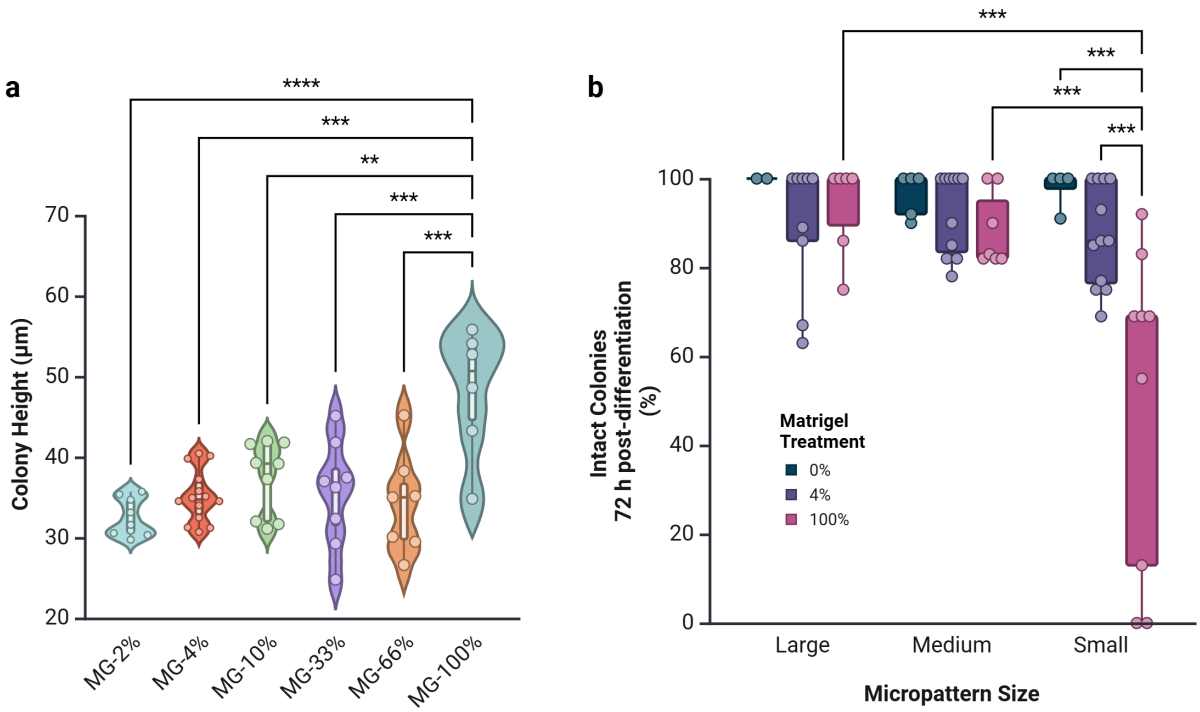

Figure 3.8 Matrigel (MG) treatments caused an increase in the average colony height, though reduced the proportion of intact colonies after 72 hours.

(a) Direct embedding of micropatterned colonies in Matrigel resulted in a significant increase in the colony height ($p < 0.05$, minimum N = 6 colonies for each treatment). (b) Large (≥ 650 µm) and medium (450 – 650 µm) micropattern diameters demonstrated improved retention of cell colonies compared to small diameter patterns (≤ 450 µm).

Low concentrations of Matrigel (2-10%) demonstrated a decreased distribution of data compared to higher concentrations. Surprisingly, due to the high variability observed in the height of both the 33% dilution (35.5 µm ± 6.6) and 66% embedding (34.3 µm ± 6.3) treatments, the average height of the 10% dilution treatment was higher (37.3 µm ± 4.5) despite the lower Matrigel concentration. This indicates that the complex interactions induced by higher concentrations of Matrigel also lead to higher inconsistencies. Indeed, the heterogeneity and batch-to-batch variability of Matrigel solutions is a well-established limitation of the ECM solution[205]. As such, future work on synthetic alternatives to Matrigel may provide more consistent results. One significant limitation of the study is the absence of a non-treated control

culture performed in parallel with the Matrigel treatments. Comparisons to control cultures would allow for a deeper understanding and evaluation of the magnitude in which tissue folding is occurring. Although the 2% Matrigel could be considered relatively similar to a non-treated control culture due to the absence of neuralised structures, future studies where controls are performed in parallel with these experiments are required.

Since the 4% Matrigel treatment was the lowest concentration tested that was able to induce neural rosette structures, we were interested in focussing on this treatment as a cost-effective method to induce neuralisation. Moreover, the relatively low variability observed in these cultures (35.2 μm ± 3.3) may be beneficial in ensuring consistency across cultures. Alternatively, the highly 3-dimensional tissues observed in the 100% embedding treatments demonstrated great potential in generating complex features, despite the high variability observed. As such, we quantified the relative success of different-sized micropatterned cultures in these treatments at the 72-hour time point. This was performed by manually identifying and counting the presence of viable colonies post-fixation. Micropattern success was evaluated as the number of viable cell colonies as a percentage of all micropatterns fabricated for large (≥ 650 μm), medium (450 – 650 μm), and small (≤ 450 μm) diameters (Figure 3.8b). Interestingly, colonies treated with 100% Matrigel exhibited the lowest average percentage of intact patterned cells on small (88.4% ± 8.4) and medium (50.0% ± 35.9) micropatterns. As such, large micropatterns treated with 100% Matrigel showed significantly higher viability (93.5% ± 10.7) than small micropattern diameters of the same treatment ($p = 0.0002$).

Generally, high variability in the percentage of intact colonies was observed across all small and medium diameter patterns. In particular, small micropatterns demonstrated relatively poor viability along with high variability between cultures in all treatment groups. The inverse relationship between Matrigel concentration and cells integrity in smaller micropatterns could

be attributed to the increased mechanical and biochemical stress imposed by a denser ECM environment. High Matrigel concentrations may create a more restrictive microenvironment, potentially leading to excessive ECM remodelling demands, limited nutrient diffusion, or altered cell-ECM interactions, which can compromise cell viability and colony cohesion in smaller micropatterns. Moreover, excessive 3-dimensionality of the cell aggregates can induce detachment and lifting of the colony during media changes.

These findings highlight a delicate balance between promoting 3D growth and maintaining structural stability. Interestingly, while 4% Matrigel was sufficient to maintain a high percentage of intact differentiating patterns on small to medium micropatterns, its effectiveness diminished on larger micropatterns, where colony integrity became more variable (between 60-100%). This may suggest that the ECM's physical properties may differentially affect colony cohesion depending on the colony size and the distribution of mechanical forces within the micropattern.

Matrigel contains a variety of ECM proteins, including laminins and collagens, which closely mimic the *in vivo* extracellular environment. The differential response of micropatterned colonies to Matrigel treatment across various concentrations (2-100%) highlights the nuanced role of ECM in modulating cellular behaviour and morphology. Our findings suggest that the addition of Matrigel in both soluble and gel forms can significantly influence the morphogenesis of neural stem cell colonies, potentially by providing the structural cues and biochemical signals necessary for 3D tissue organization. While high concentrations of Matrigel can enhance colony 3-dimensionality, enabling the engineering of more complex tissue structures, it may also introduce challenges related to colony integrity, particularly in smaller micropatterns. This balance between promoting 3D growth and maintaining viability is critical for the successful application of micropatterning techniques, particularly in the

development of neural and retinal tissues where precise control over morphogenetic processes is essential.

Future studies may explore the mechanistic basis of these observations, potentially investigating the role of specific ECM components in mediating cell-ECM interactions, the impact of mechanical forces on colony morphology, and the interplay between ECM composition and cellular signalling pathways during early differentiation. Additionally, optimising the timing and concentration of Matrigel application, perhaps in combination with other ECM components or signalling molecules, could further enhance the scalability and robustness of this approach for generating 3D neural tissues.

3.3.4 Effect of dimension and biochemical modulation in intermediate stages of neural differentiation

To further characterise early neural differentiation following 4% Matrigel treatments, we next performed experiments at extended time points of 7 days. Here, we use immunofluorescent staining to evaluate the extent of neural differentiation of these micropatterned cultures. Similar to the previous section, we differentiated cells on micropatterned substrates comprising a gradient of different diameters to observe dimension-dependent effects.

To confirm neuralisation and further examine the morphology of structures at this time point, we performed immunofluorescent staining using neural markers SOX1 and PAX6 (Figure 3.9). The presence of SOX1 during this early period can highlight differentiation towards general neural fate prior to retinal specification. At 7 days of differentiation, cells demonstrated an observable trend of increasing height with decreasing micropattern diameter, as observed through x-y projections of Z-stacks (Figure 3.9a,c). We observed that smaller micropatterns (approx. 300 μm diameter) developed a 3D budded structure, due to spatial constraints that limited lateral expansion. Alternatively, larger micropatterns (approx. 700 μm diameter) showed a flatter morphology, where the centre of the pattern was slightly raised in the absence of any budded structures. Positive neural cells were observed in all dimensions tested. Notably, in small micropatterns, the expression of early neural markers SOX1 and PAX6 was regionally localised to these budded areas, suggesting a correlation between morphological features and early neural differentiation.

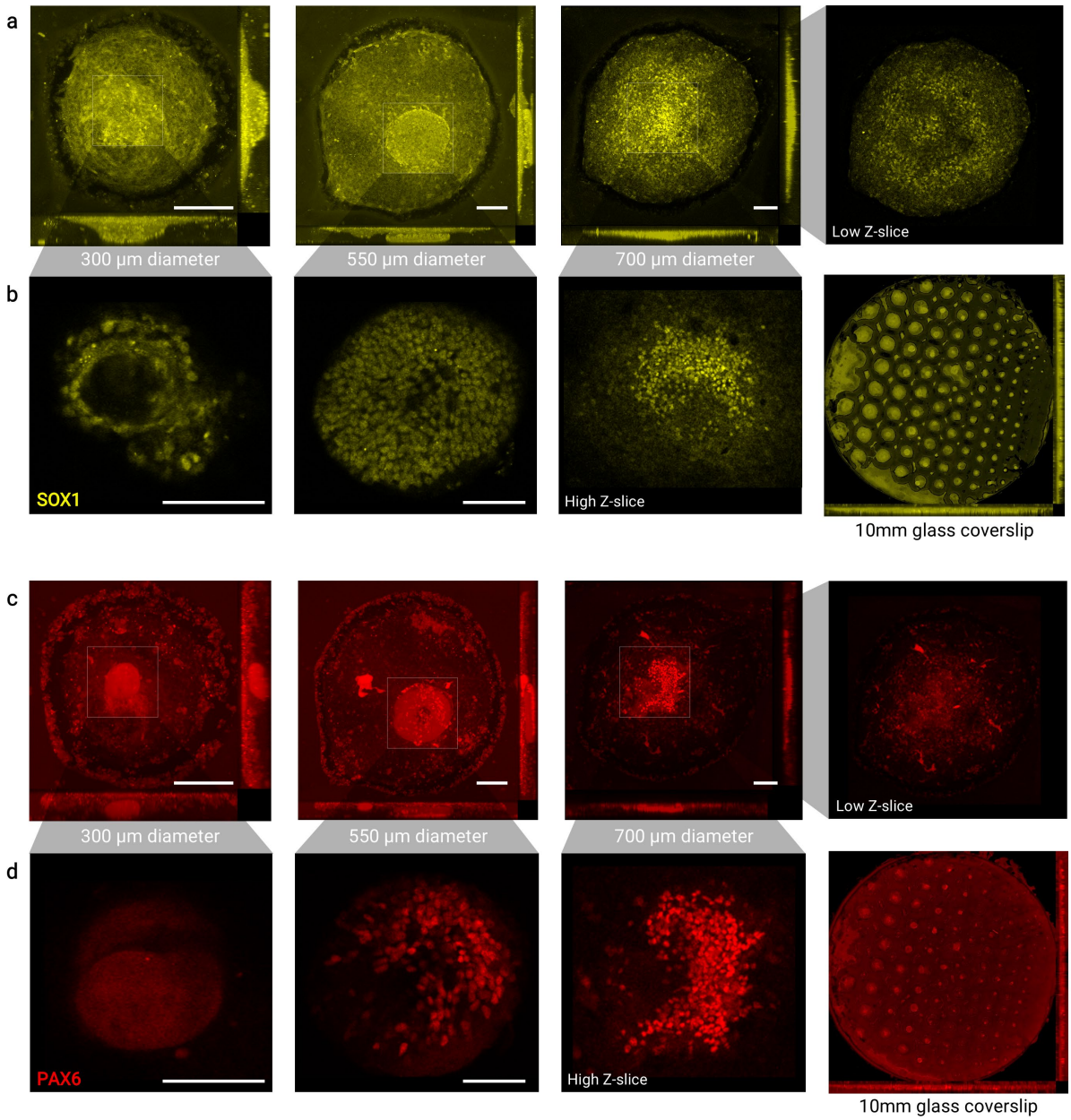

Figure 3.9 Representative images of SOX1 and PAX6 immunofluorescent stained micropatterned colonies treated with 4% Matrigel showed that decreased pattern diameter is correlated with increasing colony height.

(a,c) Maximum intensity projections, with x-y projections of z-slices, of different sized colonies reveal different levels of SOX1 and PAX6 expression. Smaller diameter patterns showed a highly budded structures while large diameter patterns remained relatively flat. Scale bar = 100 µm. (b,d) Staining for early neural makers SOX1 and PAX6 showed a size-dependent expression profile of both markers upon inspection of a single z-slice of the central region. Nuclear expression of PAX6 was not observable in small diameter patterns, indicating less neural differentiation relative to colonies in larger micropattern diameters. Images of the whole

coverslip illustrate the correlation between larger micropattern diameters and higher PAX6 expression. Scale bar = 200 μm.

In intermediate-sized patterns (approx. 550 μm diameter), the budded morphology persisted, although the diameter of the budded area remained similar to those in the smaller patterns (Figure 3.9a,c). Similar to small-sized diameters, the expression of neural markers was regionalised to the budded areas. Larger micropatterns displayed more diffuse expression of SOX1 and PAX6 throughout the colony. This pattern of marker expression, particularly the strong expression in raised areas of large micropatterns, may indicate a spatial influence on neural differentiation, with different microenvironments within a single colony promoting varying levels of neural marker expression.

Similarly to our previous study, we assessed the structural integrity of micropatterned substrates at the 7-day time point in 4% and 100% Matrigel treatments (Figure 3.10a). As previously observed, large micropatterns showed a higher percentage of intact colonies across all Matrigel treatments, with almost all cultures still attached. Again, smaller micropatterns were more prone to detachment, likely due to their increased 3-dimensionality, which can easily become detached from the culture substrate. Notably, micropatterns treated with 4% Matrigel displayed the highest percentage of intact colonies within medium (99.1% ± 2.8) and small-sized (95.9% ± 7.5) patterns, with a significantly higher retention of small colonies compared to control treatments (71.9% ± 31.7; $p = 0.0075$).

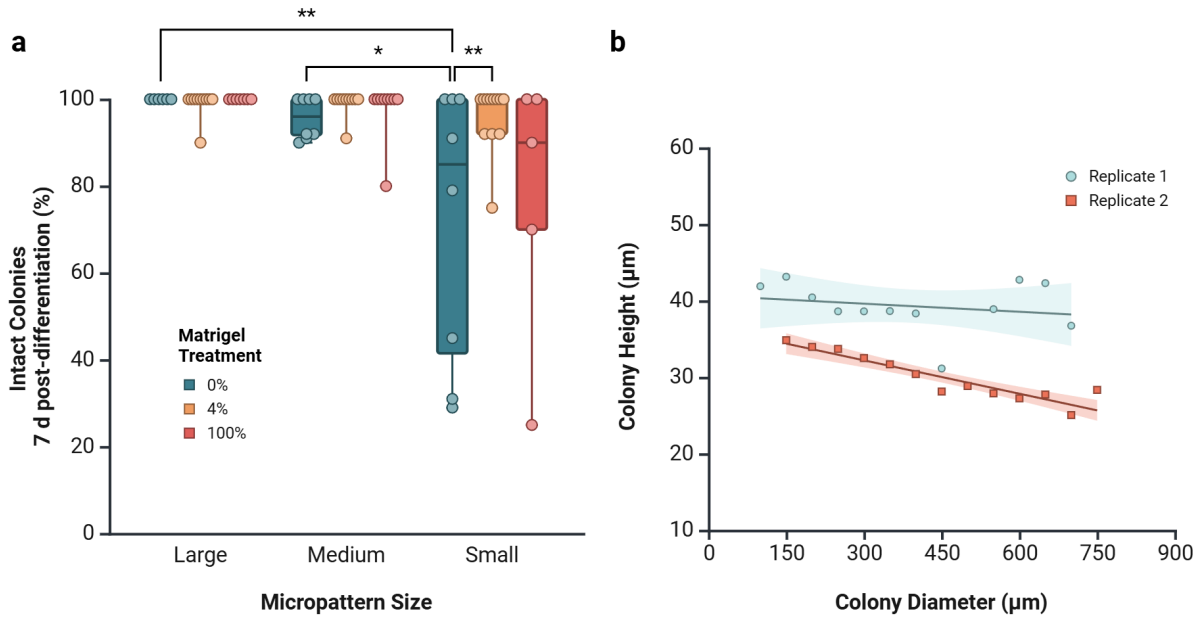

Figure 3.10 Proportion of intact colonies on different pattern sizes after one week of differentiation in proneural induction media, with and without Matrigel treatment.
(a) Smaller micropattern diameters resulted in a significant decrease in the number of intact colonies at day 7 in the absence of Matrigel treatment (minimum N = 6 colonies for each group, $p < 0.05$). (b) High variability was observed between two independent replicate experiments in non-treated cultures, with an increasing deviation in colony height with increasing micropattern diameter (data averaged within replicate batches).

To better visualise the variability across different replicates, the average height of two independent non-treated replicate cultures was quantified to discount any variabilities caused by Matrigel treatments (Figure 3.10b). Interestingly, we observed a consistent downward trend in both replicates, though higher variability in one replicate compared to the other. Within the two replicates, a greater difference was observed between the larger diameter colonies compared to smaller diameters. The high variability observed between these two cultures highlights inconsistencies commonly faced in stem cell research, where reproducibility can be relatively poor[206]. As such, further methods to enhance the consistency between stem cell cultures, with and without micropatterning techniques, are required.

Finally, to assess the longer-term potential of micropatterned substrates, we performed a preliminary study of cultures for up to 14 days of differentiation with 4% Matrigel treatments. Due to the poor viability previously observed in the smaller micropatterned cultures, we only performed a singular experiment on large-diameter micropatterns (1000-μm diameter). Upon morphological assessment of immunofluorescent stained samples, we observed disorganised structures in both the control and Matrigel-treated cultures, though relatively improved cell viability in Matrigel-treated cultures (Figure 3.11a). Quantification of colony heights revealed the persistence of high variability between the cultures treated with 4% Matrigel, where colony height within the same experiment varied to a large degree. In contrast, control cultures remained relatively consistent in height, again highlighting the potential for Matrigel to introduce inherent variability. To observe whether the Matrigel treatment could improve the differentiation of the micropatterned culture, we quantified the relative expression of SOX1 against nuclear counter-staining with Hoechst. A slight increase in SOX1 was observed in Matrigel-treated cultures (1.24 ± 0.2) compared to control cultures (1.18 ± 0.25). Collectively, these findings suggest that the Matrigel-treatment could be improving the viability and differentiation of stem cell-derived neural tissues. However, the inconsistencies and low number of replicates currently limit such generalisation.

Although Matrigel treatment can induce desirable three-dimensional features, the increased variability in morphological outcomes may limit its applicability for clinical settings, where consistency is crucial. Moreover, the tendency of small-diameter micropatterns to induce the detachment of tissues during extended culture suggests that they may not be suitable for long-term applications. The higher retention of large micropatterns indicates that they may be more suitable for sustained cultures, potentially up to one month as required in retinal organoid protocols. Given that the neural plate in stage 8 embryos is approximately 1–1.1 mm in

length[207], micropatterns of similar dimensions may more accurately mimic *in vivo* conditions, offering a promising approach for studies requiring prolonged differentiation periods. Moreover, the validation that micropatterned cultures can support neural differentiation for up to 14 days, as demonstrated through immunofluorescent staining, in both treated and non-treated cultures is promising. However, our current method of micropatterning limits the scalability of these cultures due to the extended time required for fabrication (7.5 minutes per 10-mm diameter coverslip). Our current technique has enabled the facile characterisation of numerous dimensional parameters without requiring the fabrication of different photomasks to achieve different geometries. This feature is widely beneficial for prototyping and testing various dimensional parameters. However, to reach clinically relevant scales, improved techniques to fabricate micropatterns using high-throughput methods are necessary.

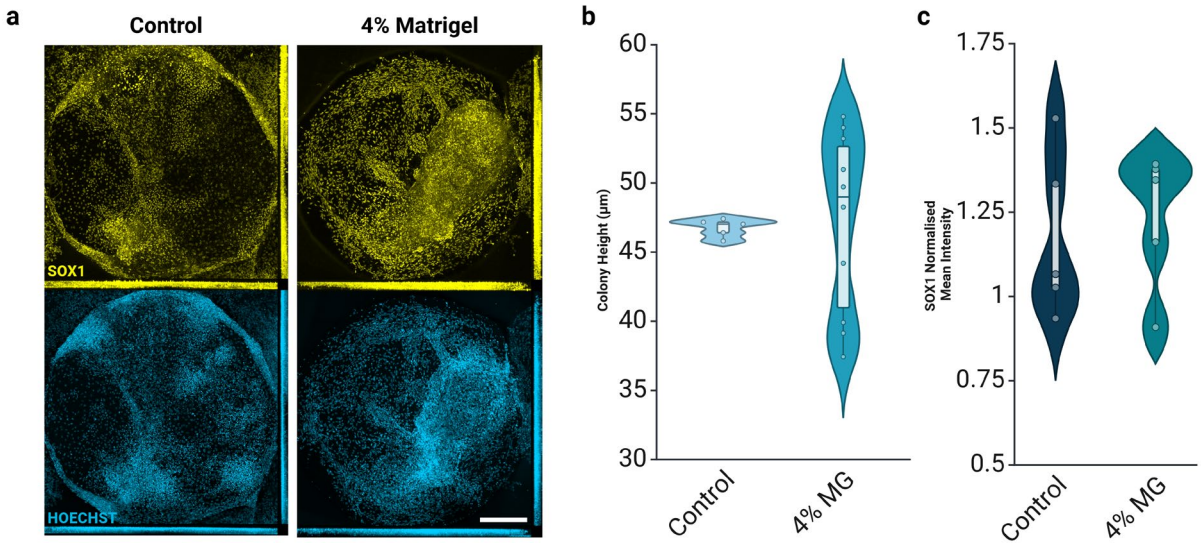

Figure 3.11 Micropatterned colonies (1 mm diameter) treated with 4% Matrigel showed complex and uncontrolled tissue organisation with high variability in colony height after 14 days of differentiation.

(a) Representative image of micropatterned cultures showing increased tissue folding after Matrigel treatment. Scale bar = 200 µm. (b) Matrigel treatment induces high variability in colony height (N = 4 colonies). (c) Matrigel treatment does not significantly alter SOX1 expression.

3.3.5 Development of a scalable method for micropatterning glass substrates

To enhance the scalability and resolution of micropattern production, a novel photomask-based method was developed, addressing key limitations of the previous laser-based approach. The laser-based method allowed for rapid prototyping of diverse shapes and sizes though required approximately 30 minutes to pattern a single 24 x 24 mm square coverslip or 7.5 minutes for 10 mm circular coverslip, which significantly limited its throughput. We first designed a high-resolution photomask comprising our desired pattern—1 mm-diameter circular geometries—using computer-aided design software (SolidWorks, Dassault Systèmes) (Figure 3.12). Other patterns of interest were also included, such as 2 mm-diameter patterns and gradient circular patterns with diameters ranging from 100 – 1000 μm. The design was fabricated on a chrome mask with the assistance of the Research and Prototype Foundry at The University of Sydney.

Building from concepts of our laser-based technology, we employed a similar method to polymerise PEG polymers in a sandwich-like layered set-up (Figure 3.13a). In this platform, we replaced the PDMS-coated glass with a glass slide coated with a thin film of SigmaCote, a water-repelling reagent, to provide improved optical clarity and to minimise our previous challenges associated with removing glass coverslips from PDMS-coated surfaces. Another alteration from the laser-based method was the direct placement of the glass coverslip onto the SigmaCote-glass surface, rather than adjusting for height using the previously designed glass chamber. To achieve this, a droplet of the PEG solution (approx. 10 μL) was placed onto the SigmaCote-glass surface, followed by the gentle placement of the coverslip on top of the droplet. As such, the PEG polymer solution was retained between the coverslip and a non-adherent glass slide. Through this method, brief exposure to UV light for 1 minute using a lamp was sufficient to polymerise the miniscule volume of PEG polymer (Figure 3.13b).

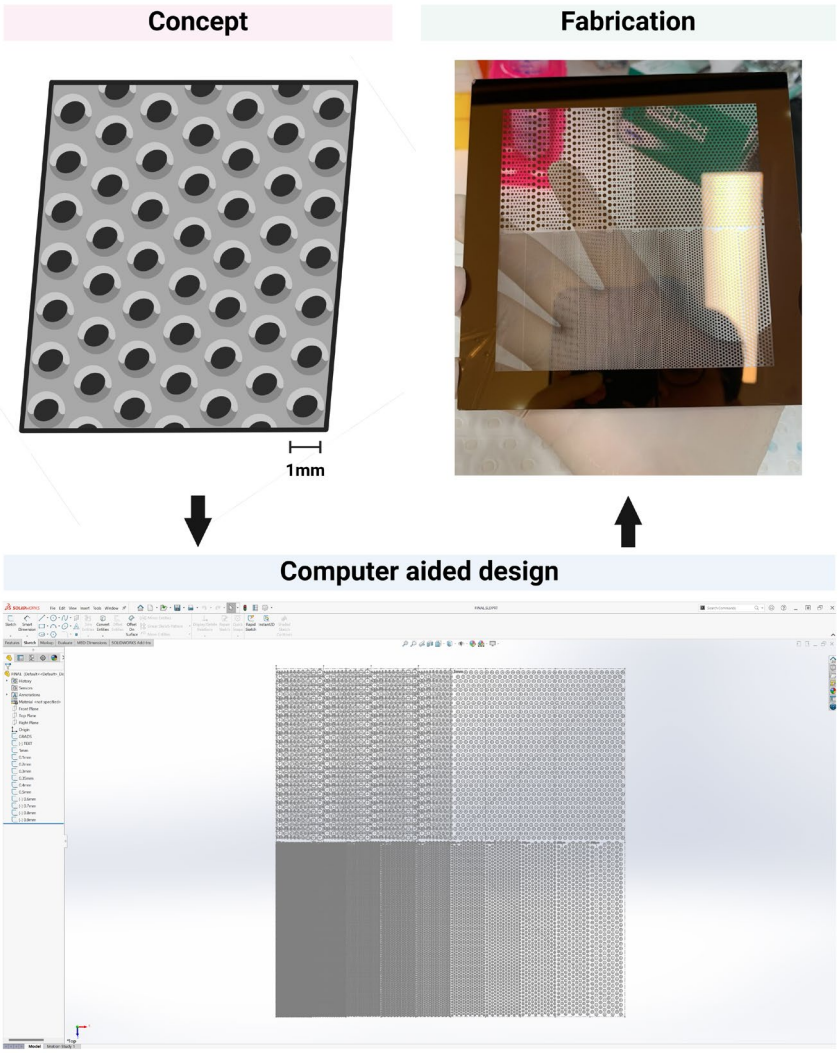

Figure 3.12 A patterned photomask was designed using computer-aided design software (SolidWorks, Dassault Systèmes) and fabricated by the Research and Prototype Foundry at the University of Sydney.

Through this method, we observed that high-resolution micropatterns corresponding to the photomask design could be fabricated with high throughput. Although we only tested the fabrication of four 10-mm diameter coverslips in parallel, for our specific photomask design, up to 25 glass coverslips can theoretically be fabricated in one minute. As such, with larger photomask designs, it is plausible that an increased number of substrates can be patterned at the same time.

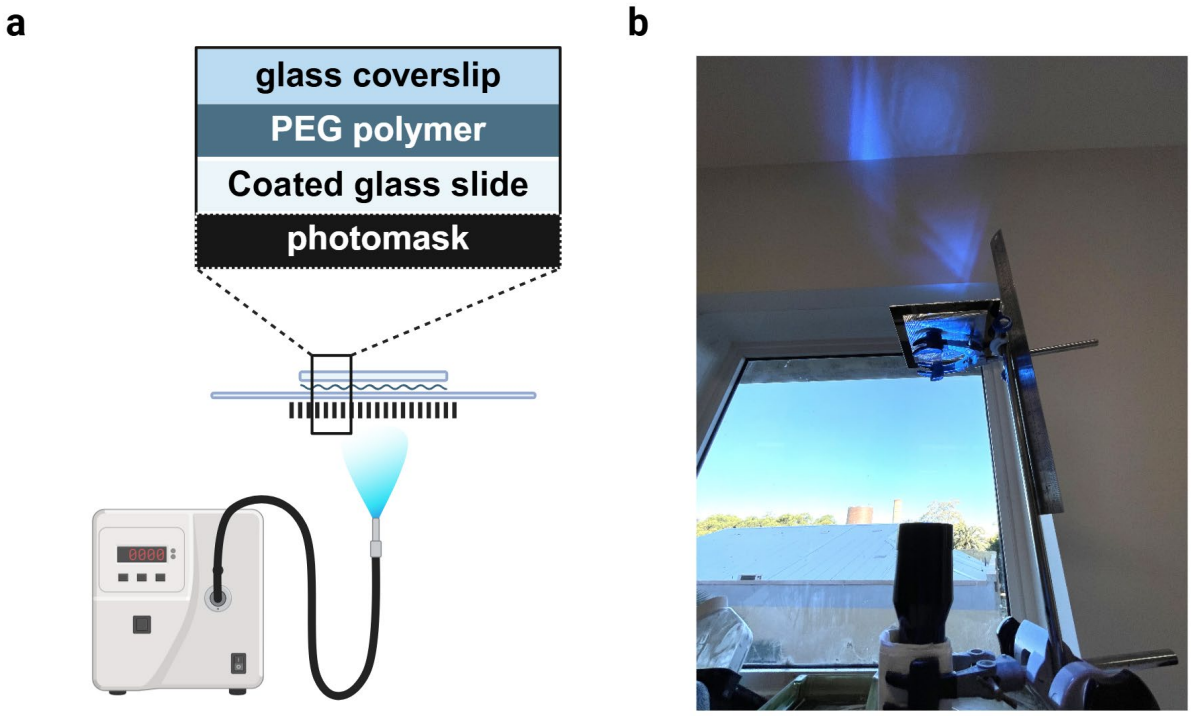

Figure 3.13 (a) Schematic of the sandwich technique for UV polymerisation of a PEG polymer solution. (b) Setup using a UV lamp, retort stand, and clamps. Created with BioRender.com.

We next tested whether these patterned substrates could support cell attachment similar to our previous method. Cells seeded on these surfaces showed suitable viability after one week of culture (Figure 3.14a). Cells that fell on the PEG polymer appeared rounded, indicative of poor attachment, and could be washed away during media changes or with PBS. The micropatterns fabricated using this method could successfully spatially confine cells and had minimal defects (Figure 3.14b), a marked improvement over the laser-based method—where the relatively lower resolution often resulted in imperfections such as jagged edges, particularly in circular or curved patterns. High-magnification imaging of the cell colony edge shows the effective confinement of these cultures, where a clear border is observed with minimal cytoplasmic extensions (Figure 3.14c). The viability and well-defined confinement of these cells indicate the potential of the new patterning technique to support and guide cell attachment. The high-

resolution curves provided by this method may ensure a smoother surface for cell confinement, minimising mechanical stimulation caused by stress concentrations associated with corners or jagged edges. Thus, this method may also reduce the risk of mechanical stress or poor viability that had been observed with the previous laser-based method.

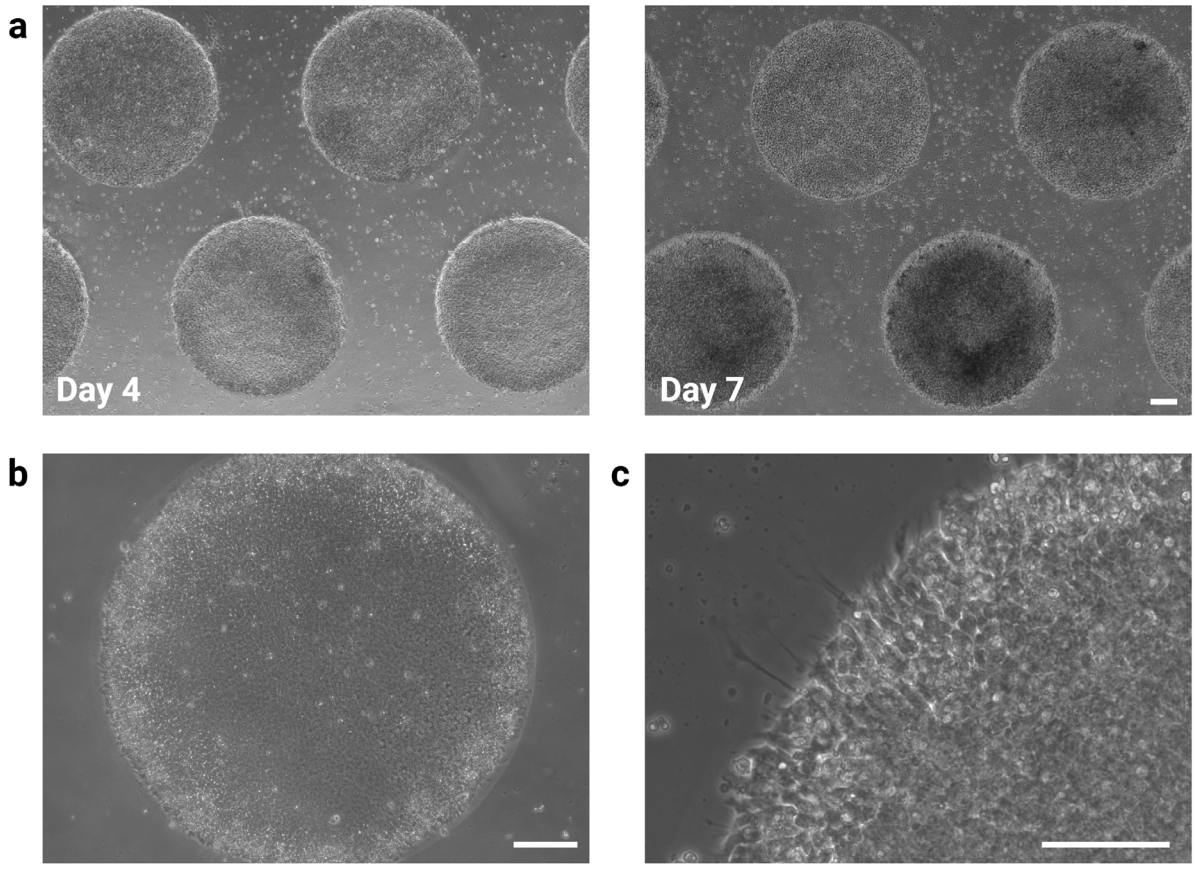

Figure 3.14 Circular micropatterns (1 mm diameter) fabricated using the newly developed method of micropatterning PEG polymers onto glass substrates.
(a) Cells seeded on the pattern were confined to the areas without PEG polymer and showed good viability after 7 days of differentiation (4x objective; Scale bar = 200 µm). High magnification images at (b) 10x objective (Scale bar = 200 µm) and (c) 20x objective showed robust cell colony confinement and clean edges (Scale bar = 100 µm).

To further characterise our new photomask-method of patterning, we performed a preliminary test on a larger diameter geometry of 2 mm. Under our standard protocol seeding density, we observed that cells could proliferate and reach completely confluency by Day 4 (Figure 3.15).

Moreover, when the neural differentiation protocol was initiated at Day 4 onwards, we observed the appearance of morphological features by Day 9 (Figure 3.15). At 3 weeks, the cells remained confined to the initial pattern, with the growth of neuralised structures within the colonies. These structures appeared similar to those found in our standard monolayer culture at early time points, though they did not mature into well-defined retinal vesicles. As such, our preliminary examination demonstrates that the fabricated micropatterns have the capacity to support cell survival for the one-month-long differentiation period. Importantly, clear confinement of the cells was observed throughout the differentiation period. Although rounded cells could occasionally be observed around the regions of PEG polymer (Figure 3.15), these were the result of a low level of poor cell attachment that is typical in standard cell cultures. No mass detachment was observed.

Through this newly developed method, we show preliminary evidence that micropatterned substrates fabricated through microlitre volumes of a PEG polymer solution can induce and maintain the spatial confinement of cells for over 3 weeks. Furthermore, the rapid polymerisation process, which enabled patterning in less than one minute, greatly enhanced the throughput and scalability of micropattern production. The high reproducibility of this method was another significant advantage, with the consistent quality of micropatterns across multiple batches eliminating the need for frequent calibration required in our previous laser-based system. This consistency is particularly valuable for large-scale applications where uniformity and reliability of cell culture environments are critical. Figure 3.16 illustrates a macroscopic view of the consistency achieved through our developed micropatterning technique.

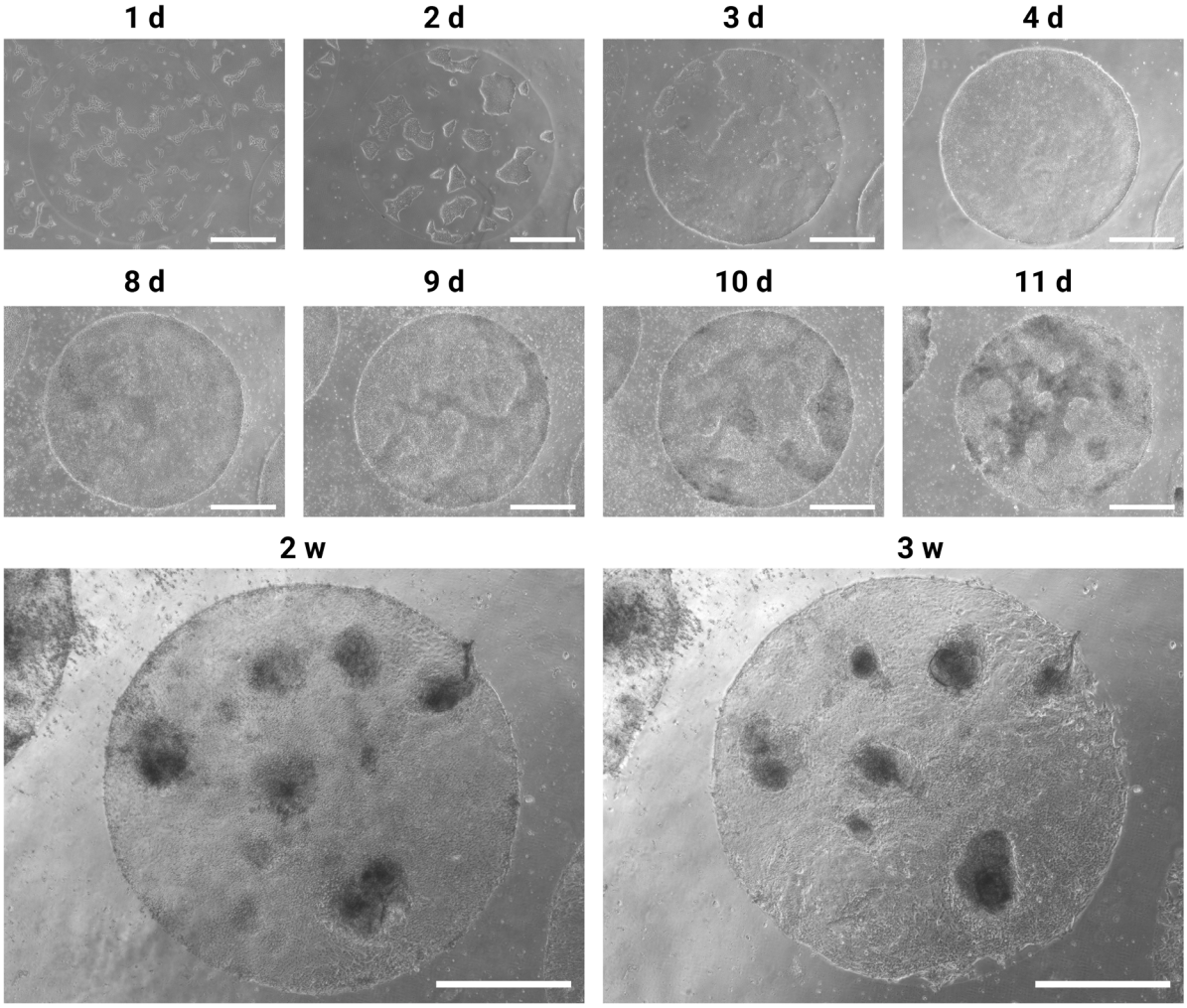

Figure 3.15 Circular micropatterns with 2 mm diameters could be fabricated at high resolution through UV polymerisation of PEG polymers onto glass substrates.

Cells seeded on the substrate demonstrated robust spatial confinement and the formation of dark tissue structures by week 2 of differentiation. Scale bar = 400 µm.

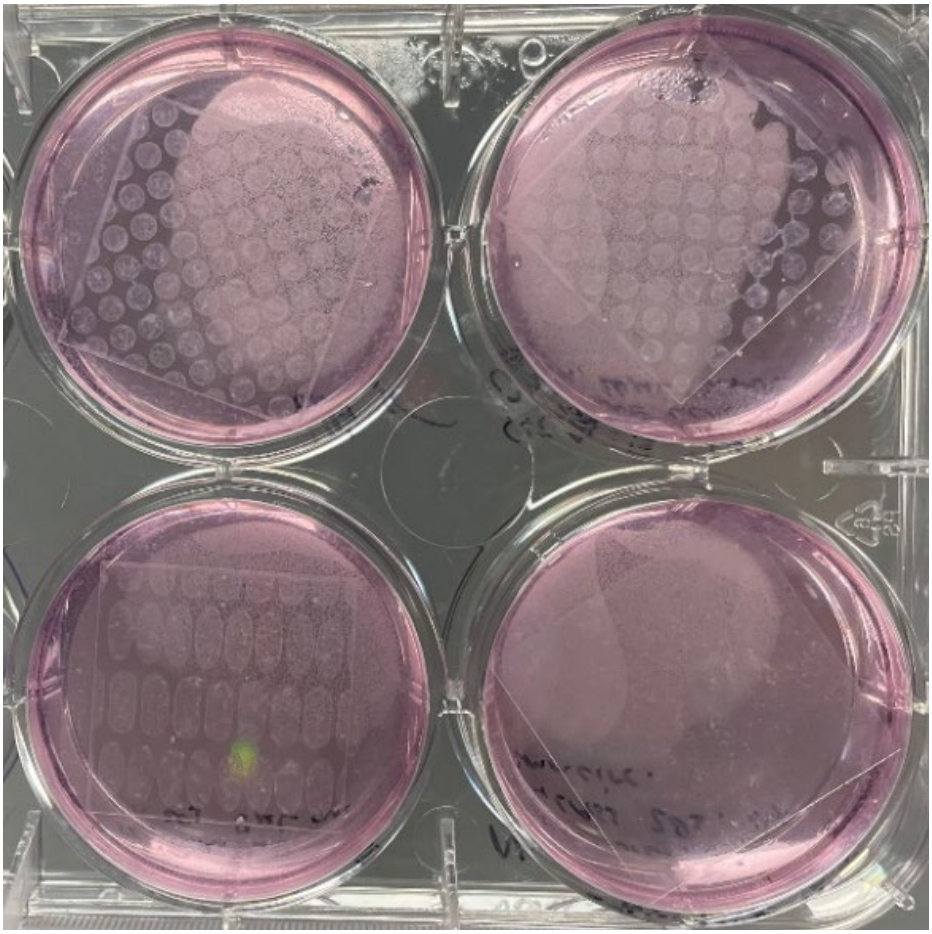

Figure 3.16 Macroscopic image of micropatterned cell cultures of different geometries on glass substrates within a 6-well plate.

The photomask-based method represents a substantial advancement in micropattern fabrication, offering high-resolution, scalable, and reproducible patterns that support cell growth over extended periods. From our preliminary studies, we show that the technique may provide a robust solution for applications requiring precise and long-term cell culture, despite the reduced flexibility in prototyping compared to the laser-based approach. Thus, the higher quality of the patterns fabricated, including smoother edges and more accurate geometric shapes, could potentiate the growth of complex tissue structures such as retinal vesicles and organoids.

3.3.6 Evaluation of long-term differentiation and viability on micropatterned glass substrates

Since our overall aim is to characterise and induce the self-organisation of retinal structures in micropatterned substrates, we next tested whether these surfaces could enable the specification of eye field regions. As these structures typically appear at about 3 – 4 weeks of culture, it is critical to monitor the time in which eye field specification occurs. However, the complexity of our batch differentiation approaches renders it difficult to characterise different time points of the culture compared to 3D protocols. For instance, to accurately analyse the specification of eye field regions over time, whole wells would need to be collected or fixed for downstream analysis. In comparison, 3D suspension protocols may enable the facile collection of a small portion of aggregates for similar downstream analysis. Considering our batch cultures are performed in 6-well plates, the resources required to culture and collect entire wells are relatively unfeasible. Moreover, the loss of spatial positioning is a major shortcoming of batch analysis methods. Therefore, we harness the availability of fluorescent reporter lines to overcome these challenges by enabling the live imaging of our confluent monolayer cultures over time. The cells utilised were genetically engineered to express a GFP reporter for the early eye field marker SIX6, as described in previous work[103]. The facile identification of SIX6 expression, one of the earliest retinal-specific transcription factors, facilitates the characterisation of distinct retinal cell populations from other non-retinal neural tissues. The robust characterisation of the SIX6-GFP reporter cell line in previous literature[103] was critical in our selection of the engineered cell line.

We first replicated our previous experiment involving 1 mm-diameter circular patterns to observe the specification of the eye field over time. However, unlike the 2 mm-diameter circular patterns, we unexpectedly observed poor long-term viability in these smaller patterns

at week 3 of differentiation (Figure 3.17). Although initial assessments demonstrated that cells exhibited robust attachment to the patterned substrates (Figure 3.14), we observed a notable decline in cell viability upon performing our full differentiation protocol. These colonies showed poor morphology, with obvious detachment of cells and tissues from the patterned substrate. This decrease in viability, coupled with the absence of a GFP signal, suggests that the micropatterned environment may impose physiological stressors that impede long-term cell survival and differentiation.

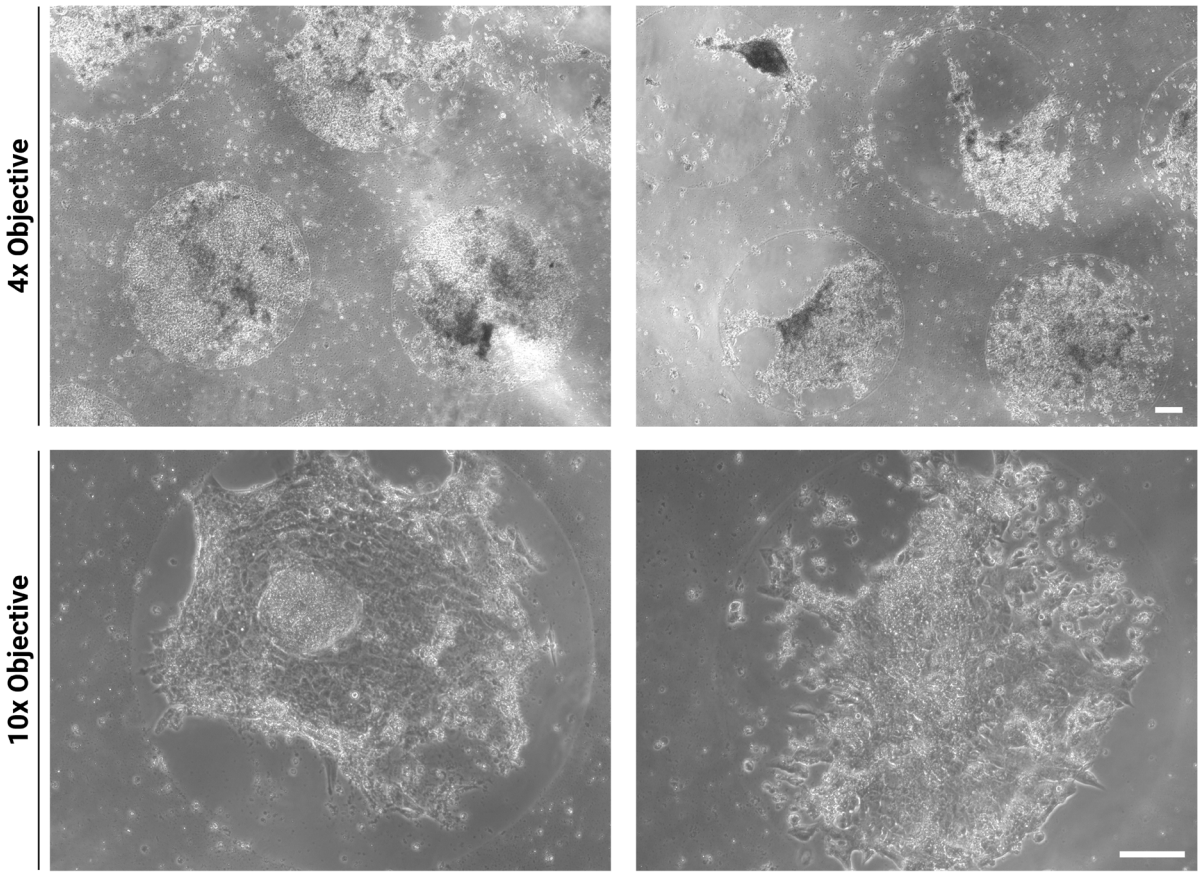

Figure 3.17 Poor viability of micropatterned cell cultures was observed on 1 mm-diameter patterns after 3 weeks of neural differentiation. 4x objective scale bar = 1050 µm; 10x objective scale bar = 400 µm.

As such, despite successful early cell attachment, the inability of cells to consistently form retinal organoids within the micropatterned substrates, regardless of the fabrication method,

highlights a significant limitation of the approach. Retinal organoid formation from confluent cultures typically requires a delicate balance of cell-cell signalling, ECM interactions, and spatial freedom to enable complex tissue architecture development. The observed detachment of a significant proportion of cells from the micropatterned substrate over time, though less pronounced than in previous studies using the laser-based micropatterning method, indicates that the micropatterns may disrupt critical cellular interactions or fail to provide adequate ECM cues, which are essential for proliferation, differentiation, and the eventual self-organisation of retinal vesicles. The lack of SIX6-GFP expression is highly likely the result of significant suboptimal cell attachment, where the activation of apoptotic pathways may be hindering differentiation processes.

Interestingly, GFP expression was prominently observed at the periphery of the glass coverslips and well plates (Figure 3.18), where the cells were exposed to different mechanical forces and spatial configurations. This peripheral GFP expression, along with the higher cell viability in these regions, indicates that the cause of substantial cell detachment was directly due to the 1 mm-diameter micropatterned environment. As these GFP+ tissues were within the same culture well as the micropatterned colonies, it is plausible that the minimal space offered by the pattern was not conducive for long-term culture. Moreover, these GFP+ tissues were only observed on tissue culture plastic regions of the well plate. Due to the square shape of the micropatterned coverslips, a portion of the cell originally seeded within the well was able to attach and proliferate on the exposed adjacent regions of tissue culture plastic.

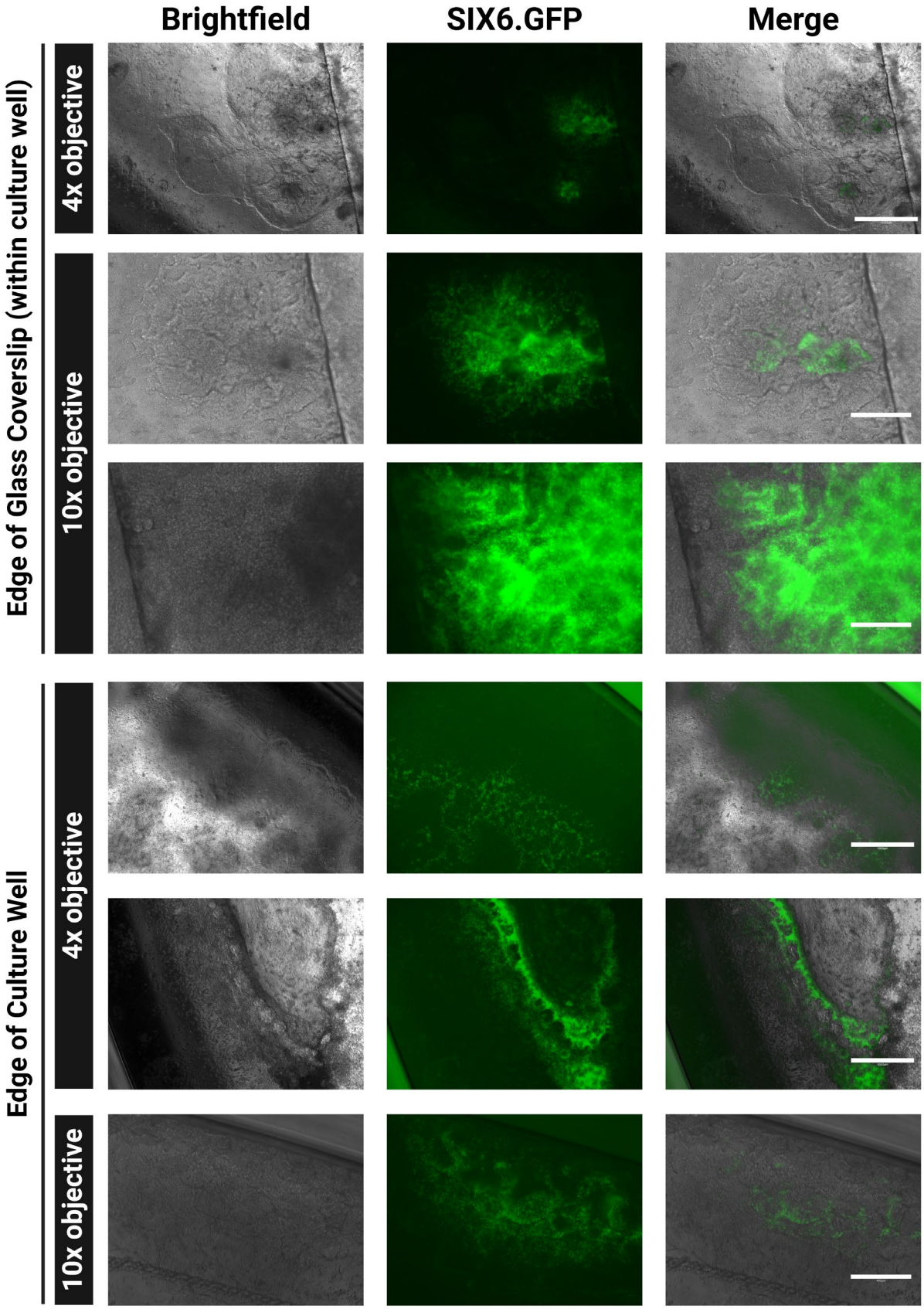
Brightfield
SIX6.GFP
Merge
Edge of Glass Coverslip (within culture well)
4x objective
10x objective
Edge of Culture Well
4x objective
10x objective

Figure 3.18 High expression of SIX6-GFP was observed in cells on tissue culture plastic regions adjacent to the edge of the glass coverslip and culture well after 3 weeks of neural differentiation. 4x objective scale bar = 1050 μm; 10x objective scale bar = 400 μm.

Since our standard protocol is performed on tissue culture plastic, it is not surprising that these cells could proliferate and differentiate well within these regions, as indicated by the high level of GFP signal. However, we unexpectedly observed a patterning effect corresponding to the edge of the glass coverslip and the edge of the well plate. Specifically, the expression of GFP almost always appeared adjacent to these edges, where some tissues even formed GFP+ strips parallel to the edge of the well (Figure 3.18). This indicates that the cells might be responding to mechanical cues associated with the edges, such as tension or compression forces. These findings could suggest that mechanical or physical stimulation, particularly those which arises from physical confinement or edge effects, could play a pivotal role in inducing morphological features and gene expression profiles associated with retinal development.

The coupled effects of tissue culture plastic surfaces and physical boundaries indicate that, although we could not successfully induce the self-organisation of retinal vesicles observed in our established protocol, spatial parameters are likely a major contributor to the specification of the developing eye field. Indeed, substrates with higher stiffnesses have been reported to result in undesirable mechanical stresses and reduced viability of neural cell phenotypes[208]. Moreover, the large surface area available in our standard protocol may be a substantial factor in supporting the long-term growth and organisation of retinal tissues, potentially through the presence of multiple cell types that may be involved in the morphogenesis of vesicle structures. As such, it may be necessary to alter either or both: (1) the properties of the culture substrate, or (2) the magnitude of spatial confinement induced.

These observations underscore the limitations of current micropatterning techniques in faithfully recapitulating the *in vivo* conditions necessary for retinal organoid formation and differentiation. Although we only tested our new micropatterning in singular preliminary experiments, the ongoing challenges observed through all our micropatterning studies performed on glass indicate a shortcoming of our methodology. Therefore, we instead chose to move towards different substrates for the subsequent experimental work rather than iterating through parameters on glass surfaces. Glass substrates were initially selected due to the ease with which they could be functionalised and printed. The findings here point towards a need for more advanced micropatterning methods that can better mimic the dynamic and multicellular environment of the developing retina. Although the current methods were unsuccessful in producing spatially patterned tissues, the knowledge and findings observed were critical in informing the work in the next chapter of this thesis.

3.4 Conclusion

Here, we tested two methods of micropatterning with the aim of differentiating retinal vesicles from confluent iPSC cultures. The first method enabled the generation of customised patterns, allowing the cost-effective characterisation of different dimensional parameters. The second method of micropatterning, a new method developed within this thesis, enabled the development of high-resolution patterns with robust spatial confinement. The assessment of cell viability and differentiation on glass coverslips featuring curved micropatterns has revealed critical insights into the influence of geometric boundaries on the formation of self-organised tissues. By iterating through different diameters of circular patterns, we identify diameters approximately within the 1 mm range to be best suited for maintaining a large enough space to prevent the excessive budding of colonies over time, while not being too large such that multiple tissue structures are able to form within the same pattern; for instance, those observed in our 2 mm-diameter patterns.

While both sinusoid and circular geometries supported initial cell attachment and short-term survival, the long-term outcomes demonstrated significant variability across different cell lines and experimental conditions. Importantly, poor viability was observed in all micropatterned cultures at the time point required for retinal vesicle self-organisation in our established protocol (minimum 4 weeks). Nevertheless, this study shows preliminary evidence that micropatterning has the potential to support the isolated generation of vesicle structures. The superior SIX6-GFP expression observed in neighbouring regions of tissue culture inform our next studies. In Chapter 4, we will develop techniques to investigate the effects of micropatterning on tissue culture plastic substrates.

Chapter 4: Micropatterning the self-organisation of pluripotent stem cells to generate neuroretinal vesicles

4.1 Introduction

While Chapter 3 explored the potential of micropatterning to create spatially defined regions of tissue growth, the limitations of glass substrates were clear. The inconsistent tissue viability and general poor long-term survival warrants the need for more innovative techniques to generate spatially defined retinal vesicle structures. The inherent stochasticity of stem cell self-organisation already results in limited scalability and high inter-batch variability, presenting significant challenges for widespread application and clinical translation. The intrinsic complexity of retinal organoid self-organisation from confluent monolayers is not readily compatible with complete spatial confinement present in current micropatterning techniques. A key scientific challenge lies in maintaining the long-term growth and viability of retinal organoids on micropatterned platforms. However, since these three-dimensional structures can be derived from the self-organisation of 2D confluent monolayers of stem cells, we sought to instead minimally alter established protocols through micropatterning techniques. One key aspect of this is the considerable difference in the substrate stiffness and surface properties between glass coverslips and tissue culture plastics (TCP). Although glass substrates have been successfully applied in micropatterned stem cell cultures[186], Chapter 3 demonstrated the limitations of such substrates for long-term retinal cultures—a tissue type that is generally known to preferentially differentiate on relatively softer substrates[209].

Our initial observations in Chapter 3 revealed that SIX6-GFP reporter cells expressed relatively higher GFP levels on TCP compared to glass surfaces within the same well. This finding led us to hypothesise that TCP surfaces might be more suitable for long-term differentiation of neural retinal cell cultures. TCP is generally treated with a plasma coating to improve cell attachment and survival. As such, we first sought to move towards these substrates while still incorporating micropatterning techniques. However, one limitation of TCP is the lack of bonds

that are available, unlike the bonds offered by silanised glass substrates. As such, a novel method is required to introduce spatial confinement in cultured cells on TCP. We first tested methods to attempt to polymerise PEG hydrogels onto TCP surfaces, as explored in Chapter 3 on glass surfaces. Upon further consideration of these techniques, we aimed to develop a method that did not require the use of biomaterials at all; thus, simplifying the overall procedure and enhancing the capacity for clinical translation due to the absence of external materials.

We hypothesise that by confining cells within defined patterns, the stochasticity of stem cell self-organisation may be better controlled. Moreover, defining the regions in which budded vesicles can grow may facilitate the facile detachment of these tissues for further 3D suspension culture. Here, we design a unique method to micropattern commercially available TCP substrates that support iPSC spatial confinement and enable the self-organisation of these initially confined colonies into retinal vesicles.

4.2 Experimental Section

4.2.1 Materials and procedures

Part of this work was performed at the Research and Prototype Foundry Core Research Facility at the University of Sydney (part of the Australian National Fabrication Facility), where a custom-made chrome photomask was fabricated. Three iPSC lines were utilised in this study: HOIK1 (HPSI0314i-hoik_1, Wellcome Trust Sanger Institute, United Kingdom)[197], and EP1.SIX6-GFP and IMR90.SIX6-GFP reporter iPSC lines[103]. The SIX6-GFP reporter iPSC lines were generously donated by A/Prof Karl Wahlin.

4.2.2 Fabrication of micropatterned plastic substrates using PEG hydrogels

Initial tests performed to develop techniques to micropattern tissue culture plastic surfaces are detailed in the Results and Discussion section. Prepolymer solutions using the formula previously described in Chapter 3 were prepared and polymerised using a UV lamp (OmniCure S1500).

4.2.3 Fabrication of micropatterned plastic substrates directly with UV light

Geltrex-coated TCP surfaces were prepared using standard procedures[46]. Excess Geltrex was then washed off with 3mL PBS and aspirated. 1 mL of PBS was added to the surface to prevent the Geltrex coating from drying. The Geltrex-coated plate was placed onto the custom photomask, using aluminium foil to block adjacent regions where UV light was not desired. A collimated UV light source (OmniCure S1500) was positioned directly below the photomask, ensuring that the light would pass through the mask and expose the Geltrex-coated surface. The distance between the lamp head and the photomask was approximately 20 cm and remained constant for all experiments. The UV light was applied at 100% power and allowed to run for either 15, 30, or 60 minutes.

After the UV exposure, all wells of the plate were washed once with 3 mL PBS. Micropatterned plates were UV-sterilised in a biosafety cabinet for 15 minutes prior to use.

4.2.4 Maintenance of iPSC lines and neural differentiation

hPSCs were cultured and differentiated as described previously in Chapter 3, according to our established protocol. One subsequent alteration was made involving an additional 24 hours of treatment with a Rock inhibitor (10 μM Y-27632) upon seeding of cells on micropatterned plates. No alteration was made to the media formulation or time points.

4.2.5 Immunohistochemistry

Immunofluorescent staining was performed as described previously in Chapter 3, with the addition of primary antibody LHX2 (1:500, ab184337, abcam).

4.2.6 Imaging of micropatterned cultures

Confocal imaging was performed as described previously in Chapter 3. Live imaging of the micropatterned substrates was performed using an EVOS FL microscope or the ImageXpress HT.ai high-throughput imaging system (Molecular Devices) for both brightfield and fluorescent (GFP) monitoring. Prior to imaging, the tissue culture plates were thoroughly cleaned on top and bottom surfaces using a KimWipe moistened with 70% ethanol. Brightfield imaging was performed on each cell line, while the GFP wavelength was additionally used for GFP reporter cell lines.

In preparation for use with the MetaXpress device, the temperature control was activated in advance to allow the system to heat to 37°C. The plates were carefully placed into the device's plate holder, ensuring a completely flat and level position. Given the slight variations in the

thickness of TCP, the microscope's focal point was adjusted to the cell monolayer or vesicles before capturing each image.

The standard settings for imaging one well of a 6-well plate involved the acquisition of an 11x11 grid, using a 10x objective. Images were stitched together with a 10% overlap. A custom protocol, 'Create Montages and Overlays', was employed to combine the individual positions within a well into a single image montage. These images were compressed to 20% zoom and exported to the IN Carta software (Molecular Devices) for subsequent analysis and quantification.

4.2.7 Quantification of micropatterned cultures

Retinal vesicles were quantified using IN Carta's built-in machine learning software (SINAP). The software was pre-trained using manual segmentation of images from mature cultures derived from all three iPSC lines. The trained model was used for cultures. Results were manually validated by ensuring the segmentation accurately captured the desired morphologies.

4.2.8 Statistical analysis

The number of independent samples performed for the direct UV-light micropatterning experiments for each cell line is stated throughout the results and figure legends. Micropatterning experiments were performed in parallel with non-treated control cultures. Experiments were performed in duplicate wells (n = 2) for each independent batch and averaged. Paired t-tests were performed for these samples (not significant "n.s." $p > 0.05$, or significant: *$p < 0.05$, **$p < 0.01$, ***$p < 0.001$).

4.3 Results and Discussion

4.3.1 Characterisation of a SIX6-GFP reporter cell line in a 2D/3D retinal organoid protocol

We characterised the SIX6-GFP reporter iPS cell line, previously used exclusively in 3D retinal organoid protocols, in our 2D monolayer culture system. In this 2D retinal organoid protocol, confluent monolayers of cells demonstrated good survival and the initiation of morphological changes by Week 2 (Figure 4.1). Notably, on Day 16, GFP expression was observed in individual cell nuclei, confined to specific regions of the monolayer, indicating the expression of the early eye field marker, SIX6. This early detection is significant as it suggests that SIX6 expression, a key marker for retinal progenitor specification, can be effectively initiated in 2D cultures using this reporter line.

Following the onset of SIX6 expression, self-organised retinal organoids emerged from the monolayer cultures, forming 3D retinal vesicle-like structures. These organoids were morphologically consistent with retinal neuroepithelial tissues, displaying the characteristic neuroepithelial border that defines retinal vesicle formation. In addition to retinal organoids, we also observed cortical brain-like structures within the same cultures. These brain organoids lacked the neuroepithelial border, and their neural rosette morphology was indicative of brain tissue. The absence of GFP expression in these brain organoids, despite the co-existence of retinal and brain tissues, further validated the specificity of the SIX6 reporter for retinal progenitors.

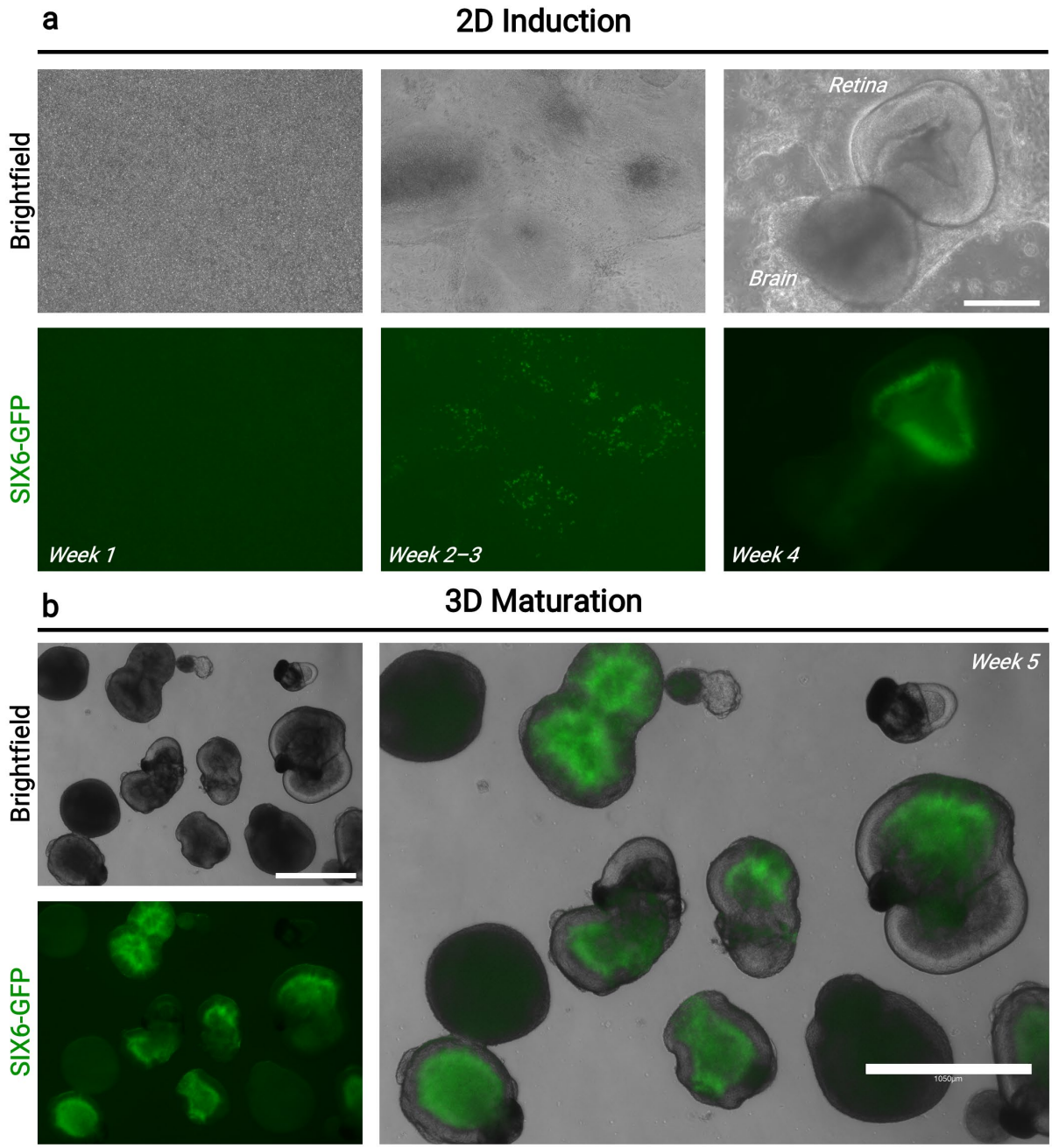

Figure 4.1 Brightfield and GFP imaging of 2D-induced confluent monolayer cultures from week 1 to 4 (top) and 3D suspension cultures of collected retinal vesicles at week 5 (bottom) using the EP1.SIX6-GFP reporter cell line.

(a) The onset of GFP expression was observed at approximately day 16 of differentiation. Retinal vesicles appeared by week 4, indicated by a translucent well-defined neuroepithelial border. Dark forebrain structures occasionally appeared adjacent to retinal tissues. GFP imaging of these regions revealed that the fluorescent reporter cell line was specific to tissues with retinal morphology. (b) GFP expression was maintained at week 5, showing specificity to retinal structures and little to no expression in dark non-retinal vesicles. Scale bar = 400 µm.

The mixed cultures provided an opportunity to isolate multiple retinal and brain organoids using fine needle techniques, allowing for their transfer to 3D suspension cultures. This manipulation was successful in maintaining the specificity of GFP expression in retinal organoids at Week 5 (Figure 4.1), with no GFP detected in brain-like structures, confirming the ongoing specificity of the SIX6 reporter.

Further morphological and fluorescent characterisation of the monolayer cultures revealed diversity in the retinal organoid structures (Figure 4.2). These included flat, round, and budded morphologies, all of which exhibited the typical neuroepithelial border. Similar to other cell lines, variations in the appearance of this border were observed, with some organoids exhibiting a brighter or relatively more pronounced neuroepithelial boundary. These differences suggest a potential difference in the maturation or stratification of the retinal tissues. For example, organoids with a pronounced continuous neuroepithelial border displayed a ring-like GFP expression pattern concentric with the border, suggesting spherical stratification of the tissue layers.

The regionalisation of GFP expression also varied according to organoid morphology. Flat organoids, for example, exhibited diffuse GFP expression, with individual nuclei clearly visible due to the 2D structure providing better visibility in a single plane. In contrast, more rounded organoids demonstrated centralised GFP expression, with less visibility of individual nuclei. This difference is likely attributed to the 3D organisation of the rounded structures, where the presence of cells at different planes in the tissue makes the visualisation of individual nuclei more difficult to resolve using the EVOS microscope, as opposed to confocal microscopy platforms. Additionally, the consistent thickness of the neuroepithelial border across organoids of different sizes indicated that the size of the GFP+ region was dependent on the overall size

of the retinal organoid, while the neuroepithelial border remained a relatively constant structural feature. GFP expression was typically absent in the neuroepithelial border.

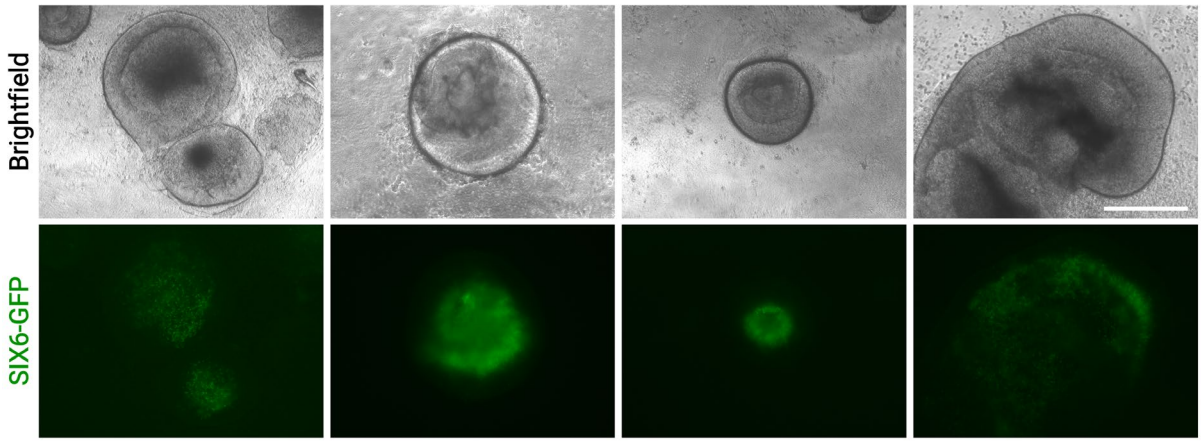

Figure 4.2 Different morphological features observed in brightfield imaging at day 37 corresponds to varied GFP regionalisation in SIX6-GFP reporter cell lines.
Variety in retinal vesicles morphologies are typical in standard protocols of batch neural differentiation cultures. The GFP reporter showed that these differences in morphology resulted in varied patterns of SIX6 expression. Flatter vesicles demonstrated more diffuse GFP expression, not necessarily localised to central regions, while budded vesicles showed a concentric expression of GFP. Scale bar = 400 μm.

In some organoids with a thicker neuroepithelial border, we observed GFP expression in a ring-like formation, suggesting stratification within the tissue. GFP+ cells appeared concentrated in a layer between the centre and the neuroepithelial border, with fewer GFP-expressing cells observed in the organoid centre. Additionally, we identified an organoid morphology that was intermediate between flat and rounded, wherein the organoid protruded from the monolayer but remained partially attached. In this morphology, GFP was concentrated near the neuroepithelial border rather than completely in the centre, similar to the flat-type organoids. These partially attached organoids allowed for the visualisation of individual GFP-labelled nuclei in the flat regions, further suggesting the influence of morphology on GFP regionalisation. Such morphological variation in SIX6 expression has not been

comprehensively described in previous studies using 2D protocols. As such, these findings provide new insights into the morphology and marker expression patterns of retinal organoids derived from monolayer cultures.

Upon further fixation and cryosectioning of the isolated 3D organoids, co-localisation of SIX6-GFP with PAX6, another early eye field marker, was confirmed through confocal imaging (Figure 4.3). This provides additional validation that the SIX6-GFP reporter accurately reflects the expression of SIX6 in retinal progenitors.

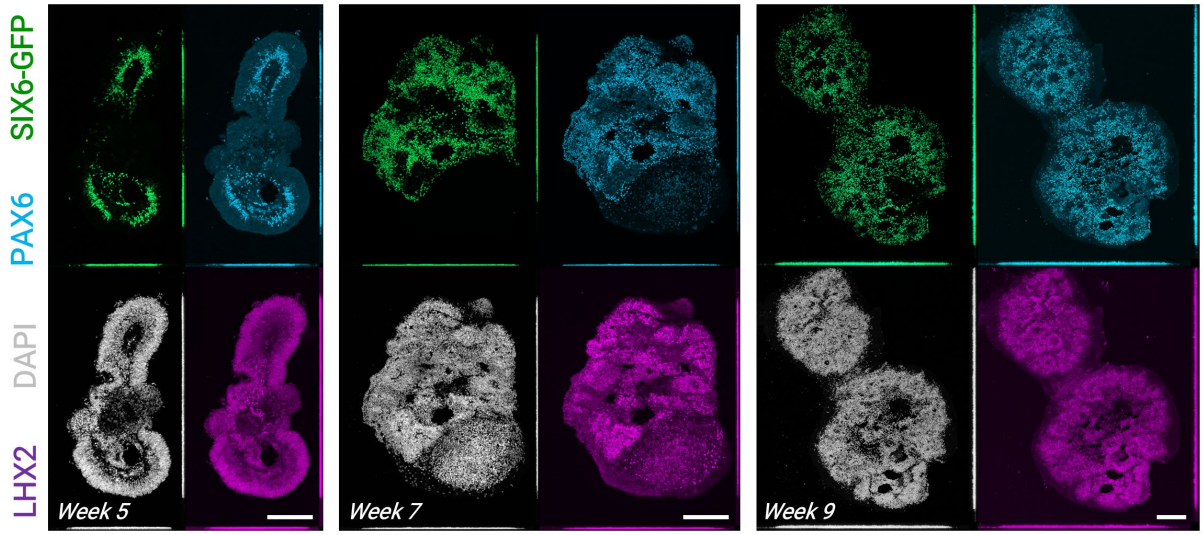

Figure 4.3 Representative immunofluorescent staining of retinal organoids at week 5, 7, and 9 using eye field markers PAX6 and LHX2, and SIX6-GFP.

Confocal imaging of retinal organoids collected at different time points show the co-localisation of SIX6-GFP with eye field marker PAX6. Clear nuclear expression of LHX2 was observed by week 7. Expression of all markers was maintained at the week 9 time point. Different tissue morphologies are attributed to the inherent heterogeneity of retinal vesicle generation. Neural rosette structures are observed in the organoids collected at week 7 and 9. Scale bar = 200 µm.

The expression of LHX2, a key transcription factor involved in retinal development, was initially low at Week 5 but increased by Week 7, predominantly in central regions of the organoids. Notably, LHX2 expression did not extensively co-localise with SIX6 or PAX6, suggesting differential regulation of these markers during the later stages of retinal development.

By Week 9, the expression of SIX6, PAX6, and LHX2 remained robust, indicating the continued development and maturation of the retinal organoids. In the case of cultures where brain and retinal structures were naturally attached, we observed that SIX6 and PAX6 expression was strictly confined to the retinal portion at week 5, while LHX2 was present in both retinal and brain regions (Figure 4.4). This is consistent with the role of LHX2 in forebrain development[210], suggesting that the attached brain-like structures may indeed by undergoing forebrain specification. The differential marker expression between retinal and brain regions further underscores the specificity of the SIX6 reporter for retinal tissue, even in complex, mixed cultures. These findings provide insight into the spatial and temporal regulation of retinal progenitor markers and further underscore the specificity of the SIX6-GFP reporter for retinal tissues.

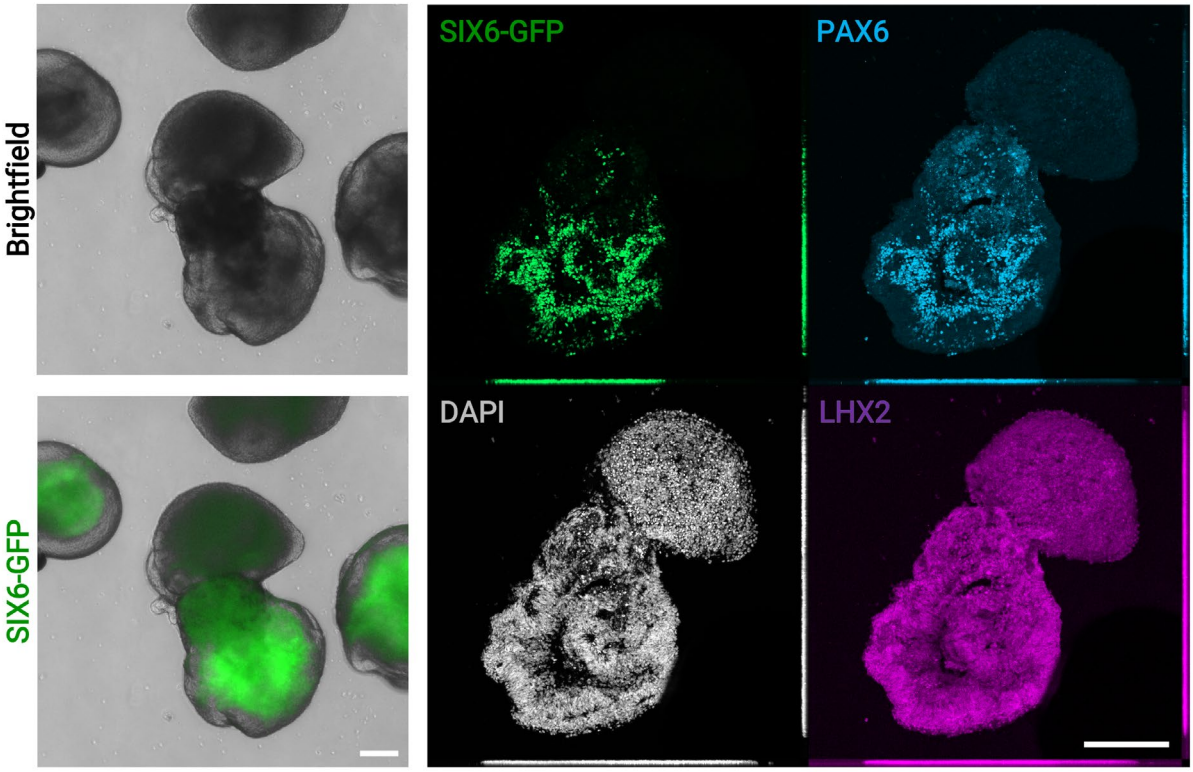

Figure 4.4 Immunofluorescent staining of connected retinal-brain structures confirms specificity of the SIX6-GFP reporter for retinal tissues.

Counter staining of collected tissues at week 5 demonstrates that darker tissues indicative of non-retinal neural tissues does not express the eye field marker PAX6. Low levels of LHX2 expression were detected in the connected brain structures, supporting the observation that these tissues are of forebrain fate. Scale bar = 200 µm.

4.3.2 Design and validation of a technique to micropattern tissue culture plastic using PEG polymers

In this study, we aimed to develop a method for patterning iPSC cells on TCP surfaces, building upon our previous work with glass substrates. We utilised the high-resolution circular patterned photomask, as previously described in Chapter 3, focussing on the 1mm-diametre patterns.

To translate our patterning method to TCP surfaces, we first performed preliminary studies to adapt our previous glass-based protocol using the sandwiching technique. This involved placing a droplet of PEG prepolymer solution on the TCP surface, positioning an un-functionalised glass slide atop the droplet, and applying UV lamp exposure through the photomask. While we successfully achieved PEG polymerisation, we observed an unexpected phenomenon: upon glass slide removal, there was complete or partial attachment of the PEG hydrogel to the glass rather than the TCP. This preference persisted even when an anti-adherent coated (SigmaCote) glass slide was utilised, likely due to differences in the functional groups available on glass surfaces. The abundance of silanol groups on glass surfaces may facilitate hydrogen bonding with PEG molecules, promoting stronger adhesion.

Given the challenges with the glass sandwich technique, we explored an alternative approach involving direct application of the prepolymer solution to TCP. We began by applying a small volume of PEG prepolymer solution (approx. 4 μL) directly to TCP, followed by a short pulse of UV light (< 1 minute). This method resulted in successful polymerisation and sufficient attachment to TCP, even after multiple washes, demonstrating the feasibility of direct patterning on TCP surfaces (Figure 4.5).

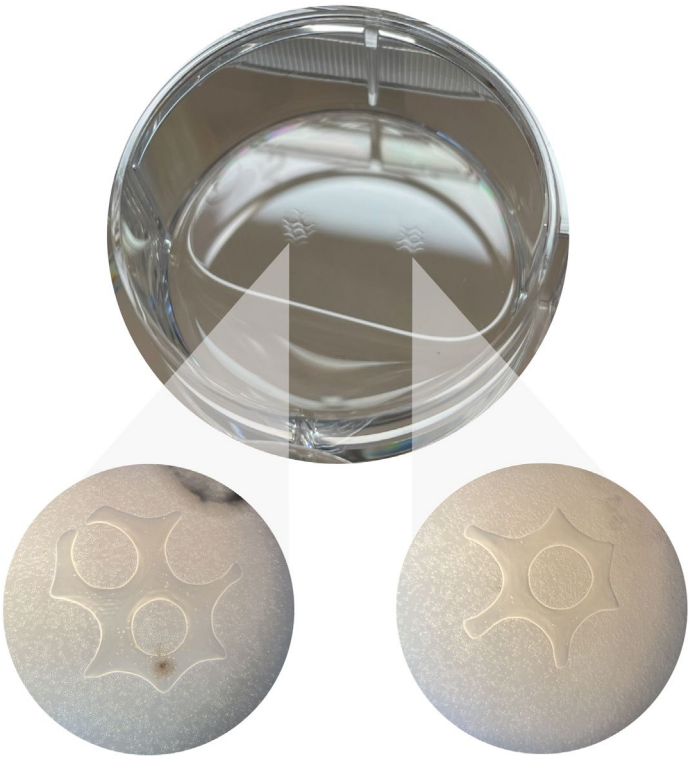

Figure 4.5 Micropatterning of PEG hydrogels on tissue culture plastic was achieved using photopolymerisation of a PEG prepolymer solution.
Microlitre volumes of a PEG-based solution was pipetted onto a well of a 6-well plate and polymerised using a UV lamp. These polymers remained attached to the plastic surface even after multiple washes with PBS. The callout shows a light microscopy image (4x objective) of cells seeded onto the culture well after 2 hours. No successful cell attachment was observed on the PEG hydrogels.

However, achieving whole well coverage proved difficult. This was primarily due to the meniscus effect of the circular well, causing the prepolymer solution to aggregate along well edges. To address this, we implemented a parafilm mask with a central triangular cut-out to control polymer distribution (Figure 4.6). Specifically, the mask acted as a hydrophobic material to break surface tension and achieve a sufficiently thin coating onto a large central area of the well (Figure 4.6c).

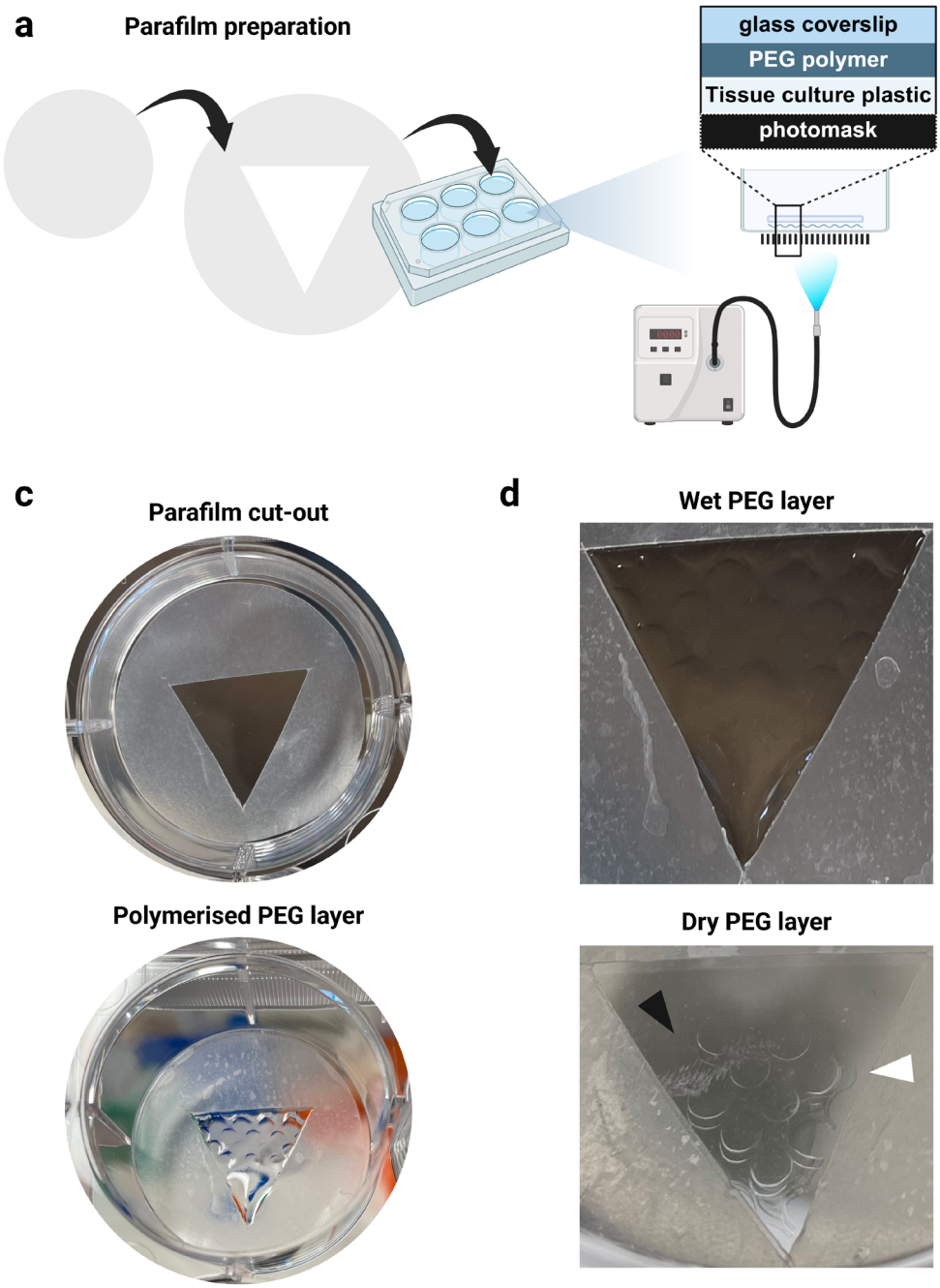

Figure 4.6 A cut out sheet of parafilm was used as a mask to define the region of polymerisation and break the surface tension of liquids on tissue culture plastic.

(a) Schematic of the preparation of parafilm mask shows that a triangular shape was cut out of circular piece of parafilm. (b) Schematic of the layers involved in the setup. (c) PEG hydrogels could be successfully polymerised. (d) The wet PEG polymer shows an intact hydrogel, while the dry PEG polymer shows degradation of the polymer (black arrowhead) and delamination caused by the attachment and subsequent detachment to the parafilm material. Created with BioRender.com.

While UV irradiation through the photomask resulted in successful PEG polymerisation, post-wash observations revealed several issues, including hydrogel delamination, imperfections in the PEG layer, and partial attachment to parafilm edges (Figure 4.6d).

These observations led us to infer that weak physical bonds were forming between PEG and TCP, in contrast to the stronger covalent bonds we previously achieved on functionalised glass surfaces. The instability of pattern geometry over time and with multiple PBS washes further supported this conclusion. This difference in bonding strength highlights the complex interplay between material properties and surface chemistry when attempting to bond different material types. The weaker PEG-TCP interaction could be advantageous in certain applications where degradable or removable patterns are desired; however, it poses challenges for the long-term culture stability required for the current study.

To overcome the limitations of direct application of PEG to TCP wells, we performed a preliminary test using the same method on plastic coverslips (Nunc Thermanox). Initial small-scale tests on quartered circular coverslips produced neat, uniform, and intact PEG layers (Figure 4.7a-c). However, when scaling up to larger surface areas of the plastic coverslip, we observed some imperfections in polymer uniformity, likely due to uneven coverslip heights during the sandwich method application (Figure 4.7d).

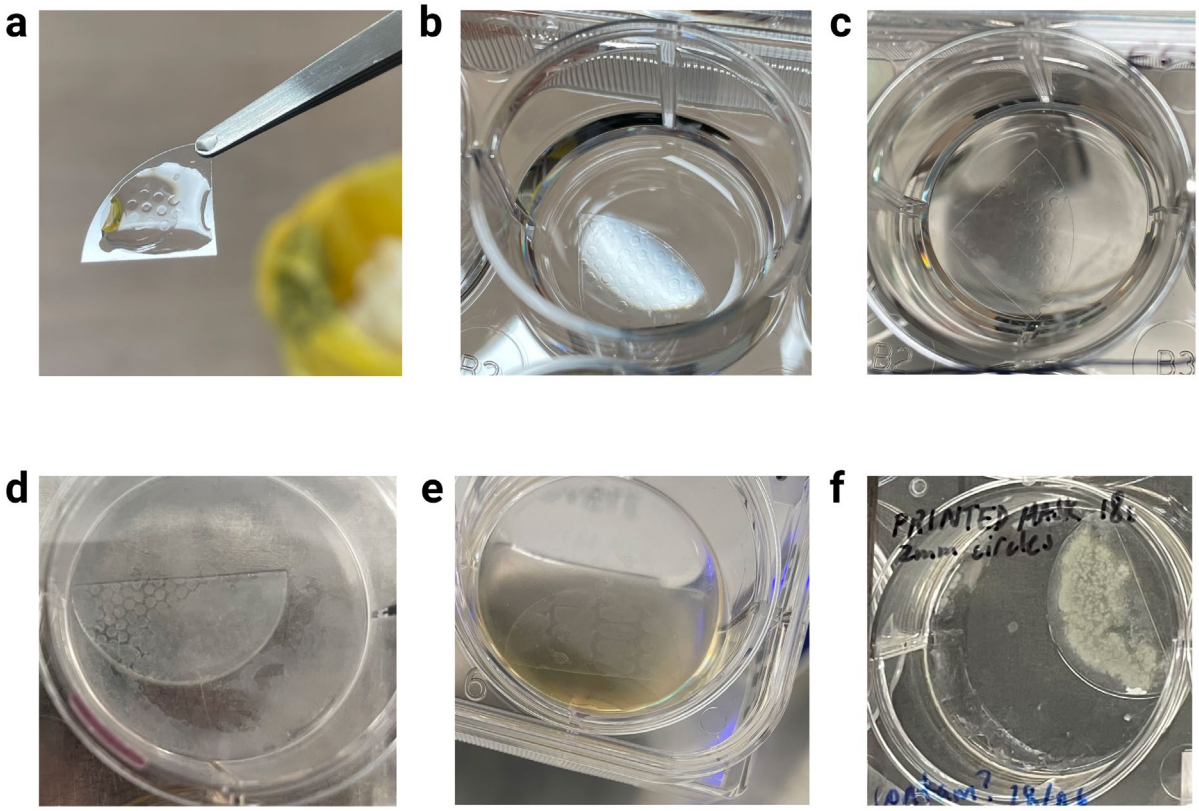

Figure 4.7 Tissue-culture treated plastic coverslips can support the attachment of PEG polymers and subsequent cell seeding.

(a) A micropatterned PEG hydrogel could be successfully attached to plastic coverslips. (b) and (c) illustrate the homogenous patterning of PEG polymers on small-sized plastic coverslips. (d) Cell seeding onto the plastic coverslip demonstrated poor homogeneity of the PEG hydrogel caused by uneven polymersiation. (e) Optimisation of the polymerisation process shows that oval patterns can be fabricated and support cell attachment. (f) demonstrates a patterned coverslip following microbial contamination after 1 week of cell culture.

Despite these imperfections, cell seeding demonstrated successful spatial confinement to areas covered by the photomask, indicated by the regions of patterned cell masses on the coverslips (Figure 4.7d,e). This partial success in cell patterning underscores the potential of our approach for controlling cellular organisation on plastic substrates. However, a significant concern emerged with long-term cultures, which showed increased susceptibility to contamination (Figure 4.7f). This observation raises important questions about the long-term stability of our

patterned surfaces and their suitability for extended culture periods. The increased contamination risk could be attributed to several factors, including potential degradation of the PEG layer over time, challenges in sterilising the patterned surfaces, or alterations in cell behaviour under confined conditions. In particular, the degree of sterilisation performed may be manageable with short-term cultures, though it eventually leads to a high potential for contamination in long-term cultures, as we sometimes observed in Chapter 3.

Our findings highlight the need for further investigation into alternative surface modification techniques or culture systems for long-term applications. One promising avenue could be the exploration of alternative polymers or crosslinking methods that offer improved stability on TCP surfaces. Adapting such materials to our patterning technique could potentially address the stability issues we encountered. However, the ongoing challenges we encountered led us to move towards other methods of micropatterning. Specifically, to reduce the potential for contamination, it may be critical to remove the need for externally introduced materials such as plastic coverslips or hydrogels. Thus, we next sought to develop a technique that does not require any introduction of materials into the culture well other than those used in standard culture.

4.3.3 Design and validation of a technique to micropattern tissue culture plastic directly using UV light

To date, micropatterned substrates for cell culture have either utilised glass substrates or the introduction of external biomaterials to induce spatial confinement. As we previously demonstrated, these methods of patterning suffer from poor long-term viability and/or high potential for microbial contamination when applied to our retinal cell cultures. Accordingly, a method to pattern cell culture surfaces without the introduction of external materials, including coverslips, may be critical to enable long-term retinal tissue cultures. Therefore, we aimed to design and characterise a method to improve the survival of spatially confined cell colonies. Importantly, this method would need to enable the self-organisation of stem cells into stratified retinal tissues as observed in our established protocol[46].

We utilised the photomask and dimensions as previously described in Chapter 3 to attempt an inverse approach to our previous methods. Rather than using a UV-photopolymerisable biomaterial to define regions to inhibit cell attachment, we aimed to instead use UV light directly as a way to pattern such areas. Since an ECM coating is typically required to support healthy iPSC attachment and survival on TCP, we hypothesised that altering the coated surface could, in turn, induce patterns of selective cell attachment. Indeed, when such methods are applied to laminin-coated glass surfaces, albeit using deep UV radiation, a micropatterned surface can be achieved[179]. Thus, this method involved first coating the 6-well plate with ECM extract (Geltrex) as is typically performed in iPSC culture followed by the application of UV lamp exposure through the patterned photomask onto the TCP surface (Figure 4.8).

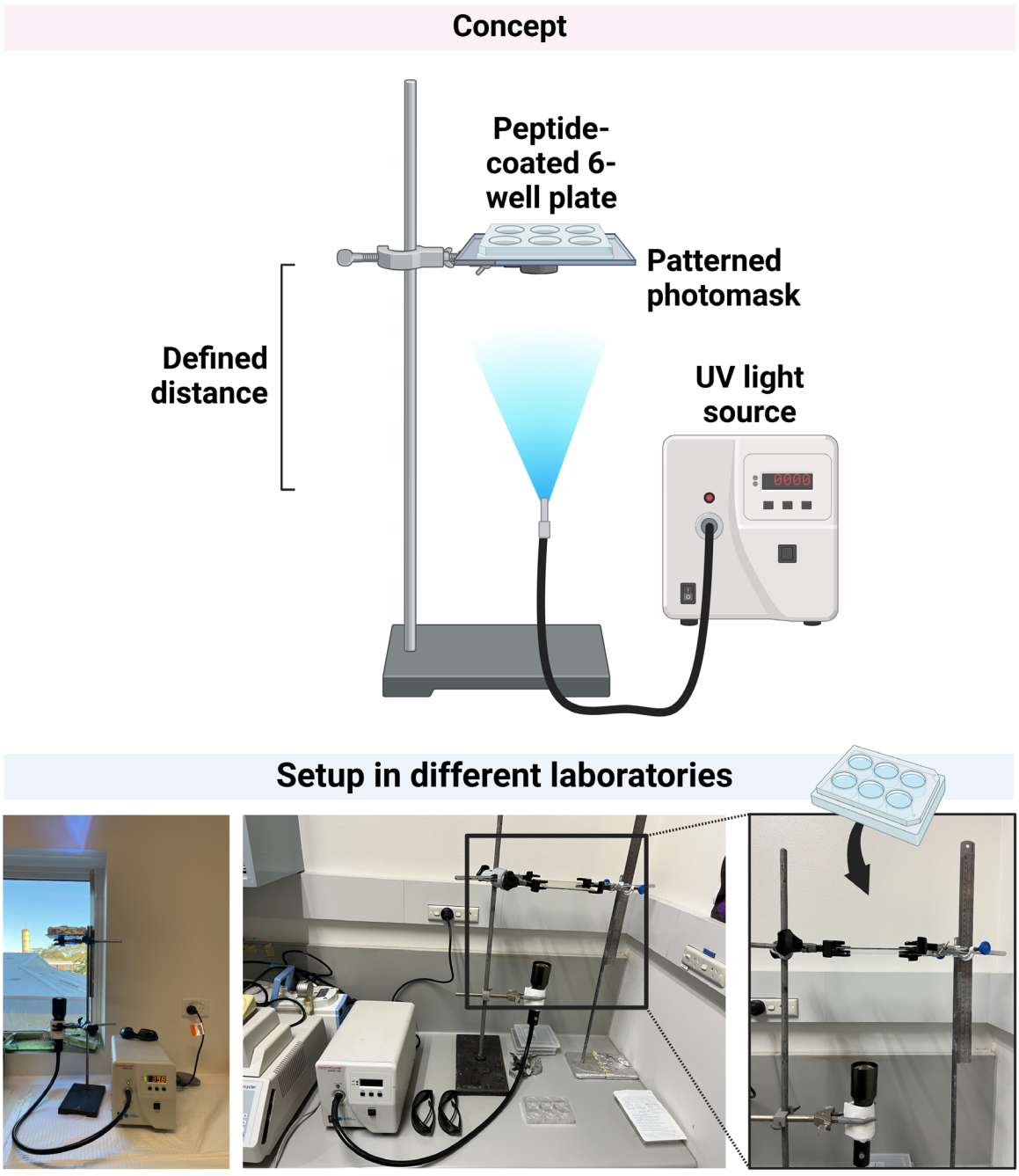

Figure 4.8 Schematic representation of the UV lamp-based micropatterning set-up (top) and successful implementation in two separate laboratories (bottom).

The Geltrex-coated tissue culture plate was placed on top of a chrome photomask and exposed to UV light. A distance of approximately 20 cm between the photomask and lamp was used. Created with BioRender.com.

An initial time point of 30 minutes was trialled as we hypothesised that an extended period of time would be required to sufficiently alter the Geltrex-coated surface enough to affect cell attachment—particularly as we are using a wavelength of UV within the UV-Vis spectrum, which is less powerful than deep UV radiation.

As there were no other observable differences in the well plate or TCP surface, the most straightforward method to verify that UV exposure had altered the Geltrex coating was by observing cell attachment. Upon cell seeding at standard protocol density and procedures, rounding of cells was observable in a patterned fashion on the day following the removal of the Rock Inhibitor (Figure 4.9a). Clear patterning of cell colonies could be observed 48 hours following this, where cells that could not attach successfully retained a rounded morphology or had detached and were washed away upon media change (Figure 4.9b). Interestingly, due to uneven seeding of the cells, we observed regions of relatively higher or lower cell densities in the same well. As expected, the colonies in the higher-density regions were larger and relatively more complete compared to lower-density regions at the same time point.

While keeping the distance constant (approx. 20 cm perpendicular height), we next applied different times of exposure of 15, 30, and 60 minutes. Following UV exposure, tilting the plate upwards revealed slightly discernible regions where small droplets of PBS were caught. This observation was particularly pronounced in wells that were treated with 30 or 60 minutes of UV exposure and consistent across duplicate wells. This behaviour is likely attributed to the hydrophilic nature of Geltrex, whereby any alterations caused by prolonged UV exposure have the potential to denature proteins and peptides in the Geltrex coating. As such, liquid molecules may be more attracted to the regions unaffected by UV exposure, creating a faintly observable pattern that reflects the photomask design when the plate is tilted back and forth.

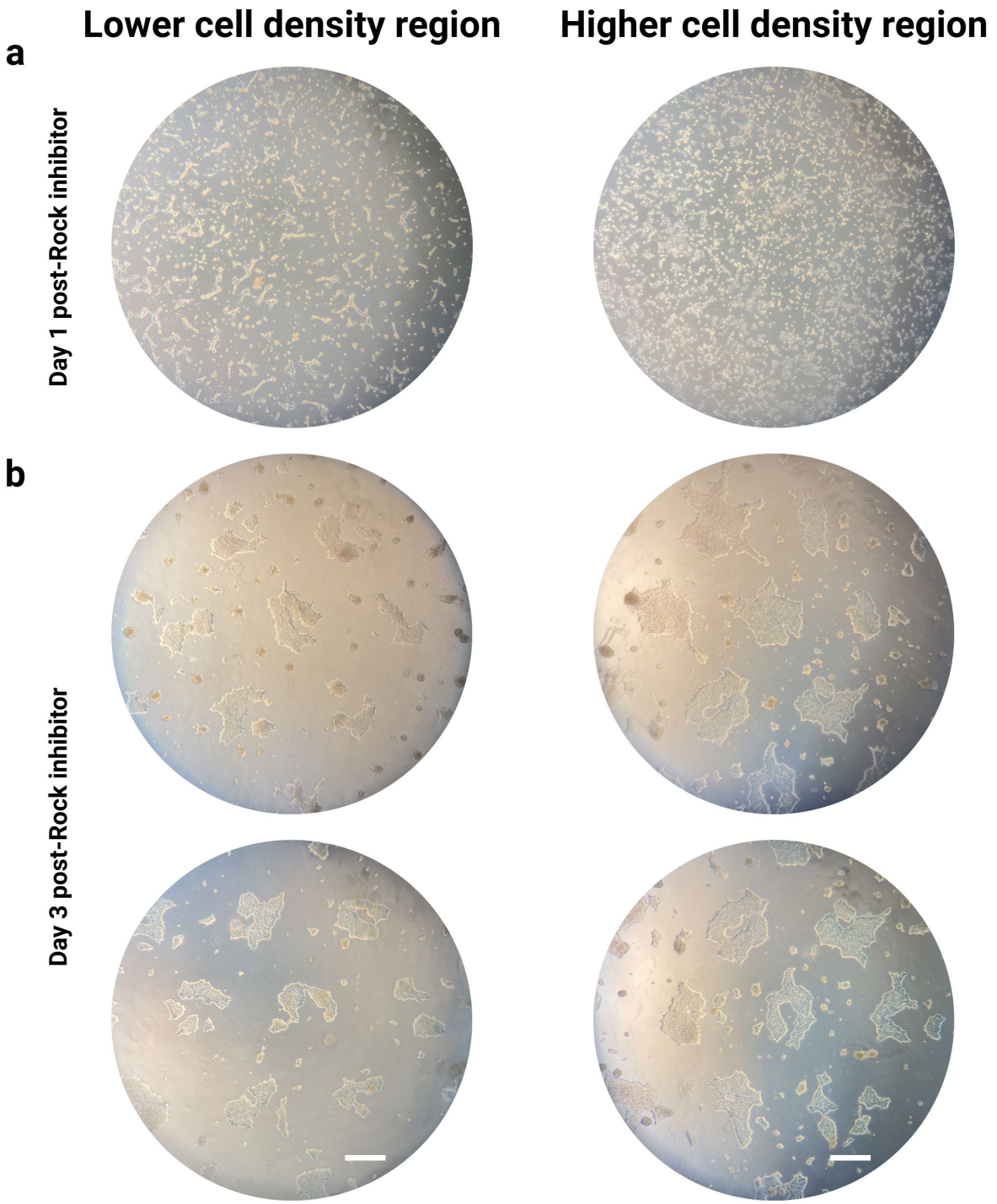

Figure 4.9 Cells seeded onto UV-micropatterned tissue culture surfaces selectively attached and proliferated on regions not exposed to UV light.

Following 30 minutes of exposure of UV light, the Geltrex coating on the tissue culture plastic was altered such that cells could not successfully attach to regions exposed to the UV lamp, as indicated by the rounded morphology of apoptotic cells. Scale bar = 500 µm.

This observation suggested that a complete or partial coating of Geltrex remained intact in areas blocked by the photomask.

Similar to the initial experiment, we observed spatial confinement of cell colonies reflecting the photomask pattern at the 30-minute UV exposure timepoint after 4 days (Figure 4.10a). In a similar fashion, wells that had been exposed to 60 minutes of UV exposure exhibited well-defined patterning and spatial confinement (Figure 4.10a). At the 15-minute time point, we observed suboptimal spatial confinement, where cells did not appear to have well-defined patterned regions of cell attachment (Figure 4.10a). This demonstrated that extended periods of UV exposure (>15 minutes) are required to sufficiently alter the Geltrex coating to such a degree that cell attachment is inhibited. As our aim focussed on spatially confining cells to a particular pattern, we did not move forward with the lower UV exposure times.

Differentiation initiation is typically performed at the time that stem cell cultures reach 80-95% confluency of a 6-well plate—dependent on the cell line used. However, as we are spatially limiting the surface area in which cells can grow, we determined the suitable time point to begin differentiation was when the cell colonies grew to approximately >90% of the circular pattern. Interestingly, this day correlated to the approximate time range required for standard monolayer cultures to reach suitable confluence for the particular cell line utilised (4 – 6 days). After 72 hours from the onset of differentiation, we observed that wells that had been exposed to 30 minutes of UV light had begun to curl at the colony edges (Figure 4.10b). This morphology is indicative of the onset of embryoid body formation, whereby the PSCs spontaneously aggregate in the absence of sufficient attachment to substrate materials. This embryoid body morphology was highly apparent in wells that were exposed to 60 minutes of UV light (Figure 4.10b). From these preliminary studies, we observe a general trend of increasing UV exposure time to increase the potential for cell colonies to form aggregated

structures. This is likely a result of increased denaturing of the attachment or supportive proteins within the ECM coating with higher exposure to UV light. Since we hypothesised that an approach that minimally altered the standard protocol would be ideal for inducing the self-organisation of retinal vesicles, we moved forward with the 30-minute UV exposure time for our particular UV setup.

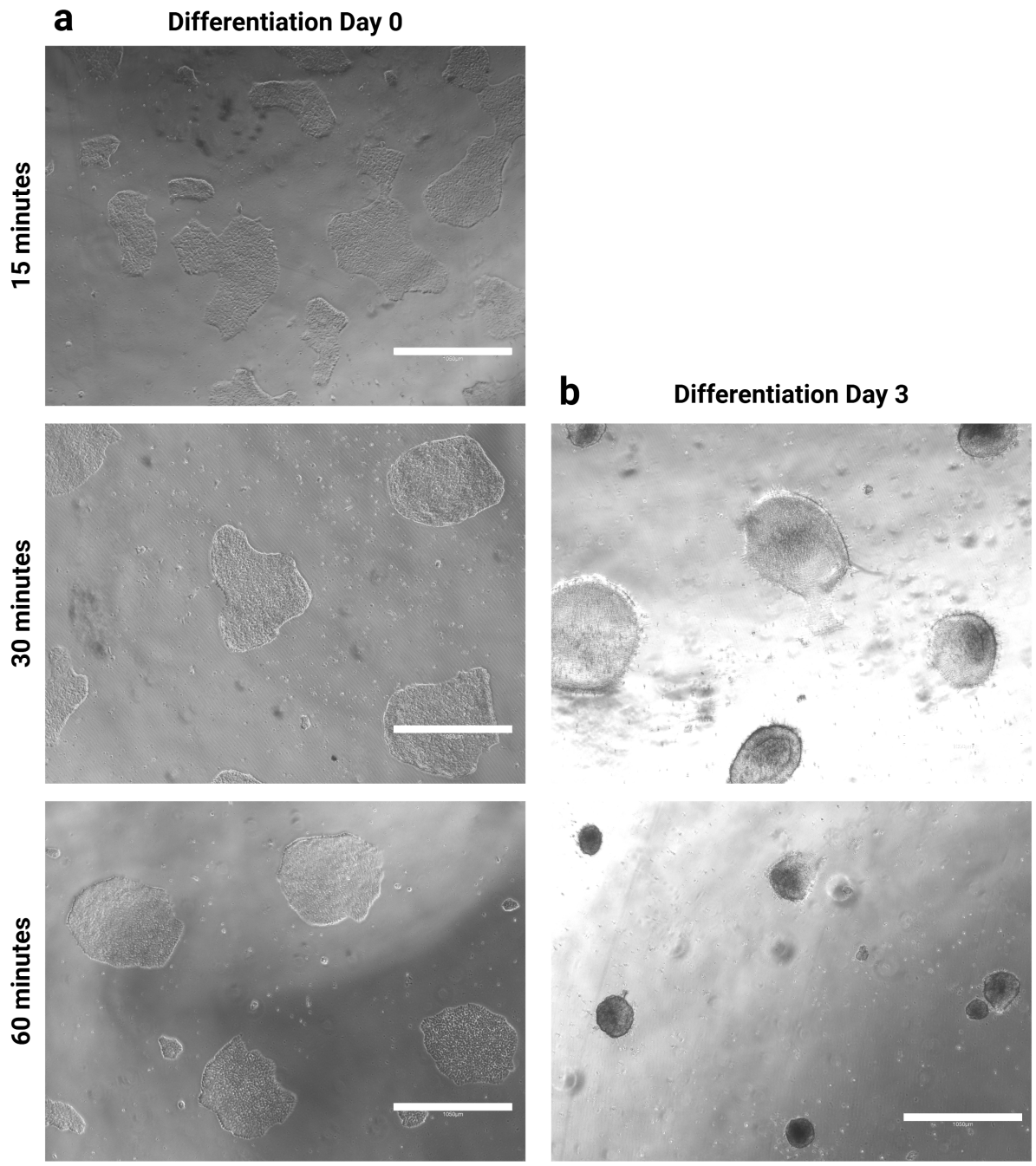

Figure 4.10 Alterations in UV exposure time resulted in distinct cell morphologies upon cell attachment and differentiation (Scale bar = 1050 µm).

(a) Differentiation was initiated at the same time for all cultures upon one of the micropatterned samples reaching 90% confluency within the patterned geometry. UV exposure of 15 minutes was insufficient to induce micropatterning, compared to 30 minutes and 60 minutes, and was discontinued. (b) At day 3 of differentiation, morphological assessment revealed that the 60-minute time point led to excessive aggregation of the cell colonies. In the cultures treated with 30 minutes of UV exposure, some colonies could remain flat while others appeared rounded, indicating heterogeneity in UV exposure.

The method was replicated across three iPS cell lines, where micropatterning of Geltrex-coated wells could affect the attachment of the cells seeded inside. This effect was observable by eye within one week of seeding (Figure 4.11). These initial studies demonstrate the capacity of UV lamp exposure to alter the cell culture surface to inhibit cell attachment in selective areas. It is likely that the cells that cannot successfully attach to the UV-exposed regions undergo anoikis or apoptosis[211], thus detaching over time or with mechanical stimulation upon media refreshment. As demonstrated in Figure 4.10b, there remained observable inconsistencies in cell morphology within different areas of the well—for instance, the rounding of some colonies while others remained flat. Based on the standard protocol and our observations in Chapter 3, it may be presumed that a flatter colony morphology may be more conducive to the self-organisation of retinal vesicles in the long term. As such, we next aimed to optimise the protocol to achieve less aggregated cell colony morphologies within these patterned well plates.

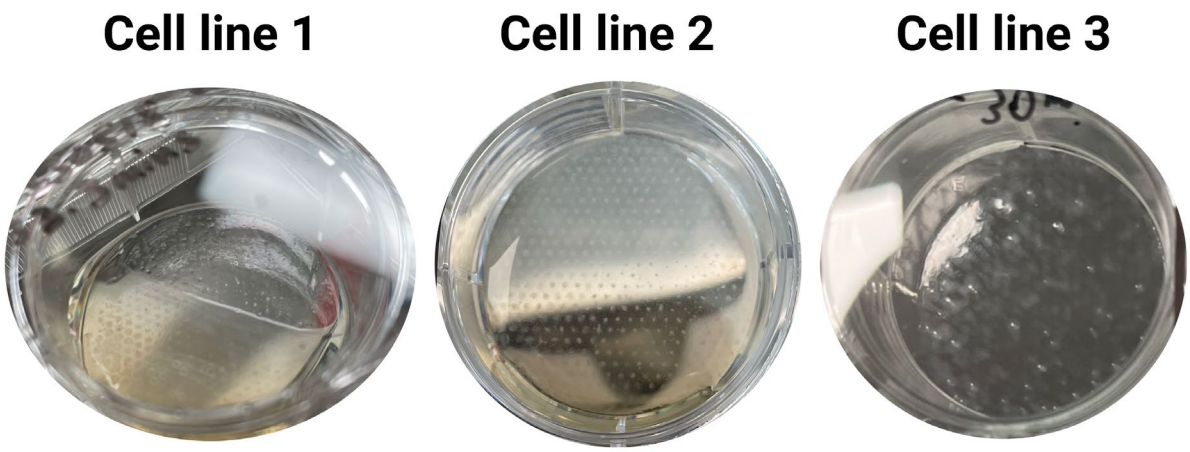

Figure 4.11 Representative images of distinct macroscopic patterning of tissue culture wells within 1 week of differentiation across the HOIK1, IMR90, and EP1 cell lines.

4.3.4 Optimisation of cell behaviour on micropatterned tissue culture plastic

The Inverse Square Law describes that the power of the UV light is inversely proportional to the distance between the sample and the lamp head, as follows[212]:

$$I_d = \frac{I_0}{d^2}$$

Where:

$$\boldsymbol{I_d}\ is\ the\ UV\ intensity\ at\ distance\ \boldsymbol{d}\ \left(in\ \frac{W}{m^2}\right).$$

$$\boldsymbol{I_0}\ is\ the\ UV\ intensity\ at\ a\ reference\ distance\ \left(in\ \frac{W}{m^2}\right).$$

$$\boldsymbol{d}\ is\ the\ distance\ from\ the\ light\ source\ (in\ metres).$$

As such, the height of the stage, which determines the distance of the plate from the light source, is critical in ensuring consistency across replicate experiments. Maintaining the well plate at a plane that is directly perpendicular and centred under the lamp head may similarly be critical. Indeed, in many of our initial studies characterising the effect of UV exposure on cell attachment, we noticed variabilities in cell morphology within the independent wells. There was an observable difference in the roundness or flatness of colonies by eye, where cells that attached closer to the centre of the well were more likely to round up compared to those further from the well (Figure 4.12a). Cells in the centre of the well were therefore more likely to detach from the well plate and become suspended in the media. Upon media change, these floating cell aggregates could be easily aspirated using the vacuum pump.

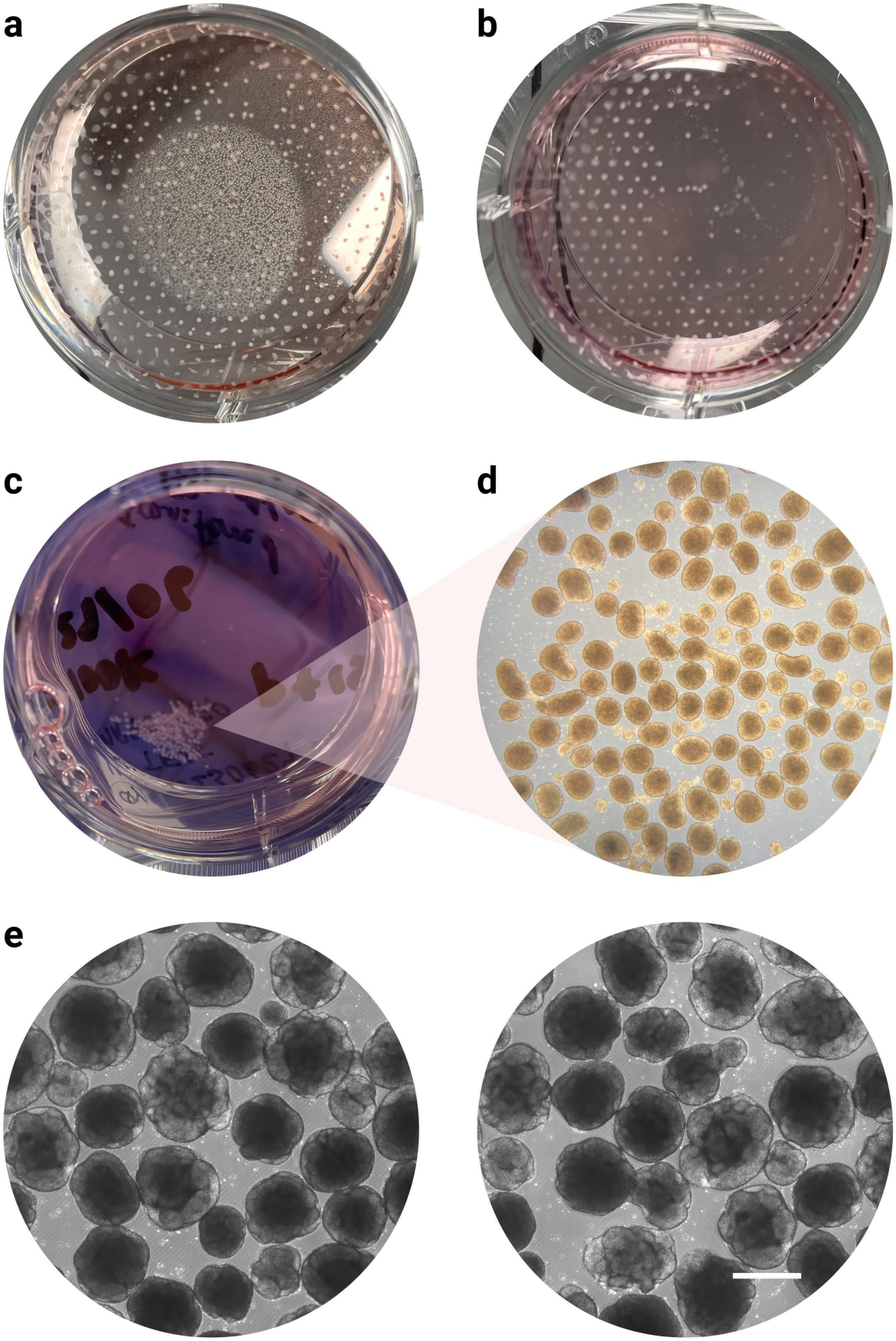
a
b
c
d
e

Figure 4.12 A high number of cell aggregates were produced in the un-optimised UV patterning protocol and could be collected for further culture.

Representative images of the culture well (a) before and (b) after collecting floating cell aggregates shows that a large gap was left in the centre of micropatterned wells. (c) Cell aggregates could be transferred to suspension cultures, (d) showing uniform morphologies. (e) At day 5, some aggregates cultured in neural induction media developed a thick, translscent, and undulated epithelial border while others remained dark and rounded. Scale bar = 500 μm.

Rather than aspirating these embryoid body (EB)-like structures, we isolated one batch by gently using a wide-bore P1000 tip to transfer the aggregates into another well of a 6-well plate (Figure 4.12c), leaving behind a gap in the middle of the original UV-patterned well (Figure 4.12b). These EB structures were relatively uniform in size (Figure 4.12d) and could be cultured in suspension akin to 3D retinal organoid differentiation protocols.

By Day 5 of differentiation, some of these suspended aggregates appear to form thick epithelia that adopted a crinkled morphology (Figure 4.12e). The capacity of UV-patterned well plates to generate a large quantity of EB-like structures is noteworthy, particularly as current protocols to generate EBs commonly require laborious steps—such as manual pipetting of counted cells into low-attachment round-bottom well plates. Such existing methods may be prone to pipetting errors, due to the cells naturally falling towards the bottom of the containing tube over time, as well as human errors. Further optimisation of the consistency of our UV-based technique may produce a method analogous to platforms such as commercially available AggreWell microwell plates, though potentially less costly. However, such studies were currently beyond the scope of this work.

To optimise the UV platform further for our current application, a few adjustments were made, including ensuring the photomask and well plate surface were flush against one another, centring the well directly superior to the UV lamp head, and adjusting the clamp of the photomask stage to be level and perpendicular to the UV light path. A substantial visible difference in consistency within individual wells was observed before (Figure 4.13a) and after (Figure 4.13b) these adjustments. As described above, a graded trend was noted in the difference in morphology for cell colonies closer or further from the centre of the well (Figure 4.13c). Although the intensity of this trend was reduced in the optimised UV platform, we still noted some areas in the centre where the uneven UV exposure affected cell morphology. This phenomenon likely stems from the shape of the UV lamp lens, which curves outwards, potentially resulting in the region directly under the well experiencing a slightly higher UV intensity than areas closer to the edge, in a gradient fashion.

Upon differentiation of the cells in the optimised patterning platform, the colonies maintained their spatially confined geometries. Some irregularities in colony morphology were observed, including flat protrusion from the colony boundaries at Day 4 post-differentiation (Figure 4.14), though these asymmetries are to be expected with the nature of iPSC cultures. Although it may be possible to rectify such morphologies through single-cell seeding, changing the protocol in such a significant deviation from standard procedures—which entails seeding cells in small clumps—would likely introduce further challenges. Interestingly, in this optimised platform, cells demonstrated the capacity to reform the confluent monolayer over time, as is present in standard cultures. As a result, the UV patterning induced selective regions of higher cell density (Figure 4.14)—a feature potentially favourable to initiate the self-organisation of these regions into retinal vesicles.

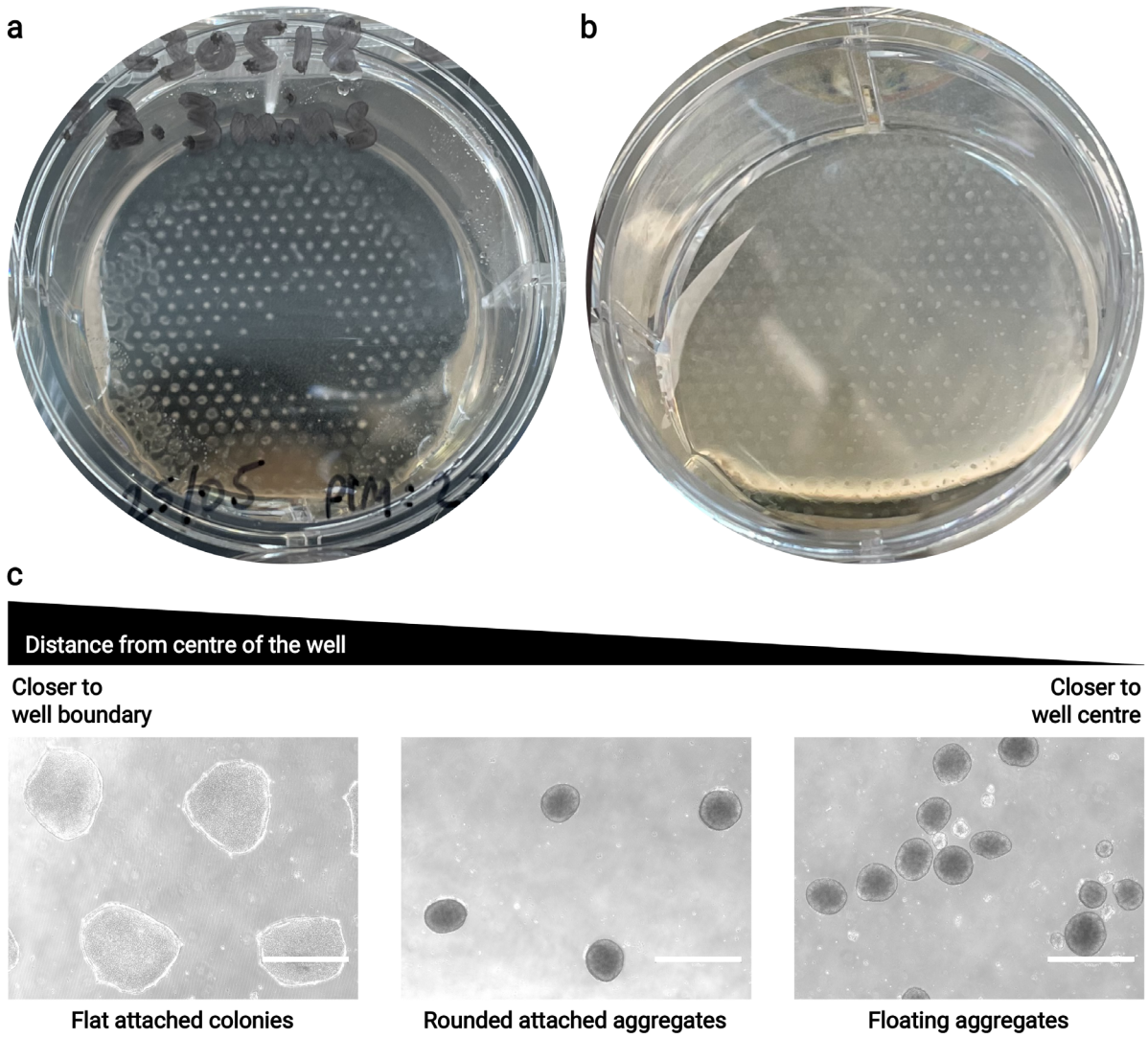

Figure 4.13 Optimisation and characterisation of the effect of distance from the centre of the well on subsequent colony morphology.

Representative images showing micropatterned cultures during week 1 of differentiation (a) before and (b) after optimisation of the protocol. (c) A relationship exists between the morphology of the cell colony and the distance from the centre of the well. Due to the concave shape of the UV lamp lens, cells in the centre of the well were potentially exposed to a higher degree of UV light to those at the edges, resulting in a rounded morphology. Prior to optimisation of the protocol, colonies at the edges remained flat while colonies closer to the centre tended to form embryoid body-like structures that either remained attached to the well or detached into the cell media. Optimisation minimised the formation of these aggregates. Scale bar = 1050 µm.

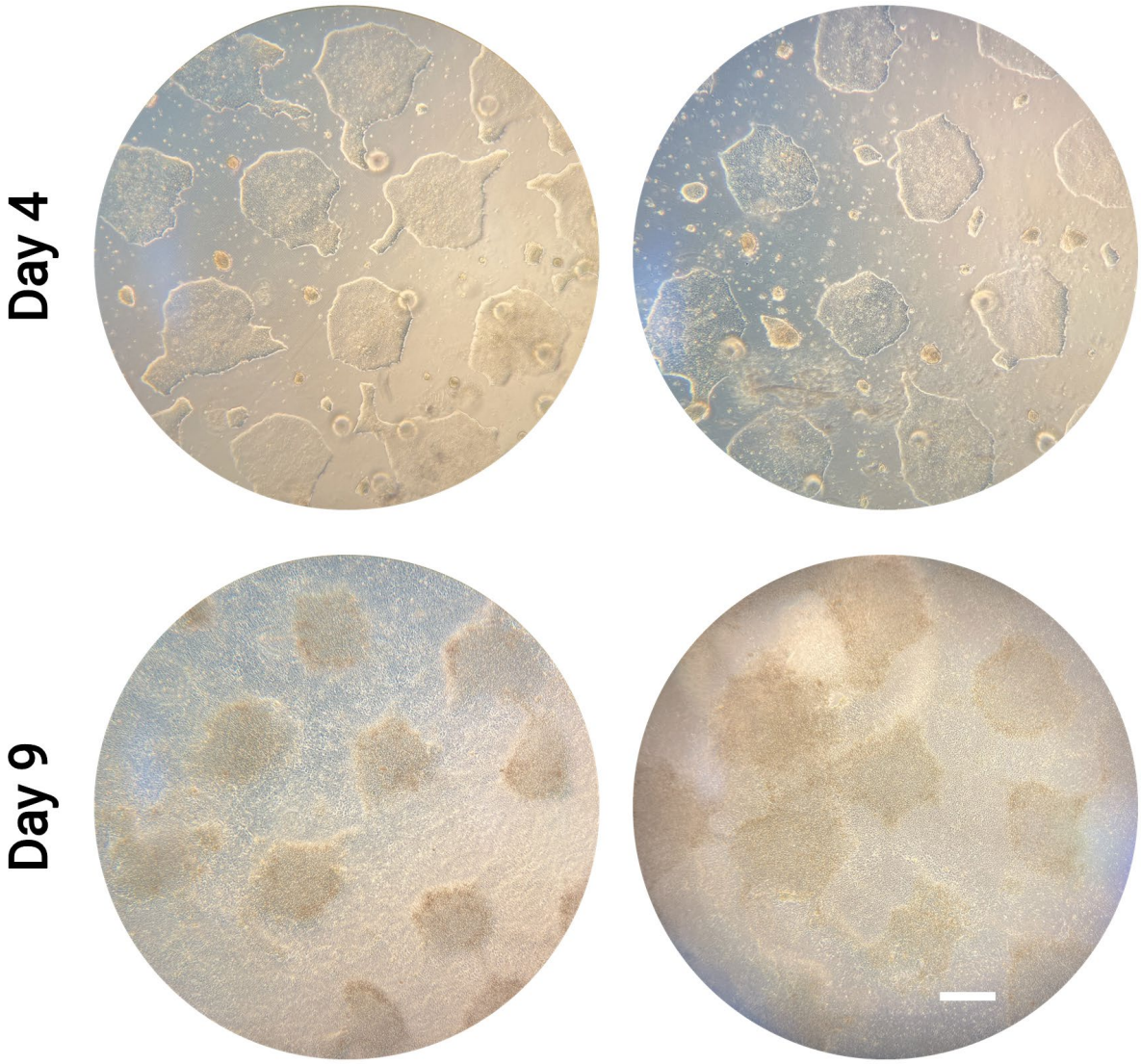

Figure 4.14 Representative images of cell colonies on UV patterned tissue culture plate following the optimisation of the protocol.

At day 4 of differentiation, cell colonies remained flat and confined to the patterned region. By day 9 of differentiation, cells within the colony were able to proliferate outwards, forming a monolayer of cells on the UV-exposed regions. This formed a patterned confluent culture with regions of higher cell density corresponding to the original spatial patterning. Scale bar = 500 µm.

As the morphology of the spatially confined colonies within independent wells was sufficiently consistent for our intended applications, we moved forward with the optimised setup without further alterations. Moreover, we hypothesised that the unintentional gradient patterning

offered by the UV platform would enable the characterisation of the effect of different initial colony morphologies on the capacity to self-organise into retinal vesicles. To ensure consistency across procedures, this newly developed technique was tested on two different 6-well plate brands (Costar and Falcon), as well as Geltrex made in two different labs. Likewise, we tested the setup across two different research laboratories (The University of Sydney School of Biomedical Engineering Campus and the Children's Medical Research Institute at Westmead) (Figure 4.8). No differences were observed between the resulting well plates or cell cultures.

Finally, the versatility of the developed method was demonstrated through the application of the technology using different photomask patterns (Figure 4.15). Large-diameter patterns (2 mm) could be successfully patterned, though the nature of the clumped cell seeding procedure led to higher inconsistencies in these larger surface area patterns. Conversely, small-diameter patterns (300 – 500 μm) led to patterned regions of higher cell densities, though these patterns were similarly inconsistent due to the nature of the seeding protocol and the random distribution of cell clumps. Patterns of a gradient of diameters could also be fabricated, in a comparable fashion to those explored in Chapter 3. This pattern somewhat reflected the morphology gradient observed from the well centre to edge in initial tests, though in a more profound manner (Figure 4.15). Similarly, small aggregates could be observed floating in the culture media over time due to colony rounding and detachment.

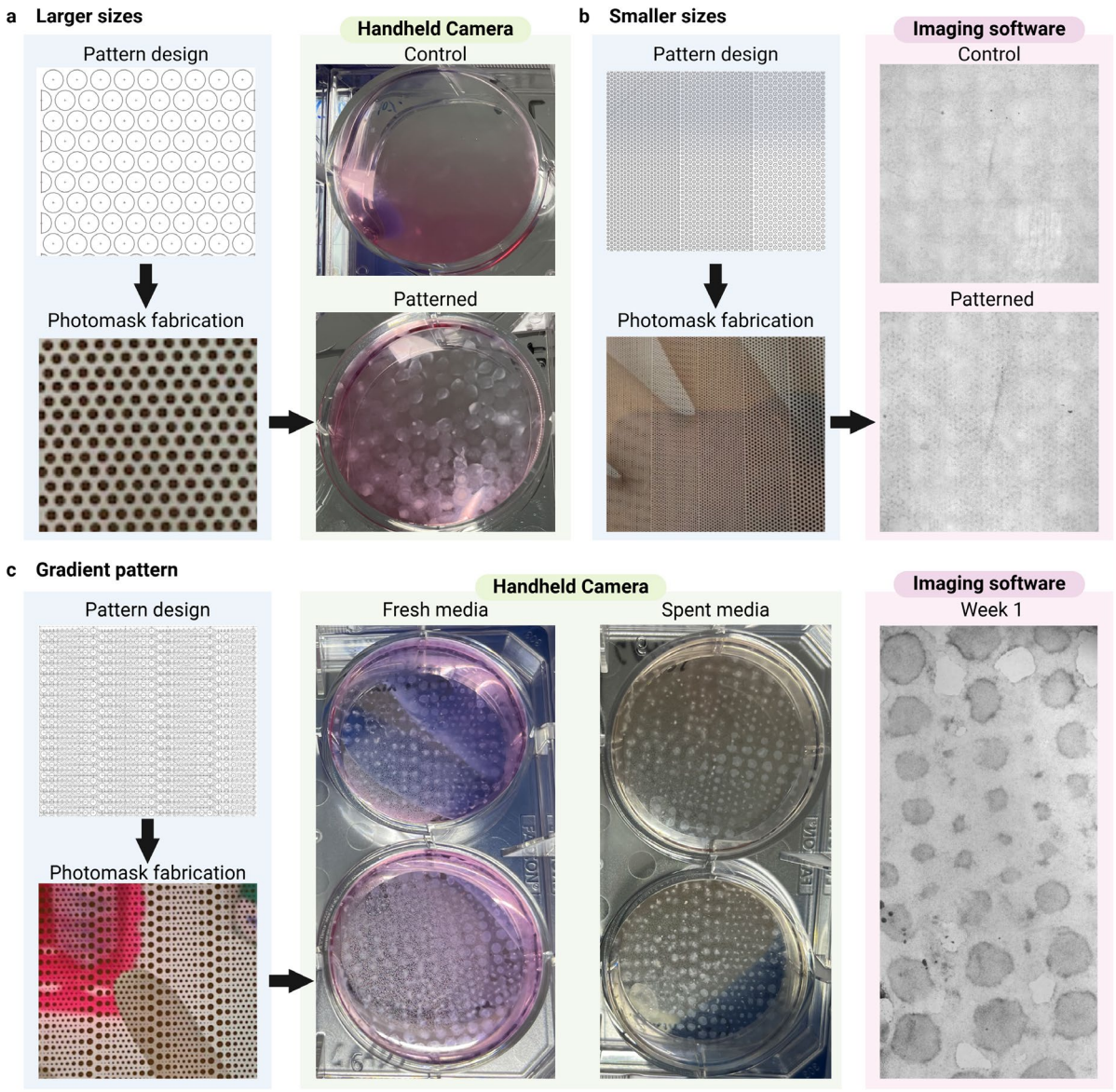

Figure 4.15 Fabrication of micropatterned tissue culture plastic using different dimensions of patterns shows the adaptability of the developed technique.

Using different photomask designs, (a) larger, (b) smaller, and (c) gradient micropatterns could be fabricated on tissue culture plastic using our newly developed method. Subsequent cell seeding demonstrated spatial confinement and/or patterning of cells after 1 week of differentiation.

The method developed in the current work demonstrates an innovative approach to spatially confining stem cell colonies in a temporary manner. The ability of cells to proliferate beyond the confined geometry shortly following the induction of retinal differentiation is notable. It is

highly plausible that a complex cascade of cell-cell interactions, as well as cell-ECM interactions, is mediating the morphological and proliferative behaviour of these cell colonies. Moreover, the complex balance of excessive or insufficient UV exposure is likely a critical factor in such observations. As explored previously, insufficient UV exposure results in a lack of attachment inhibition. However, we have now elucidated that excessive UV exposure may potentially result in the inability of cell colonies to continue to proliferate or migrate into the regions initially treated with UV light. In-depth characterisation of the UV-treated TCP surface in comparison to non-treated surfaces, such as through Fourier transform infrared spectroscopy, may reveal noteworthy insights into these surface chemistries. However, such complex compositional studies are currently beyond the scope of this thesis.

4.3.5 Long-term culture and evaluation of retinal differentiation on micropatterned tissue culture plastic

The potential for micropatterned tissue culture substrates to promote the self-organisation of retinal vesicles was investigated using our established protocol[46]. We first sought to observe the potential of the 'un-optimised' micropatterned cultures to characterise the effect of excessive rounding of colonies (Figure 4.16). Consistent with previous observations, un-optimised micropatterned colonies exhibited a pronounced tendency to round up during differentiation, particularly by day 4. The colonies adopted a dark, embryoid body-like morphology, indicative of premature aggregation and lack of attachment proteins in the surrounding substrate area. Interestingly, by day 5, the colonies began to flatten and formed neural rosettes which are commonly associated with early neuroepithelial. Cells started to spread outwards towards regions where the matrix had been removed. By day 9, the differentiating cells first present only in patterned regions merged to form a confluent monolayer. This re-spreading of colonies suggests that some differentiating cell types might be less dependent on Geltrex to grow and can, therefore, spread via the secretion of their own ECM support. Notably, the degree of colony balling directly influenced their capacity to reform a monolayer, with more rounded colonies remaining isolated and forming clusters with dark centres, which could be indicative of continued embryoid body formation or cell stress.

By weeks 2 and 3, the loss of clear micropatterning in the un-optimised conditions was evident. The cells exhibited less organised growth, and the characteristic geometric boundaries were largely lost. This observation may be consistent with a decline in the mechanical cues provided by the substrate, as cellular proliferation and differentiation likely led to a loss of the initial spatial organisation.

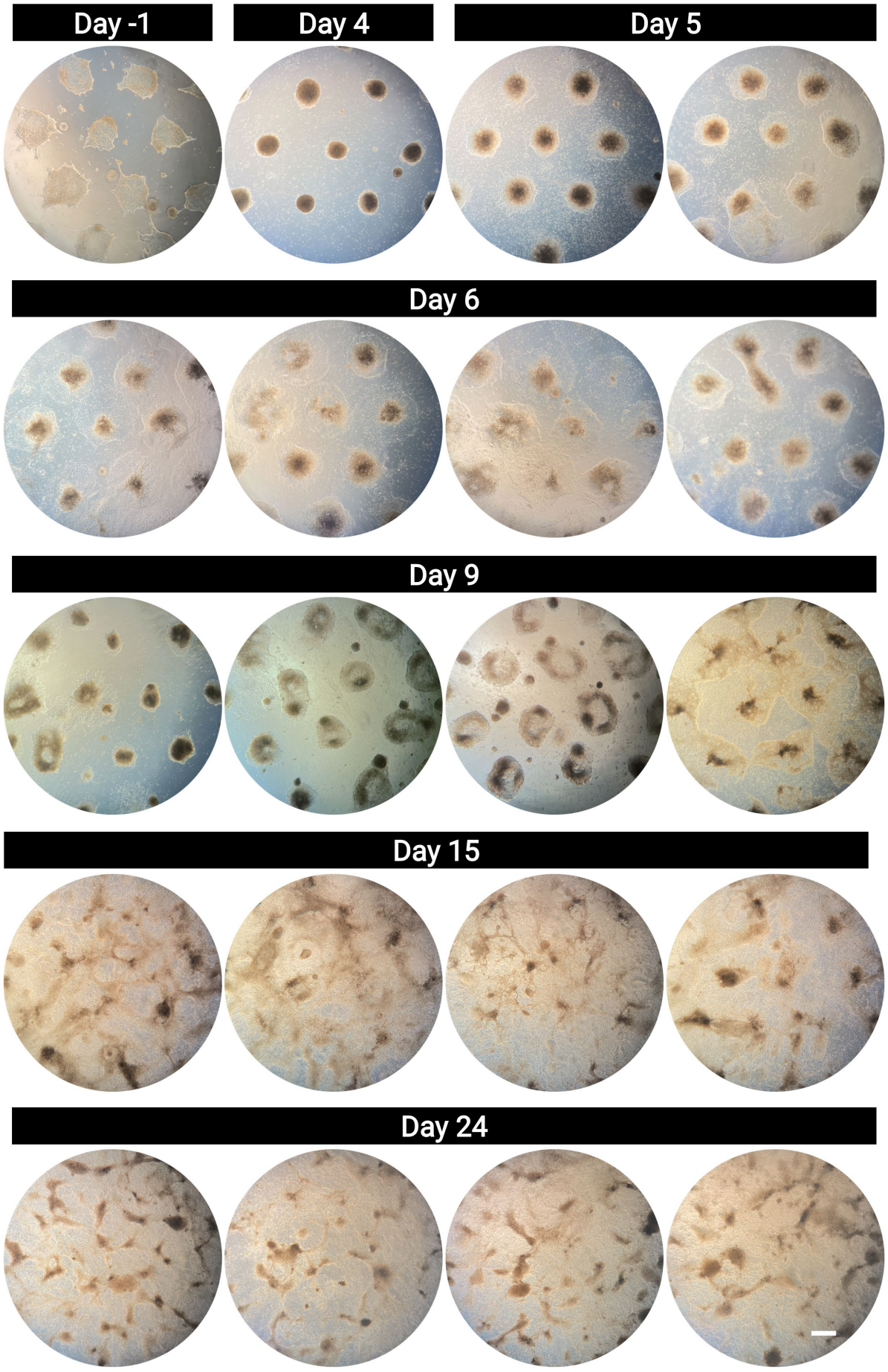
Day -1
Day 4
Day 5
Day 6
Day 9
Day 15
Day 24

Figure 4.16 Differentiation of cells on UV-micropatterned tissue culture plastic prior to optimisation of protocols reveal high levels of disorganisation by week 4.
By day 4, cells in the non-optimised micropatterned substrates become rounded, resembling embryoid body structures. These structures could remain attached to the culture surface and began to spread outwards by day 5. The cultures showed flat edges at day 6, though the centre of the colony appeared dark, resembling the onset of neural rosette formation. By day 9, a clear difference in morphology could be observed in colonies closer to the centre of the well, which appeared rounded, and colonies closer to the edge, which were able to flatten and spread outwards to form a connected monolayer. Spatial patterning was lost by day 15, with the absence of vesicle structures at day 24. Scale bar = 500 μm.

The transition from well-defined micropatterns to disorganised growth may reflect a breakdown in the mechanical stability of the colonies, further supporting the hypothesis that maintaining optimal cell attachment is crucial for preserving micropattern-induced spatial cues throughout differentiation. As such, early colony morphology could be predictive of later developmental outcomes.

To address the issue of excessive early colony rounding and improve the retention of micropattern geometries, we implemented a protocol modification by extending the initial treatment with Rock inhibitor (Y-27632) from 24 to 48 hours. This small molecule is commonly used to inhibit the RhoA/ROCK signalling pathway, reducing apoptosis and supporting cell survival in standard iPSC cultures. By prolonging this treatment, we aimed to support cell-substrate stability and maintain a flatter colony monolayer during the critical early stages of differentiation (day 1-4). The extended treatment proved beneficial, as colonies retained their flat monolayer morphology from seeding through to the onset of differentiation (Figure 4.17). Notably, the micropattern geometries were more clearly defined (Figure 4.17a), with colony borders showing evidence of proliferation, as opposed to signs of differentiation, which was previously indicated by darker, rounded colony edges. As expected, control non-

patterned wells formed a monolayer of cells with no particular morphological changes. The improved maintenance of micropattern geometries suggests that enhanced adhesion and cytoskeletal support may stabilise the colonies and prevent premature differentiation or aggregation into embryoid bodies.

The differential morphologies observed within the micropatterned colonies by week 2 were of particular interest. Some colonies retained a flatter, more organised structure, while others were more rounded and densely packed (Figure 4.17b). The flatter colonies exhibited the characteristic neural rosettes, suggesting that these regions were undergoing a more controlled neurogenesis. In contrast, the rounded colonies, which appear darker and are the result of less attachment, likely represented areas of more advanced or disorganised differentiation, possibly reflecting a shift towards embryoid body formation or excessive differentiation towards neural phenotypes, also termed neuralisation. When cultures were analysed for SIX6-GFP throughout this period no eye field formation was evident. This gradient of differentiation within the micropatterned colonies suggests that the micropatterned substrates may influence local microenvironments, potentially modulating cell-cell and cell-matrix interactions, thereby creating regions with varied differentiation trajectories.

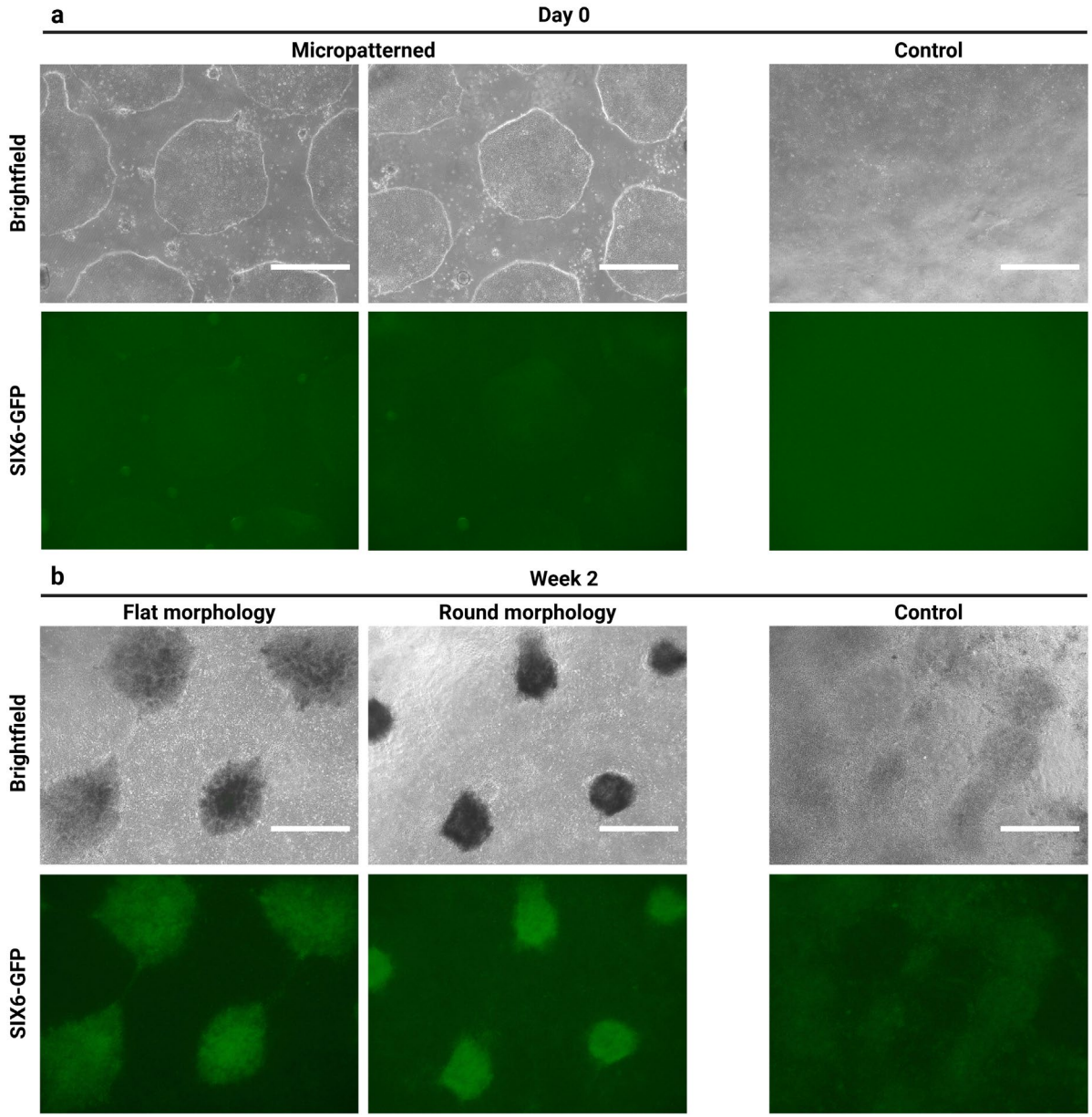

Figure 4.17 Optimised micropatterning of tissue culture plastic retained the flat morphology of cell colonies at the onset of differentiation and enabled the formation of a neat cell monolayer between patterned colonies at week 2 of differentiation.

(a) Micropatterning induced a clear spatial confinement of cell colonies, where control cultures performed simultaneously formed one continuous monolayer. (b) Patterned neural rosette morphologies were observed after 2 weeks of differentiation. Control cultures showed some morphological features at week 2, though no patterning was observable. Scale bar = 1050 µm.

By week 3, the self-organisation of SIX6-GFP positive retinal vesicles within the micropatterned cultures became evident, as marked by the appearance of transparent neuroepithelial borders (Figure 4.18a), which are characteristic of retinal vesicle formation. In comparison, the control cultures, while also forming early characteristics of retinal vesicles, lacked clear neuroepithelial borders at this time point. This suggests that micropatterning may accelerate or enhance the spatial organisation of retinal progenitors. This observation implies that micropatterned substrates provide more robust mechanical or spatial cues that promote the organisation of retinal tissue. The appearance of well-defined retinal vesicle regions in the micropatterned cultures is particularly significant, as it suggests that micropatterning may help guide the spatial arrangement of progenitor cells, thus facilitating the self-organisation of complex tissue structures.

The progression of retinal vesicle formation was more striking by week 5. Both micropatterned and control cultures developed retinal vesicles with neuroepithelial borders; however, the organisation of vesicles in micropatterned cultures was more defined, with distinct regions of retinal vesicle formation compared to the random organisation observed in the control cultures (Figure 4.18b). This result supports the hypothesis that micropatterning can provide spatial constraints that enhance tissue organisation, offering an advantage over traditional, non-patterned culture systems.

However, one limitation induced directly by the success of the micropatterning technique was the mass loss of vesicle structures over time due to high shear forces induced during media changes (Figure 4.19). The highly 3-dimensional structures generated within these patterned substrates were more likely to detach into the cell media than in control cultures. Although this feature may be advantageous in downstream applications, such as the collection of vesicles without the need for manual dissection, it likely affects the subsequent quantification of the

micropatterned cultures in the current work. As such, care was taken to not disturb these structures during media changes in all experiments.

A critical novelty lies in the capacity of the technique to function within standard tissue culture plates already utilised in clinical applications. We observed a striking difference in culture wells when compared to control wells both macroscopically (Figure 4.20) and microscopically (Figure 4.21). Importantly, the ability to induce patterned retinal vesicle formation could have significant implications for scaling organoid cultures for therapeutic applications, where spatial control can often be a limiting factor for high-throughput vesicle collection.

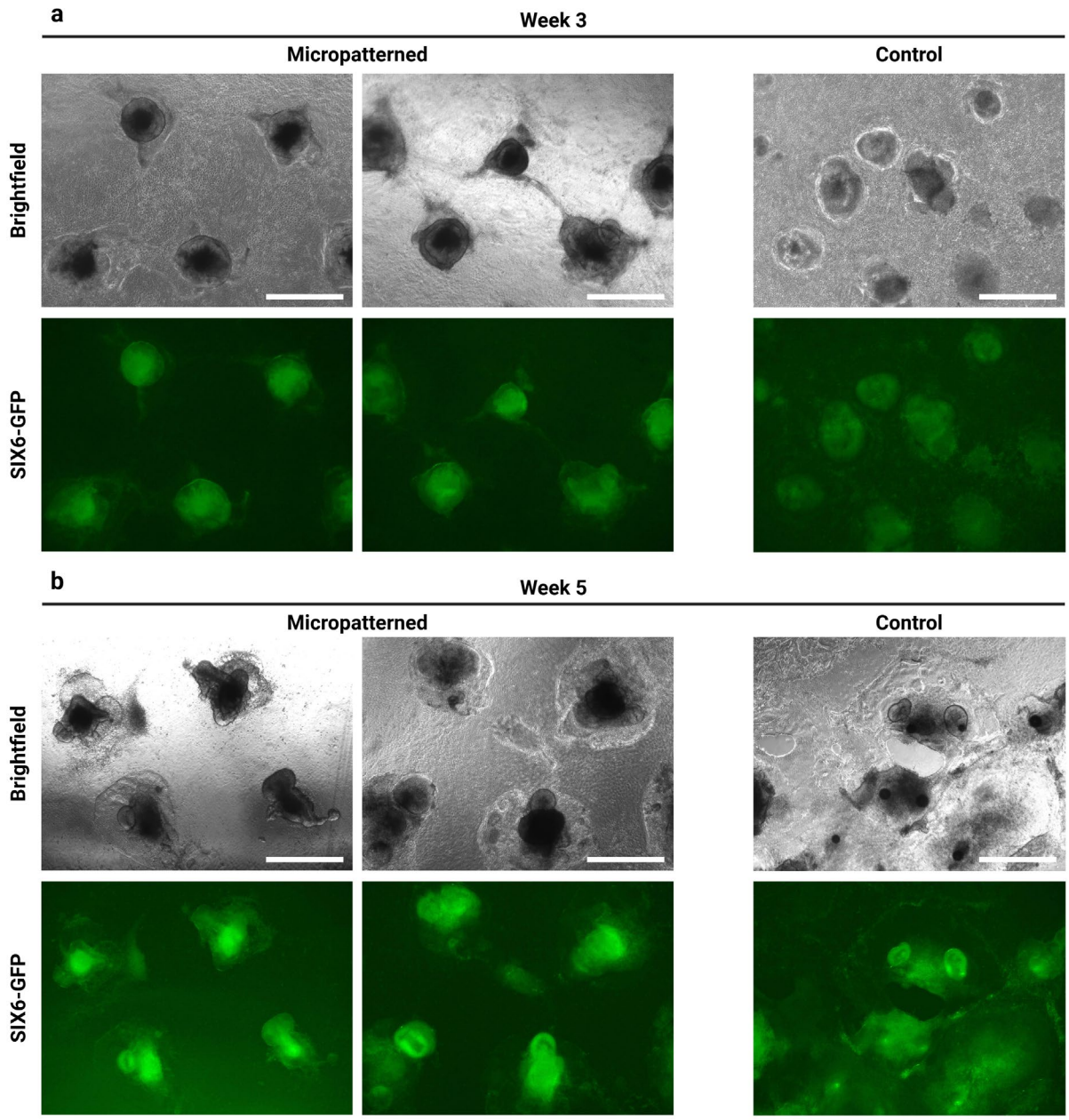

Figure 4.18 UV-treated micropatterned tissue culture plastic successfully supported the self-organisation of retinal vesicles by week 3 of differentiation.

(a) At week 3 of differentiation, clear expression of SIX6-GFP was observed in patterned cultures, specifically regionalised to the region of patterning. Control cultures showed the generation of immature vesicle structures with relatively lower levels of GFP signal compared to vesicles grown in micropatterned substrates. (b) By week 5, retinal vesicles with clear neuroepithelial borders and bright GFP signal were observed. Vesicles similarly formed in control cultures, though were less well-organised, and were adjacent to large GFP+ patches that failed to form vesicles. Scale bar = 1050 µm.

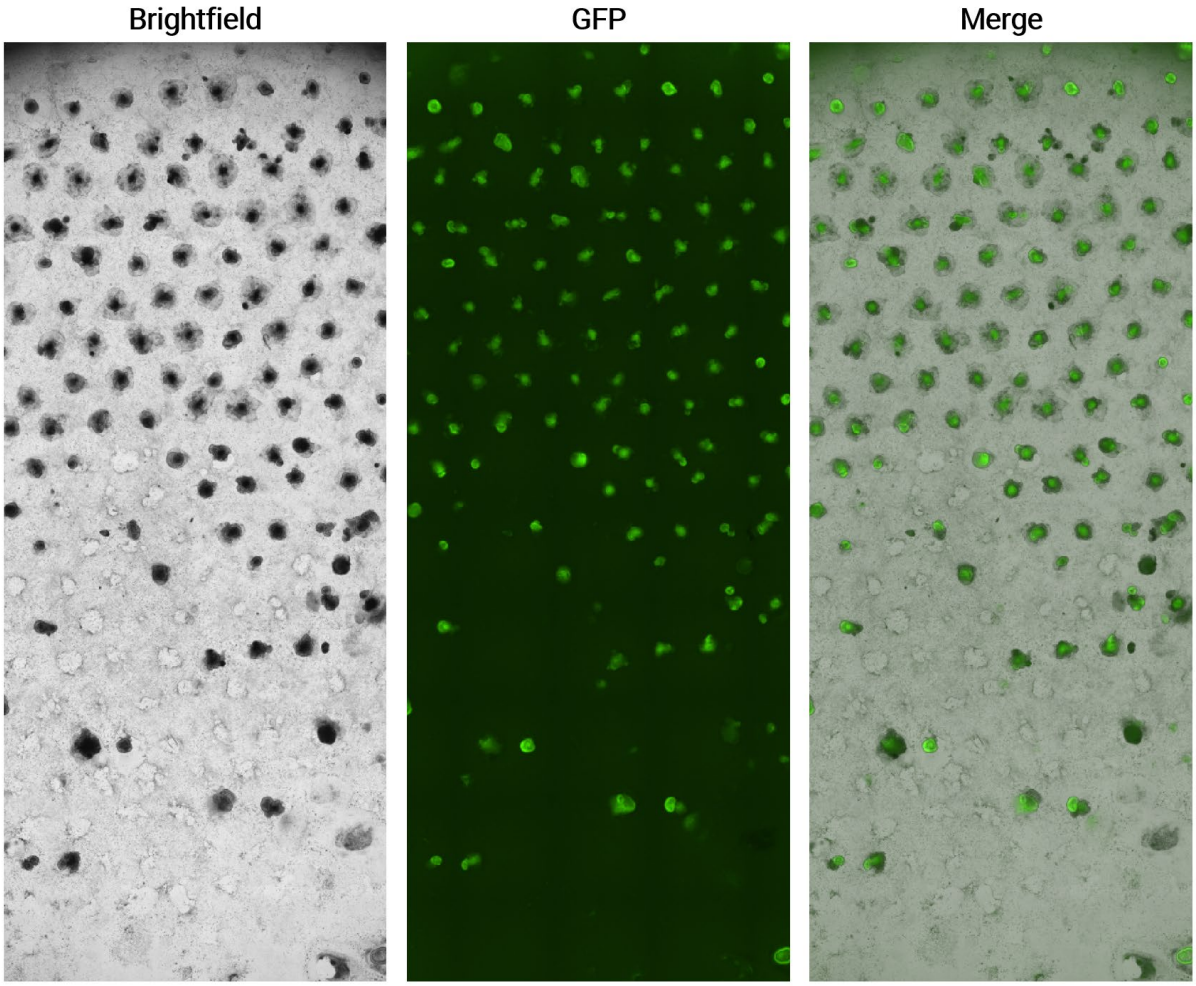

Figure 4.19 Representative image of a micropatterned culture at week 4, showing a mass loss of vesicle structures over time due to the highly budded 3D structures detaching following shear forces induced during cell media changes.

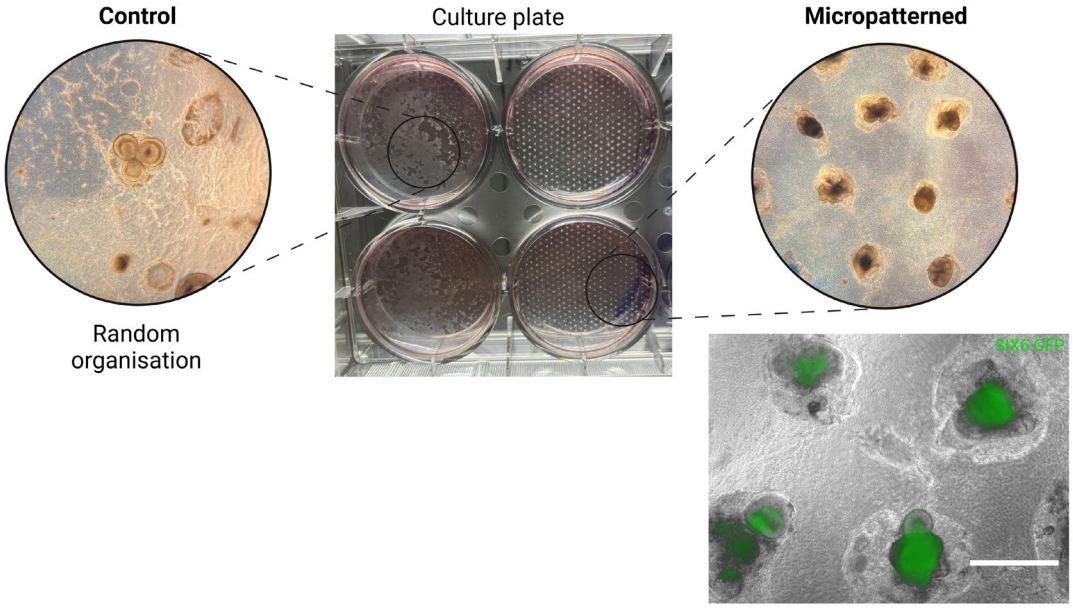

Figure 4.20 UV micropatterned cultures are visibly distinct from control cultures both macroscopically and microscopically (Scale bar = 1050 µm).

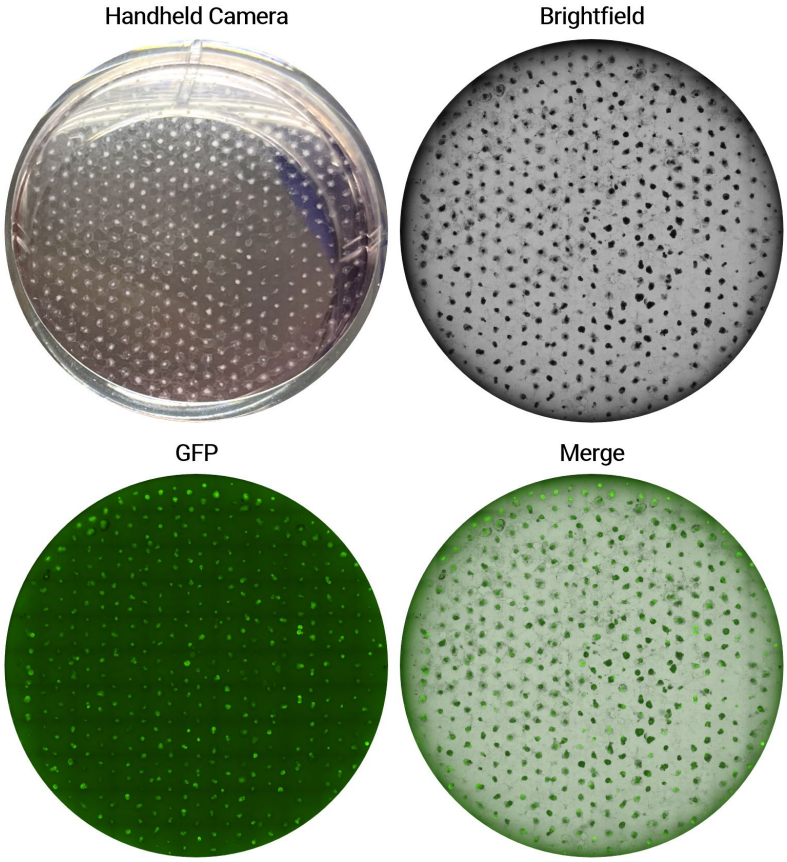

Figure 4.21 Representative images of an entire well of the micropatterned culture showing the distribution and distinct patterning of GFP+ vesicles.

A noteworthy finding was the mixed generation of retinal and cortical brain-like vesicles in these micropatterned cultures (Figure 4.20). These tissues could be easily isolated and cultured in 3D suspensions (Figure 4.22a, retina, b, brain). The noticeable higher frequency of distinct neural tissue types within the same culture, as compared to control cultures, could suggest that micropatterning may induce differential signalling environments. However, this difference was not quantified. These regulated microenvironments could be influencing the fate decisions of the progenitor cells. For instance, regions that developed cortical brain-like vesicles were characterised by the appearance of neural rosette structures, which are hallmarks of cortical neurogenesis. The co-development of retinal and cortical vesicles is common in the standard protocol[202], though the relatively increased number of co-tissue structures upon observation raises intriguing questions about the role of mechanobiological cues in guiding regional specification within organoids; however, lack of quantification limits this observation. It is plausible that micropatterning creates localised gradients of mechanical stress or differential access to growth factors, which could influence cell fate decisions in a spatially regulated manner. Further investigation into the molecular mechanisms underlying these observations could reveal new insights into how spatial organisation influences stem cell differentiation.

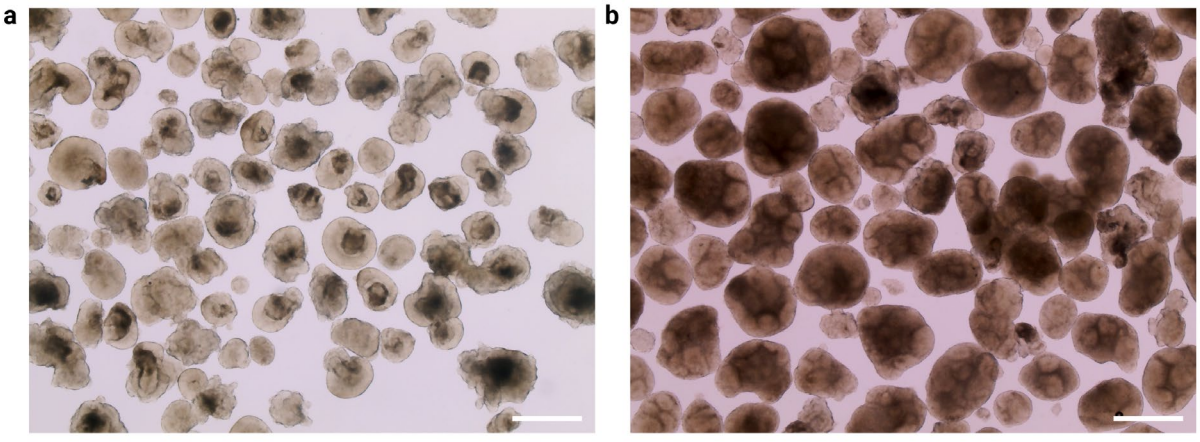

Figure 4.22 3D vesicles collected from 2D UV micropatterned cultures after 4 weeks of differentiation show clear (a) retinal and (b) brain morphologies, with no unusual features (Scale bar = 500 µm).

Interestingly, one independent batch of micropatterned cultures exclusively formed large, uniform cortical brain vesicles rather than retinal or mixed brain-retinal vesicles (Figure 4.23). The non-micropatterned control wells from the same experiment generated large, well-defined retinal vesicles. Further isolation and suspension culture of these brain vesicles at Day 40 confirmed a clear neural rosette morphology of these structures (Figure 4.24). These structures have been characterised in previous work from our lab[202], where immunofluorescent staining of these neural rosette structures confirmed cortical fate. This divergence in tissue fate between micropatterned and control cultures may reflect a competition between retinal and cortical neuralisation pathways, with the micropatterned substrate—in this case—potentially tipping the balance towards cortical differentiation. One hypothesis is that the mechanical confinement imposed by micropatterning may have altered neuralisation to the point where retinal fate is suppressed in favour of cortical development. Figure 4.25 illustrates a proposed schematic of this hypothesis, tabulating the hypothetical relationship between neuralisation and UV-induced spatial confinement. Although this outcome was not repeated in subsequent experiments, it raises important questions about the relationship between mechanical forces, substrate geometry, and neural differentiation pathways. Given that no experimental deviations were noted, the occurrence of large cortical vesicles in this batch may also represent an experimental anomaly or the result of subtle environmental variations, such as differences in UV exposure or accidental alterations in micropattern dimensions.

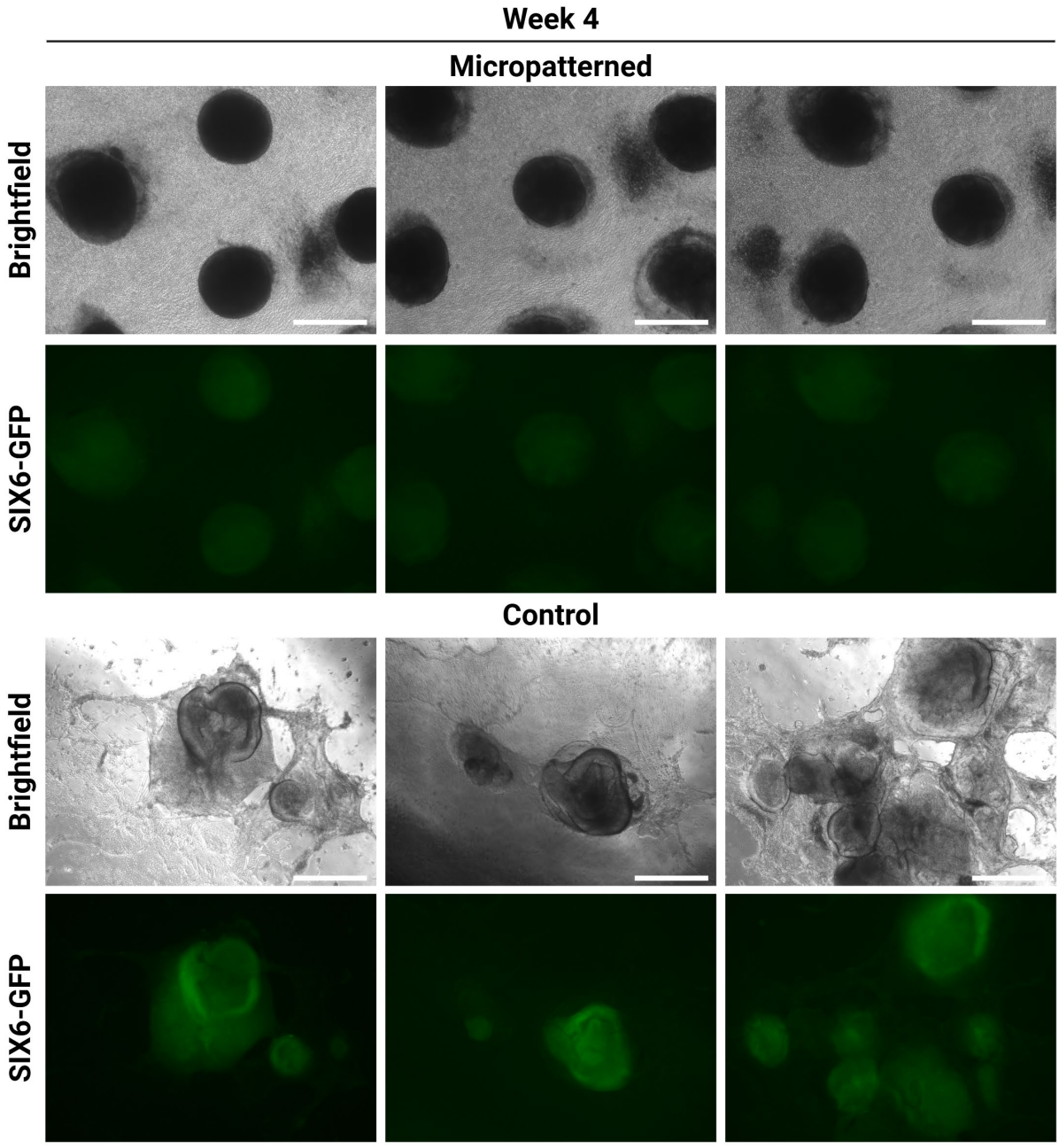

Figure 4.23 Cortical brain vesicles spontaneously formed in one independent batch of micropatterned cultures by week 4.

Micropatterned cultures developed vesicles indicative of brain organoids, further confirmed by the lack of SIX6-GFP expression. Control cultures show standard retinal vesicle morphology with high SIX6-GFP expression. Scale bar = 1050 μm.

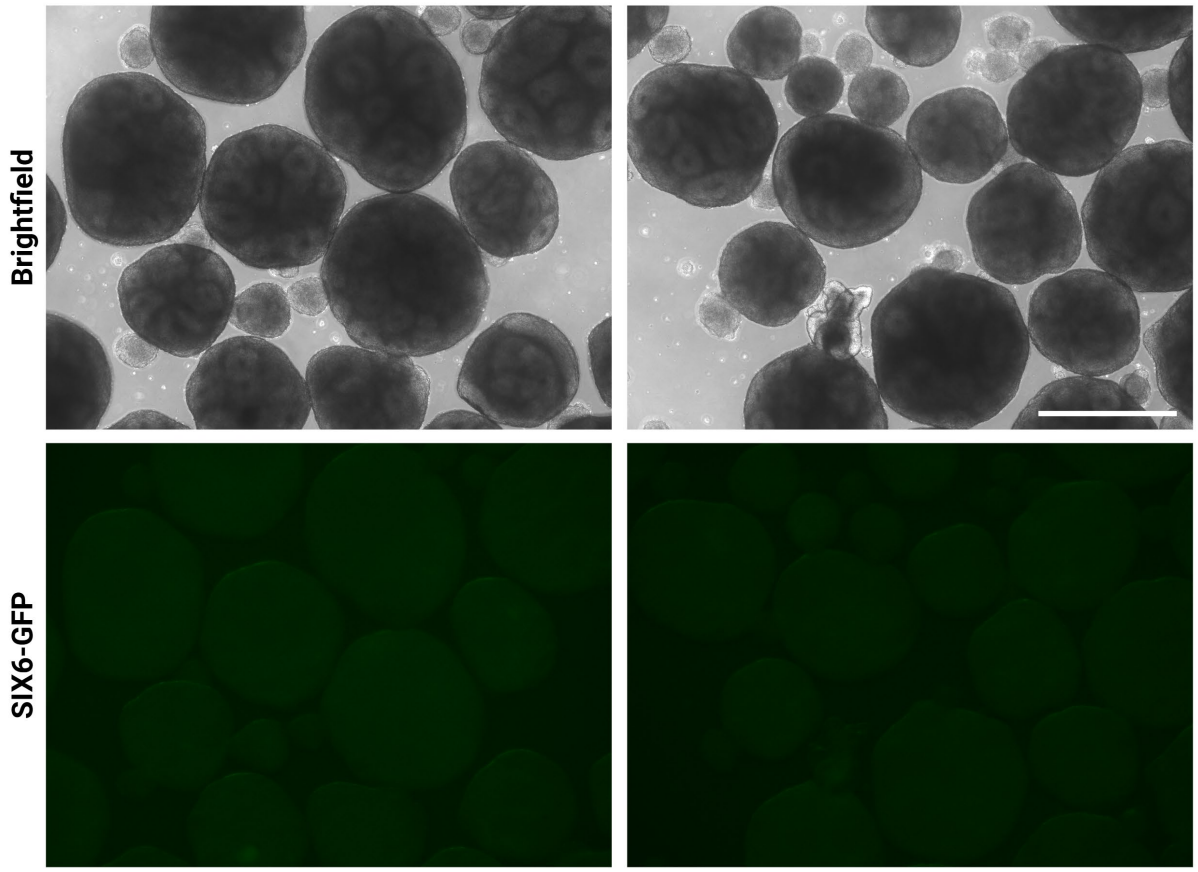

Figure 4.24 Collected brain organoids possess clear typical neural rosette morphology and no expression of SIX6-GFP (Scale bar = 1050 µm).

Collectively, these findings demonstrate that micropatterned substrates provide a valuable tool for guiding the spatial organisation of retinal vesicles. The ability to pattern retinal organoids represents a novel advancement in stem cell biology, offering potential applications in disease modelling, drug screening, and regenerative medicine. Further exploration of the mechanobiological factors influencing vesicle fate, as well as optimising the biochemical conditions of micropatterned cultures, could be critical for advancing this technology towards clinical scalability. These results provide a foundation for future studies investigating how spatial and mechanical cues influence stem cell differentiation and organoid formation, with potential implications for generating more reproducible and clinically relevant retinal tissues. Importantly, the minimal deviations from standard protocols—including retaining the same culture vessel, cell media, and seeding density—provide substantial advantages due to the

resulting equivalence of the produced vesicle structures to those produced in non-micropatterned cultures.

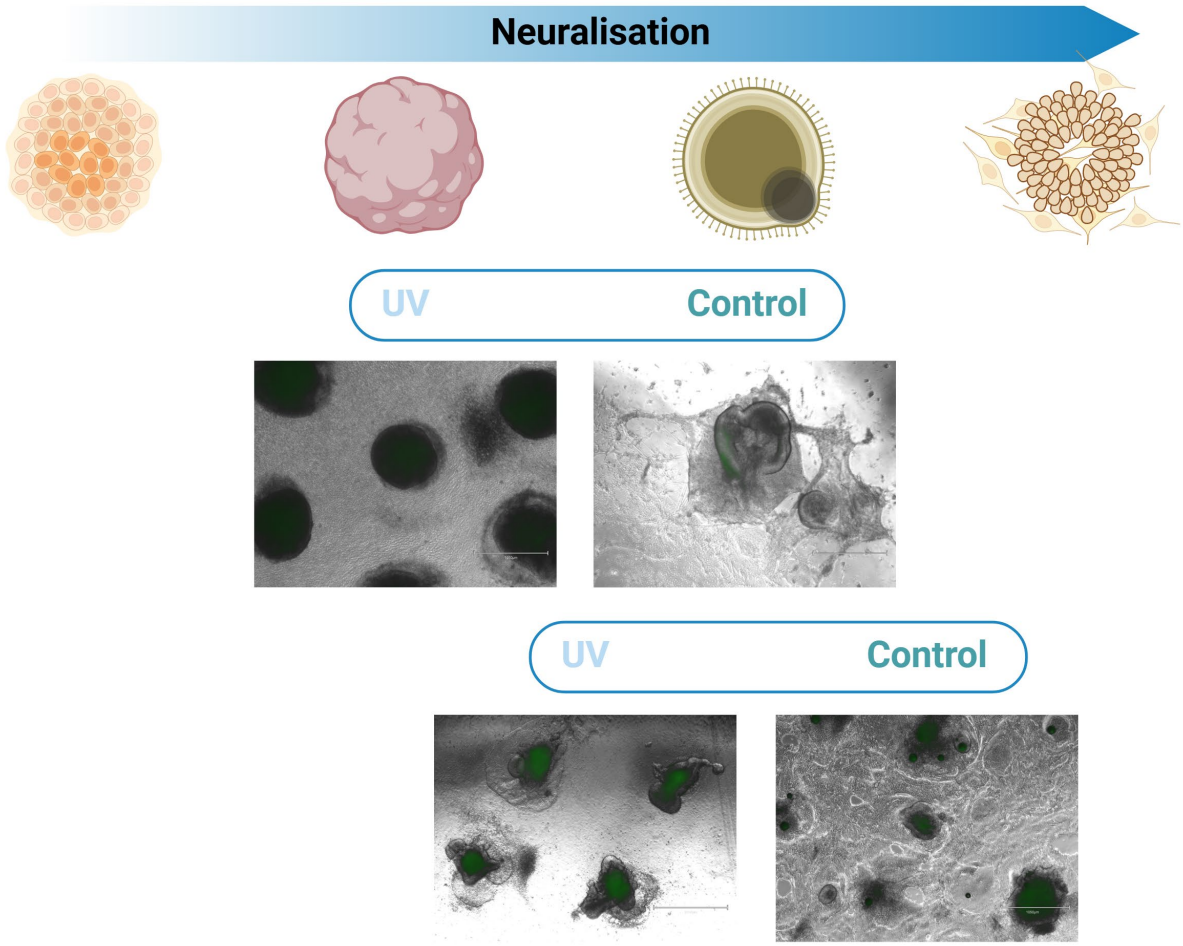

Figure 4.25 Preliminary schematic of the proposed effect of micropatterning-induced spatial confinement on the differential specification of forebrain and retinal fates. Micropatterning may have the capacity to better control the degree or distribution of neuralisation within a culture plate. Control cultures that formed well-defined retinal vesicles resulted in brain organoids in the paired micropatterned condition, while control cultures that formed highly neuralised morphologies resulted in well-defined retinal vesicles in the paired micropatterned condition. As such, spatial confinement may result in well-organised neural morphologies by creating concentrated signalling centres. Created with BioRender.com.

4.3.6 Validation and quantification of retinal organoids grown on micropatterned tissue culture plastic

The primary objective of this study was to evaluate the efficacy of micropatterned cultures in generating retinal vesicles with comparable morphological, molecular, and spatial characteristics to those generated using standard protocols. Success was defined by three key criteria: (1) the ability to produce retinal vesicles indistinguishable from those formed in standard cultures, based on brightfield imaging and neuroepithelial border formation; (2) the expression of the eye field marker SIX6, evidenced by GFP expression and fluorescent imaging; and (3) the capacity to spatially control vesicle growth for potential automation. These criteria were successfully validated above, supporting the suitability of micropatterning for retinal organoid differentiation. However, to advance the scalability of retinal organoid generation, quantification of vesicle numbers and GFP+ regions was necessary to examine both the reproducibility and potential for automation in this system.

The use of machine learning-based segmentation and quantification tools enabled precise and high-throughput analysis of vesicle and GFP+ regions across multiple cell lines. A commercially available platform (IN Carta SINAP, Molecular Devices) was used to achieve this. The algorithm in the platform was trained to create a model that effectively segmented vesicles based on neuroepithelial borders visible in brightfield images and identified GFP+ regions from fluorescent images (Figure 4.26). It is important to note that GFP-based segmentation collectively included self-organised retinal vesicles or overly neuralised tissue patches due to the higher GFP signal in these areas (Figure 4.27). This indicated that the model was sensitive enough to distinguish high-intensity signals associated with proper eye field specification from more diffuse, lower-intensity GFP signals that were apparent throughout the

culture well. Figure 4.28 illustrates a time course of a micropatterned culture, demonstrating the increasing identification of vesicle structures over a one-month period.

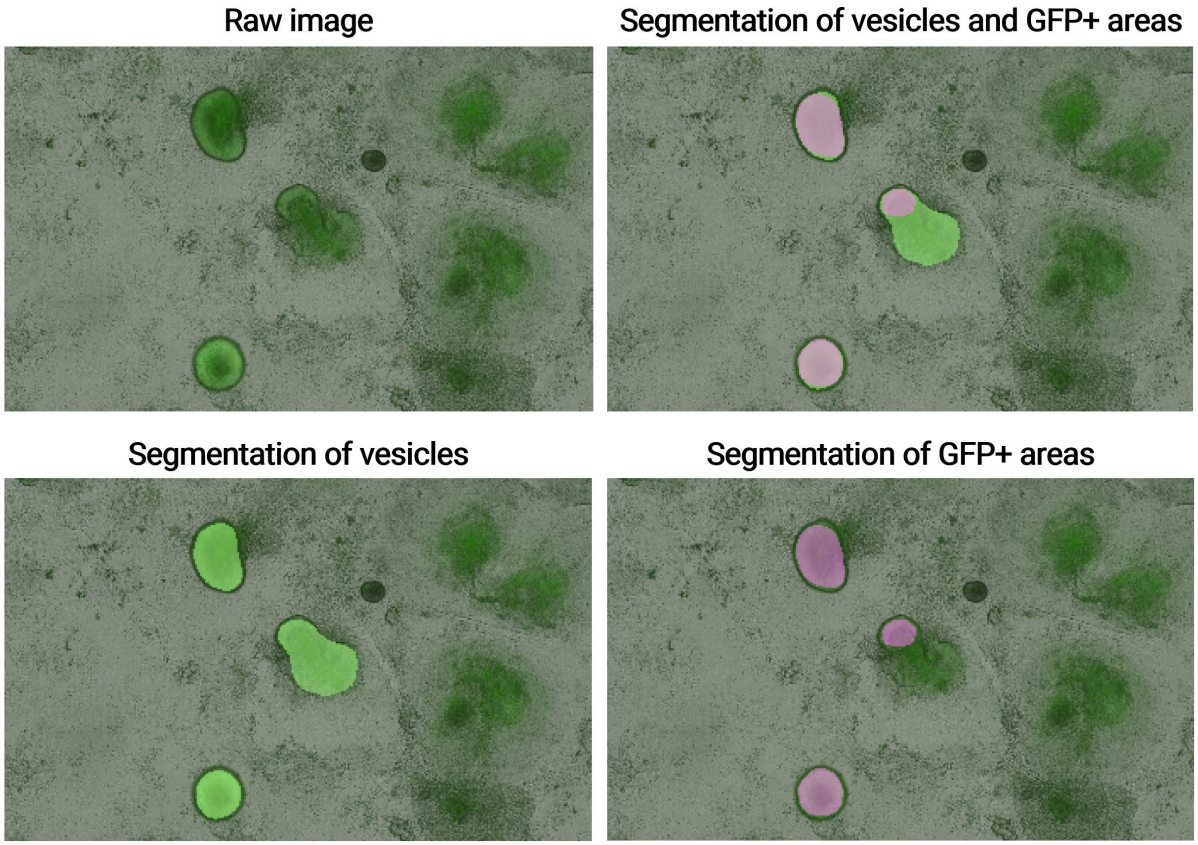

Figure 4.26 Representative images showcasing machine learning-based segmentation of 3D vesicle structures and SIX6-GFP+ regions on 2D substrates in merged brightfield and GFP image channels.

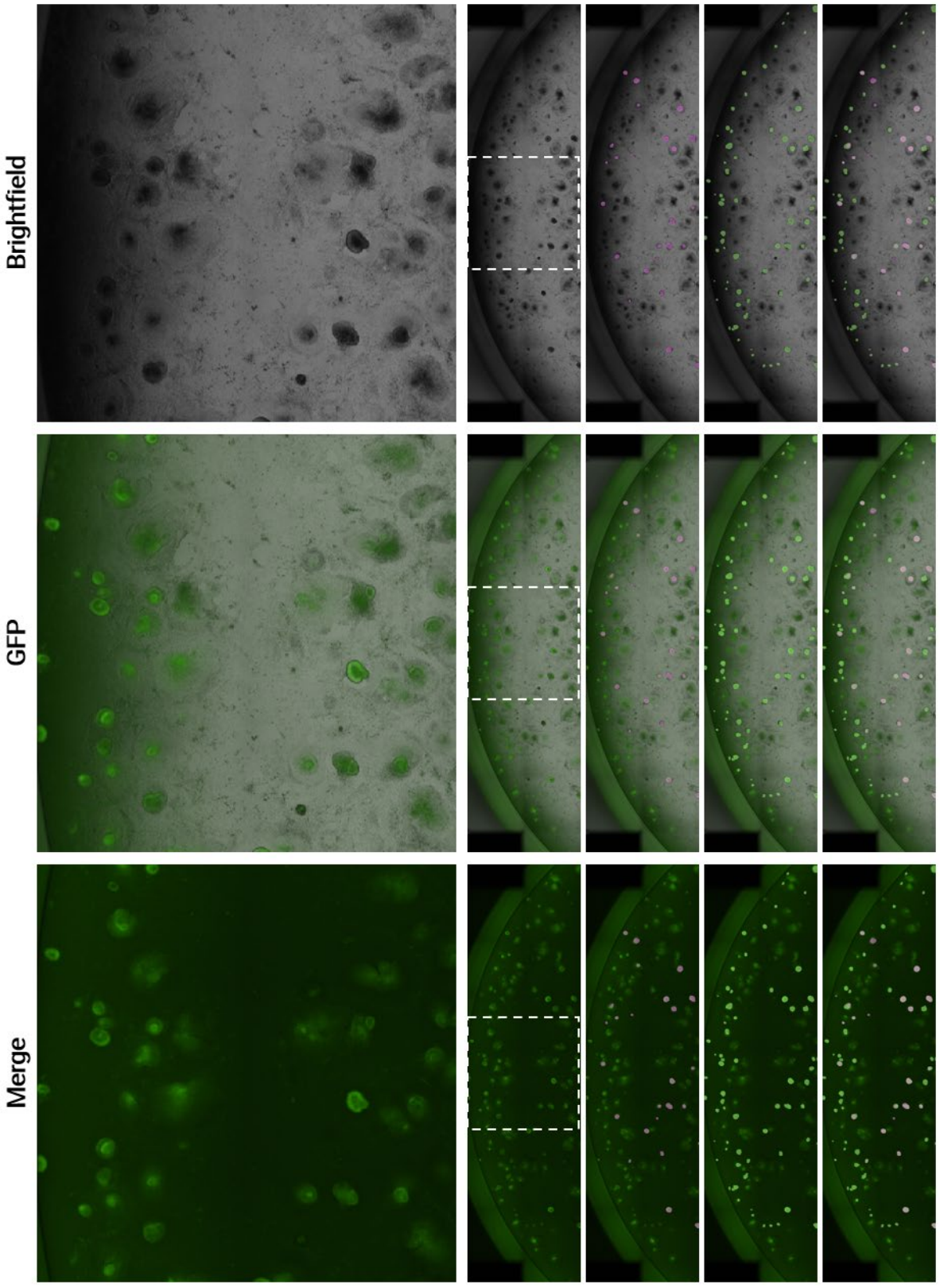

Figure 4.27 The accuracy of segmentation performed by the machine learning model is dependent on the location of the well plate.

(Left to right) Screenshot of a zoomed in region of the well plate showing retinal vesicles; a zoomed-out region of the well plate; the segmentation mask created using only the bright field channel (pink); the segmentation mask created using on the GFP channel (green); and a merged image of both of the segmentation masks showing full coverage of all vesicles. Vesicles at the edges of the well were occasionally missed by the model when only the bright field channel was used, as indicated by the pink mask. All well-defined vesicles were captured when the GFP channel was utilised, as indicated by the green mask.

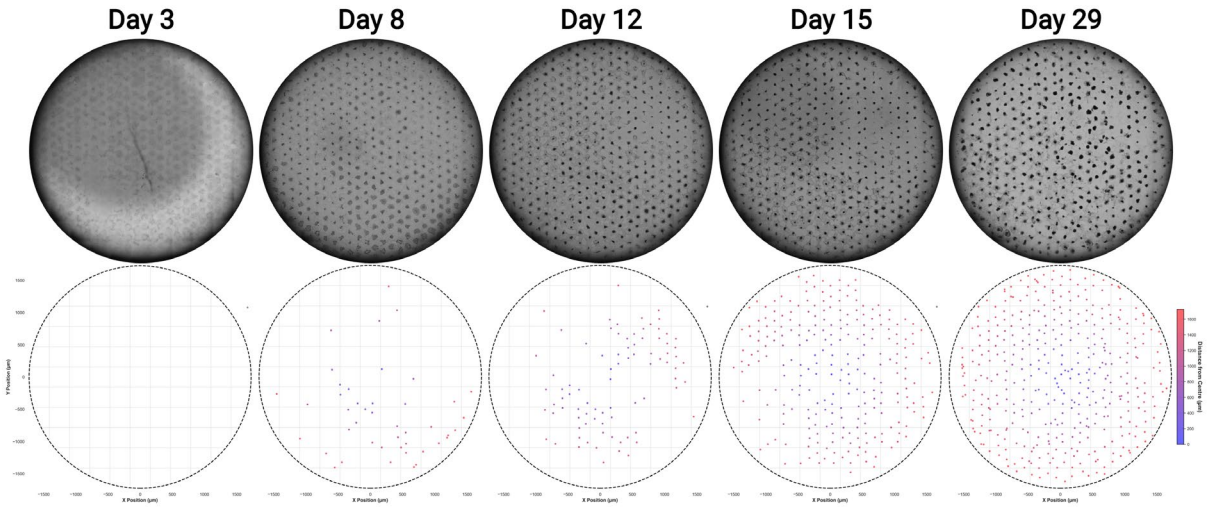

Figure 4.28 Representative images of micropatterned culture over time (top) and the plotted location of identified vesicle structures through the trained model (bottom).

For the EP1 cell line, micropatterning caused an insignificant increase in the number of SIX-GFP+ regions identified (86 areas ± 40.71) when compared to control cultures (70 areas ± 51.95) (Figure 4.29a, N = 4 independent batches). However, the distribution of data was minorly reduced in micropatterned cultures of the EP1 cell line. This could suggest enhanced uniformity in the differentiation process, which may reflect greater control over cell positioning and growth provided by the micropatterned substrate. Interestingly, the maximal number of GFP+ regions was similar between micropatterned and control samples. This suggests that while micropatterning could improve the consistency of differentiation into eye field-like regions, it did not increase the overall potential for the generation of GFP+ areas. A similar

insignificant increase was observed in the IMR90 cell line, where micropatterned cultures produced an average of 226 GFP+ areas (± 84.36) compared to 195 areas (± 111.89) in controls (Figure 4.29b, N = 10 independent batches).

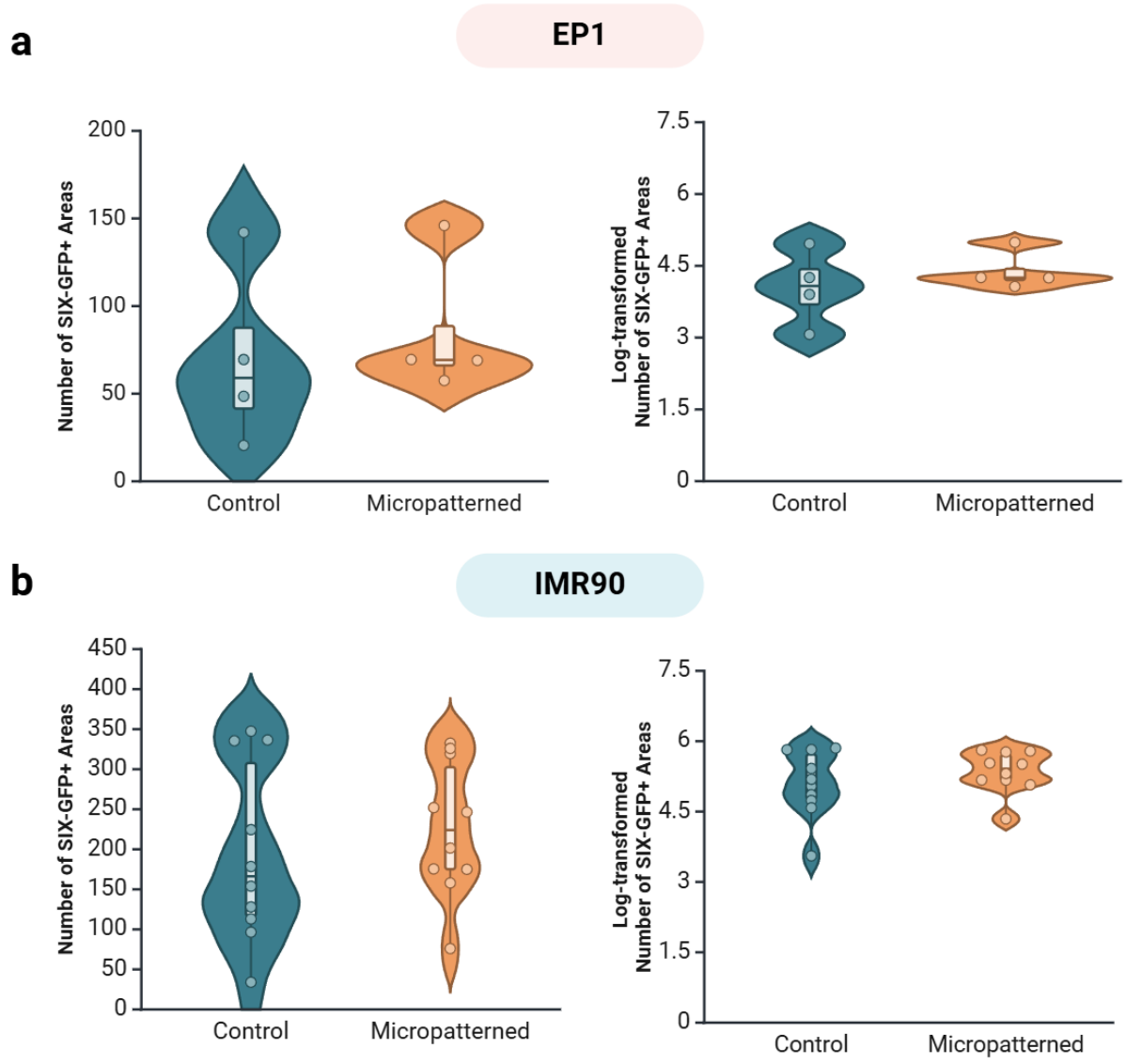

Figure 4.29 Quantification of GFP+ areas within micropatterned cultures in the SIX6-GFP reporter cell lines after 4 weeks of differentiation.

(a) Micropatterning increased the minimum number of GFP+ areas generated in the EP1 cell line (N = 4 independent batches). (b) Micropatterning did not significantly affect the number of GFP+ areas in the IMR90 cell line (N = 10 independent batches).

Interestingly, the consistent finding of a higher minimum number of GFP+ regions in the micropatterned cultures indicates that micropatterning enhances the likelihood of successful eye field specification. This is particularly significant given the stochastic nature of stem cell differentiation, where variability between replicates is a well-documented challenge. Log transformation of all data was performed to reduce skewness and improve the visualisation of data with high distributions, further confirming reduced variability—although not significant—between micropatterned samples compared to control cultures (Figure 4.29).

The reduction in variability in micropatterned cultures may result from the enhanced control of cell spatial organisation, which has been shown in other studies to influence cell fate decisions and improve reproducibility[153]. In standard cultures, cells are subject to random interactions, leading to varied differentiation outcomes, whereas micropatterning allows for a more consistent microenvironment, which may promote uniform signalling and differentiation cues. These results suggest that micropatterning provides a microenvironment conducive to reducing some of the inherent variability in organoid cultures, which has important implications for improving reproducibility in stem cell-derived organoid systems.

To further evaluate the impact of micropatterning on differentiation, fold-change analysis normalised to control samples was performed (Figure 4.30). For the EP1 cell line, the fold-change in the number of GFP+ regions showed high variability, with two biological replicates performing worse than controls, while one performed equally, and one exceeded its paired control by over 7-fold (Figure 4.30a, $p > 0.05$). This inconsistency again highlights the inherent stochasticity of different stem cell lines and underscores that specific micropatterned systems—for example, varied diameters and spacing—will have to be tested and optimised for each cell line. The IMR90 cell line, in contrast, demonstrated a more consistent increase in GFP+ regions in micropatterned cultures, although variability between replicates remained high (Figure

4.30b). The observed variability could be due to the inherent differences between cell lines in their responsiveness to micropatterning, as well as the partially spontaneous nature of self-organisation in organoid formation within 2D cultures.

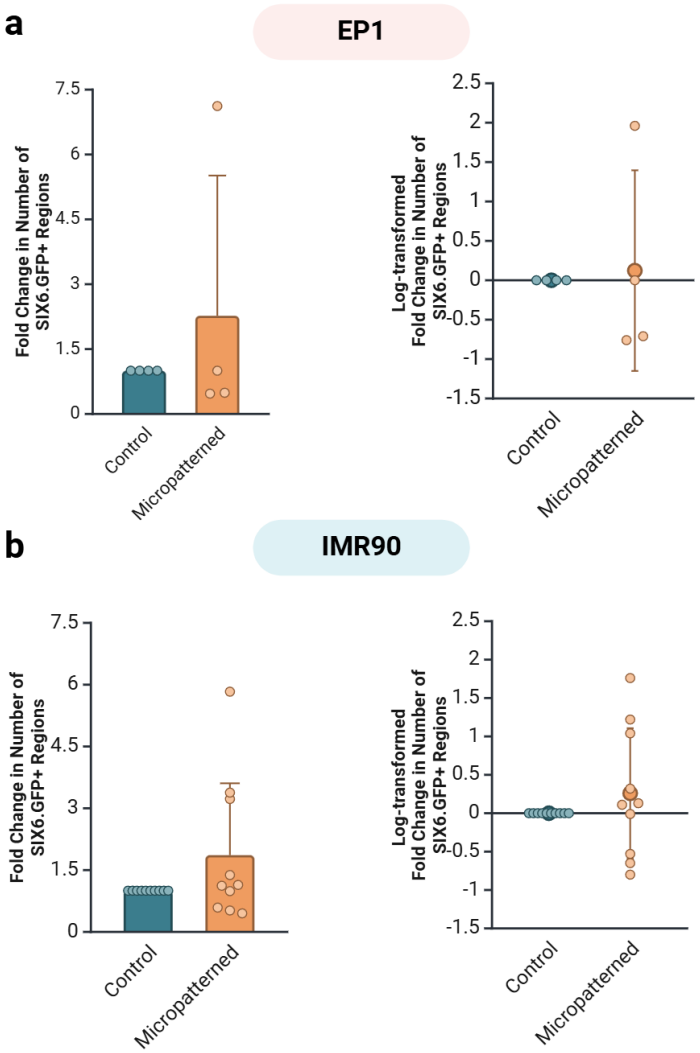

Figure 4.30 Quantification of the fold-change in GFP+ areas within paired samples of micropatterned and non-micropatterned cultures in the SIX6-GFP reporter cell lines after 4 weeks of differentiation.

(a) Micropatterning revealed highly variable effects in paired cultures of the EP1 cell line (N = 4 independent batches). (b) Micropatterning improved the number of GFP+ regions in most batches of the IMR90 cell line (N = 10 independent batches).

The lack of a statistically significant increase in GFP+ regions in micropatterned cultures relative to controls likely reflects the relatively high baseline number of GFP regions in control cultures. This demonstrates that our control cultures differentiate well towards eye field regions that might or might not develop into 3D vesicles. As observed in Chapter 3, the number of GFP+ regions does not necessarily correlate with the formation of mature retinal vesicles. Thus, to better assess the efficacy of micropatterning in promoting organised retinal vesicle formation, we performed an independent quantification of vesicles based on brightfield imaging.

Quantification of retinal vesicle structures was performed across the EP1, IMR90, and HOIK1 cell lines using brightfield imaging, which enabled the identification of vesicles based on the presence of distinct neuroepithelial borders. Similar to above, the number of vesicles generated was highly variable across all cell lines (Figure 4.31). Despite this variability, micropatterned cultures enhanced vesicle formation in all tested cell lines. The EP1 cell line produced a greater mean number of vesicles than controls (Figure 4.31a, n = 30.88 difference in vesicles ± 25.38). This result is particularly noteworthy given that the EP1 line, while forming a high number of GFP+ regions, demonstrated relatively poor capacity for vesicle self-organisation in standard culture conditions. In the IMR90 cell line, micropatterning significantly increased the mean number of vesicles produced, from 106 vesicles (± 96.96) in control cultures to 262.80 vesicles (± 97.53) (Figure 4.31b, p = 0.012). Similarly, micropatterning of the HOIK1 significantly increased the mean number of vesicles generated, from 39 vesicles (± 21.54) in control cultures to 88.38 vesicles (± 44.47) in micropatterned cultures (Figure 4.31c, N = 6 independent batches, p = 0.042). Therefore, micropatterning appears to enhance the ability of the IMR90 and HOIK1 cell lines to form vesicle structures, potentially by providing more spatial organisation and control during the early stages of differentiation.

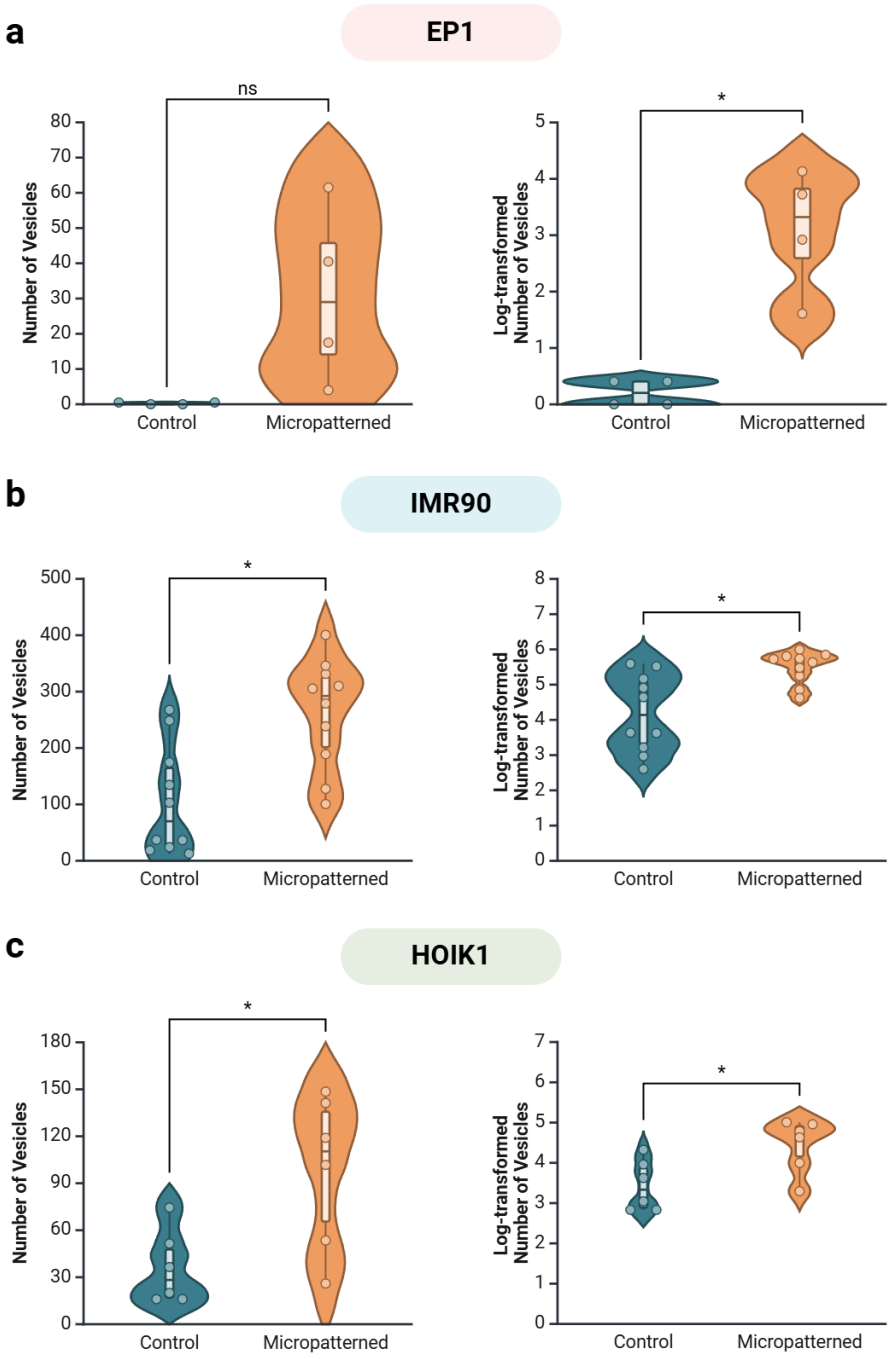

Figure 4.31 Quantification of the number of vesicles produced within micropatterned cultures across three cell lines after 4 weeks of differentiation.

(a) Micropatterning increased the maximum number of vesicles generated using the EP1 cell line (N = 4 independent batches). (b) Micropatterning significantly increased the number of vesicles formed using the (b) IMR90 cell line (N = 10 independent batches, p = 0.012) and (c) HOIK1 cell line (N = 6 independent batches, p = 0.042).

Statistical analysis of log-transformed data demonstrated a statistically significant increase in vesicle formation in micropatterned EP1 cultures (Figure 4.31a, $p = 0.013$), though further biological replicates will better elucidate the effect of micropatterning on this cell line. Due to the poor capacity of control cultures of the EP1 cell line to produce vesicles, the log-transformed micropatterning data is relatively highly distributed in comparison. Moreover, a shift in data distribution towards higher vesicle counts in micropatterned samples is apparent. The broader distribution of vesicle numbers in control cultures, with many samples showing lower vesicle counts, once again suggests that micropatterning may reduce the likelihood of poor differentiation outcomes.

These findings further support the notion that micropatterning may potentially enhance the reproducibility of vesicle formation, at least between biological replicates. The increased number of vesicles in micropatterned cultures may be partially explained by the more uniform microenvironment provided by micropatterning, which could promote more consistent signalling pathways necessary for retinal vesicle formation. Importantly, log transformation of the data for these cell lines revealed a lower variability in micropatterned samples when skewness was accounted for, suggesting that micropatterning not only increases the number of vesicles formed but may also reduce the overall variability in outcomes.

Fold-change analysis of these three cell lines similarly revealed an increase in the mean number of vesicles generated, when directly compared to paired control samples (Figure 4.32, $p > 0.05$). However, the high variability between cultures meant that these results were not statistically significant. Log-transformed fold-change data suggests a strong correlation between micropatterning and an increased number of vesicles generated when skewness is accounted for, though techniques to reduce the overall variability between cultures batches will be critical in elucidating conclusive results.

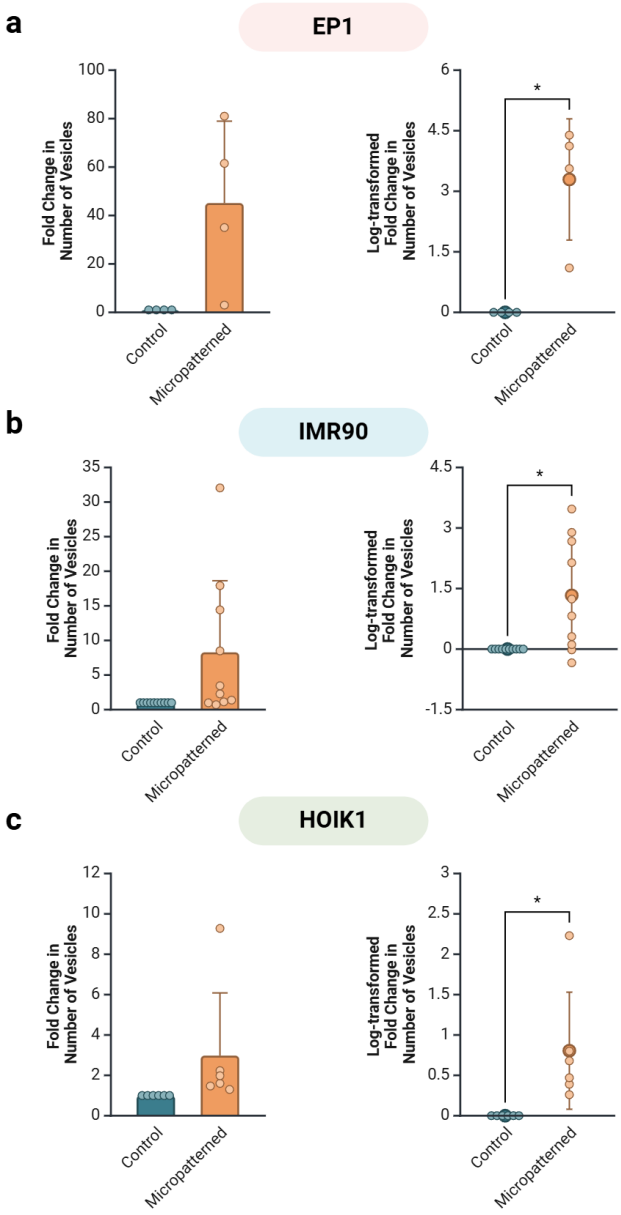

Figure 4.32 Quantification of the fold-change in the number of vesicles produced within paired samples of micropatterned and non-micropatterned cultures across three cell lines after 4 weeks of differentiation.

Compared to control samples, micropatterning increased the number of vesicles generated within all replicates grown from the (a) EP1 cell line (N = 4 independent batches) and (c) HOIK1 cell line (N = 6 independent batches). (b) Micropatterning increased the number of vesicles formed using the IMR90 cell line in all but two replicates (N = 10 independent batches).

Collectively, these results demonstrate that micropatterning may improve both the consistency and efficiency of retinal vesicle formation, with significant implications for the scalability of organoid production. While micropatterning does not appear to increase the maximum potential for GFP+ regions to form, it does appear to increase the maximum potential for the number of vesicle structures formed. Moreover, it may enhance the likelihood of successful differentiation by reducing variability and increasing the minimum number of vesicles produced. This is particularly relevant given the ongoing challenges in the stem cell field, where reproducibility remains a major barrier to large-scale organoid production.

Moreover, the controlled spatial organisation of vesicle formation afforded by micropatterning is highly advantageous for automation. The ability to localise vesicle growth to predetermined regions simplifies downstream processes, such as automated vesicle retrieval, which is critical for scaling up production. The spatial consistency provided by micropatterning ensures that vesicles are more easily accessible for extraction, potentially enabling the integration of automated systems for vesicle selection, culture maintenance, and differentiation monitoring. However, further optimisation is required to address the detachment of micropatterned colonies during media changes, which poses a challenge for long-term culture maintenance. Robotic liquid handling systems that retain vesicles—particularly through the controlled and gentle deposition of liquids during media changes—could provide a solution, ensuring greater consistency across replicates and improving the overall robustness of the culture system.

4.4 Conclusion

We have successfully developed a micropatterning technique that can define initial regions of cell attachment and possess the capacity for regrowth of cells onto areas of denatured Geltrex over time. TCP has never been patterned through a photomask and UV light method without the need for an external polymer or chemical washing steps. Critically, this method does not introduce a glass coverslip, polymer stamp, or other chemical or material to the tissue culture apparatus, which is common in most current micropatterning methods. As such, the sterility of the TCP is maintained from start to finish. In fact, exposure to UV light further sterilises TCP surfaces, minimising potential contamination. Our technology offers a GMP-friendly process for the differentiation of retinal tissues, enabling facile prediction of areas in which vesicles will grow. We show that cells can be maintained long-term (over one month) on these patterned substrates without substantially altering differentiation protocols. We anticipate that this technology will be compatible with any type of cell that is supported by peptide coatings on tissue culture surfaces, including stem cells and differentiated cell lines. We similarly anticipate that any protocol that uses the adherent culture of cells can be translated towards our method. For example, cardiac organoids that grow in confined cultures[182]. Most importantly, micropatterning commonly spatially confines cells for the entire duration of culture. Here, cells have the potential to grow beyond the confines of the pattern, dependent on the pattern size and spacing, degree of UV exposure, and behaviour of the cell or tissue under investigation. For example, cells undergoing differentiation may have a greater potential to migrate beyond micropatterned areas compared to terminally differentiated cells. This phenomenon has been poorly characterised in literature. Further improvements in automated handling and vesicle retention will be key to realising the full potential of micropatterning for large-scale applications.

Chapter 5:
Biochemical modulation of pluripotent stem cell cultures to enhance the formation of neuroretinal vesicles

5.1 Introduction

The specification of the eye field is a highly regulated process governed by the interplay of multiple transcription factors and signalling pathways. Among these transcription factors, PAX6 and SIX6 are particularly notable for their essential roles in retinal development. As explored in Chapter 3, PAX6 is a key regulator of eye development, and its interaction with other factors, such as SIX6, is critical for the proper formation of retinal structures. Our previous work demonstrated that the successful formation of retinal vesicles from confluent monolayers of iPSCs depends not only on the expression of SIX6 but also on the ability of cells to self-organise into stratified, organised tissues—a process involving morphogenetic movements that mimic *in vivo* optic cup formation. Despite the presence of eye field SIX6-GFP in various regions within the monolayer some of these areas fail to form a 3D retinal organoid, highlighting the importance of both molecular cues and morphogenesis in this process.

The formation of the human optic cup and its subsequent differentiation into retinal tissues involves several well-characterised signalling pathways, including Bone Morphogenetic Protein 4 (BMP4), Transforming Growth Factor-β (TGF-β), Sonic hedgehog (SHH), and WNT signalling[93]. These pathways are temporally and spatially regulated, playing critical roles in guiding early retinal morphogenesis. Notably, many retinal organoid differentiation protocols focus on modulating these pathways to enhance the efficiency[99], fidelity[53], and reproducibility[213] of retinal tissue generation, addressing the inherent variability observed in stem cell cultures. Inconsistent differentiation efficiencies often arise from this variability, which can hinder the reliable production of retinal organoids *in vitro*.

However, much of this established work has been performed in protocols that are initiated from 3D aggregates. Our current focus on generating retinal organoids from 2D confluent monolayers presents a critical difference in initial culture state compared to 3D protocols. This distinction is particularly significant as it may influence the spatial distribution of signalling molecules and cell-cell interactions, potentially altering the microenvironment crucial for retinal specification.

In addition to these established pathways, there are others known to be involved in retinal differentiation that have not been extensively studied in the context of early eye field and retinal vesicle formation. Pathways such as Retinoic Acid (RA), while explored in the later stages of retinal organoid maturation[46], remain underexplored in early retinal vesicle generation. Understanding how these pathways influence the early stages of retinal development could provide novel insights into improving differentiation efficiency and tissue morphology during the formation of retinal vesicles.

In this study, we aimed to improve the differentiation efficiency of retinal vesicles derived from confluent monolayers of iPSCs by biochemically modulating various signalling pathways. To minimise potential variability caused by our previous micropatterning technique, we primarily characterise these effects using our standard protocol without spatial confinement. Our approach used established protocols that typically utilise 3D embryoid body cultures, translating them into our 2D confluent monolayer system to optimise the conditions for generating retinal vesicles in a more controlled and reproducible manner. Additionally, modulation of pathways implicated in eye field specification, with a particular focus on the RA signalling pathway, was performed. Importantly, as it is challenging to quantitatively characterise the complexity of our 2D monolayer platform—beyond counting the number of

vesicles generated—the assessment of gross morphological features within the culture well is critical.

Next, we sought to combine a selection of these biochemical modulation strategies with our previously developed spatial patterning protocol. This combination will allow us to evaluate whether the efficiency of differentiation and/or the morphological characteristics of retinal vesicles can be further enhanced. To ensure the translational potential of our work, we focus on the use of GMP-friendly compounds, such as small molecules, rather than relying on animal-derived growth factors. This approach aligns with our broader goal of developing clinically relevant methods for retinal tissue generation, with the potential to advance regenerative therapies for retinal diseases.

5.2 Experimental Section

5.2.1 Materials and procedures

Three iPSC lines were utilised in this study, as previously described in Chapter 3 and 4: HOIK1[197], and EP1.SIX6-GFP and IMR90.SIX6-GFP reporter iPSC lines[103].

5.2.2 Maintenance of iPSC lines and neural differentiation

iPSCs were cultured and differentiated as described previously in Chapter 3, according to our established protocol[46]. Biochemical modulation was performed according to Table 5.1 and Figure 5.1 by supplementing differentiation media with fixed concentrations of small molecules or factors (5 µM SB431542, Stem Cell Technologies 100-1051; 300 nM SAG, Cayman 11914; 3 µM IWR-1e, Cayman 13659; 1 µM all-*trans*-RA, Sigma R2625). For micropatterned substrates, iPSCs were cultured as described previously in Chapter 4.

Table 5.1 Treatments applied to retinal differentiation protocol

Description	Treatment	Timepoints (inclusive)
Preconditioning[99]	SB431542 + SAG	Day 0
	SAG	Day 1
Timed media treatment (WNT and SHH)[103]	IWR-1e	Day 1 – 7
	SAG	Day 8 – 14
E8 Pulse	E8 media	Day 2 – 3
Intermediate RA	all-*trans*-RA	Day 10 – 16
Late RA	all-*trans*-RA	Day 14 – 20
Early RA	all-*trans*-RA	Day 6 – 12

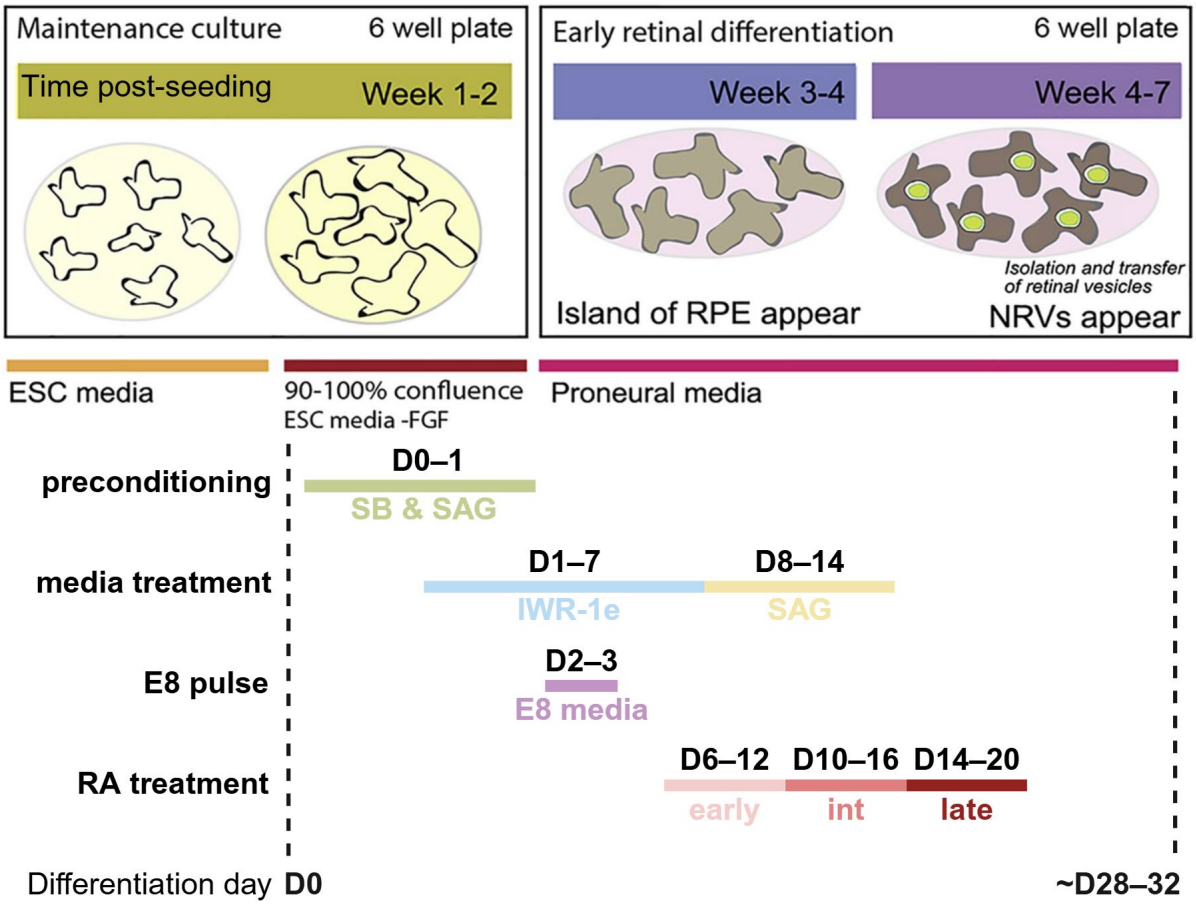

Figure 5.1 Schematic overview of the timeline of trialled biochemical modulation treatments relative to Differentiations days.

5.2.3 Imaging and quantification of culture plates

Imaging and quantification were performed as described previously in Chapter 4. Briefly, images of cultures wells were captured using the ImageXpress HT.ai system (Molecular Devices) and analysed with a trained machine learning model using IN Carta software (Molecular Devices).

5.2.4 Statistical Analysis

The number of independent samples performed for each cell line is stated throughout the results and figure legends. Experiments were performed in duplicate wells (n = 2) for each independent batch and averaged. All treatments were performed in parallel with non-treated control

cultures. Paired t-tests with control cultures were performed for samples with one treatment group, and one-way ANOVA with Tukey's method for multiple comparisons was performed for samples with two treatment groups (not significant "n.s." $p > 0.05$, or significant: $*p < 0.05$, $**p < 0.01$, $***p < 0.001$).

qPCR experiments were performed with GAPDH as the housekeeping gene. The specific primers used are detailed in Table 5.2. For qPCR fold-change analysis, the ΔCt value of the IMR90 cell line early passage group was averaged and used as the reference sample. Quantification was performed using the ΔΔCt method. To calculate outliers for passage groups, the interquartile range was used, where the upper bound = $Q3 + 1.5 \times IQR$.

Table 5.2 Primer designs for qPCR experiments

Gene	Forward / Reverse	NCBI Reference Sequence
TGF-β	5'- GGAAATTGAGGGCTTTCGCC -3' 5'- CCGGTAGTGAACCCGTTGAT -3'	NM_000660.7
Nodal	5'- GCATACATCCAGAGTCTGCT -3' 5'- CACATACAGCATGCTCAGC -3'	NM_018055.5
SHH	5'- CAAGCTGGTGAAGGACCTGA -3' 5'- CGGTCCAGGAAAGTGAGGAA -3'	NM_000193.4
WNT3A	5'- AGATTGGCATCCAGGAGTG -3' 5'- CTCCCTGGTAGCTTTGTCC -3'	NM_033131.4
GAPDH	5'- AAGCTCATTTCCTGGTATGACAAC -3' 5'- TGGTCCAGGGGTCTTACTCC -3'	NM_002046.7

5.3 Results and Discussion

5.3.1 Preconditioning of 2D confluent cultures through modulation of TGF-β/Nodal and SHH pathways

The inhibition of TGF-β and BMP signalling pathways, known as dual SMAD inhibition, plays a pivotal role in neural differentiation[214]. Recent work has demonstrated the efficacy of TGF-β inhibition in micropatterned cultures to induce reproducible neuroectoderm tissues, particularly through the use of the small molecule SB431542 (SB)[215]. As retinal tissues are derived from neuroectoderm, this approach is especially pertinent to our focus on retinal organogenesis. Several studies have similarly employed TGF-β/Nodal signalling inhibition during early retinal differentiation of hPSC-derived retinal tissues, highlighting the importance of this pathway in eye development. Notably, a protocol that preconditioned 3D iPSC aggregates through a temporary pulse of SB combined with Smoothened Agonist (SAG), an agonist of the Sonic hedgehog pathway (SHH), at the onset of differentiation demonstrated higher efficiency of retinal vesicle formation[99]. Whilst the SHH pathway is known to play broad roles in neural development and eye morphogenesis, its specific role in early retinal organoid differentiation had not been fully elucidated prior to these studies. The combination of TGF-β inhibition and SHH pathway activation suggests a complex interplay between these signalling cascades in early retinal specification.

Therefore, modulation of SB and SAG during our 2D protocol was tested on three iPSC cell lines: HOIK1, EP1, and IMR90. As our cultures initiate from confluent monolayers, we selected the onset of differentiation (day 0: SB and SAG, day 1: SAG only) to precondition our initial cell population. As such, we refer to this specific treatment regimen as preconditioning hereafter. Control wells were cultured in parallel and did not receive supplementation. Our previous studies demonstrated variability in successful retinal organoid generation and spatial

patterning capacity among these cell lines, underscoring the importance of investigating line-specific responses to this preconditioning.

The HOIK1 iPS cell line, which previously showed low capacity for spatial patterning in the micropatterning experiments (Chapter 4, Figure 4.31), was able to form vesicle structures in the preconditioning treatment. As assessed by visible changes in morphology, preconditioning the culture produced rounded, budded retinal vesicles forming by 4 weeks of differentiation (Figure 5.2, N = 7 differentiations). Control wells similarly demonstrated the formation of well-defined retinal vesicles in the majority of replicates (N = 4 differentiations). In these batches, preconditioning resulted in higher tissue heterogeneity, as observed by irregular morphological features and dark neural tissues (Figure 5.2). Nevertheless, the control wells of these cultures similar displayed a high level of morphological features in the background cell population, indicating a less organised differentiation process. The more disorganised background cell population in these cultures might indicate regions that attempted vesicle formation but lacked sufficient upregulation or downregulation of certain signalling pathways, possibly due to stochastic variations in gene expression or local microenvironmental factors. Interestingly, we observed a similar phenomenon in Chapter 4 within the control cultures of the IMR90 iPS cell line, where micropatterning was able to induce a neater background cell population.

In non-treated spontaneously differentiated cultures, endogenous cellular signalling governs cell type specification. Thus, the distribution of signalling factors is most likely dependent on the eye field inducing signalling expression in some cells rather than a homogeneous expression when signalling factors are delivered in the media to all cells. As such, preconditioning of cultures that are already at an optimal initial state for vesicle formation may induce excessive upregulation of neural differentiation pathways, resulting in the dark neural tissues observed.

Interestingly, in some replicates, the control wells showed poor vesicle formation (Figure 5.2, N = 3 differentiations). Interestingly, preconditioned wells within these batches demonstrated a rescue effect, where numerous vesicles could be clearly observed regardless of the poor differentiation of the paired control. As such, within cultures where the control wells did not have sufficient signalling to form vesicles, preconditioning may improve the likelihood of successful vesicle formation by establishing a more permissive epigenetic landscape.

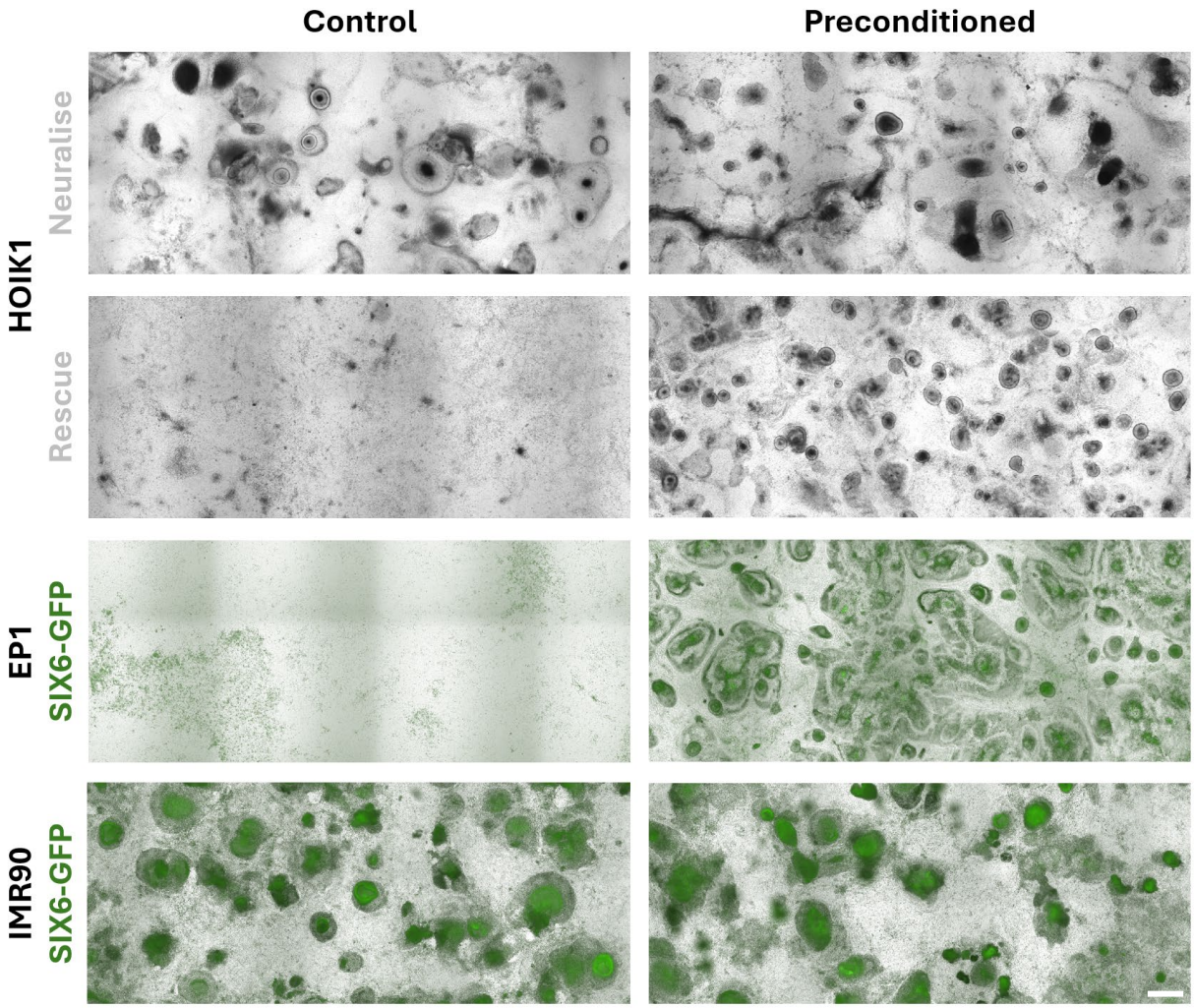

Figure 5.2 Representative images of the capacity of preconditioning treatment to improve retinal differentiation across three cell lines after 4 weeks of differentiation. In the HOIK1 cell line, preconditioning neuralised replicates in which the control cultures produced well-defined vesicles. Alternatively, a rescue effect was observed in both the HOIK1 and EP1 cell line in replicates where the control performed poorly. Preconditioning had a neuralising effect in cultures of the IMR90 cell line. Scale bar = 1000 µm.

The EP1 cultures in control wells demonstrated poor differentiation and cell viability in the majority of replicates (Figure 5.2, N = 3 of 4 differentiation). In one of these batches, preconditioning similarly exhibited a rescue effect, where many morphological features could be observed at the week 4-time point, including the formation of retinal vesicles (Figure 5.2). For the IMR90 cell line, control and preconditioning wells both appeared disorganised, where many poorly formed structures were observed among a few well-defined vesicles (Figure 5.2, N = 5 differentiations). For both SIX6-GFP reporter lines, successful retinal differentiation in the paired control culture often led to an overly neuralised morphology within the preconditioned wells, characterised by heterogeneous and disorganised cultures with rounded tissue islands that did not form retinal vesicles. In some instances, rosette-like tissues formed in these cultures, indicating a shift towards a more general neural fate rather than specific retinal lineages.

Eye field and subsequent retinal vesicle formation occur in the anterior neural plate area of the developing brain as a result of a fine-tuned balance of growth factors. In the artificial environment of differentiation cultures, this decision of neural versus retinal specification is dependent on existing endogenous levels within cells. The presence of GFP+ regions in the SIX6-GFP reporter lines (EP1 and IMR90) confirmed eye field specification, validating the efficacy of the preconditioning approach in initiating retinal differentiation. The addition of SB and SAG at the concentration tested here might be sufficient for some cell lines to generate neural and subsequent retinal tissues; though, for other cell lines, extra supplementation might be too much. Thus, the excessive neuralisation of these cultures, likely caused by TGF-β inhibition, may have hindered the cells' ability to self-organise into retinal vesicles and resulted in all cells differentiating into neural/brain tissue. We speculate that self-organisation involves multiple neural—and possibly non-neural—cell types working synchronously to form retinal

vesicles, reminiscent of the complex tissue interactions observed during *in vivo* eye development. Thus, this observation highlights the delicate balance between promoting neural fate and maintaining the population heterogeneity necessary for proper organoid formation.

When control cultures failed to differentiate or detached from the plate, preconditioning appeared to rescue differentiation by improving cell survival and long-term viability, ultimately allowing for the formation of retinal tissues in a few cases. This rescue effect suggests that preconditioning may enhance cell resilience, possibly through the upregulation of pro-survival pathways or the establishment of a more supportive extracellular matrix through cell deposition and remodelling. Future investigations into the molecular mechanisms underlying this rescue effect could provide valuable insights into strategies for improving the robustness of retinal organoid protocols.

To further elucidate the effects of preconditioning, we quantified vesicle formation across all three cell lines. Preconditioning did not increase the average number of vesicles produced from the HOIK1 cell line across replicates (Figure 5.3a, N = 7 independent batches). Across paired samples, preconditioning increased the number of vesicles generated by an average fold-change of 28.95 (± 68.56), though this change was not significant due to the high variability observed. This high variability is visualised in the log-transformed fold-change analysis, where the magnitude of change from control cultures was inconsistent (Figure 5.3a). This inconsistency may reflect the inherent heterogeneity of iPSC cultures or the presence of unidentified variables affecting differentiation efficiency.

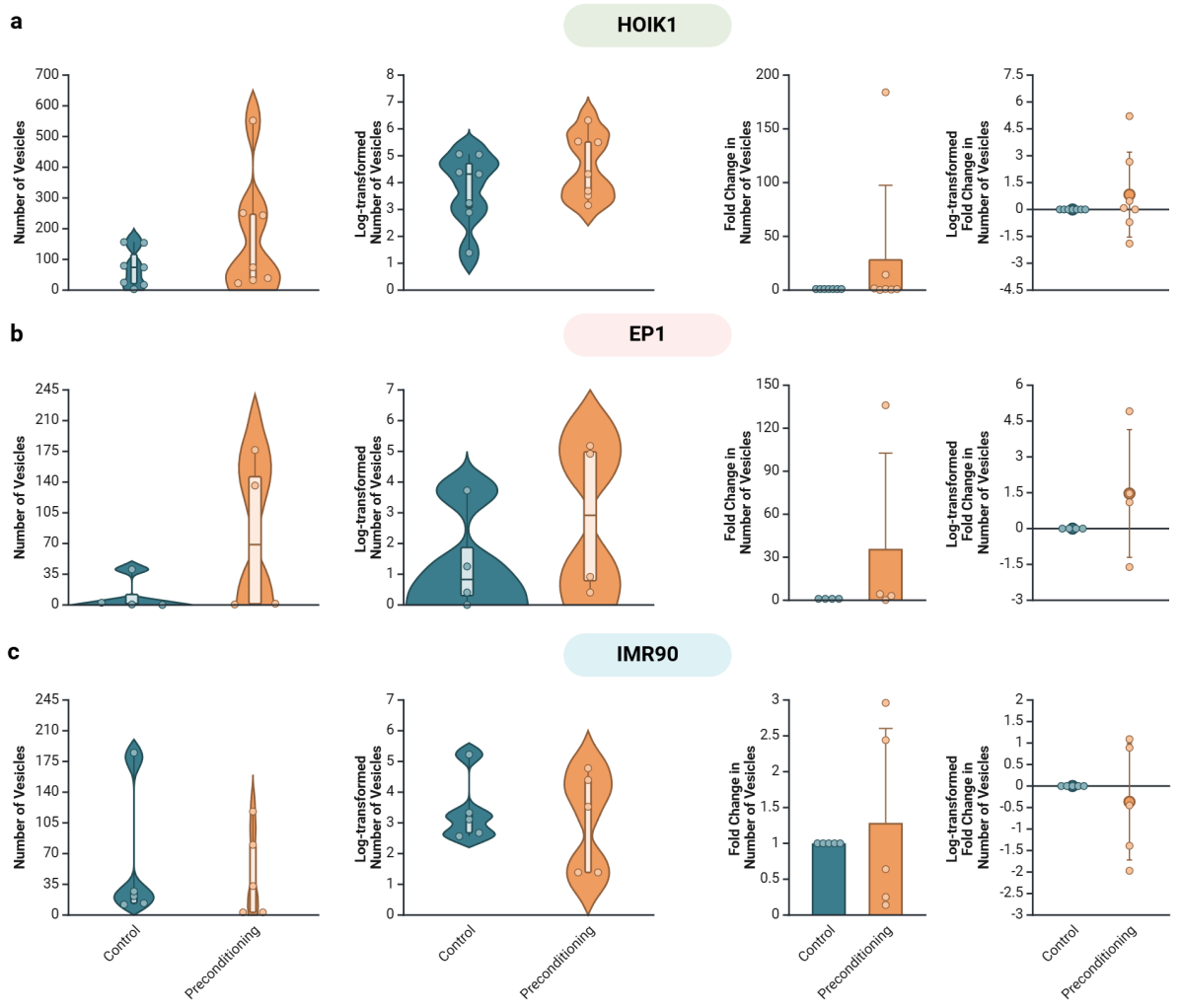

Figure 5.3 Quantification of the average number of vesicles produced (left) and the fold-change within paired samples (right) of preconditioning treated cultures and non-treated controls across three cell lines after 4 weeks of differentiation.

Preconditioning increased the maximum number of vesicles generated using the (a) HOIK1 cell line (Mean ± SD: Control [72.57 ± 63.19], Preconditioning [173.50 ± 193.58]; N = 7 independent batches) and (b) EP1 cell line (Mean ± SD: Control [10.88 ± 19.78], Preconditioning [78.63 ± 91.15]; N = 4 independent batches). (c) Preconditioning did not improve the number of vesicles produced in the majority of cultures from the IMR90 cell line (Mean ± SD: Control [51.80 ± 74.71], Preconditioning [47.40 ± 50.49]; N = 5 independent batches).

Interestingly, raw data suggested preconditioning was most effective when paired controls produced fewer organoids (approx. < 25 vesicles per well on average). This observation

supports the observed rescue effect of preconditioning on suboptimal cultures of the HOIK1 cell line, possibly by providing a stronger initial push towards retinal fate. However, this trend was inconsistent, as evidenced by one replicate experiment where preconditioning enhanced vesicle numbers (by 1.6-fold) in a culture where the paired control produced over 150 organoids on average per well. This inconsistency raises questions about the relationship between initial culture state, preconditioning effects, and ultimate differentiation outcomes and success. As such, preconditioning alone is not sufficient to reduce variability.

For the EP1 cell line, preconditioning increased the overall average number of vesicles generated from 11 vesicles (± 19.78) to 79 vesicles (± 91.15) (Figure 5.3b, N = 4 independent batches). However, it also increased data variability, as indicated by large distributions before and after log transformation. This heightened variability suggests that these lines may be more sensitive to subtle differences in preconditioning or subsequent culture conditions. Across paired samples, an average increased fold-change of 35.89 (± 66.76) was observed in preconditioned cultures.

The overall average number of vesicles generated in the IMR90 cell line was not affected by preconditioning (Figure 5.3c, N = 5 independent batches). Similarly, a non-significant fold-change increase of 1.29 (± 1.32) was observed. From the raw data, no clear trend emerged between organoid production in paired control cultures versus preconditioned cultures for both the EP1 and IMR90 lines, further emphasising the complex and line-dependent nature of the preconditioning effect in 2D confluent monolayer cultures.

Next, SIX6-GFP+ regions within the EP1 and IMR90 cultures were analysed. The EP1 cell line showed a non-significant increase in the mean number of GFP+ areas in treated wells (127 vesicles ± 157.49) when compared to control wells (65 vesicles ± 54.63) (Figure 5.4a). Across

paired samples, preconditioning increased the number of GFP+ areas by a fold-change of 4.95 (± 7.63). Similarly, the IMR90 cell line showed a non-significant increase in the mean number of GFP+ areas in treated wells (591.40 vesicles ± 210.02) when compared to control wells (226 vesicles ± 119.61) (Figure 5.4b), with a fold-change of 3.13 ± 1.74 across paired samples. All replicates of the IMR90 cell line showed an increased number of GFP+ areas under preconditioning treatments, though the magnitude varied considerably across replicates, ranging from a 1.13 to an over 5-fold change. This consistent positive GFP response in IMR90 cultures, despite the variability in magnitude, again indicates that this line may be responsive to preconditioning in a manner where eye field specification is upregulated in the absence of successful vesicle formation.

While data distribution remained increased in the EP1 cell line, the IMR90 cell line showed decreased distribution upon log-transformation of GFP+ area numbers, possibly indicating higher consistency between cultures. This improved consistency in IMR90 cultures could suggest that this line may be more amenable to standardisation of retinal differentiation protocols compared to the EP1 cell line.

These results collectively suggest that preconditioning influences the early processes of eye field formation and not the later period of vesicle generation. Accordingly, the data also show that preconditioning may also have the potential to rescue cultures that would otherwise fail to grow retinal vesicles successfully potentially because these cultures can now form eye field regions. However, the high variability observed between batch-to-batch cultures underscores the need for improved reproducibility through alternative means, such as other signalling manipulation of signalling pathways. The differential responses observed across cell lines highlight the importance of tailoring differentiation protocols to specific genetic or epigenetic

backgrounds, a consideration that has become increasingly important as the field moves towards personalised medicine applications of stem cell-derived tissues.

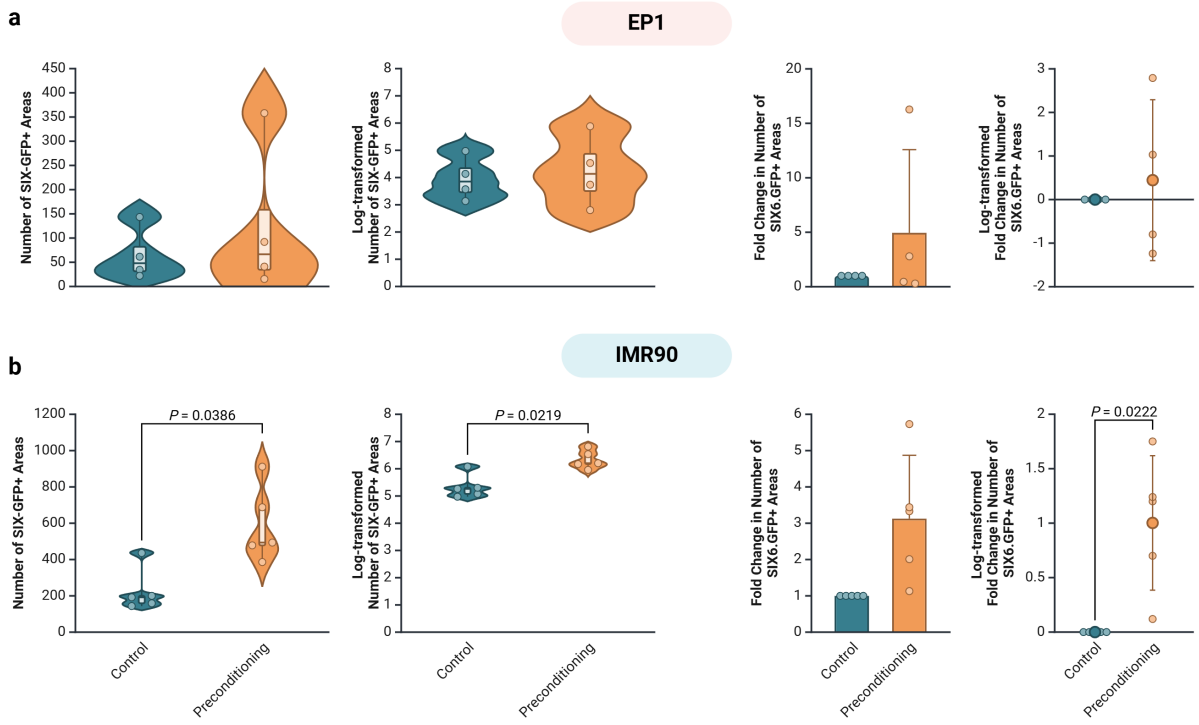

Figure 5.4 Quantification of the average number of GFP+ regions produced (left) and the fold-change within paired samples (right) of preconditioning treated cultures in SIX6-GFP reporter cell lines after 4 weeks of differentiation.

Preconditioning improved the maximum number of GFP+ regions produced in cultures of the (a) EP1 cell lines (Mean ± SD: Control [65.38 ± 54.63], Preconditioning [126.63 ± 157.49]; N = 4 independent batches) and (b) IMR90 cell line (Mean ± SD: Control [226.1 ± 119.61], Preconditioning [591.40 ± 210.02]; N = 5 independent batches).

Future work should focus on elucidating the mechanisms underlying these observed effects and developing strategies to enhance consistency across experiments and cell lines. This could involve detailed transcriptomic and epigenomic profiling of preconditioned versus control cultures to identify key molecular players in successful retinal specification. Additionally, investigating the long-term effects of preconditioning on retinal organoid maturation and functionality could provide valuable insights into optimising protocols for generating high-

quality retinal tissues from human pluripotent stem cells. The observed variability in response to preconditioning raises important questions about the nature of cellular competence in retinal differentiation. Future studies could explore whether this variability is due to intrinsic heterogeneity within iPSC populations or extrinsic factors in the culture environment. Single-cell analyses of preconditioned cultures could reveal whether preconditioning creates a more homogeneous starting population or simply shifts the proportions of pre-existing subpopulations.

Our study demonstrates the potential of preconditioning 2D iPSC cultures for enhanced retinal organoid formation, while also highlighting the complexities and challenges inherent in translating 3D protocols to 2D systems.

5.3.2 Long-term treatment of cultures through timed WNT inhibition and SHH activation

Supplementation of neural induction media is a well-established method for enhancing retinal differentiation success and forms the basis of most retinal organoid protocols. Notably, recent work has demonstrated the improved generation of SIX6-GFP positive retinal vesicles from 3D embryoid bodies through the timed inhibition of WNT signalling followed by upregulation of SHH signalling[103]. This was achieved by supplementing the growth media with IWR-1-endo (IWR), a WNT inhibitor, during week 1 of differentiation and SAG during week 2. Our study aimed to translate these 3D-based protocols to 2D confluent monolayer platforms, characterising the effects on morphology and vesicle formation efficiency.

We assessed gross morphology and quantified the number of vesicles and GFP+ areas produced within cultures supplemented with timed media treatments of IWR at days 1 – 7 followed by SAG at days 8 – 14. The morphology of cells was evaluated after 4 weeks in culture for the formation of SIX6-GFP+ areas, vesicles, and other features of the differentiating plate.

At week 4, HOIK1 iPS cell-derived cultures showed less background cell population (non-retinal tissues) upon timed media treatment with IWR and SAG compared to control cultures (Figure 5.5, N = 7 independent batches). Vesicle formation was evident in both cultures, though the treated wells appeared more clearly organised. This improved organisation could indicate a more synchronised differentiation process, potentially due to the timed modulation of WNT and SHH signalling creating a favourable signalling environment within specific regions of emerging tissues across the culture. Similar to the preconditioning effect, this occurrence may also be the result of more efficient self-assembly of retinal vesicles through the reduction of competing differentiation trajectories in the background population.

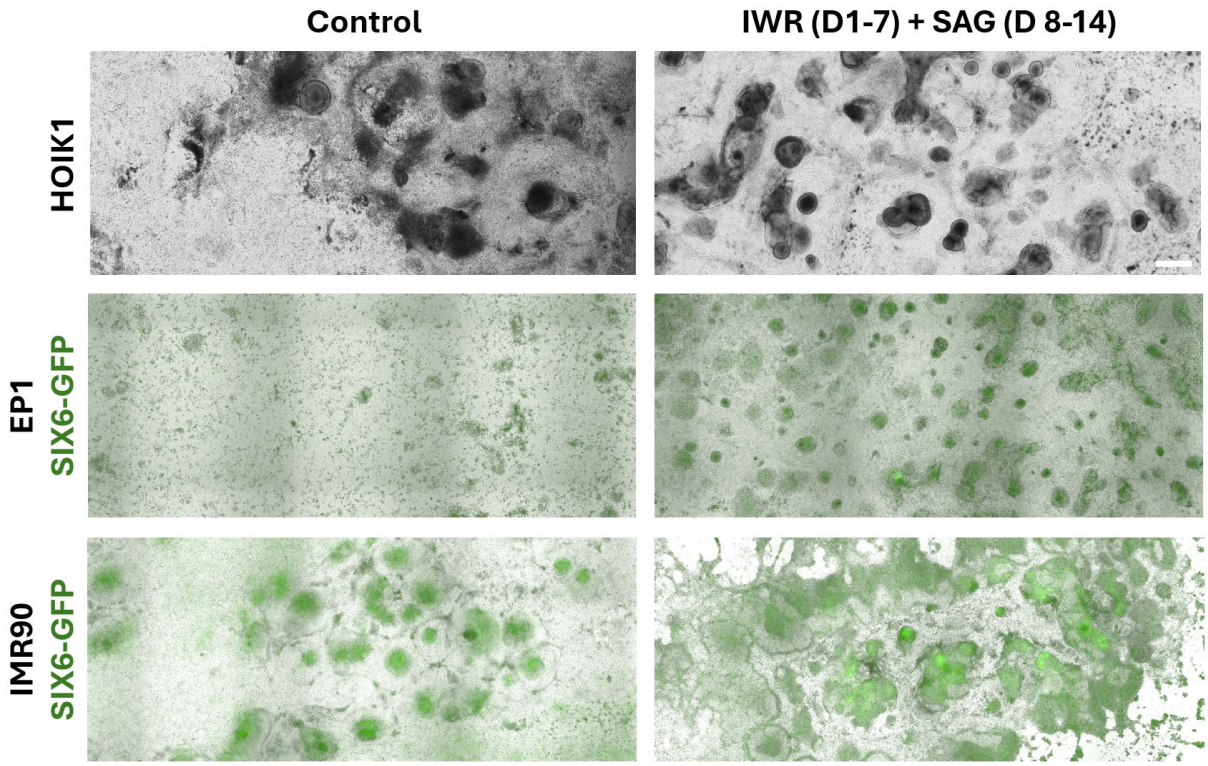

Figure 5.5 Representative images of the capacity of IWR and SAG timed media treatment to improve retinal differentiation across three cell lines after 4 weeks of differentiation.

IWR and SAG treatment had the capacity to improve the morphological features, including tissue organisation and vesicle formation, within cultures of the HOIK1 and EP1 cell line. However, the treatment caused cultures of the IMR90 cell line to become overly neuralised. Scale bar = 1000 µm.

Conversely, the EP1 cell line cultures showed an overall poor vesicle efficiency formation in both control and treated wells across replicate experiments (Figure 5.5, N = 2 independent batches). From morphology alone, a high level of immature neural structures was apparent in the treated cultures, where most regions failed to form well-defined vesicles. The control cultures, in particular, showed regions of poor cell attachment and lack of tissue organisation, suggesting that this line may be particularly sensitive to neural induction cues or may require additional factors to support survival. As such, we note that the initial state of these cells may have been suboptimal, resulting in unreliable findings—particularly as we have previously

observed in Chapter 4 that this particular cell line has the potential to form vesicles under different conditions. Due to the poor efficiency of the EP1 cell line after two replicates, we chose to discontinue this cell line with the timed media treatment and did not perform subsequent quantification.

The IMR90 cell line differentiation exhibited a response similar to that seen with preconditioning treatment. Timed treatment with IWR and SAG resulted in highly neuralised morphology (Figure 5.5, N = 5 independent batches), characterised by flat patches of dark neural rosette-like tissues with strong GFP signal or poorly formed vesicle-like structures lacking neuroepithelial borders. This excessively neuralised phenotype could potentially be attributed to a shift towards ventral forebrain fate, given the observed role of SHH in ventralisation[47]. However, this hypothesis warrants further investigation through immunological or sequencing characterisation to elucidate the biological pathways involved and potentially identify signalling thresholds that divert tissues away from retinal fates.

Quantification revealed a non-significant increase in the overall mean number of vesicles generated in the HOIK1 line following media treatment, from 111 vesicles (± 70.24) to 149 vesicles (± 113.88) (Figure 5.6a). Within paired samples, there was an observed average increase in fold-change of 2.74 (± 3.51). However, this effect was highly variable and inconsistent between batches. In one replicate, the treatment caused a 10-fold increase in the number of vesicles generated (348 in treated vs. 33.5 in controls). The distribution of the data showed increased variability between batch-to-batch cultures upon timed media treatment, which could be a consequence of the higher maximum vesicle counts achieved in treated cultures (approximately 350 vesicles, versus 200 vesicles in control cultures). This expanded range suggests that the treatment may enhance the differentiation capacity of the culture, though it also introduces greater variability.

Unlike the preconditioning experiments, no consistent pattern emerged between the success of organoid formation in control cultures and the efficacy of timed media treatment. This lack of correlation suggests that the mechanisms underlying successful organoid formation in control conditions may differ from those influenced by the timed media treatment.

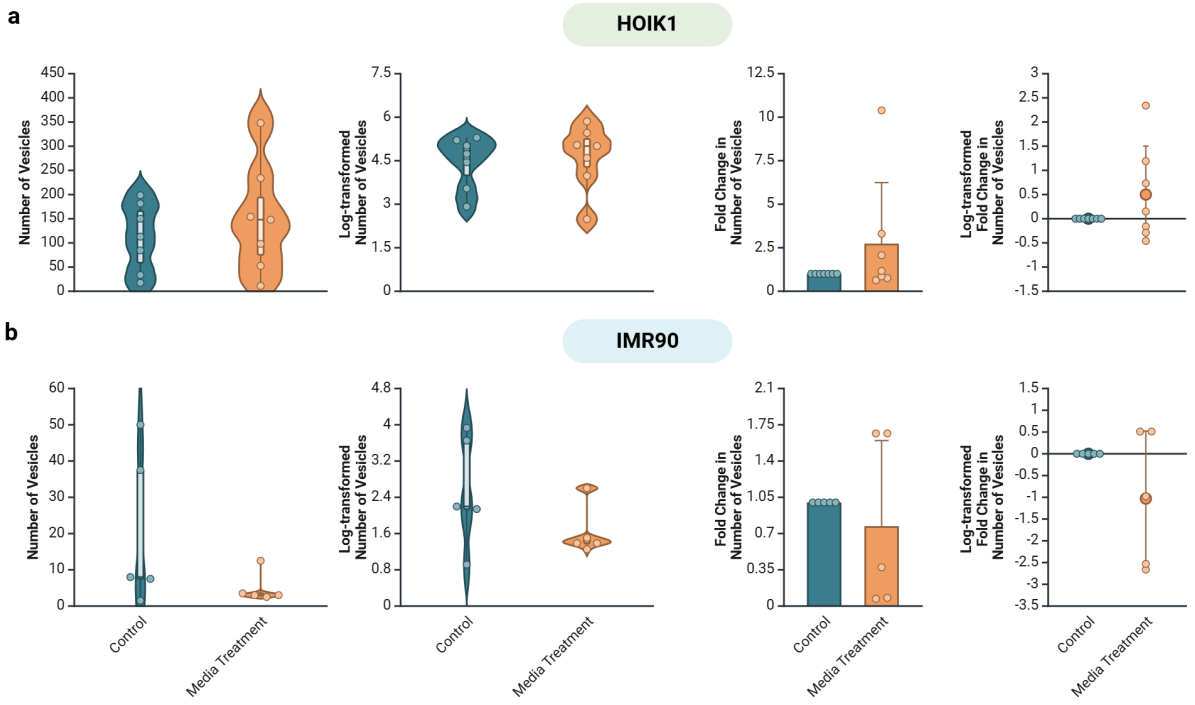

Figure 5.6 Quantification of the average number of vesicles produced (left) and the fold-change within paired samples (right) of cultures with IWR and SAG media treatments and non-treated controls across two cell lines after 4 weeks of differentiation.

(a) Media treatment with IWR and SAG improved the maximum number of vesicles generated in cultures of the HOIK1 cell line (Mean ± SD: Control [111.21 ± 70.24], media treatment [149.36 ± 113.88]; N = 7 independent batches). (b) Media treatment with IWR and SAG decreased the maximum number of vesicles produced in cultures of the IMR90 cell line (Mean ± SD: Control [20.90 ± 21.48], media treatment [4.90 ± 4.26]; N = 5 independent batches).

An intriguing observation was made regarding the impact of cell passage number on treatment efficacy. In one replicate using HOIK1 cells at a higher passage number (4 passages higher than the next highest replicate), media treatment produced a substantially lower number of vesicles compared to paired control cultures (2.86-fold decrease, from 150 vesicles in control

wells vs. 52.5 in treated wells). This observation is in accordance with established findings that extended passaging may alter endogenous signalling and gene expression levels[216], possibly due to accumulated epigenetic changes or selective pressures during culture. This observation emphasises the critical importance of standardising cell culture practices and carefully controlling for passage numbers in experimental design.

In the IMR90 cell line, media treatment generally led to poor efficiency in retinal vesicle generation (Figure 5.6b, N = 5 independent batches). Timed media treatment decreased the average number of vesicles generated compared to control cultures, from 21 vesicles (± 21.47) to 5 vesicles (± 4.26). Regardless of the success of paired control cultures, treated wells exhibited either high neuralisation or poor long-term viability, both resulting in the absence of vesicles. This consistent negative response suggests that the IMR90 line may have a lower tolerance for the signalling modulations induced by IWR and SAG treatment, possibly due to intrinsic differences in baseline WNT and SHH pathway activity or downstream effectors.

Quantification of GFP+ areas in the IMR90 line revealed an increase in the mean number of GFP+ areas following treatment, from 173.90 regions (± 111.51) to 109 regions (± 77.27) (Figure 5.7). Despite the lack of proper vesicle formation, this increase in GFP signal indicates that the media treatment successfully promoted eye field specification but failed to support the subsequent morphogenetic events required for organoid formation. Similar to our findings in the preconditioning treatment, this discrepancy between fate specification and morphogenesis reinforces the multifaceted nature of retinal organoid development and suggests that different cell lines require distinct signalling environments.

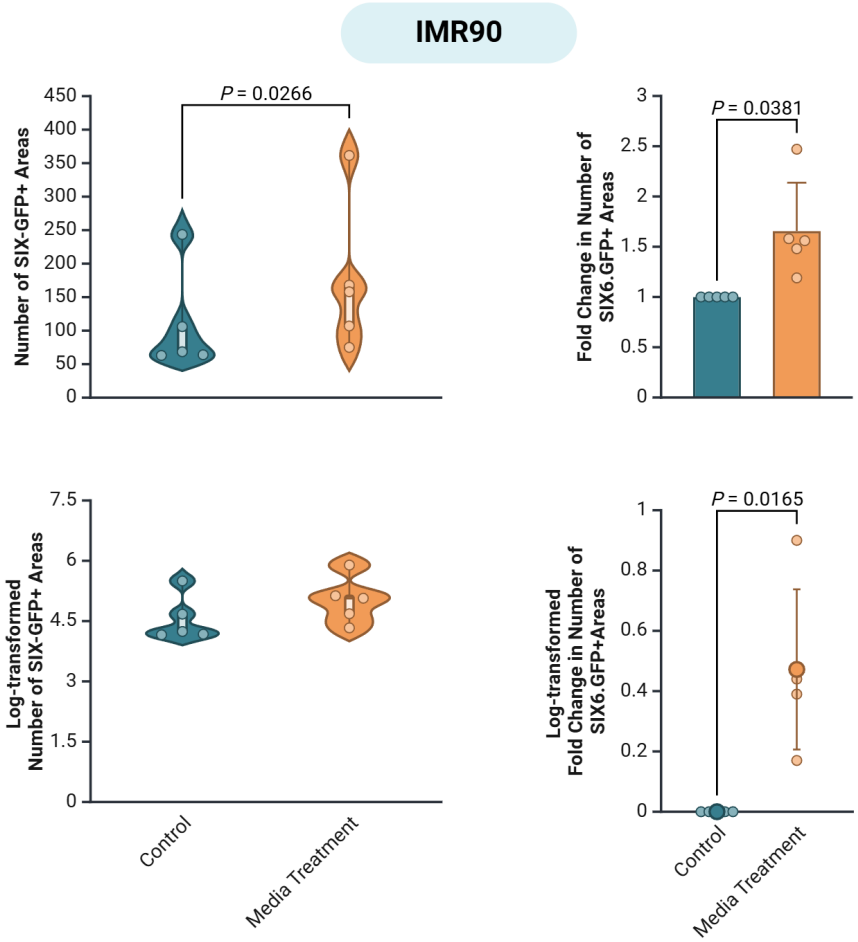

Figure 5.7 Quantification of the average number of GFP+ regions produced (left) and the fold-change within paired samples (right) of cultures with IWR and SAG media treatments and non-treated controls in a SIX6-GFP reporter cell line after 4 weeks of differentiation.

Media treatment with IWR and SAG increased the number of GFP+ regions in cultures of the IMR90 cell line across paired samples by 1.66-fold (Mean ± SD: Control [109.00 ± 77.27], media treatment [173.90 ± 111.51]; N = 5 independent batches, p = 0.0266).

Fold change analysis confirmed a significant increase in GFP+ regions across treated cultures compared to respective control samples (Figure 5.7, n = 1.66 fold-change ± 0.48, p = 0.0381). This consistent upregulation of regions of eye field specification supports the hypothesis that timed modulation of WNT and SHH signalling can effectively promote retinal fate specification. However, the failure of these GFP+ regions to organise into proper vesicles

underscores the complexity of retinal organogenesis and suggests that excessive or prolonged signalling modulation may be counterproductive in this particular cell line. Instead, our previous observations of successful retinal vesicle formation upon spatial patterning of the IMR90 cell line may indicate that the endogenous signalling levels present in this cell line may already be optimised for retinal differential using our standard induction media.

These observations support the hypothesis that successful self-organisation of retinal vesicles requires a delicate balance of multiple cell types and signalling gradients. Overly homogeneous specification of retinal fate through excessive signalling modulation may paradoxically inhibit the formation of the complex tissue architecture characteristic of retinal organoids. This insight has important implications for the design of differentiation protocols, suggesting that strategies aimed at maintaining or promoting cellular heterogeneity within a broadly retinal fate may be more successful than those that push all cells towards a single, highly specified state.

The stark differences in response between cell lines highlight the need for tailored media treatments specific to individual cell lines. This finding aligns with the growing recognition in the field of the importance of cell line characterisation to assess the propensity of specific lines in their capacity to differentiate towards certain tissue types[217]. To address this challenge, we propose that future work should incorporate comprehensive baseline characterisation of signalling pathway activity in each cell line, potentially through RNA sequencing. Such characterisation could inform the design of optimised, line-specific differentiation protocols that account for intrinsic differences in signalling pathway activation and responsiveness.

Our study demonstrates the complex and often unpredictable effects of timed media supplementation on retinal organoid formation in 2D culture systems. While showing promise in some contexts, particularly with the HOIK1 line, the high variability and line-specific responses underscore the challenges in developing universally applicable differentiation

protocols. These findings emphasise the need for a more nuanced understanding of the interplay between signalling pathways, cellular competence, and morphogenetic processes in retinal organoid formation. Future work should focus on elucidating the molecular mechanisms underlying these diverse responses and developing strategies to enhance reproducibility across cell lines and experimental batches. Ultimately, this research contributes to the ongoing refinement of retinal organoid generation, moving us closer to reliable, large-scale production of these tissues for clinical applications.

5.3.3 Modulation of 2D confluent cultures through retinoic acid signalling prior to the onset of SIX6-GFP expression

The role of RA in retinal development has been previously described[218], yet current research predominantly focuses on its effects during later stages of retinogenesis. To address this gap, we investigated the impact of RA supplementation during early retinal differentiation, specifically targeting the period immediately preceding the onset of SIX6-GFP expression in our reporter cell lines. This approach allowed us to explore the potential of RA in modulating the critical transition from pluripotency to committed retinal progenitors. We initially selected an intermediate time point for RA supplementation, spanning from Day 10 to Day 16 of differentiation. This window was chosen based on our previous observations of GFP signal onset in SIX6-GFP reporter lines at approximately Day 16, allowing us to potentially influence the eye field specification process. The selection of this timeframe highlights the importance of understanding the temporal dynamics of developmental signalling in designing effective differentiation protocols.

In the HOIK1 iPS cell line, gross morphological assessment revealed that RA supplementation during this intermediate period supported retinal vesicle growth by enhancing neuroepithelium formation (Figure 5.8). However, the differences between treated and control cultures were

subtle, suggesting that the effect of RA at this stage may be more nuanced. The observation of a somewhat neater background cell population, albeit less pronounced than in our previous treatments, indicates that RA may also play a role in refining cellular organisation or promoting more synchronous differentiation.

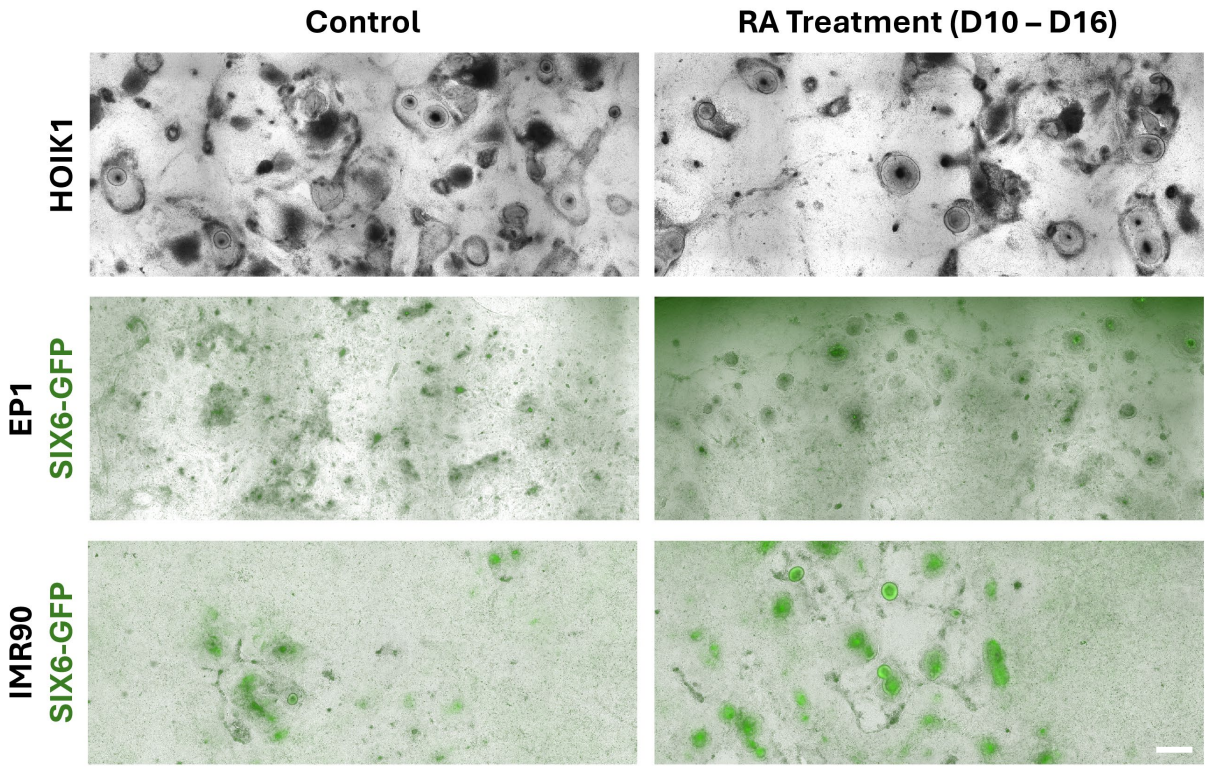

Figure 5.8 Representative images of the capacity of RA treatment from day 10 – 16 to improve retinal differentiation across three cell lines after 4 weeks of differentiation. RA treatment induced a subtle change in the HOIK1 cell line, where the background cell population appeared neater. Treatment of the EP1 and IMR90 cell lines slightly improved neuroepithelial morphology. Scale bar = 1000 µm.

Intriguingly, RA treatment demonstrated a potential minor rescue effect in the EP1 cell line, particularly in cultures where control conditions resulted in poor viability (Figure 5.8). This observation suggests that RA may have pro-survival effects on retinal progenitors or may promote the expression of factors that enhance cell-cell interactions necessary for tissue integrity. However, the resulting vesicles still appeared poorly organised, lacking clear

neuroepithelial borders. This discrepancy between improved survival and suboptimal organisation may point towards the complex and multifaceted nature of RA signalling in retinal development. Moreover, a higher concentration or altered timing of RA supplementation may instead be required to achieve more clear effects. Interestingly, the IMR90 cell line also exhibited a rescue effect in some batches, with the notable difference that these cultures formed relatively more defined neuroepithelial borders. As such, this line-specific variation in response to RA treatment may suggest the difference in baseline endogenous signalling levels between these cell lines. The improved neuroepithelial organisation in IMR90 cultures suggests that this line may possess a greater intrinsic capacity for epithelial self-organisation, which is enhanced by RA signalling.

Quantitative analysis of vesicle formation revealed unexpected line-specific effects of RA treatment. In the HOIK1 line, RA signalling consistently decreased the overall number of vesicles generated from an average of 96 vesicles (± 82.25) in control wells to 62 vesicles (± 52.75) in treated wells (Figure 5.9a, N = 3 independent batches). This finding contrasts with the supportive effect observed in gross morphology, emphasising the importance of quantitative assessment in addition to qualitative observations. The reduction in vesicle number could indicate that RA promotes the formation of larger, more complex vesicles at the expense of total vesicle count, a hypothesis that warrants further investigation through detailed morphometric analysis.

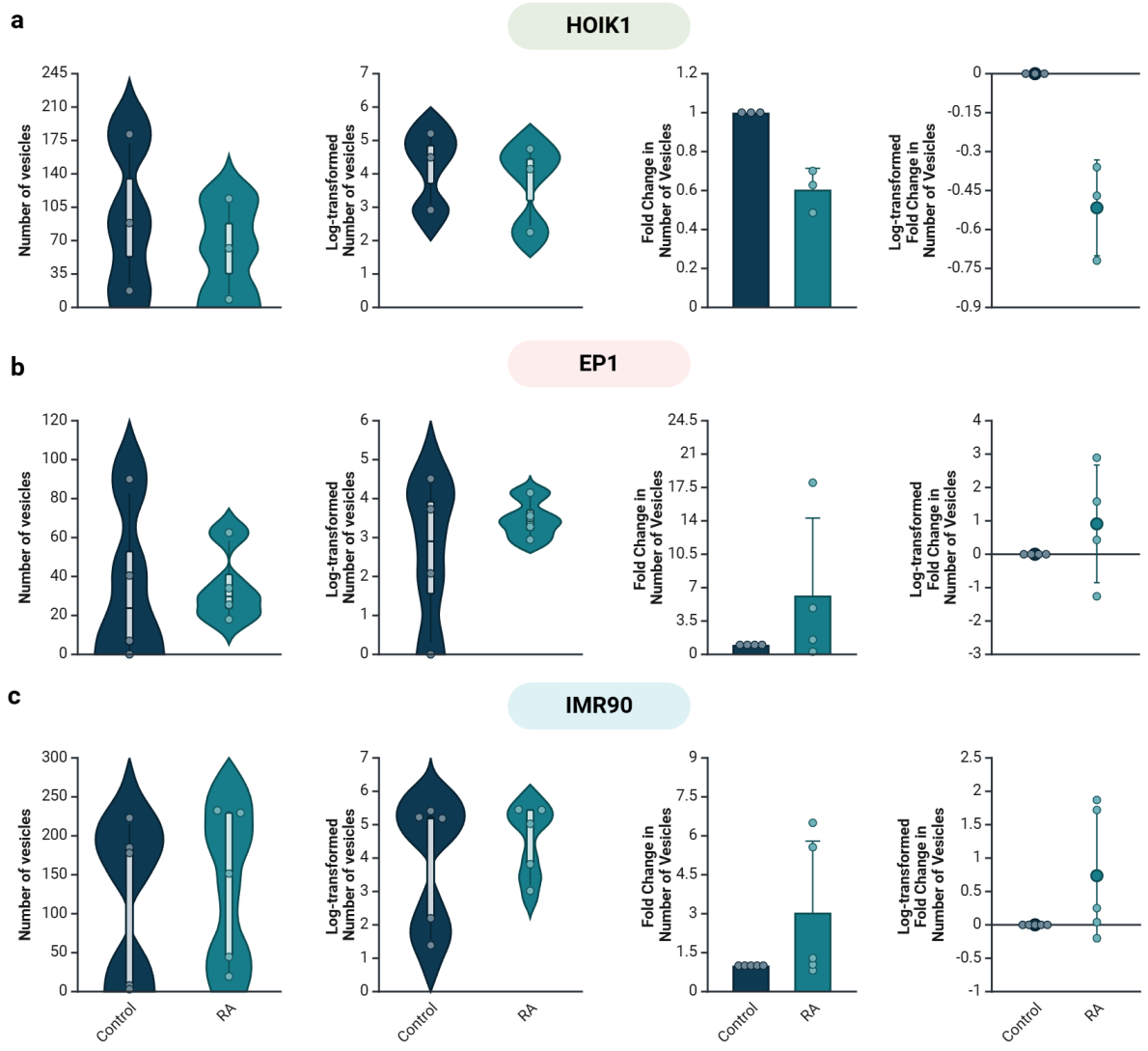

Figure 5.9 Quantification of the average number of vesicles produced (left) and the fold-change within paired samples (right) of Day 10 – 16 RA treated cultures and non-treated controls across three cell lines after 4 weeks of differentiation.

(a) RA treatment decreased the average number of vesicles formed in cultures of the HOIK1 cell line (Mean ± SD: Control [95.83 ± 82.25], RA treatment [61.50 ± 52.75]; n = 34 vesicles difference, N = 3 independent batches, $p > 0.05$). Within paired samples, RA treatment increased the number of vesicles generated in the majority of cultures of the (b) EP1 cell line (Mean ± SD: Control [34.38 ± 41.08], RA treatment [35.00 ± 19.46]; N = 4 independent batches) and (c) IMR90 cell line (Mean ± SD: Control [119.40 ± 105.39], RA treatment [135.50 ± 100.30]; N = 5 independent batches).

Conversely, the EP1 cell line demonstrated no change in the overall average number of vesicles produced in RA-treated cultures (Figure 5.9b). However, within paired samples, an average 6.17-fold (± 8.12) increase was observed. RA supplementation minorly increased the average number of vesicles produced in the IMR90 cell line from 119 vesicles (± 105.39) in controls to 136 vesicles (± 100.30) in treated cultures (Figure 5.9c). Similar to the EP1 cell line, a 3.04-fold (± 2.75) increase was observed within paired samples. Notably, the distribution of data was smaller in both of these lines, suggesting that RA signalling at this intermediate timepoint may enhance consistency across batches to a certain degree. This slightly improved reproducibility could be a valuable outcome in the context of developing robust differentiation protocols for research and potential therapeutic applications.

An intriguing and somewhat paradoxical finding emerged from the analysis of GFP+ regions (Figure 5.10). In both EP1 and IMR90 lines, RA treatment resulted in a downward trend in the number of GFP regions generated, with the majority of replicates producing fewer GFP regions compared to their paired control samples (Figure 5.10a,b). In the EP1 cell line, the average number of GFP+ regions reduced from 72 vesicles (± 89.52) to 49 vesicles (± 52.11); however, this only accounted for an 8% decrease within paired samples (Figure 5.10a). Similarly, the number of GFP+ regions in the IMR90 line reduced from 276 vesicles (± 190.48) in controls to 226 vesicles (± 143.13) in treated cultures (Figure 5.10b).

This observation appears to contradict the increased vesicle formation discussed earlier. We hypothesise that this apparent discrepancy may result from improved organisation within the culture well, where GFP+ cells become more concentrated in dedicated regions rather than being randomly distributed across the well. This consolidation of GFP signal could reflect a more efficient patterning process, potentially leading to the formation of fewer but more robust retinal domains. However, further quantitative analysis is required to confirm such hypotheses.

The contrasting effects of RA treatment compared to our previous preconditioning and timed media treatments provide valuable insights into the complexity of retinal differentiation. While preconditioning and timed media treatments showed more positive effects in the HOIK1 line, RA treatment at Day 10-16 appeared to benefit the EP1 and IMR90 lines preferentially. These findings strongly support our ongoing hypothesis that different cell lines may require tailored biochemical support to optimise retinal differentiation and successful retinal vesicle formation.

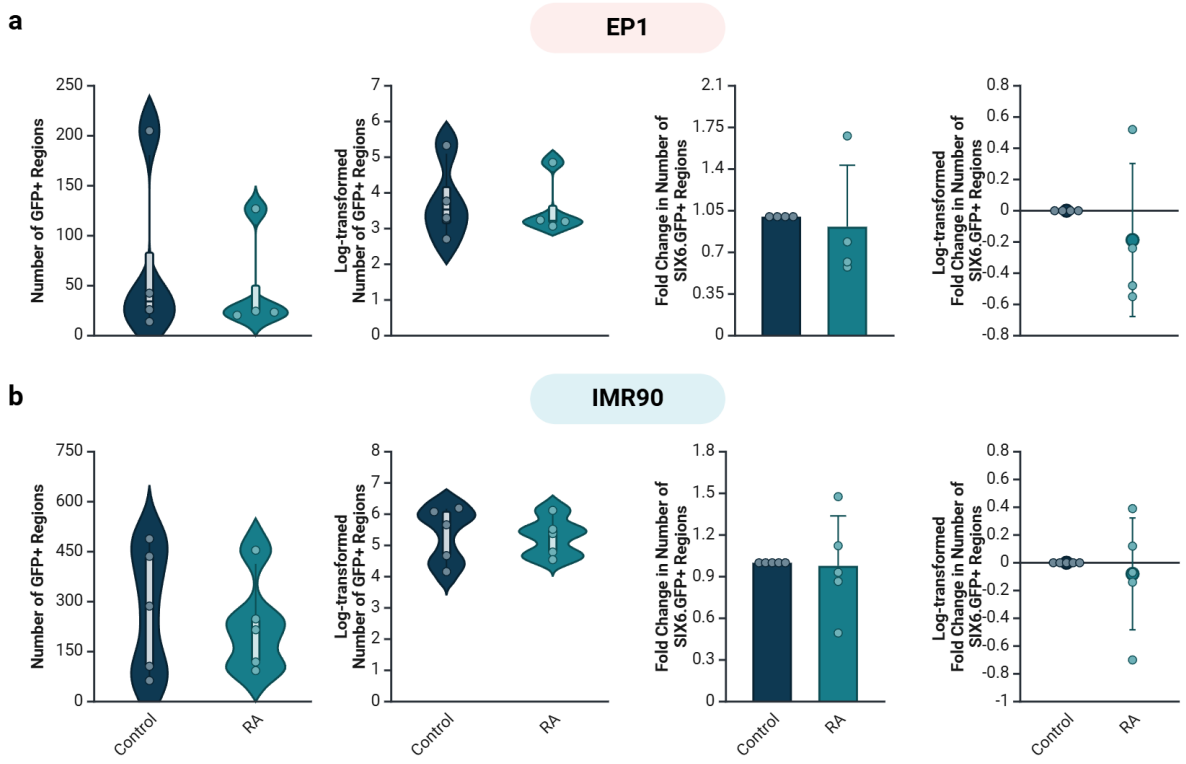

Figure 5.10 Quantification of the average number of GFP+ regions produced (left) and the fold-change within paired samples (right) of Day 10 – 16 RA treated cultures and non-treated controls in SIX6-GFP reporter cell lines after 4 weeks of differentiation.

RA treatment decreased the number of GFP+ regions in both the (a) EP1 cell line (Mean ± SD: Control [71.88 ± 89.52], RA Treatment [48.88 ± 52.11]; n = 23 vesicles difference, N = 4 independent batches, $p > 0.05$) and (b) IMR90 cell line (Mean ± SD: Control [276 ± 190.48], RA Treatment [226 ± 143.13]; n = 50 vesicles difference, N = 5 independent batches, $p > 0.05$).

The differential responses to RA across cell lines could be attributed to variations in endogenous RA signalling components, such as RA receptors or metabolising enzymes. Future studies could benefit from profiling the expression of these components across cell lines to inform more targeted approaches to RA supplementation. Additionally, investigating the interaction between RA signalling and other pathways known to be involved in eye field specification, such as BMP and FGF signalling, could provide a more comprehensive understanding of the molecular mechanisms underlying these line-specific responses.

Moreover, the timing of RA supplementation could be critical. Our choice of the Day 10-16 window, while informative, raises questions about the potential effects of earlier or later RA treatment. Our current investigation into the effects of RA on early retinal differentiation has revealed complex, line-specific responses. The potential of RA to improve vesicle formation and organisation in some lines—while possibly refining patterning in others—highlights its versatile role in early retinal development. These findings contribute to our understanding of the interplay between signalling pathways and genetic background in stem cell differentiation, paving the way for more nuanced and effective strategies in retinal organoid generation. Future work should focus on elucidating the molecular mechanisms underlying these diverse responses and exploring combinatorial approaches that leverage the strengths of different signalling modulators across various iPS cell lines.

5.3.4 Modulation of 2D confluent cultures through the late and early supplementation of retinoic acid

Following our initial investigation into the effects of retinoic acid (RA) treatment during an intermediate time point, we conducted further study to elucidate the temporal sensitivity of retinal organoid formation to RA signalling. This approach recognises the critical importance of timing in developmental processes and seeks to refine our understanding of when RA signalling exerts its most significant effects on retinal differentiation. We first examined a later time point for RA treatment, commencing approximately halfway through retinal differentiation at Week 2 (Day 14 - Day 20). This timing was selected to potentially influence the later stages of eye field specification and early optic vesicle formation, particularly as we observed morphological changes in our previous study assessing a relatively earlier time point.

Gross morphological assessment again revealed subtle but noteworthy cell line-dependent responses. In the HOIK1 line, no significant morphological changes were observed with late RA treatment (Figure 5.11, N = 3 independent batches). This lack of response contrasts with the effects seen at earlier time points, suggesting that HOIK1 cells may have a narrower window of sensitivity to RA signalling during retinal differentiation.

The EP1 line showed potential for more well-defined neuroepithelial borders in RA-treated samples (Figure 5.11, N = 1 independent batches). However, the limited replication for this cell line at this time point necessitates caution in interpretation. Similarly, the IMR90 cell line exhibited more defined neuroepithelial borders, particularly in thicker appearing neuroepithelium, though these differences were not significant (Figure 5.11, N = 2 independent batches). The low sample number for this cell line also limits the generalisability of these observations. These preliminary findings, while promising, warrant increased biological replicates to establish robust conclusions about the effects of late RA treatment.

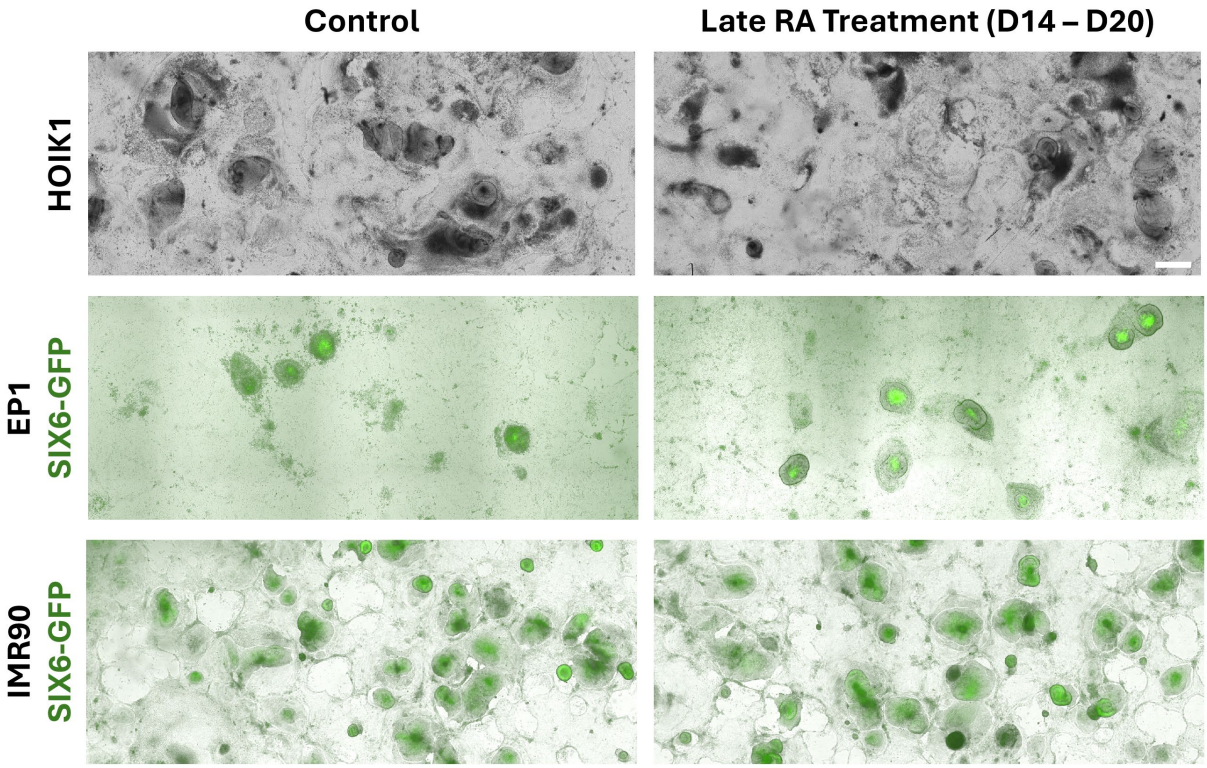

Figure 5.11 Representative images of the capacity of late RA treatment (Day 14 – 20) to improve retinal differentiation across three cell lines after 4 weeks of differentiation. RA treatment did not have a visible effect on the HOIK1 cell line, though appeared to improve neuroepithelium formation in both the EP1 and IMR90 cell lines. Scale bar = 1000 µm.

Quantitative analysis of the HOIK1 and both of the SIX6-GFP reporter cell lines was performed. Consistent with our previous observations, the HOIK1 cell line consistently showed a decrease in vesicle formation upon RA treatment (82 vesicles ± 14.51) compared to controls (112 vesicles ± 37.44) (Figure 5.12a). This further supports our hypothesis that the cell line may be particularly sensitive to RA-induced perturbations in retinal differentiation.

Conversely, the SIX6-GFP reporter cell lines (EP1 and IMR90) were largely unaffected by late RA treatment in terms of vesicle formation (Figure 5.12b). While fold-change analysis demonstrated wide data distribution, the absolute differences in vesicle numbers were relatively small (maximum difference of 16 vesicles). Given that the maximum observed vesicle count was an average of 249 tissues per well, these variations likely fall within the range

of batch-to-batch variability inherent in stem cell differentiation protocols. This relative insensitivity to late RA treatment could imply that, by Week 2, the retinal progenitors in these lines may have already committed to their fate, becoming less responsive to exogenous signalling modulation.

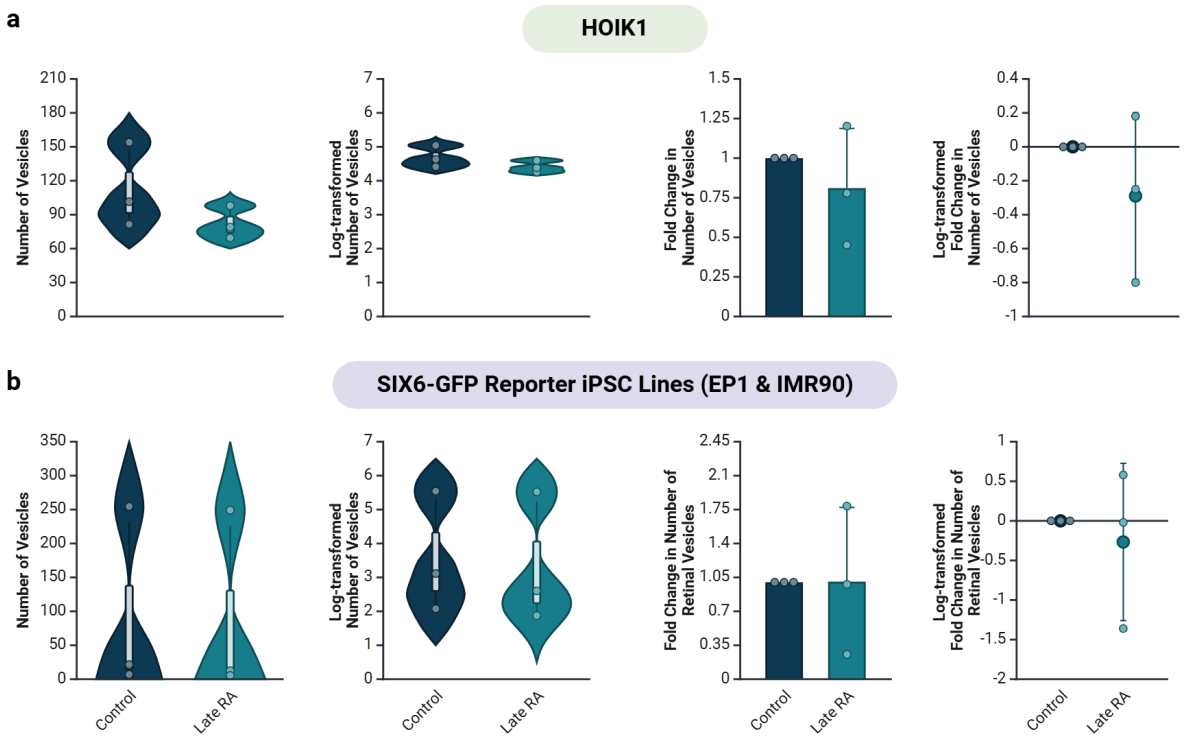

Figure 5.12 Quantification of the average number of vesicles produced (left) and the fold-change within paired samples (right) of late RA treated cultures (Day 14 – 20) and non-treated controls across three cell lines after 4 weeks of differentiation.

(a) Late RA treatment decreased the number of vesicles generated by the HOIK1 cell line (Mean ± SD: Control [112.33 ± 37.44], Late RA Treatment [82.17 ± 14.51]; n = 30 vesicles difference, N = 3 independent batches, $p > 0.05$). (b) Late RA treatment did not significantly affect the number of vesicles produced in the SIX6-GFP reporter cell lines (Mean ± SD: Control [94.33 ± 138.90], Late RA Treatment [89 ± 138.61]; N = 3 independent batches).

Analysis of GFP+ regions in the SIX6 reporter lines yielded similar results, with minimal differences between RA-treated and control samples (Figure 5.13). The largest observed difference of approximately 15 GFP+ regions is again relatively small considering the inherent

variability in these cultures. This consistency in GFP expression further supports the notion that late RA treatment has limited impact on eye field specification at this time point in these cell lines.

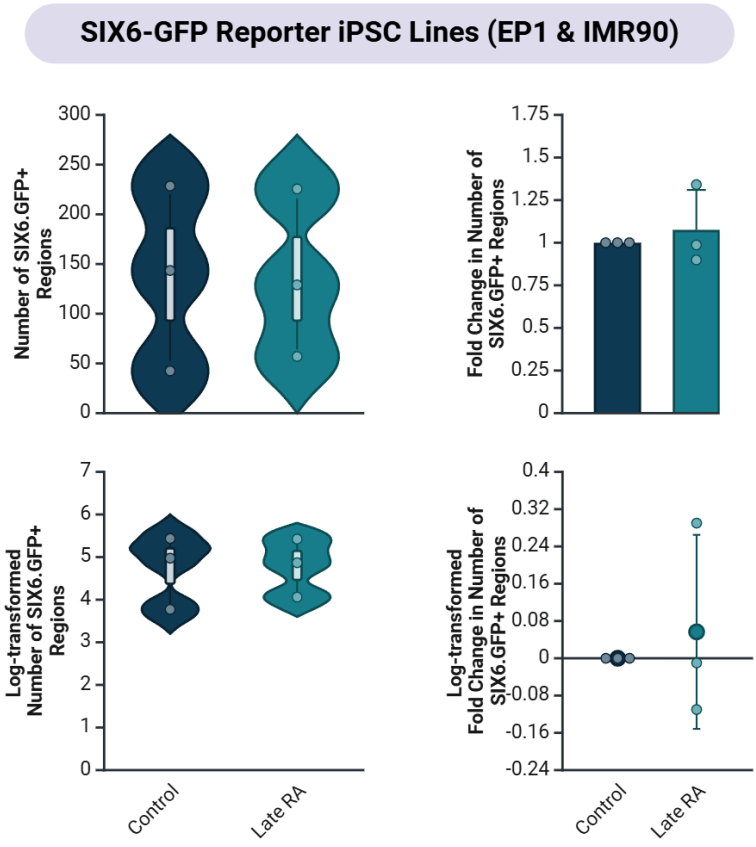

Figure 5.13 Quantification of the average number of GFP+ regions produced (left) and the fold-change within paired samples (right) of late RA treated cultures (Day 14 – 20) and non-treated controls in SIX6-GFP reporter cell lines after 4 weeks of differentiation. Late RA treatment did not affect the number of GFP+ regions produced in GFP reporter cell lines (Mean ± SD: Control [138.17 ± 93.11], Late RA Treatment [137.17 ± 84.55]; N = 3 independent batches).

These findings collectively suggest a potential window of competence for RA responsiveness that may close by Week 2 of differentiation, particularly in the EP1 and IMR90 lines. The slightly improved morphology observed, while requiring further characterisation, hints at a potential role for late RA treatment in refining tissue architecture rather than influencing cell

fate decisions. This distinction between effects on fate specification and tissue organisation is an important consideration for future protocol optimisation.

To further explore the temporal dynamics of RA sensitivity, we conducted a brief investigation into early RA treatment, defined as treatment starting from Week 1 (Day 6-12). This early intervention aimed to potentially influence the initial stages of eye field specification and neural induction.

Early RA treatment elicited more pronounced morphological changes across all three cell lines (Figure 5.14). The HOIK1 line showed potential for subtle improvement in the formation of well-defined neuroepithelial borders in retinal vesicles, a feature not prominently observed in control cultures (Figure 5.14, N = 2 independent batches). This observation suggests that early RA signalling may play a role in establishing proper neuroepithelial organisation in this line, potentially by modulating the expression of cell adhesion molecules or cytoskeletal regulators. However, the low sample number again limits such conclusions.

The EP1 line similarly demonstrated the formation of more well-defined tissues resembling vesicles upon early RA treatment, contrasting with the lack of well-defined tissues in control samples (Figure 5.14, N = 1 independent batch). While clear retinal vesicles were not observed, this improvement in tissue organisation hints at a potential role for early RA signalling in priming cells for subsequent morphogenetic events. Similar to the HOIK1 cell line, the single replicate limits any generalised observations.

In the IMR90 cell line, early RA treatment led to more defined neuroepithelial formation, with these effects being more pronounced in cultures where the paired control did not form well-defined neuroepithelium or formed vesicles that were relatively small in appearance (Figure 5.14, N = 3 independent batch). This subtle rescue effect of early RA treatment on

neuroepithelial organisation is particularly intriguing, suggesting that RA signalling may compensate for other factors that normally drive this process.

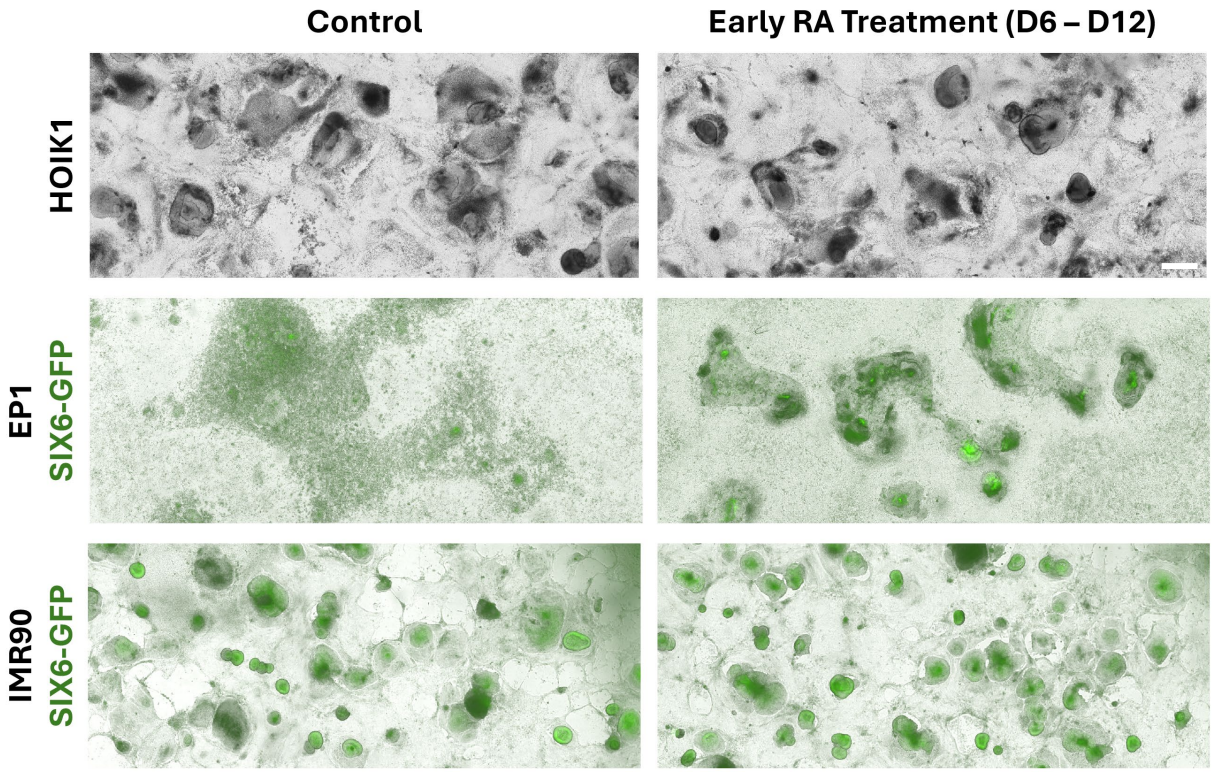

Figure 5.14 Representative images of the capacity of early RA treatment (Day 6 – 12) to improve retinal differentiation across three cell lines after 4 weeks of differentiation. Early RA treatment induced subtle improvements across all cell lines, including visibly improved neuroepithelial structures in the EP1 and IMR90 cell lines. Scale bar = 1000 µm.

Consistent with morphological assessment, quantitative analysis of the IMR90 cell line revealed a non-significant increase in the average number of vesicles generated upon early RA treatment (244 vesicles ± 122.48) compared to controls (150 vesicles ± 120.41) (Figure 5.15a). No decrease in the number of vesicles generated upon early RA treatment was observed in any replicate culture. Within paired samples, an average 2.97-fold (± 2.55) increase was noted. However, similar to our observations with intermediate RA treatment, a non-significant downward trend in the number of GFP+ regions was demonstrated with early RA treatment from 303 areas (± 161.51) to 177 areas (± 104.54) in controls. This result suggests that RA

treatment, especially at earlier time points (before Day 14), may be affecting the spatial organisation of SIX6-expressing regions in batch stem cell-derived retinal cultures. The consistent enhancement of vesicle formation contrasts with the variable effects observed at later time points, underscoring the importance of early developmental events in determining overall differentiation outcomes.

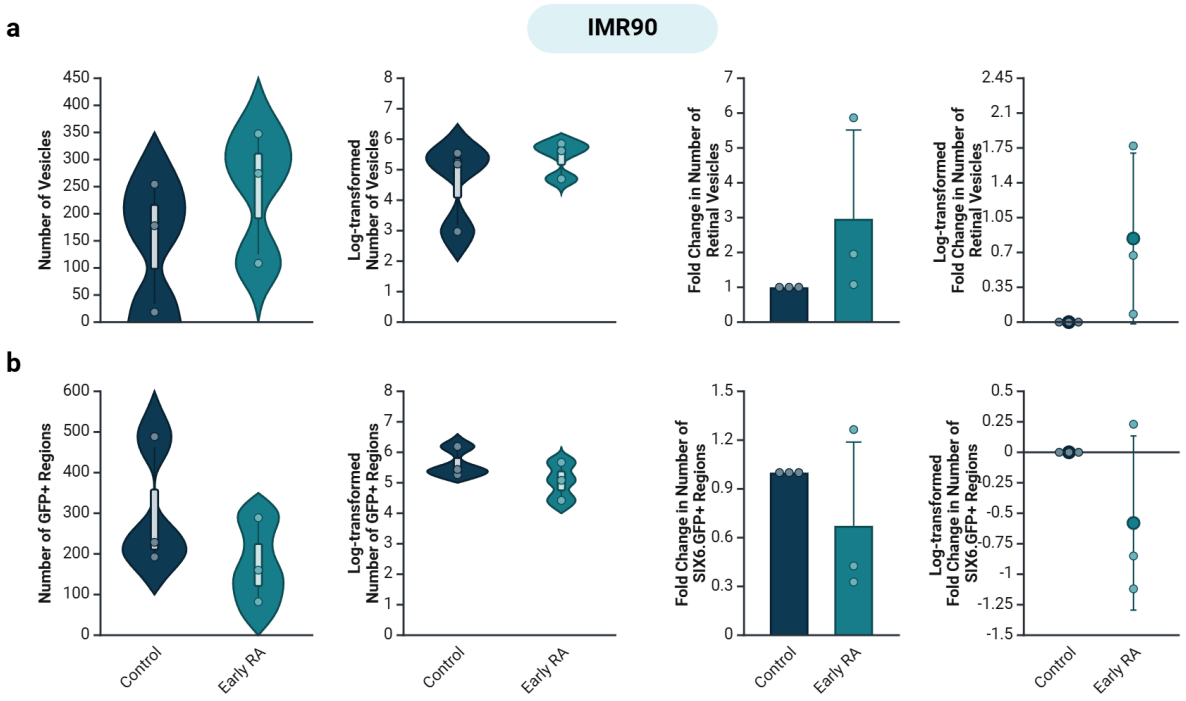

Figure 5.15 Quantification of the average number of vesicles produced (left) and the fold-change within paired samples (right) of early RA treated cultures (Day 6 – 12) and non-treated controls after 4 weeks of differentiation (N = 3 independent batches).

(a) Early RA treatment improved the number of vesicles generated in all replicate cultures of the IMR90 cell line (Mean ± SD: Control [150.33 ± 120.41], Early RA Treatment [243.50 ± 122.48]; n = 93 vesicles difference, $p > 0.05$). (b) Early RA treatment decreased the number of GFP+ areas produced in the IMR90 cell line in all but one replicate (Mean ± SD: Control [303.17 ± 161.51], Early RA Treatment [177 ± 104.54]; n = 126 vesicles difference, $p > 0.05$).

These findings raise several interesting possibilities: (1) RA may promote the consolidation of SIX6-expressing cells into more discrete, organised domains, potentially mimicking the process of optic vesicle formation in vivo; (2) early RA treatment might accelerate the

differentiation process, leading to a more rapid transition through the SIX6+ progenitor stage and into more mature retinal cell types; (3) RA could modulate the expression of other transcription factors involved in eye field specification, potentially altering the balance between different retinal progenitor subtypes. These hypotheses warrant further investigation; for instance, through time-course analysis of gene expression and detailed spatial mapping of retinal marker expression within the developing organoids.

Our current exploration of the temporal dynamics of RA sensitivity in retinal organoid formation has revealed complex, line-specific responses that underscore the critical importance of timing in developmental signalling. The differential effects of early, intermediate, and late RA treatment highlight the dynamic nature of cellular competence during retinal differentiation and suggest that optimal protocols may need to incorporate precisely timed signalling modulations specific to particular cell lines or stem cell states. At the optimal time point, RA treatment may play a critical role in establishing the structural foundations necessary for proper retinal organoid formation. However, the contradictory effects on the number of SIX6-GFP+ regions formed emphasise the need for a more nuanced understanding of how RA signalling interacts with the gene regulatory networks governing eye field specification and early retinal development. As such, future work should focus on elucidating the molecular mechanisms underlying these temporal- and line-specific responses to RA treatment, such as through comprehensive transcriptomic and epigenomic profiling of different cell lines at various time points.

Ultimately, these findings contribute to our growing understanding of the complex interplay of a multitude of factors when utilising more directed differentiation protocols. By refining our ability to modulate these factors, we move closer to developing more robust and efficient methods for generating retinal organoids.

5.3.5 Initialising 2D confluent cultures through an early transient pulse of FGF2 and TGF-β using E8 media

To further elucidate the complex interplay of signalling pathways in retinal organoid formation, we investigated the potential effects of fibroblast growth factor 2 (FGF2), as well as TGF-β upregulation, on retinal differentiation. While FGF2 is known to play a broad role in neural retinal differentiation[219], its precise function remains unclear, particularly in the context of *in vitro* retinal organoid generation. This exploration represents an important step in characterising pathways that influence retinal differentiation but have not been extensively studied in the literature.

We devised a cost-effective approach to modulate FGF2 signalling by leveraging the composition of commonly used stem cell maintenance media. Our standard protocol initiates differentiation by transitioning from E8 medium, which contains both FGF2 and TGF-β, to E6 medium, which lacks these factors. We hypothesised that a brief reintroduction of these factors during early differentiation might influence retinal fate specification and organoid formation.

The experimental design involved a 48-hour pulse of E8 medium at Day 2 of differentiation, followed by a return to the standard protocol from Day 4 onwards. This approach allowed us to stimulate FGF2 and TGF-β signalling transiently during a critical window of early neural and retinal fate specification. Importantly, this method adheres to cGMP-compliant practices, enhancing its potential for translation to clinical applications.

Gross morphological analysis was performed as previously. In the HOIK1 cell line, we observed a marked improvement in the generation of neuroepithelial borders in retinal vesicles (Figure 5.16a, N = 4 independent batches). This effect was particularly pronounced in cultures where paired control samples exhibited poor morphology and failed to generate vesicles with clear neuroepithelial borders (Figure 5.16a). Moreover, a neater background cell population

was observed in cultures treated with an early pulse of E8, where paired control samples appeared more disorganised and neuralised in comparison. As such, transient FGF2 and/or TGF-β signalling could play a subtle role in establishing or maintaining neuroepithelial organisation in this cell line.

Quantitative analysis of vesicle formation provided further insights into the line-specific effects of the E8 pulse treatment (Figure 5.16b). In the HOIK1 line, we observed an increase in the average number of vesicles generated across replicates in E8-treated cultures, from 115 vesicles (± 72.98) in controls to 175 vesicles (± 73.55) in treated cultures. The majority of replicates—all but one sample—demonstrated an increase in vesicle numbers, although the magnitude of this increase varied considerably between experiments. This variability is consistent with our observations in other treatments performed.

The EP1 and IMR90 differentiation cultures exhibited a visibly decreased degree of neuralisation compared to paired control samples following the E8 pulse treatment (Figure 5.16a). Paired control cultures of these lines appeared relatively more neuralised in morphology, with dark neural rosette morphologies. We hypothesise that this effect may be primarily attributed to the presence of TGF-β in the E8 medium, given our previous observations that TGF-β inhibition induces a neuralised morphology in these cell lines. However, the limited replication (N = 1 independent batch for EP1; N = 2 independent batches for IMR90) necessitates caution in interpreting these results and warrants additional experiments to draw definitive conclusions.

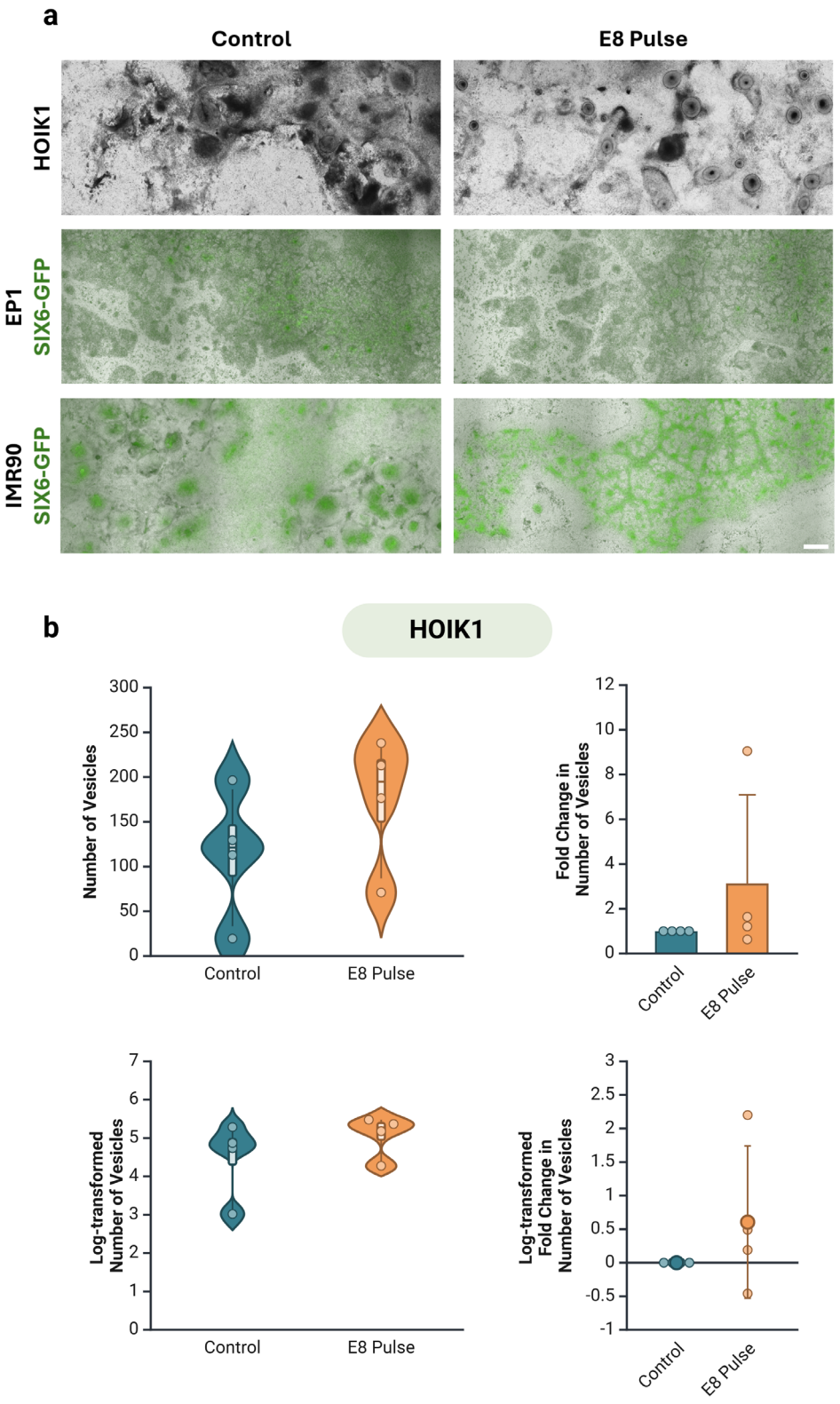

Figure 5.16 Representative images of the capacity of E8 pulse treatment across three cell lines after 4 weeks of differentiation, and quantification of the number of vesicles produced in the HOIK1 cell line.

(a) Treatment with a pulse of E8 improved the morphology of vesicles in the HOIK1 cell line; however, treated cells in the EP1 and IMR90 cell line appeared less neuralised compared to control cultures. Scale bar = 1000 μm. (b) E8 pulse treatment improved the number of vesicles generated in all but one replicated in the HOIK1 cell line (Mean ± SD: Control [114.63 ± 72.98], E8 Pulse [174.63 ± 73.55]; n = 60 vesicles difference, N = 4 independent batches)

These SIX6-GFP reporter cell lines (EP1 and IMR90) showed a non-significant decrease in the number of vesicle structures formed, from 20 vesicles (± 25.93) in control cultures to 12 vesicles (± 18.62) in treated cultures. However, poor self-organisation capacity was observed, with 2 of 3 differentiation batches failing to form more than 10 organoids in both the control and treated samples. No significant alteration in the number of GFP+ regions formed was observed following E8 pulse treatment. This aligns with our morphological observations of reduced neuralisation in these cell lines. However, the low sample numbers for these cell lines as well as the poor capacity for self-organisation warrant further investigation.

The contrasting responses of HOIK1 versus EP1 and IMR90 lines to E8 pulse treatment are similarly consistent with previous treatment regimens. The increase in vesicle formation observed in the HOIK1 line suggests that either FGF2 or TGF-β signalling may enhance differentiation efficiency specifically in this cell line.

We propose an intriguing hypothesis to explain these divergent responses: the 'under'-neuralisation induced by TGF-β within the E8 pulse treatment may paradoxically benefit the HOIK1 line. Control cultures of HOIK1 often appear disorganised with numerous morphological features across the culture well, potentially indicating 'over'-neuralisation caused by our standard proneural induction media. The transient introduction of TGF-β via the E8 pulse may, therefore, reduce the degree of neuralisation, resulting in improved long-term differentiation outcomes for this specific line.

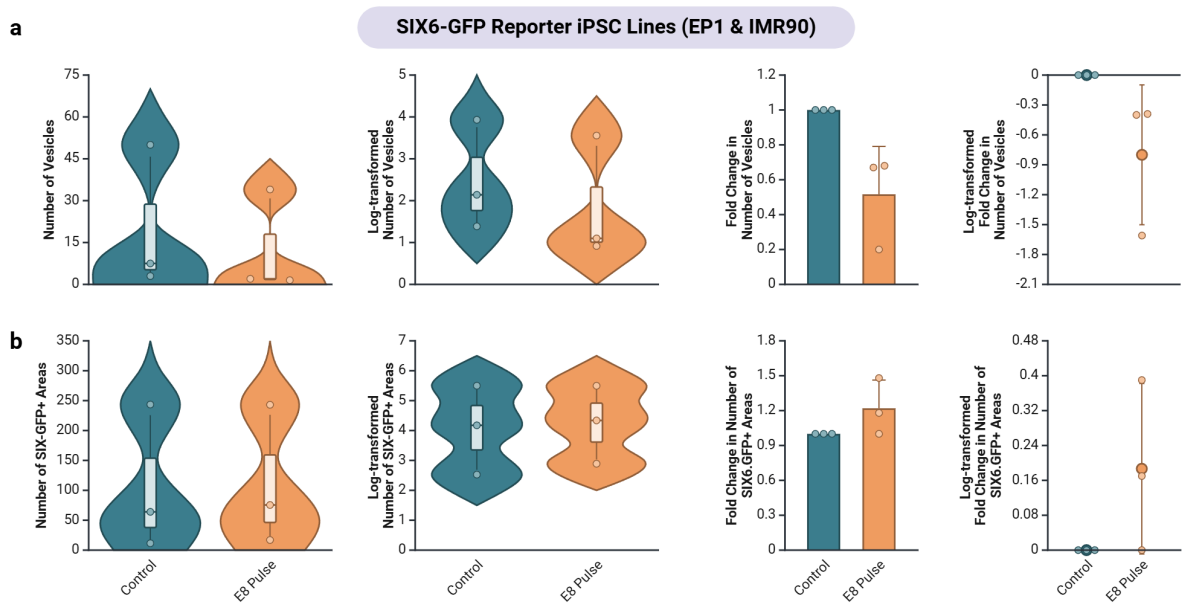

Figure 5.17 Quantification of the average number of vesicles and GFP+ regions produced within paired samples of E8 pulse treated cultures and non-treated controls in SIX6-GFP reporter cell lines after 4 weeks of differentiation (N = 3 independent batches). (a) E8 pulse treatment reduced the number of vesicles formed in all replicate cultures (Mean ± SD: Control [20.17 ± 25.93], E8 Pulse [12.5 ± 18.62]; n = 8 vesicles difference). (b) E8 pulse treatment did not significantly alter the number of GFP+ regions generated (Mean ± SD: Control [106.33 ± 121.66], E8 Pulse [111.83 ± 117.30]).

This hypothesis aligns with established concepts in developmental biology that emphasise the importance of balanced signalling in tissue specification[219]. Excessive neuralisation may limit the diversity of cell types necessary for proper retinal organoid formation, while a more moderated approach might allow for the establishment of crucial signalling gradients and cellular interactions. FGF signalling is known to play diverse roles in eye development, including the regulation of the ciliary margin[220] and the specification of certain retinal subtypes[221]; however, the specific role of FGF2 in this process remains less clear and warrants further investigation.

To elucidate the specific contributions of FGF2 and TGF-β in our E8 pulse treatment, future studies should employ these growth factors individually or with selective inhibitors to dissect

their individual roles. Additionally, comprehensive transcriptomic analysis at various time points following E8 pulse treatment could provide valuable insights into the molecular mechanisms underlying the observed effects. Moreover, the temporal dynamics of FGF2 and TGF-β sensitivity during retinal differentiation require further exploration. Our 48-hour pulse at Day 2 was chosen based on practical considerations, however, systematic variation of the timing, duration, and concentration of growth factor exposure could reveal optimal windows for modulating these pathways.

The potential of this simple, cGMP-compliant method to improve organoid formation in certain cell lines is particularly exciting from a translational perspective, despite ongoing challenges with variability. Exploring the long-term consequences of early E8 pulse treatment on organoid maturation and functionality, particularly in the HOIK1 cell line, will be crucial for assessing the full potential of this approach.

5.3.6 Characterisation of the endogenous signalling levels of key signalling pathways across different stages of passage numbers of three iPS cell lines

To better understand the underlying factors contributing to the variability observed in retinal organoid formation across different cell lines, we conducted a comprehensive qPCR analysis of key signalling pathways in our three iPSC lines at various passage numbers. This investigation aimed to characterise the baseline expression of TGF-β, Nodal, SHH, and WNT (WNT3A) pathways in the undifferentiated state, providing crucial insights into the intrinsic signalling landscapes that may influence subsequent differentiation outcomes.

Samples from early, intermediate, and late passages for each stem cell line were collected and specific passage ranges for the IMR90, EP1, and IPE2 lines were defined. For the IMR90 and EP1 cell line, the defined ranges of early, intermediate, and late passages were p+5 – p+8, p+9 – p+10, and p+11 – p+15, respectively. For the IPE2 cell line, the defined ranges of early, intermediate, and late passages were p27 – p30, p31 – p33, and p34 – p37, respectively. This systematic approach allowed us to assess not only line-specific differences but also potential changes in gene expression profiles as a function of passage number. Log_2 transformation was performed on fold change data for enhanced visualisation of proportional changes.

TGF-β expression analysis revealed line-specific patterns. The IMR90 line exhibited relatively higher average expression compared to EP1 and HOIK1, with late passages of HOIK1 showing particularly low baseline TGF-β expression (Figure 5.19, N = 4 independent batches). Interestingly, early and intermediate passages of HOIK1 maintained higher baseline levels compared to late passages. These findings present a complex picture, especially considering the HOIK1 cell line's responsiveness to both TGF-β inhibition (via preconditioning and timed media treatments) and transient TGF-β exposure (via E8 media pulse). This paradoxical behaviour could suggest that optimal retinal organoid formation may require a delicate balance

of TGF-β signalling, rather than simple activation or inhibition. Moreover, it is likely that the interaction of other signalling pathways plays a significant role.

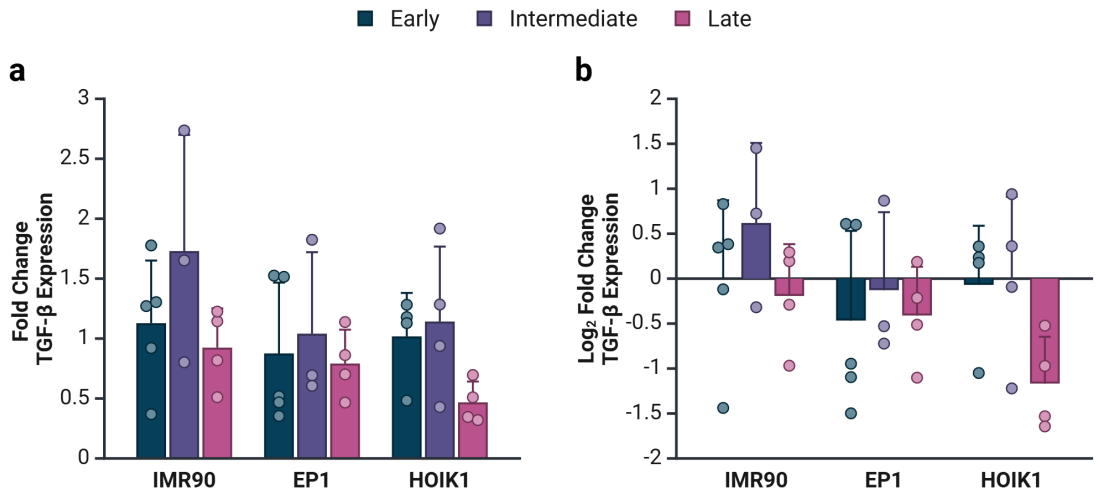

Figure 5.18 Quantitative analysis of TGF-β expression across early, intermediate, and late passage number groups across three iPSC lines at the pluripotent stage prior to differentiation (N = 4 independent batches).

(a) Fold change analysis of TGF-β expression across the three cell lines shows that expression was generally higher in the intermediate passage group. (b) Log-transformation of fold change expression shows that, between cell lines, TGF-β was observed to be higher in the IMR90 cell line than the EP1 and HOIK1 cell lines.

The high baseline TGF-β signalling observed in the IMR90 iPS cell line across all passage groups is particularly noteworthy, given this line's relatively consistent ability to produce retinal vesicles under control conditions. This observation challenges the simplistic view that lower TGF-β signalling is universally beneficial for retinal differentiation and highlights the need for nuanced, line-specific approaches to pathway modulation. A general trend of increased TGF-β signalling in intermediate passage numbers was observed across all lines, followed by early and late passages. This pattern might reflect the cumulative effect of exposure to TGF-β in E8 medium used for iPSC maintenance. However, the substantial variability in the data, particularly in the intermediate passage group, necessitates caution in

drawing definitive conclusions about the relationship between passage number and TGF-β signalling.

Analysis of Nodal expression, a key component of the TGF-β/Nodal pathway inhibited by SB treatment, revealed similar patterns to TGF-β expression (Figure 5.19a, N = 4 independent batches). The IMR90 line showed the highest level of endogenous Nodal signalling, followed by EP1 and HOIK1. Early passages of the IMR90 cell line showed a significantly increased level of Nodal expression compared to early passages of HOIK1 ($p = 0.004$) and EP1 ($p = 0.002$) cell lines. Moreover, log-transformed data revealed a significant increase of 3.3-fold increase in the Nodal expression between early IMR90 passages and early HOIK1 passages (Figure 5.19b, $p = 0.003$). Interestingly, this analysis also revealed a significant 2.7-fold decrease in Nodal expression between the late HOIK1 passage group and the late IMR90 passage group ($p = 0.038$). The relatively lower expression of both TGF-β and Nodal in the HOIK1 line is intriguing and warrants further investigation to understand its unique responsiveness to pathway modulation during differentiation.

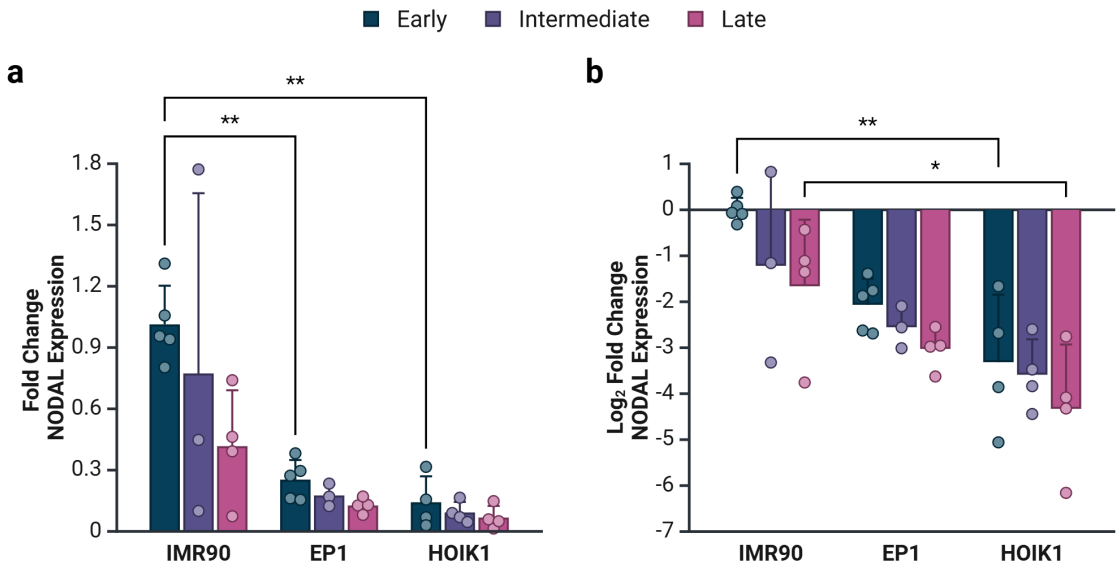

Figure 5.19 Quantitative analysis of Nodal expression across early, intermediate, and late passage number groups across three iPSC lines at the pluripotent stage prior to differentiation (N = 4 independent batches).

(a) Fold change analysis of Nodal expression across the three cell lines shows that expression was generally higher in the early passage group. (b) Log-transformation of fold change expression shows that, between cell lines, Nodal was observed to be higher in the IMR90 cell line than the EP1 and HOIK1 cell lines.

Sonic hedgehog (SHH) signalling quantification presented significant challenges due to high sample variability. As such, we performed outlier removal based on interquartile range calculations to compare and better visualise data (Figure 5.20, N = 5 independent batches). With outliers included, early passage numbers of all cell lines showed relatively higher expression than intermediate and late passage groups (Figure 5.20a, $p > 0.05$). After outlier removal, early passage groups still demonstrated higher SHH expression in IMR90 and HOIK1 lines (Figure 5.20b, $p > 0.05$). However, the EP1 early passage group had a high proportion of outliers, significantly altering the data mean upon removal. Late passage groups of IMR90 and HOIK1 showed relatively lower SHH expression compared to other passage groups within the same line, while EP1 showed no differences (Figure 5.20c,d; $p > 0.05$). These results suggest a potential downward correlation between SHH expression and increasing passage number, though the high variability necessitates further characterisation for definitive conclusions.

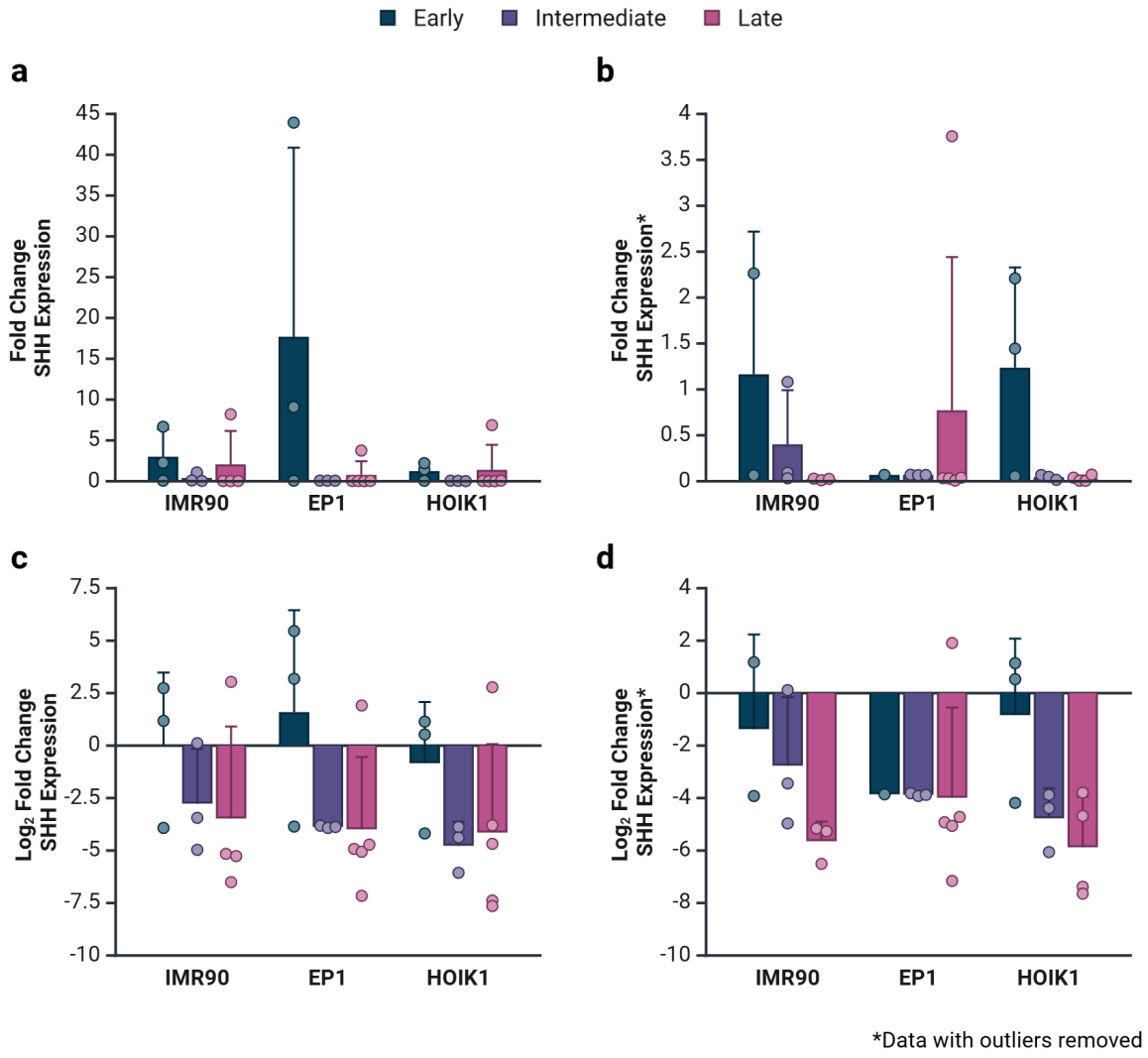

Figure 5.20 Quantitative analysis of SHH expression across early, intermediate, and late passage number groups across three iPSC lines at the pluripotent stage prior to differentiation (N = 5 independent batches).

(a,c) Fold change analysis of SHH expression across the three cell lines shows that expression was highest in the early passage group of the EP1 cell line. (b,d) Outlier removal in the early passage group of the EP1 cell line shows high variability across cell lines and passage groups.

WNT signalling analysis revealed high baseline expression in the early group of EP1 and the intermediate group of IMR90 (Figure 5.21a, N = 4 independent batches). The early passage group of the EP1 cell line showed significantly higher WNT expression compared to the HOIK1 early passage group ($p = 0.008$), as well as the EP1 late ($p = 0.005$) and intermediate ($p = 0.006$) passage groups. Notably, the HOIK1 line exhibited consistently low WNT

signalling across all passage groups. This observation is particularly intriguing given HOIK1's enhanced responsiveness to timed WNT inhibition treatments in our previous experiments. This discrepancy underscores the complex and often counterintuitive relationship between baseline signalling states and responsiveness to pathway modulation during differentiation. As such, endogenous signalling of these key pathways alone may not be a key indicator of a cell line's response towards biochemical modulation.

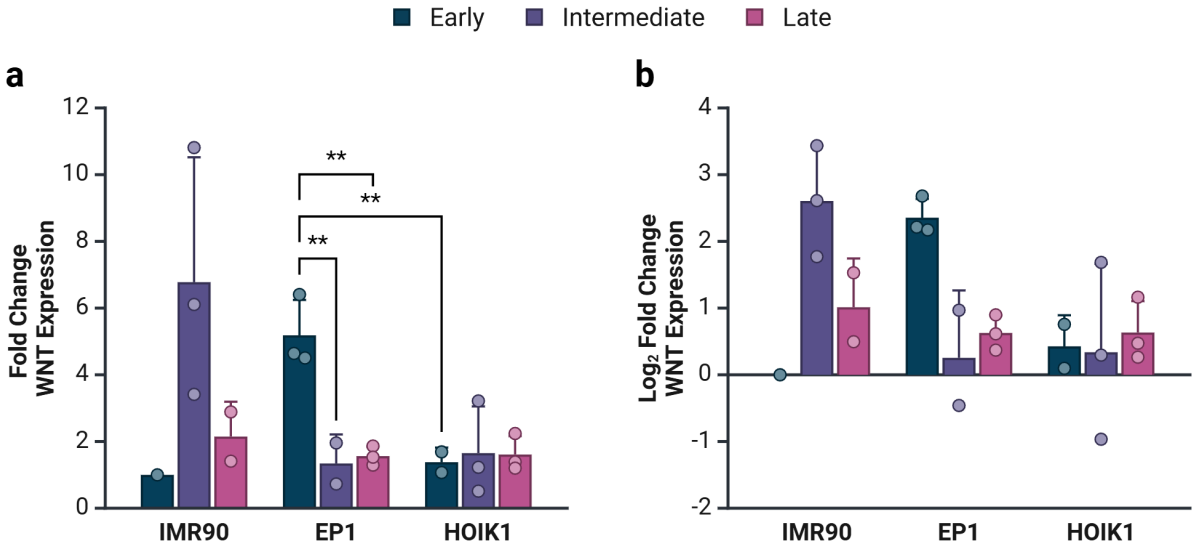

Figure 5.21 Quantitative analysis of WNT3A expression across early, intermediate, and late passage number groups across three iPSC lines at the pluripotent stage prior to differentiation (N = 4 independent batches).

(a,b) Fold change analysis across the three cell lines shows that WNT3A expression in the early passage group of the EP1 cell line was significantly higher than the other passage groups within the same cell line.

The pervasive high variability observed across all cell lines and passage groups in our qPCR analysis provides critical insights into our ongoing challenges of reproducibility. This intrinsic variability likely contributes significantly to the batch-to-batch inconsistencies observed in retinal differentiation outcomes, even when using cells from the same nominal passage number. Several factors may contribute to this variability, including subtle differences in cell handling, microenvironmental fluctuations, and stochastic gene expression patterns. The importance of

consistent iPSC maintenance practices cannot be overstated; factors such as precise and consistent timing of media changes, careful control of cell confluency, and minimisation of mechanical stress during passaging are all known to play crucial roles in maintaining stable pluripotent populations[222,223]. The observed variability also highlights the limitations of using bulk qPCR analysis for characterising heterogeneous stem cell populations. Future studies employing single-cell RNA sequencing could provide more granular insights into the distribution of signalling states within and between iPSC lines, potentially revealing subpopulations with distinct differentiation potentials.

Automated liquid handling systems and robotic cell culture platforms offer promising solutions for standardising crucial parameters such as media change timing, cell dissociation forces, and seeding densities. These technologies not only promise to reduce variability introduced by human handling but also pave the way for scaled-up production necessary for clinical translation of stem cell-derived therapies. Moreover, the line-specific and passage-dependent variations in baseline signalling highlight the need for tailored differentiation protocols. One-size-fits-all approaches to retinal organoid generation are likely to yield inconsistent results across different cell lines. Future protocol optimisation strategies should incorporate baseline signalling characterisation as a key parameter, potentially allowing for dynamic adjustment of differentiation cues based on the starting state of each culture.

Our analysis of baseline signalling pathway activation in three iPSC lines across different passage numbers provides crucial context for interpreting the variable responses to differentiation protocols observed in our previous experiments. The high degree of variability observed, both within and between lines, emphasises the need for advanced technologies or methods to improve the robustness of stem cell stability between batches and over continuous passages.

5.3.7 Evaluating the combined treatment of micropatterned substrates and preconditioning on retinal differentiation

To consolidate our previous findings, we selected specific treatments to establish whether synergistic effects of combined biochemical and biophysical modulation treatments exist. We employed a combination of preconditioning treatment using SB and SAG alongside our previously established micropatterning technique. We performed these experiments in parallel with a non-preconditioned micropatterned control culture and a non-micropatterned non-preconditioned control. This approach aimed to integrate biochemical signalling modulation with spatial control, potentially recapitulating key aspects of embryonic retinal development.

In the HOIK1 cell line, the combination of preconditioning and micropatterning did not result in the formation of many clearly defined vesicles, contrary to our initial expectations (Figure 5.22, N = 2 independent batches). However, we observed the development of neat, rounded tissue islands with some evidence of neuroepithelial tissue formation. These cultures appeared more organised than both the control and micropatterning-only cultures, suggesting that further optimisation of these conditions might potentially lead to the ideal formation of micropatterned vesicles in this cell line, which had previously shown poor performance on micropatterned surfaces. The improved organisation observed in HOIK1 cultures may be attributed to the combined effects of preconditioning, which likely enhanced neural induction and patterning, while the micropatterning provided spatial cues for tissue organisation. This synergy between biochemical and biophysical factors may reflect the complex interplay of signalling and mechanical forces during *in vivo* retinal development.

At week 4, the EP1 cell line exhibited a marked improvement in the maintenance of spatial patterning when preconditioned, compared to non-preconditioned micropatterned cultures (Figure 5.22, N = 2 independent batches). However, the resulting tissues appeared relatively

neuralised and were unable to form clear neuroepithelial structures, despite displaying a low-level GFP signal. These observations suggest that a reduced level of preconditioning or comparable treatments might preserve spatial patterning while enabling the self-organisation of these patterned regions into retinal vesicles. The enhanced neuralisation observed in EP1 cultures may indicate a heightened sensitivity to the SB and SAG treatment, potentially leading to an accelerated or exaggerated neural fate commitment. Again, this phenomenon underscores the delicate balance required between promoting neural identity and maintaining the capacity for complex tissue morphogenesis.

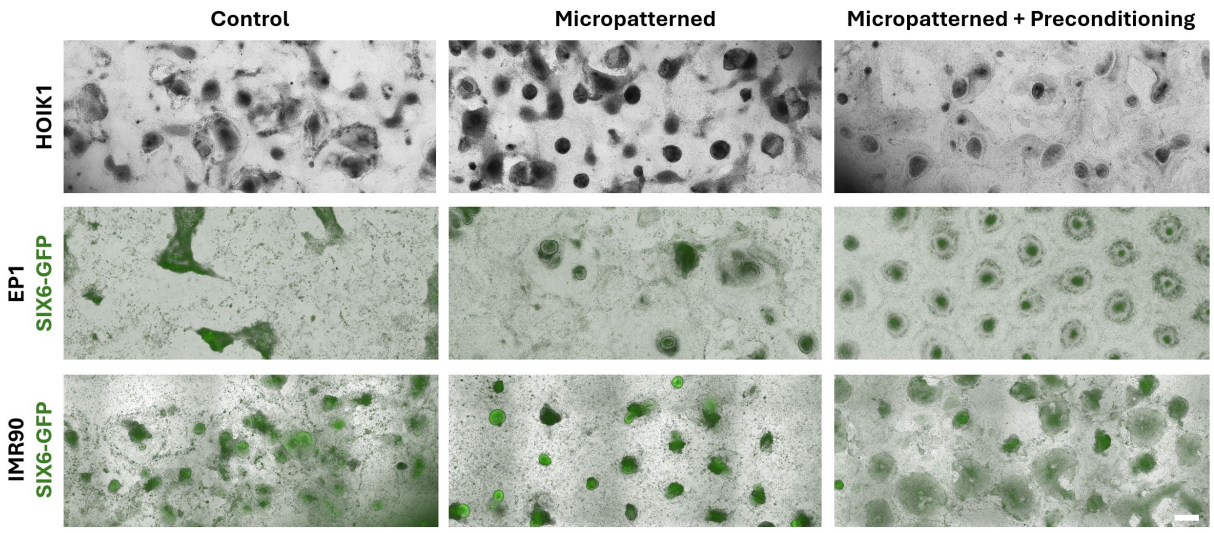

Figure 5.22 Representative images of the capability of combined UV micropatterning and preconditioning treatments to improve or alter retinal differentiation across three cell lines after 4 weeks of differentiation.
Combined treatment improved the formation of immature neuroepithelial structures in the HOIK1 cell line and the retention of spatial patterning in the EP1 cell line, while inducing excessive neuralisation in the IMR90 cell line. Scale bar = 1000 µm.

Interestingly, the IMR90 cell line displayed a contrasting response to the combined treatment. Preconditioning led to a loss of spatial patterning over time, with GFP+ regions appearing less well-organised (Figure 5.22, N = 3 independent batches). This stark contrast to the neatly organised, clear neuroretinal vesicles formed in non-preconditioned micropatterned cultures

suggests that the additional preconditioning treatment may have pushed the IMR90 cells beyond an optimal state for spatial patterning. It is possible that the background cell population, which may be required to support retinal vesicle formation, became overly neuralised, potentially depleting nutrients or signalling molecules from areas attempting to form vesicles. As such, precise levels of signalling factors may be crucial for proper tissue patterning and morphogenesis. These observations are consistent with our previous treatments, where differential responses are observed across our three cell lines, highlighting the intrinsic variability in stem cell populations.

Quantification of vesicle numbers revealed that preconditioning affected the average across all cell lines compared to both micropatterned and non-micropatterned control cultures (Figure 5.23). In HOIK1, preconditioning of micropatterned cultures led to a non-significant decrease in vesicle generation (67 vesicles ± 18.38) compared to non-preconditioned micropatterned cultures (100 vesicles ± 26.52) (Figure 5.23a). Importantly, the significant increase in vesicles enabled by micropatterned controls, when compared to control cultures ($n = 45$ vesicles, $p = 0.004$), was lost with the addition of preconditioning treatments. Despite improved morphological features in preconditioned cultures, the associated lack of vesicle formation likely caused this decrease. This apparent trade-off between overall tissue organisation and specific morphological features (i.e., vesicle formation) raises intriguing questions about the molecular mechanisms governing these processes. It is plausible that the combined micropatterning and preconditioning treatment alters the expression or activity of key transcription factors involved in eye field specification, potentially affecting the balance between neural progenitor maintenance and differentiation.

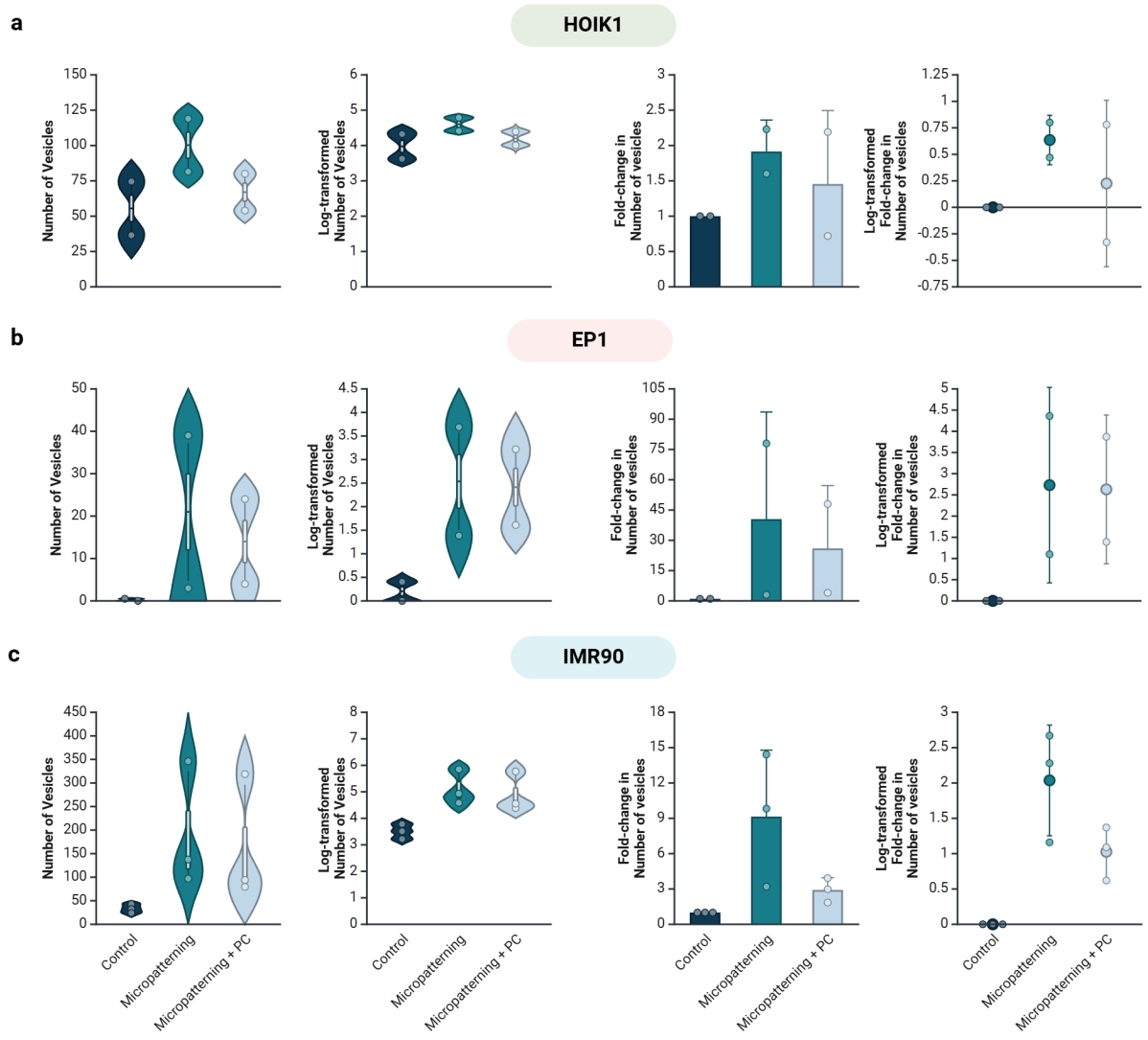

Figure 5.23 Quantification of the average number of vesicles produced (left) and the fold-change within paired samples (right) of combined micropatterning and preconditioning (PC) treatments, non-treated micropatterned controls, and non-treated, non-micropatterned controls across three cell lines after 4 weeks of differentiation.

Preconditioning reduced the average number of vesicles produced compared to non-treated micropatterned cultures in the (a) HOIK1 cell line (Mean ± SD: Control [55.50 ± 26.87], Micropatterned [100.25 ± 26.52], Micropatterned + Preconditioning [67 ± 18.38]; N = 2 independent batches, $p > 0.05$), (b) EP1 cell line (Mean ± SD: Control [0.25 ± 0.35], Micropatterned [21 ± 25.46], Micropatterned + Preconditioning [14 ± 14.14]; N = 2 independent batches, $p > 0.05$), and (c) IMR90 cell line (Mean ± SD: Control [33.17 ± 9.52], Micropatterned [193.50 ± 133.61], Micropatterned + Preconditioning [164.17 ± 134.29]; N = 3 independent batches, $p > 0.05$).

The EP1 cell line similarly showed a non-significant reduction in vesicle formation in preconditioned micropatterned cultures (21 vesicles ± 25.46) compared to non-preconditioned cultures (14.00 vesicles ± 14.14) (Figure 5.23b). Interestingly, while spatial patterning was better maintained in preconditioned micropatterned cultures, this rarely resulted in fully formed vesicles. Instead, we observed spatially patterned, poorly formed vesicles to varying degrees. This phenomenon suggests that while the combined treatment enhanced the initial patterning, it may have interfered with subsequent morphogenetic processes required for complete vesicle formation. Future studies could explore the temporal dynamics of key developmental regulators, such as members of the WNT and BMP pathways, to elucidate the molecular basis of this observation.

For the IMR90 cell line, preconditioning again reduced the overall average number of vesicles in preconditioning treatments (164.17 vesicles ± 134.29) compared to non-preconditioned micropatterned cultures (193.50 vesicles ± 133.61) (Figure 5.23c, $p > 0.05$). Both preconditioned and non-preconditioned micropatterned cultures outperformed control cultures in vesicle formation ($p > 0.05$). The loss of spatial patterning in preconditioned micropatterned IMR90 cultures may be attributed to the excessive neuralisation of cell types present, leading to poor overall organisation and relatively poor vesicle formation. Similar to our previous results, this observation raises questions regarding the level of cellular heterogeneity necessary for proper organoid formation.

Evaluation of the number of GFP+ regions formed in the SIX6 reporter cell lines reveal similar trends to our previous observations (Figure 5.24). In the EP1 cell lines, we observed high variability between the two replicates we performed in this preliminary study (Figure 5.24a). The extreme difference in these replicates limits the generalisability of these results. The trend observed in the IMR90 cell line is consistent with previous observations, where

preconditioning increases the number of GFP+ regions formed (Figure 5.24b). Accordingly, a non-significant increase in the number of GFP+ regions was observed between the control and the combined micropatterned and preconditioning treatment (n = 240 vesicle difference). The high degree of neural phenotypes observed in these cultures also reflects this increase.

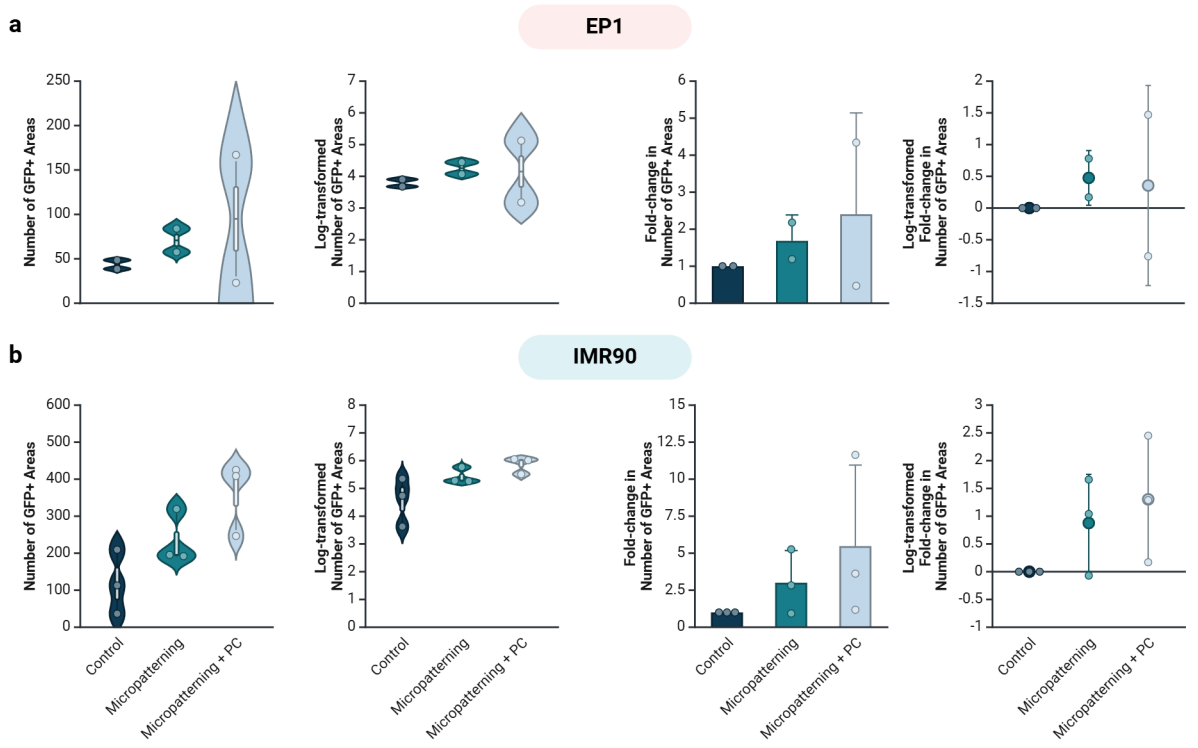

Figure 5.24 Quantification of the average number of GFP+ regions produced (left) and the fold-change within paired samples (right) of combined micropatterning and preconditioning treatments, non-treated micropatterned controls, and non-treated, non-micropatterned controls in SIX6-GFP reporter cell lines after 4 weeks of differentiation. (a) Combined treatment induced highly variable effects in the EP1 cell line (Mean ± SD: Control [43.50 ± 7.07], Micropatterned [70.75 ± 18.74], Micropatterned + Preconditioning [95 ± 101.82]; N = 2 independent batches). (b) Combined treatment improved the number of GFP+ areas generated in the IMR90 cell lines compared to micropatterning alone (Mean ± SD: Control [119.67 ± 86.69], Micropatterned [235.67 ± 72.62], Micropatterned + Preconditioning [360 ± 98.64]; N = 3 independent batches).

Our findings suggest that cell lines performing well in control cultures might not benefit from this combination treatment, while those excelling in micropatterned substrates alone may not respond favourably to the combined micropatterning and preconditioning approach. This observation hints at our hypothesis of distinct initial states among different cell lines, where their intrinsic properties predispose them to respond differently to various combinations of biochemical and biophysical cues. Elucidating the molecular basis of these competence states could provide valuable insights into the fundamental principles governing stem cell fate decisions and tissue morphogenesis. As such, the optimisation process for HOIK1 and EP1 cell lines is likely to be more complex than simply adjusting small molecule concentrations, particularly due to the high stochasticity observed between batches. This complexity reflects the multifaceted nature of retinal development, involving numerous interacting signalling pathways and mechanical forces, as we now better understand.

Future optimisation efforts may benefit from a systems biology approach, integrating data from transcriptomics, proteomics, and metabolomics to build comprehensive models of the differentiation process. Such models could guide the design of more refined and robust protocols, potentially incorporating additional factors such as extracellular matrix components or other forms of mechanical stimulation.

A bottom-up approach might prove more effective, beginning with an in-depth characterisation of the IMR90 cell line to understand its amenability to spatial patterning. This knowledge could then be applied to characterise other cell lines, including HOIK1 and EP1, and tailor small molecule treatments to achieve a similar initial state as the IMR90 line. This approach aligns with the concept of developmental trajectories in stem cell biology, where understanding the sequence of molecular events leading to a desired cell fate can inform more effective differentiation strategies. The incorporation of advanced techniques such as transcriptomics

analysis and deep learning classification could significantly enhance our ability to elucidate trends and patterns in the differentiation process. For instance, single-cell RNA sequencing at various time points during differentiation could reveal the emergence of distinct cell populations and key transcriptional regulators driving retinal fate specification. Machine learning algorithms could then be employed to identify subtle patterns in gene expression or morphological features that predict successful organoid formation, potentially leading to more robust and reproducible protocols.

5.3.8 Evaluating the combined treatment of micropatterned substrates and RA treatment on retinal differentiation

For our second and final combination we performed preliminary studies on micropatterned substrates with the early retinoic acid (RA) treatment at Day 6-12. As we previously observed altered morphology of the vesicles as a result of early RA treatment, specifically in improved neuroepithelium tissue of the generated vesicles, we hypothesised that combining early RA treatment with micropatterned substrates would improve morphological features such as tissue lamination without severe effects on the number of vesicles generated. Similar to the previous study, we performed these experiments in parallel with a non-micropatterned non-preconditioned control and a non-preconditioned micropatterned control culture.

Consistent with our previous study, the assessment of the gross morphology of the HOIK1 cell line revealed that early RA did not drastically alter the organisation of the cultures compared to control samples and non-treated micropatterned samples (Figure 5.25, N = 2 independent batches). For the HOIK1 cell line, we often observed the presence of rounded dark vesicle structures upon growth on micropatterned substrates. However, treatment with early RA has resulted in the loss of these structures. This unexpected finding suggests a potential interaction between RA signalling and the cellular response to topographical cues, possibly involving alterations in cytoskeletal arrangement or cell-substrate adhesion dynamics. Moreover, we observe less distinct spatial patterning, consistent with our previous findings that the RA treatment may be affecting cell and tissue organisation. However, upon observation, these cultures were relatively more spatially patterned compared to non-micropatterned controls, indicating partial preservation of the micropatterning effect.

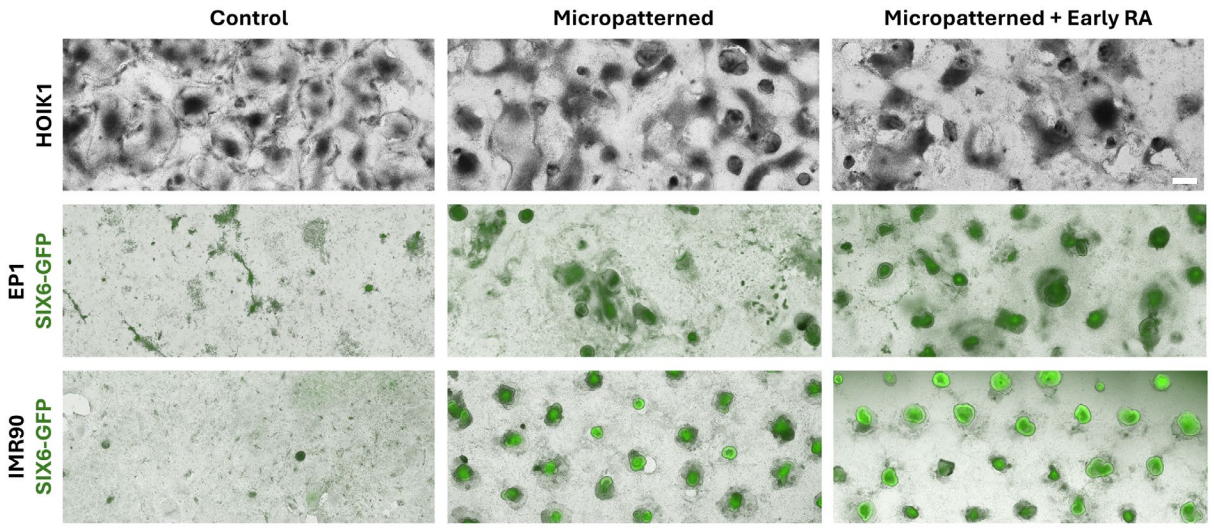

Figure 5.25 Representative images of the capacity of combined micropatterning and early RA treatments (Day 6 – 12) to improve retinal differentiation across three cell lines after 4 weeks of differentiation.

In micropatterned cultures, early RA treatment improved the retention of spatial patterning in the EP1 cell line and improved the formation of neuroepithelium in the IMR90 cell line. Combined treatment did not show a significant effect on HOIK1 cultures. Scale bar = 1000 µm.

In the EP1 cell line, the biochemical treatment relatively improved the maintenance of spatial patterning when combined with micropatterning (Figure 5.25, N = 2 independent batches). We observe the loss of spatial patterning in the non-treated micropatterned cultures, highlighting the potential of RA to stabilise substrate-induced organisational cues in the EP1 cell line. Although this is inconsistent with the observed effects within the HOIK1 cell line, this finding aligns with the role of RA in maintaining positional identity[224] in developing tissues and suggests a potential mechanism for enhancing long-term culture stability. In one particular sample, we surprisingly observed the generation of vesicles with clear neuroepithelial borders in the RA-treated micropatterned culture. This intriguing result, although not entirely consistent throughout the whole well, demonstrates the potential for synergistic effects between biochemical and biophysical cues in organoid development. The fact that the EP1 control

culture possessed no vesicles at all further underscores the transformative potential of this combined approach. This outcome shows the promise of the combined treatment regimen in optimising cell lines that normally do not perform well, possibly by simultaneously providing positional information and fate-specification signals.

Under optimised conditions, with consistency in media handling, cell seeding, and other manual tasks, it is plausible that this result can be achieved consistently throughout the whole tissue culture well. This points to the critical importance of standardisation in complex organoid protocols and suggests that the variability often observed in stem cell-derived organoids might be mitigated through careful control of both biochemical and biophysical parameters. However, due to resource limitations, we did not have the capacity to fully optimise these cultures nor have optimised liquid-handling robotic platforms that could perform such tasks. The potential for automation in this context is substantial, as it could greatly enhance reproducibility and scalability. Regardless, this provides a solid foundation to build upon, in which robust, consistent, and reproducible protocols can then be achieved.

In the IMR90 cell line, we observed a clear difference in morphology upon the combination of the early RA treatment with micropatterned cultures in some samples (Figure 5.25, N = 4 independent batches). We observed the spatial patterning of retinal vesicles with nicely formed and clear neuroepithelial borders. These vesicles had an observable bright GFP signal and a neat background cell population. This improvement in organoid morphology suggests that the IMR90 line may be particularly responsive to the combined treatment, possibly due to its intrinsic state or expression profile of RA receptors. Once again, although there were areas in the well that were less well-formed, improving the consistency of manual tasks such as media changes and cell seeding will likely improve consistency across the entire well; for instance, by minimising human errors and reducing variability caused by inconsistent parameters, such

as the time of day in which media is changed and how much time a tissue culture plate spends outside the incubator. Such platforms may highlight the often-overlooked importance of precise timing and handling in stem cell cultures, where even minor variations in culture conditions can have significant impacts on organoid development[225].

When quantification of the vesicles generated was performed, we observed mixed results in the HOIK1 cell line, likely due to the low number of replicates that were performed (Figure 5.26a). In one replicate, the cells were unable to remain attached to the micropatterned substrate, leading to the loss of cells and, thus, poor formation of any kind of tissue structure due to the lack of cell population. Since the paired control cultures continued to form vesicle structures, a large decrease in fold change was observed for this replicate. This outcome points to the critical role of cell-substrate adhesion in the success of micropatterned cultures and suggests that optimisation of substrate coating or modification of surface chemistry might be necessary for some cell lines. Treatment with RA was not able to rescue this culture, indicating that the biochemical stimulus alone may, at times, be insufficient to overcome fundamental issues with cell attachment. In the other replicate sample, micropatterning improved the overall number of vesicle structures formed, as indicated by one data point showing an increased fold change in the HOIK1 cell line (Figure 5.26a). However, as previously discussed, these structures had poorly formed neuroepithelium and appeared quite dark. This observation raises questions about the relationship between vesicle quantity and quality, and whether the mechanisms driving vesicle formation might be partially decoupled from those governing proper neuroepithelial organisation. RA treatment of this micropatterned culture increased the number of vesicles generated by 28, accounting for a 2.4-fold increase (Figure 5.26a). Although this may provide some small insight into the potential of early RA treatment in improving micropatterned cultures, further replicates are required for any conclusions to be drawn.

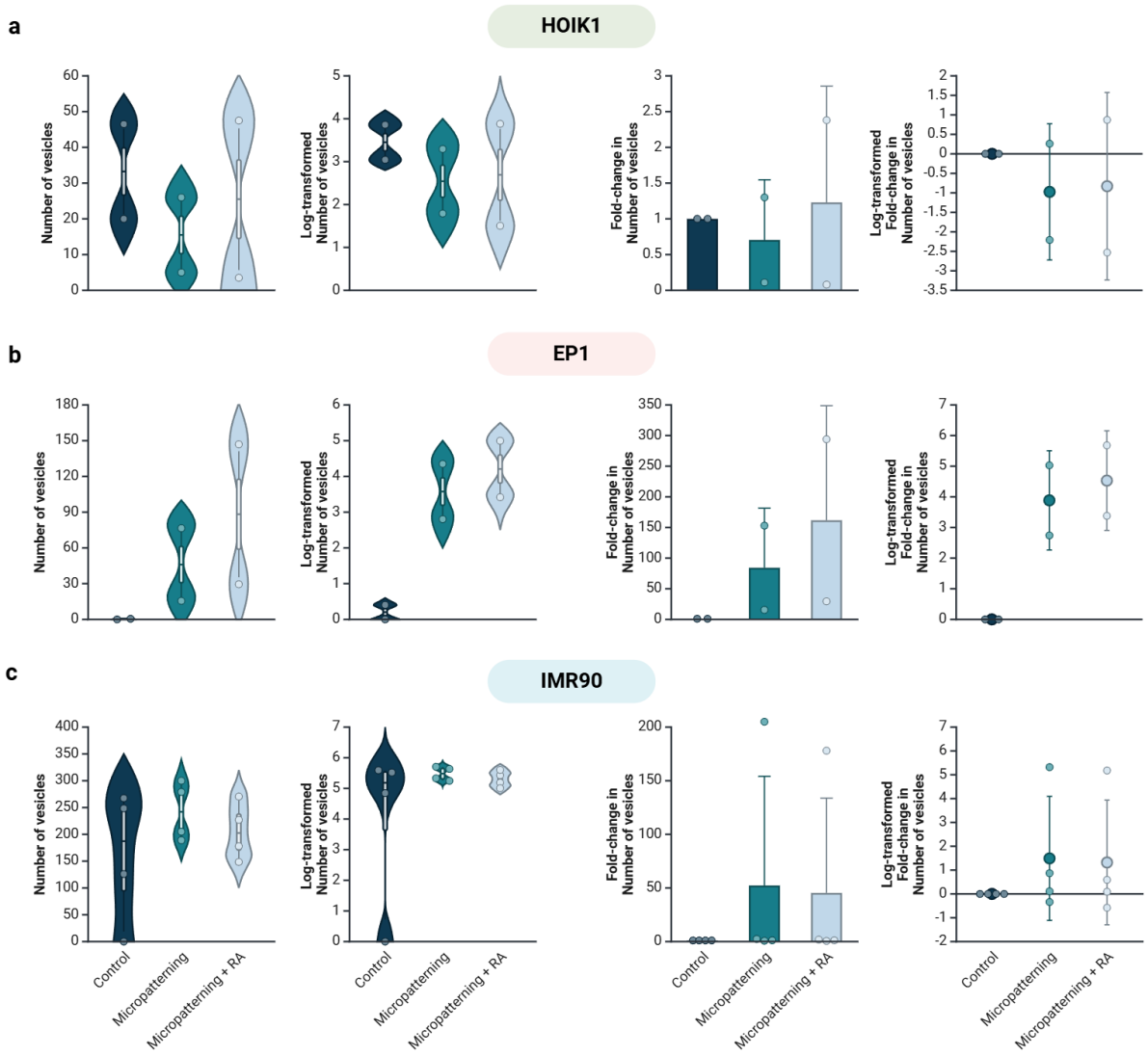

Figure 5.26 Quantification of the average number of vesicles produced (left) and the fold-change within paired samples (right) of combined micropatterning and RA treatments (Day 6 – 12), non-treated micropatterned controls, and non-treated, non-micropatterned controls across three cell lines after 4 weeks of differentiation.

Combined treatments improved the number of vesicles generated in the (a) HOIK1 cell line (Mean ± SD: Control [34.33 ± 13.38], Micropatterned [28.17 ± 24.32], Micropatterned + RA Treatment [35.17 ± 27.65]; N = 2 independent batches, $p > 0.05$) and (b) EP1 cell line (Mean ± SD: Control [0.33 ± 0.29], Micropatterned [36.50 ± 34.66], Micropatterned + RA Treatment [68.50 ± 67.98]; N = 2 independent batches, $p > 0.05$). (c) RA treatment decreased the number of vesicles generated in micropatterned cultures of the IMR90 cell line (Mean ± SD: Control [160.50 ± 124.02], Micropatterned [243.25 ± 54.48], Micropatterned + RA Treatment [206 ± 53.83]; n = 37 mean vesicles difference, N = 4 independent batches, $p > 0.05$).

In the EP1 cell line, both micropatterning with and without RA treatment increased the number of vesicles generated on average (Figure 5.26b, $p > 0.05$). This is mainly the result of the control cultures producing no vesicles at all. As such, micropatterning may have had a strong rescue effect on this cell line. The improvement could suggest the potential of biophysical cues to fundamentally alter the developmental trajectory of stem cell cultures, possibly by creating local microenvironments that mimic aspects of the *in vivo* stem cell niche. Moreover, the high degree of cell crowding offered by spatial confinement may be particularly beneficial for this cell line. As we previously reported in Chapter 3, some cell lines perform favourably under high cell density conditions. Early RA treatment further enhanced the number of vesicles generated (88 vesicles ± 83.09), compared to micropatterned cultures alone (46 vesicles ± 43.13). This may be the result of the RA treatment improving the overall morphogenesis of the vesicles, as we observed from gross morphology alone. Although highly variable, the synergistic effect observed here suggests that combining appropriately timed biochemical signals with optimised physical environments may be a powerful strategy for enhancing organoid generation across various stem cell lines.

Since the EP1 cell line failed to produce vesicles in the control culture in both of our replicate experiments, it remains unclear how the combined micropatterning and RA treatment will affect cultures where the paired control samples successfully produce vesicles. As we previously note, the success of vesicle formation can be dependent on many factors, such as the previous handling and maintenance of the cells, emphasising the need for rigorous standardisation.

However, our previous experiments where micropatterning and RA treatment were performed separately on control cultures that successfully formed organoids strongly suggest that this combined treatment regimen could perform even better when the EP1 cell line is at an initial

state where organoids will successfully form in control cultures. Theoretically, early RA treatment may enable the long-term maintenance of the spatial patterning offered by the micropatterned substrate. The ongoing challenge with this cell line involved the partial loss of spatial patterning over time, though we now have preliminary evidence that early RA treatment has the potential to rectify this, allowing for long-term retention of the patterning. This finding has significant implications for the long-term culture and maturation of organoids, suggesting that periodic or sustained RA treatment might be necessary to maintain optimal organoid architecture over extended culture periods.

Interestingly, in the IMR90 cell line, RA treatment of micropatterned cultures decreased the number of vesicles generated compared to non-treated micropatterned cultures (Figure 5.26c, n = 37 vesicle difference). However, both micropatterned cultures with and without RA treatment performed better than controls on average by 45-fold and 52-fold, respectively ($p > 0.05$). This apparent trade-off between vesicle number and quality—as indicated by improved morphological features—raises important questions about the root cause of the differences between these parameters. It must be noted that a large variation in data was observed for the control cultures due to one replicate sample where the control failed to survive the one-month-long differentiation period.

An important observation was made during the culture of these micropatterned samples. We observed a mass loss of tissue structures over time, predominantly in the micropatterned wells, due to the shear forces caused by fluid flow during media changes. Occasionally, we would observe vesicles floating in the culture, having detached from the cell monolayer due to the highly 3-dimensional structure causing it to bud off from the substrate. This observation should be a key consideration in scaling up organoid production: the need to balance the benefits of 3D structure formation with the practical limitations of current culture systems. As such, it is

expected that, with more gentle handling procedures such as through liquid handling robotic platforms, micropatterned cultures could generate a higher number of vesicles than in the current study. This points to the potential benefits of automating aspects of organoid culture, not just for increased throughput, but also for improving culture outcomes through more consistent and gentle handling.

However, the improved morphological features observed in the RA-treated micropatterned cultures far outweigh the insignificant decrease in the overall number of vesicles generated. This observation is important in consideration of multiple quality parameters when optimising organoid protocols, rather than focusing solely on yield. As such, this combination method of micropatterning and RA treatment is relatively promising in improving the morphological features, the defined spatial location, and the scalability of cell lines that have similar behaviour to the IMR90 cell line.

Quantification of the number of GFP+ areas demonstrated similar results to our previous observations. Although the EP1 cell line resulted in poorly formed vesicles in control cultures, there was a high quantity of GFP+ regions (114 areas ± 74.60) compared to micropatterned (52.50 areas ± 26.87) and treated micropatterned cultures (74.00 areas ± 26.16) (Figure 5.27a). However, we observed that this was the result of poorly formed tissue structures that had a high GFP signal, though they were disorganised and did not form laminated structures. This highlights the limitations of using reporter gene expression alone as a measure of successful organoid formation and emphasises the need for multifaceted assessment of organoid quality, including detailed morphological and functional analyses.

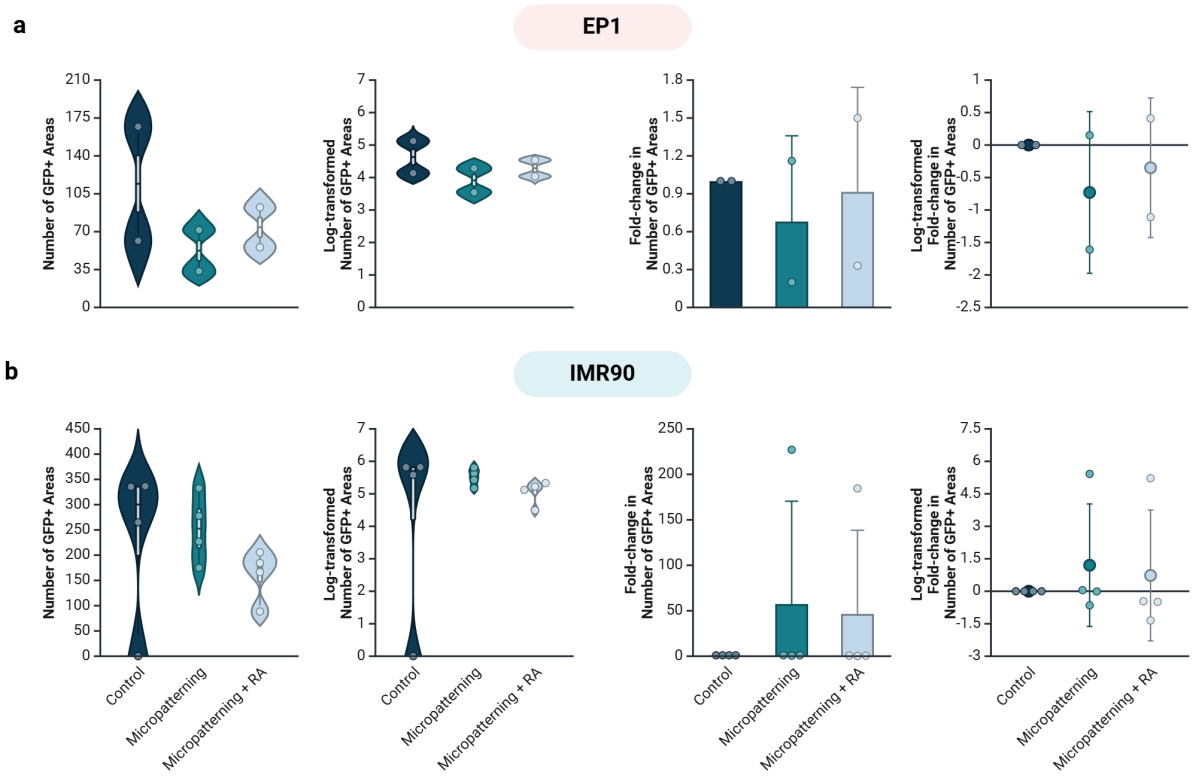

Figure 5.27 Quantification of the average number of GFP+ regions produced (left) and the fold-change within paired samples (right) of combined micropatterning and RA treatments (Day 6 – 12), non-treated micropatterned controls, and non-treated, non-micropatterned controls in SIX6-GFP reporter cell lines after 4 weeks of differentiation. The number of GFP+ regions in micropatterned cultures (a) increased in the EP1 cell line (Mean ± SD: Control [114.2 ± 74.60], Micropatterned [52.50 ± 26.87], Micropatterned + RA Treatment [74 ± 26.16]; N = 2 independent batches, $p > 0.05$) and (b) decreased in the IMR90 cell line (Mean ± SD: Control [234.25 ± 159.71], Micropatterned [253.13 ± 67.59], Micropatterned + RA Treatment [161.25 ± 51.05]; N = 4 independent batches, $p > 0.05$).

Consistent with previous observations, RA treatment of the IMR90 cell line resulted in a decreased number of GFP+ areas formed (161.25 vesicles ± 51.05) compared to non-treated micropatterned cultures (253.12 vesicles ± 67.59) and non-micropatterned controls (234 vesicles ± 159.71) (Figure 5.27b, $p > 0.05$). As we previously hypothesised, early RA treatment may cause stronger signalling centres where the nutrients and signalling molecules are concentrated. As such, these areas result in a high-intensity GFP signal, though an overall

reduced number of unique GFP+ regions. This observation aligns with the current understanding of morphogen gradient formation in developing tissues[225] and suggests that our combined treatment approach may potentially be creating more physiologically relevant signalling environments within the organoid cultures.

As such, future work to characterise the distribution of GFP intensity throughout the well will provide interesting insights into the modulation of SIX6 signalling and eye field specification dynamics occurring within the batch culture. These insights will inform future experiments and optimisation steps and provide a better understanding of how RA signalling, as well as micropatterning, affects the overall culture. However, as we are concerned mainly with spatial patterning and the quantity of vesicles successfully produced, such in-depth quantitative analysis is currently outside of the scope of this work. Nonetheless, this line of inquiry represents an exciting direction for future research, potentially linking macro-scale culture outcomes with molecular-level patterning events.

Overall, this technique shows strong promise in potentiating the clinical translation of retinal vesicles for cell replacement therapies. It is likely that thousands of organoids will need to be produced to meet the scale of photoreceptor cells required for clinical outcomes. Not only is it challenging to achieve this due to the stochasticity and variability of stem cell cultures, but this task would require hours of manual labour to selectively collect the grown vesicles for long-term maturation in suspension culture. Even with the use of automated systems to collect these tissues, the random locations in which these tissues appear is a significant challenge and would still likely require manual supervision to correctly identify whether a tissue is retinal, cortical, or another tissue type—particularly since fluorescent reporter cell lines cannot be utilised for transplantation applications. These techniques may require high skill, expertise, and experience, and can inherently induce human bias and error.

As such, techniques to spatially define where vesicles can grow within the 2D culture plate are critical for the clinical translation of these protocols. Moreover, ensuring these tissues have a well-defined morphology that is consistent between batches is equally crucial. In platforms where vesicle formation is highly predictable, simple automation can be achieved by defining where robotic platforms can collect grown tissues. As such, minimal human supervision could be required, allowing for high scalability and less error, assuming an optimised robotic platform. This approach represents a significant step towards addressing the bottlenecks in large-scale production of high-quality organoids for clinical applications, potentially bridging the gap between laboratory-scale organoid research and clinical-scale tissue engineering.

5.4 Conclusion

Our comprehensive investigation into the optimisation of retinal vesicle generation from confluent stem cell populations has revealed complex, line-specific responses to various signalling pathway modulations. We explored the effects of preconditioning, timed media treatments, RA supplementation, and transient FGF2/TGF-beta stimulation. Crucially, we utilised three different cell lines to assess the broader applicability of these treatments, recognising the potential for line-specific responses to signalling modulation.

Preconditioning through dual SMAD inhibition showed the potential to improve retinal vesicle formation, particularly in the HOIK1 line. Timed media treatments involving WNT inhibition and SHH pathway activation demonstrated variable efficacy, with the HOIK1 line showing the most consistent improvements. RA supplementation at different time points revealed a critical window for intervention, with early treatment (Day 6-12) generally yielding more positive outcomes across all lines. Transient FGF2 and TGF-beta stimulation through an E8 medium pulse unexpectedly improved vesicle formation in the HOIK1 line while decreasing neuralisation in EP1 and IMR90 lines. This finding underscores the delicate balance of signalling required for successful retinal differentiation and the potential benefits of brief exposure to pluripotency-maintaining factors.

Importantly, our qPCR analysis of baseline signalling pathway activation in undifferentiated iPSCs revealed significant variability both within and between cell lines across different passage numbers. This intrinsic variability likely contributes to the inconsistent outcomes observed in retinal differentiation experiments and highlights the need for tailored line-specific approaches.

Collectively, these findings emphasise the complexity involved in the biochemical modulation of retinal vesicle morphogenesis. We demonstrate that there may be a fine balance between excessive modulation and harnessing the inherent capacity of iPSCs to self-organise in highly structured tissues under certain conditions. However, as we apply an iterative top-down approach based predominantly on tissue-scale morphological features, we recognise that further characterisation of these cell populations at the molecular level will better elucidate the mechanisms underlying retinal morphogenesis *in vitro*.

Chapter 6: Conclusions and Recommendations

6.1 Conclusions

The current research has made substantial progress in identifying parameters required for spatial patterning and improving the generation of stem cell-derived retinal vesicles from 2D confluent monolayers. By utilising engineering techniques and iterative parameter testing, we have developed innovative solutions to enhance the generation and potential scalability of retinal organoid formation—a critical source of human photoreceptor cells for cell replacement therapies.

As eye field specification initiates within the anterior neural plate of the developing embryo, we initially explored the behaviour of iPSC-derived neural tissues on micropatterned glass substrates. We effectively fabricated PEG-based micropatterns using our in-house custom-built printer and, subsequently, through our newly developed high-throughput and high-resolution photomask method. While we demonstrated that various sizes and geometries could support short-term tissue growth, particularly when supplemented with Matrigel to form 3D structures, long-term viability proved challenging. Within the 4-week differentiation period, some vesicle structures formed, but we observed poor viability and high variability. This unexpected result provided crucial insights, indicating that neural cells have limited capacity to thrive on glass substrates in the long term, especially when spatially confined.

These findings led us to shift our focus towards the substrate in which we know retinal vesicles can grow—tissue culture-treated plastics. Through extensive iteration and methodology development, we discovered a novel method for micropatterning TCP. This unique approach used direct UV light to alter regions of the standard ECM coating, effectively defining areas for cell attachment on the TCP surface. We observed that cells attached and grew well on patterns containing ECM. Surprisingly, differentiating cells could eventually outgrow this

initial spatial confinement—a behaviour not previously reported in established work, except in cases of suboptimal micropatterning. This unexpected phenomenon proved critical in enabling the spatially defined self-organisation of retinal vesicles.

In the final phase of our research, we characterised biochemical modulation treatments that had yet to be applied to 2D confluent monolayer cultures for retinal organoid generation. Our top-down approach, building from previous literature, proved valuable in better understanding how the modulation of specific pathways affects retinal vesicle morphogenesis. We began by translating established treatments to our 2D platform, which allowed us to characterise the morphological behaviours of batch retinal cultures. This understanding informed the development of tailored treatment regimens more suited to our platform.

The combination of biochemical treatments with micropatterning techniques showed potential for synergistic effects, moving us closer to the large-scale generation of well-organised retinal vesicles. Our results indicated improvements in vesicle generation for at least one of the tested cell lines for each individual treatment group, though the effects were highly cell line-dependent and variable. This variability highlighted the importance of tailoring treatment regimens to cell lines and the ongoing need for improved batch-to-batch reproducibility.

Throughout our work, we focused on enhancing the formation of vesicles with a characteristic neuroepithelial border through biophysical and biochemical alterations. While our methods showed promise in improving both the number and structural morphology of generated vesicles, we recognise that further research is needed to fully optimise these processes. Our work forms a foundation for enabling the clinical translation of iPSC-derived retinal tissues formed from confluent monolayers. By addressing the current limitations of random

organisation in traditional platforms, we have taken important steps towards more controlled and efficient production of retinal organoids.

Our findings open new avenues for research and development in the field of regenerative medicine. As we continue to refine these techniques, we move closer to realising the potential of cell replacement therapies for retinal diseases.

6.2 Limitations of the current work

The experimental work conducted in this thesis established key biophysical and biochemical parameters required to spatially define the self-organisation of retinal vesicles. Nevertheless, there were limitations to our study that must be acknowledged. Restrictions in resources and time influenced both the breadth and depth of the performed experiments, particularly in drawing more defined conclusions from our collected results. It is also recognised that the COVID-19 pandemic, which caused mass lockdowns in Sydney from June to October 2021, caused major disruption and delay to the experimental work due to restricted access to the laboratory—particularly in the first year where much of the hands-on laboratory skills are learned and developed. Specific limitations of the experimental work presented in this thesis are as follows:

In Chapter 2, describing glass micropatterning techniques, some limitations included the resolution of the patterning. The custom-built printer used for glass micropatterning provided high precision in controlling the laser position in the x-y plane. However, achieving optimal laser focus on the sample was critical for fabricating desired geometries with high fidelity. This task demanded considerable skill and understanding of the platform to attain accurate calibration as guided by the designed g-code scripts. Due to time constraints, we acknowledge that this calibration was not always achieved to an optimum level.

Regions of cell detachment were frequently observed in some of our replicate micropatterned cultures, even in the absence of noticeable microbial contamination. Owing to limitations in time and analytical resources, we were unable to conduct experimental work to determine the cause of this phenomenon. Consequently, the outcomes of this work were occasionally

influenced by unexpected poor cell attachment. Analysis of these substrates was performed on a limited number of sample replicates due to the aforementioned attachment issues.

For Chapters 3 and 4, the developed method of tissue culture plastic micropatterning included some limitations. The micropatterning setup developed for tissue culture, while effective, was rudimentary. Working within the constraints of available resources and time, we were unable to create a more sophisticated platform. This resulted in limitations in the consistency of micropatterning both within individual wells and between different wells. Nevertheless, the simplicity of the technology is attractive to widespread implementation in many laboratories.

Furthermore, and not surprisingly, we observed that cell lines behaved differently on the micropatterned substrates. Ideally, optimisation of culture conditions for each cell line would have provided better insights into cell line-dependent requirements. However, the extended culture period required for retinal vesicle formation, typically a minimum of one month, precluded us from optimising conditions for each cell line due to time constraints. Instead, all cell lines were subjected to the same treatment. While this approach limited our ability to gain detailed insights into each cell line, it allowed for a broader understanding of how different cell lines respond to uniform conditions.

The use of manual pipetting, rather than automated liquid handling, occasionally resulted in the detachment of vesicles grown on micropatterned plates. This significantly affected the final vesicle count due to the loss of these detached structures. While we sometimes observed this loss in non-micropatterned control cultures as well, it was more prominent in micropatterned cultures due to the significant three-dimensionality of the generated tissues, which made them more susceptible to detachment from excessive pipetting force. In fact, this feature will be

beneficial in the long term where we aim to lift off vesicles out of the 2D plate by simply shaking the plate.

Although we did not perform extensive analysis of the generated vesicles post-micropatterning, the core of the original protocol remained largely unchanged, with our modifications primarily targeting the culture vessel. This gave us a strong rationale to expect that the fundamental characteristics of the organoids would remain consistent with those previously reported for this protocol.

In Chapter 5, where biochemical modulation was applied to cultures, some limitations to the work include the reliance on two SIX6-GFP reporter cell lines to confirm retinal cell fate, specifically early eye field specification, and tissue morphology was used to confirm successful self-organisation. While the use of endogenous cell lines is a state-of-the-art method to establish efficient differentiation and formation of vesicle structures, we acknowledge that no further investigations, such as immunohistochemistry and in-depth RNA sequencing techniques, were performed to further characterise tissue fate. Nevertheless, the use of GFP reporters provided a reliable, non-invasive method to confirm organoid identity throughout the culture period without the need for fixation and immunostaining.

The challenges of maintaining consistent stem cell cultures over extended periods are well-recognised in the field. Our study reflected this reality, with some experimental work having low sample numbers due to time limitations and culture variability. We occasionally experienced unexpected cell detachment and spontaneous differentiation for unknown reasons, which reduced the number of replicates we could perform and impacted our ability to draw strong statistical conclusions. It's worth noting that while some of our sample sizes may seem

small, they represent a significant investment of time and resources in iPSC-derived organoid research, with each replicate demanding a full month to complete.

Long-term analysis of how treatments affect cell composition was unfeasible within the scope of this project, as such studies can take up to four months per replicate, and we had numerous different treatments to assess. Our decision to focus on shorter-term outcomes allowed for the evaluation of a wider range of conditions, providing a broad foundation for understanding the early stages of retinal organoid formation. While we recognise the value of long-term studies, the insights gained from these shorter-term experiments guided the selection of the most promising conditions for future, more extended studies.

Other general limitations that are worth noting include the potential impact of well position on experimental outcomes. This was not systematically tested in our study; however, to mitigate this, we consistently placed control cultures in the left wells of the culture plates and conducted all experiments in duplicate. While this approach provided some control over positional variables, it falls short of a fully randomised design, which would be ideal for eliminating position-related bias.

Excessive mechanical stress during routine media changes resulted in areas of high shear forces in some culture wells. This shear force-induced damage likely affected the growth and development of organoids in these areas, potentially impacting the overall results. The consistent occurrence of this phenomenon across conditions allowed for comparative analysis but highlights the need for gentler media change techniques in future studies, particularly for potential clinical applications.

Significant variability was observed between different batches of cells used in the experiments. While this variability is a well-recognised challenge in stem cell research, it introduces an

additional layer of complexity to data interpretation. However, the use of multiple batches also enhances the robustness and generalisability of consistent findings, providing a more realistic representation of the variability that would be encountered in scaled up or clinical applications.

A machine learning model was employed to quantify the bulk of the data, trained on images from all cell types used in the study. While this approach allowed for efficient processing of large datasets, limitations in the accuracy of vesicle structure segmentation were noted. Some segmented areas were larger or smaller than what would be identified by manual segmentation. Despite these limitations, the consistency of the approach across all samples allowed for valid comparisons between conditions.

Both raw data and fold-change data were used to visualise changes caused by the experimental treatments. While fold-change data effectively illustrates relative changes compared to time-matched controls, it can potentially exaggerate effects when control numbers are very low. For instance, a change from a single vesicle in the control to ten in the treatment would result in a large fold-change, potentially overstating the magnitude of the treatment's effects.

The study heavily relied on brightfield imaging for assessing organoid development. While this method provided crucial qualitative data and allowed for real-time, non-disruptive monitoring of organoid formation and structural integrity, it limited the depth of quantitative analysis possible. The choice of brightfield imaging was justified by the nature of early-stage organoid development, where few relevant quantitative measurements could be consistently applied across all conditions and time points. Moreover, the non-destructive nature of the analysis technique—where other techniques would require the collection and, thus, destruction of a sample—was critical due to the stochastic nature of our cellular studies. To complement these

qualitative assessments, the number of successfully formed organoids under each condition was quantified, providing a numerical measure of protocol efficacy.

These limitations reflect the complex challenges inherent in stem cell and organoid research. While they present obstacles to data interpretation and generalisability, they also provide valuable insights for future studies. The approaches chosen represent pragmatic solutions to the constraints of time, resources, and technical capabilities within the scope of this work. By transparently acknowledging these limitations, we aim to contextualise our findings and contribute to the ongoing refinement of methodologies in stem cell and organoid research.

6.3 Future recommendations

The following section outlines key directions for future research and recommendations to build upon and extend the findings of this study.

One of the most promising directions for future work is the translation of the developed protocols to other tissue types. While our focus has been on retinal vesicles, the principles of spatial patterning and biochemical modulation could potentially be applied to generate other complex tissues such as brain organoids, vascular structures, or cardiac tissues. This translation would not only validate the broader applicability of our approach but could also lead to significant advancements in various areas of regenerative medicine. Already, we have observed the micropatterned generation of cortical brain organoids, where further assessment of these tissues—such as through immunofluorescent co-staining or functional assays—could advance high-throughput outcomes in this research area. We recommend collaborative projects with researchers specialising in other tissue types to adapt and optimise our protocols. This could involve modifying the micropatterning geometries to suit different tissue architectures and adjusting biochemical treatments to target tissue-specific developmental pathways. Moreover, further characterisation of the micropatterned features and surface—such as through electron microscopy or Fourier transform infrared spectroscopy—may lead to meaningful insights into topology-specific cues affecting cell behaviours.

While our current platform has demonstrated the feasibility of spatially defining retinal vesicle formation, there is significant room for optimisation to enhance uniformity and enable high-throughput production. This is crucial for scaling up the technology for potential clinical applications and large-scale drug screening efforts. We recommend developing an automated system for micropatterning. The group is currently developing automation for the maintenance

of pluripotent stem cells and organoid cultures. This involves the design of specialised liquid handling robots for gentle media changes and the creation of standardised, mass-producible culturing, which will be adapted for micropatterned substrates. Additionally, investigating the use of microfluidic devices to provide consistent nutrient and growth factor gradients across cultures could further enhance the uniformity of organoid production.

Our current study primarily relied on morphological assessment and GFP reporter expression to characterise the formed tissues. To gain a more comprehensive understanding of the cellular composition and developmental trajectories of the generated vesicles, more advanced molecular analyses are necessary. We recommend conducting in-depth RNA and protein sequencing studies on vesicles formed under different conditions to elucidate the molecular mechanisms underlying successful organoid formation. Such protein-level studies could be crucial in elucidating key pathways driving retinal differentiation, particularly in conjunction with biochemical modulation studies. Moreover, cell isolation techniques such as fluorescence- or magnetic-activated cell sorting can provide higher precision in the quantification of the retinal tissue cellular composition. These insights are critical in improving our understanding of the heterogeneity of cell populations present and the consistency of organoids within and between differentiation batches.

A deeper understanding of the cell population dynamics within the culture well and the mechanics of morphogenesis and self-organisation is crucial for optimising and controlling organoid formation. We suggest utilising live-cell and three-dimensional imaging techniques in high throughput confocal microscopes, such as the system applied in this work, to track cell movements and divisions during vesicle formation. Combining this with computational modelling to simulate and predict the physical forces and cellular interactions driving self-organisation could provide valuable insights. Optimising the initial cell seeding density may

further elucidate the influence of cell-cell and cell-matrix interactions and potentially enhance micropatterned cultures. Additionally, investigating the role of extracellular matrix components in guiding tissue formation by manipulating matrix composition and stiffness could further our understanding of the self-organisation process.

While our study explored various pattern dimensions, a thorough investigation of the optimal spacing between patterns for different cell lines. Cell line-specific optimisation could significantly impact the efficiency and quality of organoid formation. We recommend conducting a systematic study varying the spacing between micropatterned areas for each cell line used in the study. This could reveal cell line-specific preferences for spatial confinement or expansion, potentially leading to tailored protocols for different stem cell sources. Utilising high-content imaging and machine learning approaches similar to the ones used in this study to efficiently analyse the large datasets generated from these experiments would continue to be beneficial.

The wealth of time point image data collected during this study presents numerous opportunities for further analysis and exploration. While the current research focused on quantifying the final number of tissue structures formed at ~day 30 in culture, several additional analytical approaches could yield valuable insights into the self-organisation process. We recommend developing spatial distribution maps to visualise the likelihood of tissue formation across different areas of the culture well, analysing colour and intensity changes in culture images over time, conducting growth rate analysis of individual tissue structures, performing detailed morphological analysis, employing machine learning approaches for predictive modelling, and creating time-lapse visualisations of tissue development. Research on some of these analyses is currently underway in our lab.

Understanding the long-term maturation and stability of spatially patterned retinal vesicles is crucial for their potential therapeutic applications. We suggest the long-term culture of these structures, potentially up to four months or longer. Investigating the effect of different culture conditions, such as mechanical stimulation or co-culture with supportive cell types, on the maturation and functionality of the retinal tissues could similarly provide valuable insights. The assays being developed in the laboratory to assess the electrophysiological properties and light responsiveness of the mature organoids are crucial for evaluating the potential of organoids for therapeutic efficacy.

To move towards clinical applications, it is essential to adapt the developed protocols to fully GMP-compliant systems. Technologies such as closed-system liquid handling robotics for organoid production that meet GMP standards are essential. Since our platform can be feasibly utilised without ever requiring the lid of a tissue culture plate to be removed outside of the biosafety cabinet, we envision the high potential for translation towards automated closed systems.

The field of tissue engineering is rapidly evolving, and integrating our approach with other cutting-edge technologies could lead to significant advancements. We suggest exploring the combination of our spatial patterning techniques with bioprinting technologies to create more complex, multi-layered retinal tissues. Investigating the use of stimuli-responsive biomaterials could allow dynamic control over tissue organisation.

The future directions and recommendations outlined here represent a roadmap for building upon the foundational work presented in this thesis. By pursuing these lines of inquiry, future research could significantly advance our understanding of retinal organoid formation and self-organisation, potentially leading to improved methods for controlling and predicting tissue

formation in culture. These advancements could have far-reaching implications for tissue engineering, regenerative medicine, and our broader understanding of developmental biology. As we continue to unravel the complex processes underlying tissue self-organisation, the insights gained from these proposed studies could contribute to the development of more efficient and predictable methods for generating complex tissue structures *in vitro*. By addressing the challenges and pursuing the opportunities identified in this thesis, future research can continue to push the boundaries of what is possible in organoid technology.

Postscript

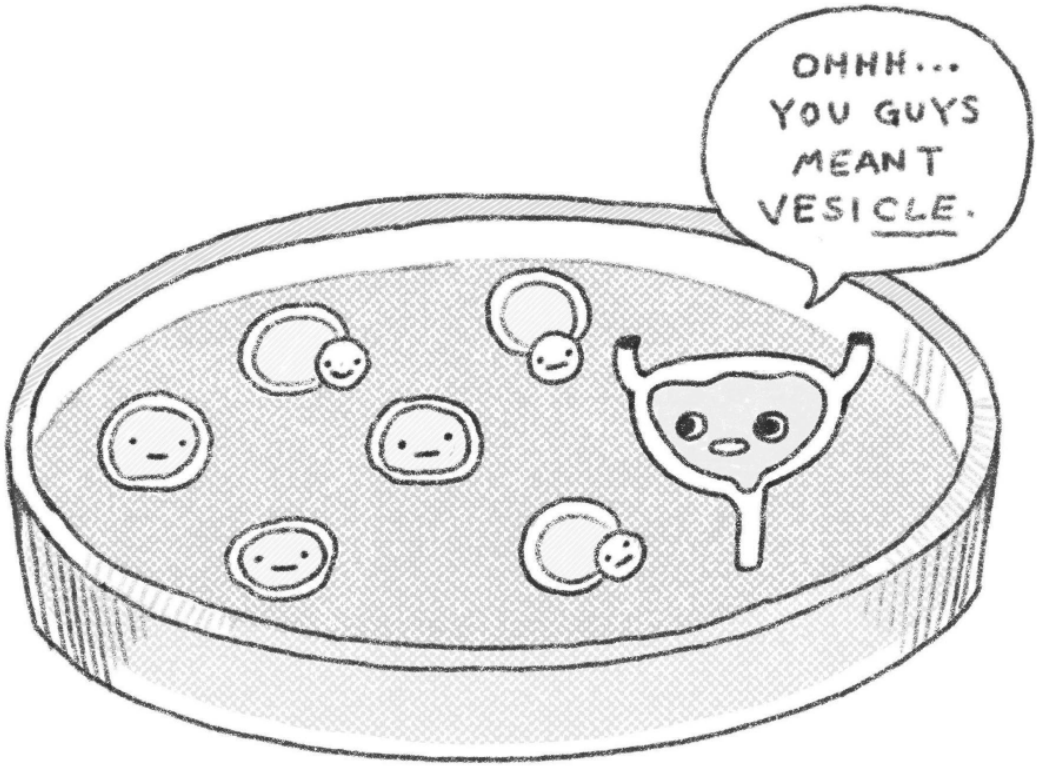

"Brain or retinal, vesicle or vesical, you're always welcome here."

List of References

1 Thomson, J. A. *et al.* Embryonic stem cell lines derived from human blastocysts. *Science (New York, N.Y.)* **282**, 1145-1147, doi:10.1126/science.282.5391.1145 (1998).

2 Hochedlinger, K. & Jaenisch, R. Nuclear reprogramming and pluripotency. *Nature* **441**, 1061-1067, doi:10.1038/nature04955 (2006).

3 Takahashi, K. & Yamanaka, S. Induction of pluripotent stem cells from mouse embryonic and adult fibroblast cultures by defined factors. *Cell* **126**, 663-676, doi:10.1016/j.cell.2006.07.024 (2006).

4 Hofer, M. & Lutolf, M. P. Engineering organoids. *Nature Reviews Materials* **6**, 402-420 (2021).

5 Antfolk, M. & Jensen, K. B. A bioengineering perspective on modelling the intestinal epithelial physiology in vitro. *Nature Communications* **11**, 6244 (2020).

6 Song, G. *et al.* The application of brain organoid technology in stroke research: challenges and prospects. *Frontiers in Cellular Neuroscience* **15**, 646921 (2021).

7 Singh, M. S. *et al.* Retinal stem cell transplantation: Balancing safety and potential. *Progress in retinal and eye research* **75**, 100779 (2020).

8 Zhao, Z. *et al.* Organoids. *Nature Reviews Methods Primers* **2**, 94 (2022).

9 Marques, A. P. *et al.* Global economic productivity losses from vision impairment and blindness. *EClinicalMedicine* **35**, 100852 (2021).

10 de Guimaraes, T. A. C., Varela, M. D., Georgiou, M. & Michaelides, M. Treatments for dry age-related macular degeneration: therapeutic avenues, clinical trials and future directions. *British Journal of Ophthalmology* **106**, 297-304 (2022).

11 Gasparini, S. J., Llonch, S., Borsch, O. & Ader, M. Transplantation of photoreceptors into the degenerative retina: Current state and future perspectives. *Progress in retinal and eye research* **69**, 1-37 (2019).

12 Sharma, R., Bose, D., Maminishkis, A. & Bharti, K. Retinal pigment epithelium replacement therapy for age-related macular degeneration: are we there yet? *Annual Review of Pharmacology and Toxicology* **60**, 553-572 (2020).

13 O'Hara-Wright, M. & Gonzalez-Cordero, A. Retinal organoids: a window into human retinal development. *Development* **147**, dev189746 (2020).

14 Afanasyeva, T. A. *et al.* A look into retinal organoids: Methods, analytical techniques, and applications. *Cellular and Molecular Life Sciences* **78**, 6505-6532 (2021).

15 da Cruz, L. *et al.* Phase 1 clinical study of an embryonic stem cell–derived retinal pigment epithelium patch in age-related macular degeneration. *Nature Biotechnology* **36**, 328-337 (2018).

16 Kashani, A. H. *et al.* A bioengineered retinal pigment epithelial monolayer for advanced, dry age-related macular degeneration. *Science translational medicine* **10**, eaao4097 (2018).

17 Gagliardi, G., M'Barek, K. B. & Goureau, O. Photoreceptor cell replacement in macular degeneration and retinitis pigmentosa: a pluripotent stem cell-based approach. *Progress in retinal and eye research* **71**, 1-25 (2019).

18 Hirami, Y. *et al.* Safety and stable survival of stem-cell-derived retinal organoid for 2 years in patients with retinitis pigmentosa. *Cell Stem Cell* **30**, 1585-1596. e1586 (2023).

19 National Institute of Public Health of Japan. *Japan Registry of Clinical Trials*, <https://jrct.niph.go.jp/en-latest-detail/jRCTa050200027> (2020).

20 Arthur, P. *et al.* Bioengineering human pluripotent stem cell-derived retinal organoids and optic vesicle-containing brain organoids for ocular diseases. *Cells* **11**, 3429 (2022).

21 Kolb, H., Nelson, R. F., Ahnelt, P. K., Ortuño-Lizarán, I. & Cuenca, N. The architecture of the human fovea. *Webvision: The Organization of the Retina and Visual System [Internet]* (2020).

22 Naylor, A., Hopkins, A., Hudson, N. & Campbell, M. Tight junctions of the outer blood retina barrier. *International journal of molecular sciences* **21**, 211 (2019).

23 Campochiaro, P. A., Hackett, S. F. & Vinores, S. A. Growth factors in the retina and retinal pigmented epithelium. *Progress in Retinal and Eye Research* **15**, 547-567 (1996).

24 Sethna, S. *et al.* CIB2 regulates mTORC1 signaling and is essential for autophagy and visual function. *Nature communications* **12**, 1-19 (2021).

25 Yang, S., Zhou, J. & Li, D. Functions and diseases of the retinal pigment epithelium. *Frontiers in Pharmacology*, 1976 (2021).

26 Booij, J. C., Baas, D. C., Beisekeeva, J., Gorgels, T. G. & Bergen, A. A. The dynamic nature of Bruch's membrane. *Progress in retinal and eye research* **29**, 1-18 (2010).

27 Fuhrmann, S. Eye morphogenesis and patterning of the optic vesicle. *Current topics in developmental biology* **93**, 61-84 (2010).

28 Li, H.-s., Tierney, C., Wen, L., Wu, J. Y. & Rao, Y. A single morphogenetic field gives rise to two retina primordia under the influence of the prechordal plate. *Development* **124**, 603-615 (1997).

29 Elkouris, M. *et al.* Sox1 maintains the undifferentiated state of cortical neural progenitor cells via the suppression of Prox1-mediated cell cycle exit and neurogenesis. *Stem Cells* **29**, 89-98 (2011).

30 Venere, M. *et al.* Sox1 marks an activated neural stem/progenitor cell in the hippocampus. *Development* **139**, 3938-3949 (2012).

31 Kamachi, Y., Uchikawa, M., Collignon, J., Lovell-Badge, R. & Kondoh, H. Involvement of Sox1, 2 and 3 in the early and subsequent molecular events of lens induction. *Development* **125**, 2521-2532 (1998).

32 Pevny, L. H., Sockanathan, S., Placzek, M. & Lovell-Badge, R. A role for SOX1 in neural determination. *Development* **125**, 1967-1978 (1998).

33 Hufnagel, R. & Brown, N. L. Specification of retinal cell types. (2013).

34 Chen, J. *et al.* Analysis of expression of transcription factors in early human retina. *International Journal of Developmental Neuroscience* **60**, 94-102 (2017).

35 Coutinho, P. *et al.* Discovery and assessment of conserved Pax6 target genes and enhancers. *Genome research* **21**, 1349-1359 (2011).

36 Yasue, A. *et al.* Relationship between somatic mosaicism of Pax6 mutation and variable developmental eye abnormalities—an analysis of CRISPR genome-edited mouse embryos. *Scientific reports* **7**, 1-10 (2017).

37 Porter, F. D. *et al.* Lhx2, a LIM homeobox gene, is required for eye, forebrain, and definitive erythrocyte development. *Development* **124**, 2935-2944 (1997).

38 Rohde, K., Bering, T., Furukawa, T. & Rath, M. F. A modulatory role of the Rax homeobox gene in mature pineal gland function: Investigating the photoneuroendocrine circadian system of a Rax conditional knockout mouse. *Journal of Neurochemistry* **143**, 100-111 (2017).

39 Toy, J., Yang, J.-M., Leppert, G. S. & Sundin, O. H. The Optx 2 homeobox gene is expressed in early precursors of the eye and activates retina-specific genes. *Proceedings of the National Academy of Sciences* **95**, 10643-10648 (1998).

40 Toy, J. & Sundin, O. H. Expression of the optx2 homeobox gene during mouse development. *Mechanisms of development* **83**, 183-186 (1999).

41 Capowski, E. E. *et al.* Loss of MITF expression during human embryonic stem cell differentiation disrupts retinal pigment epithelium development and optic vesicle cell proliferation. *Human molecular genetics* **23**, 6332-6344 (2014).

42 Irie, S. *et al.* Rax homeoprotein regulates photoreceptor cell maturation and survival in association with Crx in the postnatal mouse retina. *Molecular and cellular biology* **35**, 2583-2596 (2015).

43 Amini, R., Rocha-Martins, M. & Norden, C. Neuronal migration and lamination in the vertebrate retina. *Frontiers in neuroscience* **11**, 742 (2018).

44 O'Rahilly, R. R. & Fabiola, M. *The embryonic human brain: an atlas of developmental stages*. (John Wiley & Sons, 2006).

45 Reichman, S. *et al.* From confluent human iPS cells to self-forming neural retina and retinal pigmented epithelium. *Proceedings of the National Academy of Sciences* **111**, 8518-8523 (2014).

46 Gonzalez-Cordero, A. *et al.* Recapitulation of human retinal development from human pluripotent stem cells generates transplantable populations of cone photoreceptors. *Stem cell reports* **9**, 820-837 (2017).

47 Nakano, T. *et al.* Self-formation of optic cups and storable stratified neural retina from human ESCs. *Cell Stem Cell* **10**, 771-785 (2012).

48 Eiraku, M. *et al.* Self-organizing optic-cup morphogenesis in three-dimensional culture. *Nature* **472**, 51-56 (2011).

49 Zhong, X. *et al.* Generation of three-dimensional retinal tissue with functional photoreceptors from human iPSCs. *Nature Communications* **5**, 1-14 (2014).

50 Cowan, C. S. *et al.* Cell types of the human retina and its organoids at single-cell resolution. *Cell* **182**, 1623-1640. e1634 (2020).

51 Meyer, J. S. *et al.* Optic vesicle-like structures derived from human pluripotent stem cells facilitate a customized approach to retinal disease treatment. *Stem Cells* **29**, 1206-1218 (2011).

52 Capowski, E. E. *et al.* Reproducibility and staging of 3D human retinal organoids across multiple pluripotent stem cell lines. *Development* **146**, dev171686 (2019).

53 Kim, H. J. *et al.* Comprehensive characterization of fetal and mature retinal cell identity to assess the fidelity of retinal organoids. *Stem cell reports* **18**, 175-189 (2023).

54 West, E. L. *et al.* Antioxidant and lipid supplementation improve the development of photoreceptor outer segments in pluripotent stem cell-derived retinal organoids. *Stem cell reports* **17**, 775-788 (2022).

55 Saha, A. *et al.* Cone photoreceptors in human stem cell-derived retinal organoids demonstrate intrinsic light responses that mimic those of primate fovea. *Cell Stem Cell* **29**, 460-471. e463 (2022).

56 Oswald, J. & Baranov, P. Regenerative medicine in the retina: from stem cells to cell replacement therapy. *Therapeutic advances in ophthalmology* **10**, 2515841418774433 (2018).

57 Ribeiro, J. *et al.* Restoration of visual function in advanced disease after transplantation of purified human pluripotent stem cell-derived cone photoreceptors. *Cell Reports* **35**, 109022 (2021).

58 Mandai, M. *et al.* iPSC-derived retina transplants improve vision in rd1 end-stage retinal-degeneration mice. *Stem cell reports* **8**, 69-83 (2017).

59 Garita-Hernandez, M. *et al.* Restoration of visual function by transplantation of optogenetically engineered photoreceptors. *Nature Communications* **10**, 4524 (2019).

60 Gagliardi, G. *et al.* Characterization and transplantation of CD73-positive photoreceptors isolated from human iPSC-derived retinal organoids. *Stem cell reports* **11**, 665-680 (2018).

61 Zhu, J., Cifuentes, H., Reynolds, J. & Lamba, D. A. Immunosuppression via loss of IL2rγ enhances long-term functional integration of hESC-derived photoreceptors in the mouse retina. *Cell Stem Cell* **20**, 374-384. e375 (2017).

62 Shirai, H. *et al.* Transplantation of human embryonic stem cell-derived retinal tissue in two primate models of retinal degeneration. *Proceedings of the National Academy of Sciences* **113**, E81-E90 (2016).

63 Tu, H.-Y. *et al.* Medium-to long-term survival and functional examination of human iPSC-derived retinas in rat and primate models of retinal degeneration. *EBioMedicine* **39**, 562-574 (2019).

64 Uyama, H. *et al.* Competency of iPSC-derived retinas in MHC-mismatched transplantation in non-human primates. *Stem cell reports* **17**, 2392-2408 (2022).

65 Das, T. *et al.* The transplantation of human fetal neuroretinal cells in advanced retinitis pigmentosa patients: results of a long-term safety study. *Experimental neurology* **157**, 58-68 (1999).

66 Humayun, M. S. *et al.* Human neural retinal transplantation. *Investigative Ophthalmology & Visual Science* **41**, 3100-3106 (2000).

67 Radtke, N. D., Seiler, M. J., Aramant, R. B., Petry, H. M. & Pidwell, D. J. Transplantation of intact sheets of fetal neural retina with its retinal pigment epithelium in retinitis pigmentosa patients. *American Journal of Ophthalmology* **133**, 544-550 (2002).

68 Kaplan, H. J., Tezel, T. H., Berger, A. S., Wolf, M. L. & Del Priore, L. V. Human photoreceptor transplantation in retinitis pigmentosa: a safety study. *Archives of Ophthalmology* **115**, 1168-1172 (1997).

69 Radtke, N. D. *et al.* Vision improvement in retinal degeneration patients by implantation of retina together with retinal pigment epithelium. *American Journal of Ophthalmology* **146**, 172-182. e171 (2008).

70 Schwartz, S. D., Tan, G., Hosseini, H. & Nagiel, A. Subretinal transplantation of embryonic stem cell–derived retinal pigment epithelium for the treatment of macular degeneration: an assessment at 4 years. *Investigative Ophthalmology & Visual Science* **57**, ORSFc1-ORSFc9 (2016).

71 Mandai, M. *et al.* Autologous induced stem-cell–derived retinal cells for macular degeneration. *New England Journal of Medicine* **376**, 1038-1046 (2017).

72 Rizzolo, L. J., Nasonkin, I. O. & Adelman, R. A. Retinal cell transplantation, biomaterials, and in vitro models for developing next-generation therapies of age-related macular degeneration. *Stem Cells Translational Medicine* **11**, 269-281 (2022).

73 Assawachananont, J. *et al.* Transplantation of embryonic and induced pluripotent stem cell-derived 3D retinal sheets into retinal degenerative mice. *Stem cell reports* **2**, 662-674 (2014).

74 Han, I. C. *et al.* Biocompatibility of Human Induced Pluripotent Stem Cell–Derived Retinal Progenitor Cell Grafts in Immunocompromised Rats. *Cell transplantation* **31**, 09636897221104451 (2022).

75 Jonas, J. B., Schneider, U. & Naumann, G. O. Count and density of human retinal photoreceptors. *Graefe's Archive for Clinical and Experimental Ophthalmology* **230**, 505-510 (1992).

76 Panda-Jonas, S., Jonas, J. B. & Jakobczyk-Zmija, M. Retinal pigment epithelial cell count, distribution, and correlations in normal human eyes. *American Journal of Ophthalmology* **121**, 181-189 (1996).

77 Kashani, A. H. *et al.* Survival of an HLA-mismatched, bioengineered RPE implant in dry age-related macular degeneration. *Stem cell reports* **17**, 448-458 (2022).

78 Kashani, A. H. *et al.* One-year follow-up in a phase 1/2a clinical trial of an allogeneic RPE cell bioengineered implant for advanced dry age-related macular degeneration. *Translational vision science & technology* **10**, 13-13 (2021).

79 Stanzel, B. V. *et al.* Subretinal delivery of ultrathin rigid-elastic cell carriers using a metallic shooter instrument and biodegradable hydrogel encapsulation. *Investigative Ophthalmology & Visual Science* **53**, 490-500 (2012).

80 Cheng, X. *et al.* Injectable composite hydrogels encapsulating gelatin methacryloyl/chitosan microspheres as ARPE-19 cell transplantation carriers. *Biomaterials Science* **11**, 278-287 (2023).

81 Kim, H. S. *et al.* Engineering retinal pigment epithelial cells regeneration for transplantation in regenerative medicine using PEG/Gellan gum hydrogels. *International journal of biological macromolecules* **130**, 220-228 (2019).

82 Lee, I.-K. *et al.* Micromolded honeycomb scaffold design to support the generation of a bilayered RPE and photoreceptor cell construct. *Bioactive Materials* **30**, 142-153 (2023).

83 Thomas, B. B. *et al.* Co-grafts of human embryonic stem cell derived retina organoids and retinal pigment epithelium for retinal reconstruction in immunodeficient retinal degenerate royal college of surgeons rats. *Frontiers in neuroscience* **15**, 752958 (2021).

84 Lee, I.-K. *et al.* Ultrathin micromolded 3D scaffolds for high-density photoreceptor layer reconstruction. *Science Advances* **7**, eabf0344 (2021).

85 Dorgau, B. *et al.* Decellularised extracellular matrix-derived peptides from neural retina and retinal pigment epithelium enhance the expression of synaptic markers and light responsiveness of human pluripotent stem cell derived retinal organoids. *Biomaterials* **199**, 63-75 (2019).

86 Jung, Y. H. *et al.* 3D Microstructured Scaffolds to Support Photoreceptor Polarization and Maturation. *Advanced Materials* **30**, e1803550 (2018).

87 Lamba, D. A., Karl, M. O., Ware, C. B. & Reh, T. A. Efficient generation of retinal progenitor cells from human embryonic stem cells. *Proceedings of the National Academy of Sciences* **103**, 12769-12774 (2006).

88 Karamali, F., Esfahani, M.-H. N., Taleahmad, S., Satarian, L. & Baharvand, H. Stem cells from apical papilla promote differentiation of human pluripotent stem cells towards retinal cells. *Differentiation* **101**, 8-15 (2018).

89 Ovando-Roche, P., Georgiadis, A., Smith, A. J., Pearson, R. A. & Ali, R. R. Harnessing the potential of human pluripotent stem cells and gene editing for the treatment of retinal degeneration. *Current Stem Cell Reports* **3**, 112-123 (2017).

90 Boulting, G. L. *et al.* A functionally characterized test set of human induced pluripotent stem cells. *Nature Biotechnology* **29**, 279-286 (2011).

91 Weed, L. S. & Mills, J. A. Strategies for retinal cell generation from human pluripotent stem cells. *Stem Cell Investigation* **4** (2017).

92 Achberger, K., Haderspeck, J. C., Kleger, A. & Liebau, S. Stem cell-based retina models. *Advanced Drug Delivery Reviews* **140**, 33-50 (2019).

93 Wagstaff, P. E. *et al.* The role of small molecules and their effect on the molecular mechanisms of early retinal organoid development. *International Journal of Molecular Sciences* **22**, 7081 (2021).

94 Sanjurjo-Soriano, C. *et al.* Retinoic acid delays initial photoreceptor differentiation and results in a highly structured mature retinal organoid. *Stem Cell Research & Therapy* **13**, 1-17 (2022).

95 Wagstaff, P. E., Ten Asbroek, A. L., Ten Brink, J. B., Jansonius, N. M. & Bergen, A. A. An alternative approach to produce versatile retinal organoids with accelerated ganglion cell development. *Scientific reports* **11**, 1-17 (2021).

96 Eldred, K. C. *et al.* Thyroid hormone signaling specifies cone subtypes in human retinal organoids. *Science (New York, N.Y.)* **362**, eaau6348 (2018).

97 Tanaka, T. *et al.* Generation of retinal ganglion cells with functional axons from human induced pluripotent stem cells. *Scientific reports* **5**, 1-11 (2015).

98 Chichagova, V. *et al.* Human iPSC differentiation to retinal organoids in response to IGF1 and BMP4 activation is line-and method-dependent. *Stem Cells* **38**, 195-201 (2020).

99 Kuwahara, A. *et al.* Preconditioning the initial state of feeder-free human pluripotent stem cells promotes self-formation of three-dimensional retinal tissue. *Scientific reports* **9**, 1-16 (2019).

100 Kumar, R., Harris-Hooker, S., Kumar, R. & Sanford, G. Co-culture of retinal and endothelial cells results in the modulation of genes critical to retinal neovascularization. *Vascular cell* **3**, 1-15 (2011).

101 Baranov, P. Y., Tucker, B. A. & Young, M. J. Low-oxygen culture conditions extend the multipotent properties of human retinal progenitor cells. *Tissue Engineering Part A* **20**, 1465-1475 (2014).

102 Wahlin, K. J. *et al.* Photoreceptor outer segment-like structures in long-term 3D retinas from human pluripotent stem cells. *Scientific reports* **7**, 1-15 (2017).

103 Wahlin, K. J. *et al.* CRISPR Generated SIX6 and POU4F2 Reporters Allow Identification of Brain and Optic Transcriptional Differences in Human PSC-Derived Organoids. *Frontiers in cell and developmental biology* **9** (2021).

104 Garreta, E. *et al.* Rethinking organoid technology through bioengineering. *Nature Materials* **20**, 145-155 (2021).

105 Kruczek, K. & Swaroop, A. Pluripotent stem cell-derived retinal organoids for disease modeling and development of therapies. *Stem Cells* **38**, 1206-1215 (2020).

106 Brassard, J. A. & Lutolf, M. P. Engineering stem cell self-organization to build better organoids. *Cell stem cell* **24**, 860-876 (2019).

107 Sarkar, N., Bhumiratana, S., Geris, L., Papantoniou, I. & Grayson, W. L. Bioreactors for engineering patient-specific tissue grafts. *Nature Reviews Bioengineering*, 1-17 (2023).

108 Dutt, K. *et al.* Generation of 3D retina-like structures from a human retinal cell line in a NASA bioreactor. *Cell transplantation* **12**, 717-731 (2003).

109 Kumar, R. & Dutt, K. Enhanced neurotrophin synthesis and molecular differentiation in non-transformed human retinal progenitor cells cultured in a rotating bioreactor. *Tissue Engineering* **12**, 141-158 (2006).

110 Kumar, R., Harris-Hooker, S. & Sanford, G. L. The expression of growth factors and their receptors in retinal and endothelial cells co-cultured in the rotating bioreactor. *Ethnicity and Disease* **18**, 44-50 (2008).

111 Dutt, K. & Cao, Y. Engineering retina from human retinal progenitors (cell lines). *Tissue Engineering Part A* **15**, 1401-1413 (2009).

112 Dutt, K. & Cao, Y. Attachment to cytodex beads enhances differentiation of human retinal progenitors in 3-D bioreactor culture. *Current Stem Cell Research & Therapy* **6**, 350-361 (2011).

113 DiStefano, T. *et al.* Accelerated and improved differentiation of retinal organoids from pluripotent stem cells in rotating-wall vessel bioreactors. *Stem cell reports* **10**, 300-313 (2018).

114 Ovando-Roche, P. *et al.* Use of bioreactors for culturing human retinal organoids improves photoreceptor yields. *Stem Cell Research & Therapy* **9**, 1-14 (2018).

115 Baakdhah, T. & van der Kooy, D. Expansion of retinal stem cells and their progeny using cell microcarriers in a bioreactor. *Biotechnology progress* **35**, e2800 (2019).

116 Demers, C. J. *et al.* Development-on-chip: in vitro neural tube patterning with a microfluidic device. *Development* **143**, 1884-1892 (2016).

117 Achberger, K. *et al.* Merging organoid and organ-on-a-chip technology to generate complex multi-layer tissue models in a human retina-on-a-chip platform. *Elife* **8**, e46188 (2019).

118 Achberger, K. *et al.* Human stem cell-based retina on chip as new translational model for validation of AAV retinal gene therapy vectors. *Stem cell reports* **16**, 2242-2256 (2021).

119 Xue, Y. *et al.* Retinal organoids on-a-chip: A micro-millifluidic bioreactor for long-term organoid maintenance. *Lab on a Chip* **21**, 3361-3377 (2021).

120 Dodson, K. H., Echevarria, F. D., Li, D., Sappington, R. M. & Edd, J. F. Retina-on-a-chip: a microfluidic platform for point access signaling studies. *Biomedical microdevices* **17**, 1-10 (2015).

121 Cipriano, M. *et al.* Human immunocompetent choroid-on-chip: a novel tool for studying ocular effects of biological drugs. *Communications Biology* **5**, 52 (2022).

122 Chung, M. *et al.* Wet-AMD on a chip: Modeling outer blood-retinal barrier in vitro. *Advanced healthcare materials* **7**, 1700028 (2018).

123 Toda, S., Blauch, L. R., Tang, S. K., Morsut, L. & Lim, W. A. Programming self-organizing multicellular structures with synthetic cell-cell signaling. *Science (New York, N.Y.)* **361**, 156-162 (2018).

124 Salmon, I. *et al.* Engineering neurovascular organoids with 3D printed microfluidic chips. *Lab on a Chip* **22**, 1615-1629 (2022).

125 Quintard, C. *et al.* A microfluidic platform integrating functional vascularized organoids-on-chip. *Nature Communications* **15**, 1452 (2024).

126 Zhu, W. *et al.* 3D printing of functional biomaterials for tissue engineering. *Current opinion in biotechnology* **40**, 103-112 (2016).

127 Ng, W. L., Lee, J. M., Yeong, W. Y. & Naing, M. W. Microvalve-based bioprinting–process, bio-inks and applications. *Biomaterials science* **5**, 632-647 (2017).

128 Masaeli, E. *et al.* Tissue engineering of retina through high resolution 3-dimensional inkjet bioprinting. *Biofabrication* **12**, 025006 (2020).

129 Lorber, B., Hsiao, W.-K., Hutchings, I. M. & Martin, K. R. Adult rat retinal ganglion cells and glia can be printed by piezoelectric inkjet printing. *Biofabrication* **6**, 015001 (2013).

130 Zhou, D. *et al.* Bioinks for jet-based bioprinting. *Bioprinting* **16**, e00060 (2019).

131 Song, M. J. *et al.* Bioprinted 3D outer retina barrier uncovers RPE-dependent choroidal phenotype in advanced macular degeneration. *Nature Methods*, 1-13 (2022).

132 Mayer, F. *et al.* Multimaterial 3D laser microprinting using an integrated microfluidic system. *Science Advances* **5**, eaau9160 (2019).

133 Yang, C. *et al.* Spatially patterned matrix elasticity directs stem cell fate. *Proceedings of the National Academy of Sciences* **113**, E4439-E4445 (2016).

134 Skylar-Scott, M. A., Mueller, J., Visser, C. W. & Lewis, J. A. Voxelated soft matter via multimaterial multinozzle 3D printing. *Nature* **575**, 330-335 (2019).

135 Newman, P. L. *et al.* Programming of Multicellular Patterning with Mechano-Chemically Microstructured Cell Niches. *Advanced Science* **10**, 2204741 (2023).

136 Anscombe, N. Direct laser writing. *Nature Photonics* **4**, 22-23 (2010).

137 Worthington, K. S. *et al.* Two-photon polymerization for production of human iPSC-derived retinal cell grafts. *Acta Biomaterialia* **55**, 385-395 (2017).

138 Thompson, J. R. *et al.* Two-photon polymerized poly (caprolactone) retinal cell delivery scaffolds and their systemic and retinal biocompatibility. *Acta Biomaterialia* **94**, 204-218 (2019).

139 Decembrini, S., Hoehnel, S., Brandenberg, N., Arsenijevic, Y. & Lutolf, M. P. Hydrogel-based milliwell arrays for standardized and scalable retinal organoid cultures. *Scientific reports* **10**, 10275 (2020).

140 Rashidi, H. *et al.* Generation of 3D retinal tissue from human pluripotent stem cells using a directed small molecule-based serum-free microwell platform. *Scientific reports* **12**, 1-13 (2022).

141 Sun, X. *et al.* One-stop assembly of adherent 3D retinal organoids from hiPSCs based on 3D-printed derived PDMS microwell platform. *Biofabrication* **15**, 035005 (2023).

142 Matsumoto, E. *et al.* Fabricating retinal pigment epithelial cell sheets derived from human induced pluripotent stem cells in an automated closed culture system for regenerative medicine. *PLoS One* **14**, e0212369 (2019).

143 Regent, F. *et al.* Automation of human pluripotent stem cell differentiation toward retinal pigment epithelial cells for large-scale productions. *Scientific reports* **9**, 10646 (2019).

144 Truong, V. *et al.* Automating human induced pluripotent stem cell culture and differentiation of iPSC-derived retinal pigment epithelium for personalized drug testing. *SLAS Technology* **26**, 287-299 (2021).

145 Kegeles, E., Perepelkina, T. & Baranov, P. Semi-Automated Approach for Retinal Tissue Differentiation. *Transl Vis Sci Technol* **9**, 24 (2020).

146 Kanda, G. N. *et al.* Robotic search for optimal cell culture in regenerative medicine. *Elife* **11**, e77007 (2022).

147 Kegeles, E., Naumov, A., Karpulevich, E. A., Volchkov, P. & Baranov, P. Convolutional neural networks can predict retinal differentiation in retinal organoids. *Frontiers in cellular neuroscience* **14**, 537942 (2020).

148 Watari, K. *et al.* Self-organization, quality control, and preclinical studies of human iPSC-derived retinal sheets for tissue-transplantation therapy. *Communications Biology* **6**, 164, doi:10.1038/s42003-023-04543-5 (2023).

149 Hallam, D. *et al.* Human-induced pluripotent stem cells generate light responsive retinal organoids with variable and nutrient-dependent efficiency. *Stem Cells* **36**, 1535-1551 (2018).

150 Lin, Y.-Y. *et al.* Development of polydimethylsiloxane-based biomimetic scaffolds with cylinder micropillars for retinal pigment epithelial cell cultivation. *Journal of the Chinese Medical Association* **83**, 1029-1033 (2020).

151 Peng, C.-H. *et al.* Laminin modification subretinal bio-scaffold remodels retinal pigment epithelium-driven microenvironment in vitro and in vivo. *Oncotarget* **7**, 64631 (2016).

152 Krishna, Y., Sheridan, C. M., Kent, D. L., Grierson, I. & Williams, R. L. Polydimethylsiloxane as a substrate for retinal pigment epithelial cell growth. *Journal of Biomedical Materials Research Part A* **80**, 669-678 (2007).

153 Warmflash, A., Sorre, B., Etoc, F., Siggia, E. D. & Brivanlou, A. H. A method to recapitulate early embryonic spatial patterning in human embryonic stem cells. *Nature Methods* **11**, 847-854 (2014).

154 Karzbrun, E. *et al.* Human neural tube morphogenesis in vitro by geometric constraints. *Nature* (2021).

155 Haremaki, T. *et al.* Self-organizing neuruloids model developmental aspects of Huntington's disease in the ectodermal compartment. *Nature biotechnology* **37**, 1198-1208 (2019).

156 Nelson, C. M. *et al.* Emergent patterns of growth controlled by multicellular form and mechanics. *Proceedings of the National Academy of Sciences* **102**, 11594-11599 (2005).

157 Peerani, R. *et al.* Niche-mediated control of human embryonic stem cell self-renewal and differentiation. *The EMBO journal* **26**, 4744-4755 (2007).

158 Bauwens, C. L. *et al.* Control of human embryonic stem cell colony and aggregate size heterogeneity influences differentiation trajectories. *Stem cells* **26**, 2300-2310 (2008).

159 Deglincerti, A. *et al.* Self-organization of human embryonic stem cells on micropatterns. *Nature Protocols* **11**, 2223-2232 (2016).

160 Sakai, Y., Yoshiura, Y. & Nakazawa, K. Embryoid body culture of mouse embryonic stem cells using microwell and micropatterned chips. *Journal of bioscience and bioengineering* **111**, 85-91 (2011).

161 Tewary, M. *et al.* High-throughput micropatterning platform reveals Nodal-dependent bisection of peri-gastrulation–associated versus preneurulation-associated fate patterning. *PLoS Biology* **17**, e3000081 (2019).

162 Nazareth, E. J. *et al.* High-throughput fingerprinting of human pluripotent stem cell fate responses and lineage bias. *Nature methods* **10**, 1225-1231 (2013).

163 Blin, G. Quantitative developmental biology in vitro using micropatterning. *Development* **148**, dev186387 (2021).

164 Falconnet, D., Csucs, G., Grandin, H. M. & Textor, M. Surface engineering approaches to micropattern surfaces for cell-based assays. *Biomaterials* **27**, 3044-3063 (2006).

165 Doyle, A. D., Wang, F. W., Matsumoto, K. & Yamada, K. M. One-dimensional topography underlies three-dimensional fibrillar cell migration. *Journal of cell biology* **184**, 481-490 (2009).

166 Tseng, Q. *et al.* A new micropatterning method of soft substrates reveals that different tumorigenic signals can promote or reduce cell contraction levels. *Lab on a Chip* **11**, 2231-2240 (2011).

167 Samal, P. *et al.* Polystyrene pocket lithography: sculpting plastic with light. *Advanced Materials* **34**, 2200687 (2022).

168 Samal, P. *et al.* Direct deep UV lithography to micropattern PMMA for stem cell culture. *Materials Today Bio* **22**, 100779 (2023).

169 Kshitiz *et al.* Control of stem cell fate and function by engineering physical microenvironments. *Integrative biology* **4**, 1008-1018 (2012).

170 Nakatoh, T. *et al.* Cell behaviors within a confined adhesive area fabricated using novel micropatterning methods. *Plos one* **17**, e0262632 (2022).

171 Casey, M. A., Lusk, S. & Kwan, K. M. Build me up optic cup: intrinsic and extrinsic mechanisms of vertebrate eye morphogenesis. *Developmental biology* **476**, 128-136 (2021).

172 Kusuma, S., Smith, Q., Facklam, A. & Gerecht, S. Micropattern size-dependent endothelial differentiation from a human induced pluripotent stem cell line. *Journal of tissue engineering and regenerative medicine* **11**, 855-861 (2017).

173 Smith, Q., Stukalin, E., Kusuma, S., Gerecht, S. & Sun, S. X. Stochasticity and spatial interaction govern stem cell differentiation dynamics. *Scientific reports* **5**, 12617 (2015).

174 Toh, Y.-C., Xing, J. & Yu, H. Modulation of integrin and E-cadherin-mediated adhesions to spatially control heterogeneity in human pluripotent stem cell differentiation. *Biomaterials* **50**, 87-97 (2015).

175 Gjorevski, N. *et al.* Tissue geometry drives deterministic organoid patterning. *Science (New York, N.Y.)* **375**, eaaw9021 (2022).

176 Kowalczewski, A. *et al.* Design optimization of geometrically confined cardiac organoids enabled by machine learning techniques. *Cell Reports Methods* **4** (2024).

177 Xing, J., Toh, Y.-C., Xu, S. & Yu, H. A method for human teratogen detection by geometrically confined cell differentiation and migration. *Scientific reports* **5**, 10038 (2015).

178 Metzger, J. J. *et al.* Deep-learning analysis of micropattern-based organoids enables high-throughput drug screening of Huntington's disease models. *Cell Reports Methods* **2** (2022).

179 Martyn, I., Kanno, T., Ruzo, A., Siggia, E. & Brivanlou, A. Self-organization of a human organizer by combined Wnt and Nodal signalling. *Nature* **558**, 132-135 (2018).

180 Srivastava, P. *et al.* Defined microenvironments trigger in vitro gastrulation in human pluripotent stem cells. *Advanced Science* **10**, 2203614 (2023).

181 Muncie, J. M. *et al.* Mechanical tension promotes formation of gastrulation-like nodes and patterns mesoderm specification in human embryonic stem cells. *Developmental cell* **55**, 679-694. e611 (2020).

182 Ma, Z. *et al.* Self-organizing human cardiac microchambers mediated by geometric confinement. *Nature communications* **6**, 7413 (2015).

183 Hoang, P., Wang, J., Conklin, B. R., Healy, K. E. & Ma, Z. Generation of spatial-patterned early-developing cardiac organoids using human pluripotent stem cells. *Nature protocols* **13**, 723-737 (2018).

184 Hoang, P. *et al.* Engineering spatial-organized cardiac organoids for developmental toxicity testing. *Stem Cell Reports* **16**, 1228-1244 (2021).

185 Rosado-Olivieri, E. *et al.* Organotypic human lung bud microarrays identify BMP-dependent SARS-CoV-2 infection in lung cells. *Stem Cell Reports* **18**, 1107-1122 (2023).

186 Uchida, H. *et al.* A xenogeneic-free system generating functional human gut organoids from pluripotent stem cells. *JCI insight* **2** (2017).

187 Sahni, G. *et al.* A micropatterned human-specific neuroepithelial tissue for modeling gene and drug-induced neurodevelopmental defects. *Advanced Science* **8**, 2001100 (2021).

188 Esfahani, S. N. *et al.* Microengineered human amniotic ectoderm tissue array for high-content developmental phenotyping. *Biomaterials* **216**, 119244 (2019).

189 Sen, D., Voulgaropoulos, A. & Keung, A. J. Effects of early geometric confinement on the transcriptomic profile of human cerebral organoids. *BMC biotechnology* **21**, 1-16 (2021).

190 Ripolles-Garcia, A. *et al.* Systemic immunosuppression promotes survival and integration of subretinally implanted human ESC-derived photoreceptor precursors in dogs. *Stem Cell Reports* **17**, 1824-1841 (2022).

191 Stenkamp, D. L. Development of the vertebrate eye and retina. *Progress in molecular biology and translational science* **134**, 397-414 (2015).

192 Eichmüller, O. L. & Knoblich, J. A. Human cerebral organoids—a new tool for clinical neurology research. *Nature Reviews Neurology* **18**, 661-680 (2022).

193 Wang, Y. *et al.* Micropattern-controlled chirality of focal adhesions regulates the cytoskeletal arrangement and gene transfection of mesenchymal stem cells. *Biomaterials* **271**, 120751 (2021).

194 Yang, Y. *et al.* Influence of cell spreading area on the osteogenic commitment and phenotype maintenance of mesenchymal stem cells. *Scientific reports* **9**, 6891 (2019).

195 Zhu, Y., Sazer, D., Miller, J. S. & Warmflash, A. Rapid fabrication of hydrogel micropatterns by projection stereolithography for studying self-organized developmental patterning. *Plos one* **16**, e0245634 (2021).

196 Karzbrun, E. *et al.* Human neural tube morphogenesis in vitro by geometric constraints. *Nature* **599**, 268-272 (2021).

197 Kilpinen, H. *et al.* Common genetic variation drives molecular heterogeneity in human iPSCs. *Nature* **546**, 370-375 (2017).

198 Brzoska, J., Azouz, I. B. & Rondelez, F. Silanization of solid substrates: a step toward reproducibility. *Langmuir* **10**, 4367-4373 (1994).

199 Matisons, J. G. Silanes and siloxanes as coupling agents to glass: a perspective. *Silicone Surface Science*, 281-298 (2012).

200 Grigoryan, B. *et al.* Development, characterization, and applications of multi-material stereolithography bioprinting. *Scientific Reports* **11**, 3171 (2021).

201 Revzin, A. *et al.* Fabrication of poly (ethylene glycol) hydrogel microstructures using photolithography. *Langmuir* **17**, 5440-5447 (2001).

202 Fernando, M. *et al.* Differentiation of brain and retinal organoids from confluent cultures of pluripotent stem cells connected by nerve-like axonal projections of optic origin. *Stem Cell Reports* **17**, 1476-1492 (2022).

203 Lundholt, B. K., Scudder, K. M. & Pagliaro, L. A simple technique for reducing edge effect in cell-based assays. *Journal of biomolecular screening* **8**, 566-570 (2003).

204 Venugopal, B., Mogha, P., Dhawan, J. & Majumder, A. Cell density overrides the effect of substrate stiffness on human mesenchymal stem cells' morphology and proliferation. *Biomaterials science* **6**, 1109-1119 (2018).

205 Aisenbrey, E. A. & Murphy, W. L. Synthetic alternatives to Matrigel. *Nature Reviews Materials* **5**, 539-551 (2020).

206 Anderson, N. C. *et al.* Balancing serendipity and reproducibility: Pluripotent stem cells as experimental systems for intellectual and developmental disorders. *Stem cell reports* **16**, 1446-1457 (2021).

207 O'rahilly, R. & Müller, F. Developmental stages in human embryos: revised and new measurements. *Cells Tissues Organs* **192**, 73-84 (2010).

208 Zhang, C. *et al.* Exploration of the effects of substrate stiffness on biological responses of neural cells and their mechanisms. *ACS omega* **5**, 31115-31125 (2020).

209 Teixeira, A. I. *et al.* The promotion of neuronal maturation on soft substrates. *Biomaterials* **30**, 4567-4572 (2009).

210 Chou, S.-J. & Tole, S. Lhx2, an evolutionarily conserved, multifunctional regulator of forebrain development. *Brain research* **1705**, 1-14 (2019).

211 Gao, L. *et al.* Post-passage rock inhibition induces cytoskeletal aberrations and apoptosis in human embryonic stem cells. *Stem cell research* **41**, 101641 (2019).

212 Taghavi, N., Zhuang, W.-Q. & Baroutian, S. Enhanced biodegradation of non-biodegradable plastics by UV radiation: Part 1. *Journal of Environmental Chemical Engineering* **9**, 106464 (2021).

213 Harkin, J. *et al.* A highly reproducible and efficient method for retinal organoid differentiation from human pluripotent stem cells. *Proceedings of the National Academy of Sciences* **121**, e2317285121 (2024).

214 Chambers, S. M. *et al.* Highly efficient neural conversion of human ES and iPS cells by dual inhibition of SMAD signaling. *Nature biotechnology* **27**, 275-280 (2009).

215 Britton, G., Heemskerk, I., Hodge, R., Qutub, A. A. & Warmflash, A. A novel self-organizing embryonic stem cell system reveals signaling logic underlying the patterning of human ectoderm. *Development* **146**, dev179093 (2019).

216 Mayshar, Y. *et al.* Identification and classification of chromosomal aberrations in human induced pluripotent stem cells. *Cell stem cell* **7**, 521-531 (2010).

217 Cooke, J. A. *et al.* Propensity of patient-derived iPSCs for retinal differentiation: implications for autologous cell replacement. *Stem cells translational medicine* **12**, 365-378 (2023).

218 Duester, G. Retinoic acid synthesis and signaling during early organogenesis. *Cell* **134**, 921-931 (2008).

219 Pittack, C., Grunwald, G. B. & Reh, T. A. Fibroblast growth factors are necessary for neural retina but not pigmented epithelium differentiation in chick embryos. *Development* **124**, 805-816 (1997).

220 Balasubramanian, R. *et al.* Phase transition specified by a binary code patterns the vertebrate eye cup. *Science Advances* **7**, eabj9846 (2021).

221 Makrides, N., Wang, Q., Tao, C., Schwartz, S. & Zhang, X. Jack of all trades, master of each: the diversity of fibroblast growth factor signalling in eye development. *Open Biology* **12**, 210265 (2022).

222 Takahashi, K. *et al.* A stress-reduced passaging technique improves the viability of human pluripotent cells. *Cell reports methods* **2** (2022).

223 Rivera, T., Zhao, Y., Ni, Y. & Wang, J. Human-induced pluripotent stem cell culture methods under cGMP conditions. *Current Protocols in Stem Cell Biology* **54**, e117 (2020).

224 Okada, Y., Shimazaki, T., Sobue, G. & Okano, H. Retinoic-acid-concentration-dependent acquisition of neural cell identity during in vitro differentiation of mouse embryonic stem cells. *Developmental biology* **275**, 124-142 (2004).

225 Pagliaro, A. *et al.* Temporal morphogen gradient-driven neural induction shapes single expanded neuroepithelium brain organoids with enhanced cortical identity. *Nature Communications* **14**, 7361 (2023).

Thesis Appendix

MATLAB script to extract shape metrics from .czi images of micropatterned samples.

This script uses the function Hough transform for circles developed by David Young.

```
close all; clc; clearvars; clear;
% Circle identification code from: https://dsp.stackexchange.com/questions/5930/detection-of-
a-circle-in-noisy-image-data

% Import necessary packages
addpath(genpath('\bfmatlab'));
javaaddpath('\bfmatlab\bioformats_package.jar');
addpath(genpath('\circle_hough'));

% Find images to open
if ~exist('dirName','var')
    %uiwait(msgbox('select working directory'))
    dirName = uigetdir; cd(dirName)
end

% Get a list of all files in the folder with the desired file name pattern
filePattern = fullfile(dirName, '**/*.czi');
% filePattern = fullfile(dirName, '**/*).czi');
allFiles = dir(filePattern);


is_file = ~[allFiles.isdir];  % Logical array: 1 for files, 0 for directories
filteredFiles = allFiles(is_file);  % Only keep file entries
validFolders = {filteredFiles.folder};
validFiles = {filteredFiles.name};

ref_ims = ["__[0,0.8,1].tif", "__[1,0,0].tif", "__[1,1,0].tif", "__[1,0,1].tif"];

for file_num = 1 : length(validFiles)

  cd(dirName)

  baseFileName = validFiles(file_num);
  baseFileName = baseFileName{1,1};
  fullFileName = fullfile(validFolders(file_num), baseFileName);
  fullFileName = fullFileName{1,1};

  % Check file size > 50MB
  fileInfo = dir(fullFileName);
  fileSize = fileInfo.bytes/1024^2; % in MB

  meanDiameter = [];
  meanEntropy = [];
  meanOvalness = [];
  meanArea = [];
  meanSkew = [];
  meanKurt = [];
  meanHeight = [];

  % check if files already exist
  fileFolder = fileInfo.folder;
  folderInfo = dir(fileFolder);
  folderInfo = {folderInfo.name};
  numFiles = length(folderInfo)-3;


    cziCount = sum(endsWith(folderInfo,'.czi')); % Check how many files end in '.czi'
    if numFiles/15 == cziCount % Check if there are already 'enough' files
        disp('Files already exist');
        continue
    end


  if fileSize > 10
```

```
    subpath = strrep(fullFileName, baseFileName, '');
    tifsubpath = ['__' baseFileName(1:end-4) '__1'];
    disp(['Loading: ' tifsubpath]);
    tifpath = fullfile(subpath, tifsubpath);

    txtFileName = [baseFileName '.txt'];

    if contains(fileFolder,'RE-DO')
        disp('failed projection');
        continue
    end


    % Load the image
    data = bfopen(fullFileName);


    % Extract metadata
    omeMeta = data{1, 4};

    ZStack = omeMeta.getPixelsSizeZ(0).getValue(); % Z-Stack
    ZScaling = omeMeta.getPixelsPhysicalSizeZ(0).value(ome.units.UNITS.MICROMETER);
    ZScaling = ZScaling.doubleValue();
    Channels = omeMeta.getPixelsSizeC(0).getValue(); % Channels
    Scaling = omeMeta.getPixelsPhysicalSizeX(0).value(ome.units.UNITS.MICROMETER); % Scaling
    ImageSizePixels = double(omeMeta.getPixelsSizeX(0).getValue()); % Image Size (Pixels)
    ImageSizePixelsStr = [num2str(ImageSizePixels) ' x ' num2str(ImageSizePixels)];
    ImageSizeScaled = double(ImageSizePixels) * double(Scaling); % Image Size (Scaled)
    ImageSizeScaledStr = [num2str(ImageSizeScaled) ' mm x ' num2str(ImageSizeScaled) ' mm'];
    BitDepth = omeMeta.getPixelsType(0); % Bit Depth


    % Save metadata to .txt file
    fileID = fopen([fullFileName '.txt'], 'w');
    fprintf(fileID, 'Z-Stack: %d\nZ-Scaling: %d\nChannels: %d\nScaling (per Pixel): %f\nImage
Size (Pixels): %s\nImage Size (Scaled): %s\nBit Depth: %s\n', ZStack, ZScaling, Channels,
Scaling, ImageSizePixelsStr, ImageSizeScaledStr, char(BitDepth));
    fclose(fileID);

    for chan = 1:length(ref_ims)

        cd(tifpath);
        ref_im = char(ref_ims(chan));
        ref_im = join(ref_im,'');
        ref_im_x = [ref_im(1:end-4) '__x_projection.tif'];
        ref_im_y = [ref_im(1:end-4) '__y_projection.tif'];

        %% Get mip Data
        if exist(ref_im, 'file') == 2

            im_og = imread(ref_im);

            im = im_og;
            im = im2gray(im);
            level1 = graythresh(im);
            disp(["LEVEL 1: " level1]);
            im = imbinarize(im,level1); % Otsu threshold


            % Adjust for optimal output
            im = imclose(im, strel('disk', 10)); % close small gaps
            im = bwareaopen(im, 100); % delete if fewer than X pixels
            im = imfill(im,'holes'); % fill in holes
            im = bwareaopen(im, 500); % delete if fewer than X pixels

            imgOtsuThreshold = im;

            % Compute the area of the binary mask
            binaryMaskArea = sum(imgOtsuThreshold(:))*1.1;

            % Compute area of a circle which has a diameter equal to the image dimensions
            circleDiameter = max(size(im)); % Diameter is the larger of the x and y dimensions
            circleArea = pi * (circleDiameter / 2)^2;

            % Check if the binary mask area is larger than the circle area
```

```
            if binaryMaskArea > circleArea
                % If so, apply Otsu's thresholding again to the thresholded image
                level2 = graythresh(im2gray(im_og));
                disp(["LEVEL 2: " level2]);
                imgOtsuThreshold2 = imbinarize(im2gray(im_og), level2);
                imgOtsuThreshold2 = bwareaopen(imgOtsuThreshold2, 100);
                imgOtsuThreshold2 = imclose(imgOtsuThreshold2, strel('disk', 50));
                imgOtsuThreshold2 = imfill(imgOtsuThreshold2,'holes');
                imgOtsuThreshold2 = bwareaopen(imgOtsuThreshold2, 500); X pixels
            else
                imgOtsuThreshold2 = imgOtsuThreshold;
            end

            imgOtsuThreshold = imgOtsuThreshold2;

            binaryMaskArea = sum(imgOtsuThreshold(:))*1.1;

            if binaryMaskArea > circleArea
                % If so, apply Otsu's thresholding again to the thresholded image
                maskedImg = im2gray(im_og);
                maskedImg(~imgOtsuThreshold) = 0;

                level3 = graythresh(maskedImg);
                disp(["LEVEL 3: " level3]);
                imgOtsuThreshold2 = imbinarize(maskedImg, level3);
                imgOtsuThreshold2 = bwareaopen(imgOtsuThreshold2, 100);
                imgOtsuThreshold2 = imclose(imgOtsuThreshold2, strel('disk', 50));
                imgOtsuThreshold2 = imfill(imgOtsuThreshold2,'holes');
                imgOtsuThreshold2 = bwareaopen(imgOtsuThreshold2, 500);
            else
                imgOtsuThreshold2 = imgOtsuThreshold;
            end

            figure('Position',[0 50 200 100]);
            fig = gcf; % Get the current figure handle
            fig.Position(3:4) = 2 * fig.Position(3:4);
            subplot(1,2,1), imshow(im), title('Original Threshold');
            subplot(1,2,2), imshow(imgOtsuThreshold2), title('Second Thresholded Image');
            pause(1)

            im = imgOtsuThreshold2;


            ims = conv2(double(im), ones(7,7),'same');
            imbw = ims>6;
            props =
regionprops(imbw,'Area','PixelIdxList','MajorAxisLength','MinorAxisLength');
            if isempty(props)
                disp("Nothing segmented... Skipping");

                fileID = fopen([fullFileName '.txt'], 'a');
                fprintf(fileID, '%s Diameter (um): %s\n', ref_im, '');
                fprintf(fileID, '%s Max Area: %s\n', ref_im, '');
                fprintf(fileID, '%s Circularity: %s\n', ref_im, '');
                fprintf(fileID, '%s Ovalness: %s\n', ref_im, '');
                fprintf(fileID, '%s Entropy: %s\n', ref_im, '');
                fprintf(fileID, '%s Mean Intensity: %s\n', ref_im, '');
                fprintf(fileID, '%s Min Intensity: %s\n', ref_im, '');
                fprintf(fileID, '%s Max Intensity: %s\n', ref_im, '');
                fprintf(fileID, '%s Skewness: %s\n', ref_im, '');
                fprintf(fileID, '%s Kurtosis: %s\n', ref_im, '');
                fclose(fileID);


            else


                [~,indexOfMax] = max([props.Area]);
                largestBlobIndexes  = props(indexOfMax).PixelIdxList;
                bw = false(size(im));
                bw(largestBlobIndexes) = 1;
                bw = imfill(bw,'holes');
                bw = imfill(bw,round(size(bw)/2),8);

                arraySize = max(size(im));
```

```
                [x, y] = meshgrid(1:arraySize, 1:arraySize);
                centerArray = arraySize / 2;
                distance = sqrt((x - centerArray).^2 + (y - centerArray).^2);
                circleMask = distance <= centerArray;
                circleMask = imcomplement(circleMask);

                if sum(size(bw) < size(circleMask))
                    bw_x = size(bw,1);
                    bw_y = size(bw,2);
                    circle_x = size(circleMask,1);
                    circle_y = size(circleMask,2);

                    sizeDiff_x = circle_x - bw_x;
                    sizeDiff_y = circle_y - bw_y;

                    if bw_x < circle_x
                        circleMask = circleMask(1:end-sizeDiff_x, :);
                    elseif bw_y < circle_y
                        circleMask = circleMask(:, 1:end-sizeDiff_y);
                    end
                end


                bw = bw & ~circleMask;

                figure('Position',[0 50 200 100]);
                fig = gcf; % Get the current figure handle
                fig.Position(3:4) = 2 * fig.Position(3:4);
                subplot(1,2,1), imshow(im_og), title('Original Image');
                subplot(1,2,2), imshow(bw), title('Final Thresholded Image');
                pause(1);


                % Get properties of mask
                s = regionprops(bw, 'Area', 'Centroid', 'MajorAxisLength', 'MinorAxisLength',
'Perimeter');
                maxArea = max([s.Area]);
                idxMaxArea = find([s.Area] == maxArea);
                circularity = (4 * pi * s(idxMaxArea).Area) / (s(idxMaxArea).Perimeter^2);
                ovalness = s(idxMaxArea).MajorAxisLength / s(idxMaxArea).MinorAxisLength;

                masked_img = im2uint8(double(im2gray(im_og))/255 .* bw);
                masked_img_colour = im2uint8(double(im_og)/255 .* bw);
                flattened_img = reshape(masked_img, [], 1);
                flattened_img = flattened_img(flattened_img ~= 0);
                skew_val = skewness(flattened_img);
                kurt_val = kurtosis(flattened_img);

                % use grayscale image to get properties
                s = regionprops(bw, masked_img,'Area', 'MeanIntensity', 'MinIntensity',
'MaxIntensity', 'PixelValues');
                % entropies = arrayfun(@(x) entropy(x.PixelValues), s);

                maxArea = max([s.Area]);
                idxMaxArea = find([s.Area] == maxArea);

                meanIntensity = s(idxMaxArea).MeanIntensity;
                minIntensity = s(idxMaxArea).MinIntensity;
                maxIntensity = s(idxMaxArea).MaxIntensity;
                pixelValues = s(idxMaxArea).PixelValues;
                pixelValuesScaled = rescale(pixelValues);
                entropyMax = entropy(pixelValuesScaled);

                props_bw =
regionprops(bw,'Area','PixelIdxList','MajorAxisLength','MinorAxisLength');
                [~,indexOfMax_bw] = max([props_bw.Area]);
%                 approximateRadius =  props_bw(indexOfMax).MajorAxisLength/2;
%                 approximateRadius =  props_bw(indexOfMax_bw).MinorAxisLength/2;
                approximateRadius =
(props_bw(indexOfMax_bw).MajorAxisLength+props_bw(indexOfMax_bw).MinorAxisLength)/4;

                pad_size = [round(size(im, 1)/5) round(size(im, 2)/5)];
                pad_value = 0;
                bw = padarray(bw, pad_size, pad_value, 'both');
```

```
                radiuses = round ( (approximateRadius-5):0.5:(approximateRadius+5) );
                h = circle_hough(edge(bw), radiuses, 'same');

                [~,maxIndex] = max(h(:));
                [i,j,k] = ind2sub(size(h), maxIndex);
                radius = radiuses(k);
                center.x = j;
                center.y = i;


                im_og = padarray(im_og, pad_size, pad_value, 'both');

                figure('Position',[0 50 200 100]);
                fig = gcf;
                fig.Position(3:4) = 2 * fig.Position(3:4);
                subplot(1,2,1), imshow(im_og), title('Original Image');
                subplot(1,2,2), imshow(edge(bw)), title('Edge');

                figure;

                imshow(im_og);imellipse(gca,[center.x-radius  center.y-radius 2*radius
2*radius]);
                scaledradius = double(radius) * double(Scaling);
                scaledArea = (pi * (scaledradius/1000)^2);
                title(['Image size is ' ImageSizeScaledStr '. Estimated diameter is '
num2str(round(scaledradius)*2) 'um']);

                % Save image
                cd(tifpath);
                imwrite(getframe(gcf).cdata, [fullFileName ref_im(1:end-4) '_circle.tif']);
                imwrite(masked_img_colour, [fullFileName ref_im(1:end-4) '_masked.tif'])


                % Save metadata to .txt file
                fileID = fopen([fullFileName '.txt'], 'a');
                fprintf(fileID, '%s Diameter (um): %f\n', ref_im, 2*scaledradius);
                fprintf(fileID, '%s Max Area: %f\n', ref_im, scaledArea);
                fprintf(fileID, '%s Circularity: %f\n', ref_im, circularity);
                fprintf(fileID, '%s Ovalness: %f\n', ref_im, ovalness);
                fprintf(fileID, '%s Entropy: %f\n', ref_im, entropyMax);
                fprintf(fileID, '%s Mean Intensity: %f\n', ref_im, meanIntensity);
                fprintf(fileID, '%s Min Intensity: %d\n', ref_im, minIntensity);
                fprintf(fileID, '%s Max Intensity: %d\n', ref_im, maxIntensity);
                fprintf(fileID, '%s Skewness: %f\n', ref_im, skew_val);
                fprintf(fileID, '%s Kurtosis: %f\n', ref_im, kurt_val);
                fclose(fileID);

                meanDiameter(chan) = 2*scaledradius;
                meanEntropy(chan) = entropyMax;
                meanOvalness(chan) = ovalness;
                meanArea(chan) = scaledArea;
                meanSkew(chan) = skew_val;
                meanKurt(chan) = kurt_val;

                close all;
            end
        else
            disp([ref_im ' does not exist']);

            fileID = fopen([fullFileName '.txt'], 'a');
            fprintf(fileID, '%s Diameter (um): %s\n', ref_im, '');
            fprintf(fileID, '%s Max Area: %s\n', ref_im, '');
            fprintf(fileID, '%s Circularity: %s\n', ref_im, '');
            fprintf(fileID, '%s Ovalness: %s\n', ref_im, '');
            fprintf(fileID, '%s Entropy: %s\n', ref_im, '');
            fprintf(fileID, '%s Mean Intensity: %s\n', ref_im, '');
            fprintf(fileID, '%s Min Intensity: %s\n', ref_im, '');
            fprintf(fileID, '%s Max Intensity: %s\n', ref_im, '');
            fprintf(fileID, '%s Skewness: %s\n', ref_im, '');
            fprintf(fileID, '%s Kurtosis: %s\n', ref_im, '');

            fprintf(fileID, '%s Diameter (um): %s\n', ref_im_x, '');
            fprintf(fileID, '%s Major Axis (um): %s\n', ref_im_x, '');
            fprintf(fileID, '%s Minor Axis (um): %s\n', ref_im_x, '');
            fprintf(fileID, '%s Max Area: %s\n', ref_im_x, '');
```

```
    fprintf(fileID, '%s Mean Intensity: %s\n', ref_im_x, '');
    fprintf(fileID, '%s Min Intensity: %s\n', ref_im_x, '');
    fprintf(fileID, '%s Max Intensity: %s\n', ref_im_x, '');
    fprintf(fileID, '%s Skewness: %s\n', ref_im_x, '');
    fprintf(fileID, '%s Kurtosis: %s\n', ref_im_x, '');

    fprintf(fileID, '%s Diameter (um): %s\n', ref_im_y, '');
    fprintf(fileID, '%s Major Axis (um): %s\n', ref_im_y, '');
    fprintf(fileID, '%s Minor Axis (um): %s\n', ref_im_y, '');
    fprintf(fileID, '%s Max Area: %s\n', ref_im_y, '');
    fprintf(fileID, '%s Mean Intensity: %s\n', ref_im_y, '');
    fprintf(fileID, '%s Min Intensity: %s\n', ref_im_y, '');
    fprintf(fileID, '%s Max Intensity: %s\n', ref_im_y, '');
    fprintf(fileID, '%s Skewness: %s\n', ref_im_y, '');
    fprintf(fileID, '%s Kurtosis: %s\n', ref_im_y, '');
    fclose(fileID);

    continue
end


%% Get x projection Data
if exist(ref_im_x, 'file') == 2

    im_og_x = imread(ref_im_x);

    im_x = im_og_x;
    im_x = im2gray(im_x);
    level1 = graythresh(im_x);
    disp(["LEVEL 1: " level1]);
    im_x = imbinarize(im_x,level1); % Otsu threshold


    im_x = imclose(im_x, strel('disk', 10)); % close small gaps
    im_x = bwareaopen(im_x, 50); % delete if fewer than X pixels
    im_x = imfill(im_x,'holes'); % fill in holes
%     im = imclose(im, strel('disk', 10)); % close small gaps
    im_x = bwareaopen(im_x, 50); % delete if fewer than X pixels

    imgOtsuThreshold = im_x;
    % imshow(imgOtsuThreshold); pause(10)

    % Compute the area of the binary mask
    binaryMaskArea = sum(imgOtsuThreshold(:))*1.1;

    circleDiameter = max(size(im_x));
    circleArea = pi * (circleDiameter / 2)^2;

    % Check if the binary mask area is larger than the circle area
    if binaryMaskArea > circleArea
        % If so, apply Otsu's thresholding again to the thresholded image
        level2 = graythresh(im2gray(im_og_x));
        disp(["LEVEL 2: " level2]);
        imgOtsuThreshold2 = imbinarize(im2gray(im_og_x), level2);
        imgOtsuThreshold2 = bwareaopen(imgOtsuThreshold2, 50);
        imgOtsuThreshold2 = imclose(imgOtsuThreshold2, strel('disk', 50));
        imgOtsuThreshold2 = imfill(imgOtsuThreshold2,'holes');
        imgOtsuThreshold2 = bwareaopen(imgOtsuThreshold2, 50);
    else
        imgOtsuThreshold2 = imgOtsuThreshold;
    end

    imgOtsuThreshold = imgOtsuThreshold2;

    % Compute the area of the binary mask
    binaryMaskArea = sum(imgOtsuThreshold(:))*1.1;

    % Compute the area of a circle
    circleDiameter = max(size(im_x));
    circleArea = pi * (circleDiameter / 2)^2;

    if binaryMaskArea > circleArea
        % If so, apply Otsu's thresholding again to the thresholded image
        maskedImg = im2gray(im_og_x);
        maskedImg(~imgOtsuThreshold) = 0;
```

```
                level3 = graythresh(maskedImg);
                disp(["LEVEL 3: " level3]);
                imgOtsuThreshold2 = imbinarize(maskedImg, level3);
                imgOtsuThreshold2 = bwareaopen(imgOtsuThreshold2, 100);
                imgOtsuThreshold2 = imclose(imgOtsuThreshold2, strel('disk', 50));
                imgOtsuThreshold2 = imfill(imgOtsuThreshold2,'holes');
                imgOtsuThreshold2 = bwareaopen(imgOtsuThreshold2, 500);
            else
                imgOtsuThreshold2 = imgOtsuThreshold;
            end

            figure('Position',[0 50 200 100]);
            fig = gcf; % Get the current figure handle
            fig.Position(3:4) = 2 * fig.Position(3:4);
            subplot(1,2,1), imshow(im_x), title('Original Threshold');
            subplot(1,2,2), imshow(imgOtsuThreshold2), title('Final Thresholded Image');
            pause(1)

            im_x = imgOtsuThreshold2;

            figure('Position',[0 50 200 100]);
            fig = gcf; % Get the current figure handle
            fig.Position(3:4) = 2 * fig.Position(3:4);
            subplot(1,2,1), imshow(im_og_x), title('Original Image');
            subplot(1,2,2), imshow(im_x), title('Final Thresholded Image');
            pause(1)

            ims = conv2(double(im_x), ones(7,7),'same');
            imbw = ims>6;

            props =
regionprops(imbw,'Area','PixelIdxList','MajorAxisLength','MinorAxisLength');
            if isempty(props)
                disp("Nothing segmented... Skipping");

                fileID = fopen([fullFileName '.txt'], 'a');
                fprintf(fileID, '%s Diameter (um): %s\n', ref_im_x, '');
                fprintf(fileID, '%s Major Axis (um): %s\n', ref_im_x, '');
                fprintf(fileID, '%s Minor Axis (um): %s\n', ref_im_x, '');
                fprintf(fileID, '%s Max Area: %s\n', ref_im_x, '');
                fprintf(fileID, '%s Mean Intensity: %s\n', ref_im_x, '');
                fprintf(fileID, '%s Min Intensity: %s\n', ref_im_x, '');
                fprintf(fileID, '%s Max Intensity: %s\n', ref_im_x, '');
                fprintf(fileID, '%s Skewness: %s\n', ref_im_x, '');
                fprintf(fileID, '%s Kurtosis: %s\n', ref_im_x, '');
                fclose(fileID);

            else

                [~,indexOfMax] = max([props.Area]);
                approximateRadius =  props(indexOfMax).MajorAxisLength/2;

                largestBlobIndexes  = props(indexOfMax).PixelIdxList;
                bw = false(size(im_x));
                bw(largestBlobIndexes) = 1;
                bw = imfill(bw,'holes');

                % Get properties of mask
                s = regionprops(bw, 'Area', 'Centroid', 'MajorAxisLength', 'MinorAxisLength',
'Perimeter');
                maxArea = max([s.Area]);
                idxMaxArea = find([s.Area] == maxArea);
                radius = max([s.MajorAxisLength])/2;

                majorAxis = s(idxMaxArea).MajorAxisLength;
                minorAxis = s(idxMaxArea).MinorAxisLength;

                masked_img = im2uint8(double(im2gray(im_og_x))/255 .* bw);
                masked_img_colour = im2uint8(double(im_og_x)/255 .* bw);
                flattened_img = reshape(masked_img, [], 1);
                flattened_img = flattened_img(flattened_img ~= 0);
                skew_val = skewness(flattened_img);
                kurt_val = kurtosis(flattened_img);
```

```
                % Use grayscale image to get properties
                s = regionprops(bw, masked_img,'Area', 'MeanIntensity', 'MinIntensity',
'MaxIntensity', 'PixelValues');

                maxArea = max([s.Area]);
                idxMaxArea = find([s.Area] == maxArea);


                meanIntensity = s(idxMaxArea).MeanIntensity;
                minIntensity = s(idxMaxArea).MinIntensity;
                maxIntensity = s(idxMaxArea).MaxIntensity;
                pixelValues = s(idxMaxArea).PixelValues;
                pixelValuesScaled = rescale(pixelValues);
                entropyMax = entropy(pixelValuesScaled);



                pad_size = [round(size(im_x, 1)/5) round(size(im_x, 2)/5)];
                pad_value = 0;
                bw = padarray(bw, pad_size, pad_value, 'both');


                im_og_x = padarray(im_og_x, pad_size, pad_value, 'both');

                % Save image
                cd(tifpath);
                imwrite(masked_img_colour, [fullFileName ref_im(1:end-4)
'_x_proj_masked.tif'])

                scaledHeight_x = minorAxis*ZScaling;

                % Save metadata to .txt file
                fileID = fopen([fullFileName '.txt'], 'a');
                fprintf(fileID, '%s Diameter (um): %f\n', ref_im_x, majorAxis*ZScaling);
                fprintf(fileID, '%s Major Axis (um): %f\n', ref_im_x, majorAxis*ZScaling);
                fprintf(fileID, '%s Minor Axis (um): %f\n', ref_im_x, scaledHeight_x);
                fprintf(fileID, '%s Max Area: %f\n', ref_im_x, scaledArea);
                fprintf(fileID, '%s Mean Intensity: %f\n', ref_im_x, meanIntensity);
                fprintf(fileID, '%s Min Intensity: %d\n', ref_im_x, minIntensity);
                fprintf(fileID, '%s Max Intensity: %d\n', ref_im_x, maxIntensity);
                fprintf(fileID, '%s Skewness: %f\n', ref_im_x, skew_val);
                fprintf(fileID, '%s Kurtosis: %f\n', ref_im_x, kurt_val);
                fclose(fileID);

                meanHeight(1,chan) = scaledHeight_x;

                close all;
            end
        else

            disp([ref_im_x ' does not exist']);

            fileID = fopen([fullFileName '.txt'], 'a');
            fprintf(fileID, '%s Diameter (um): %s\n', ref_im_x, '');
            fprintf(fileID, '%s Major Axis (um): %s\n', ref_im_x, '');
            fprintf(fileID, '%s Minor Axis (um): %s\n', ref_im_x, '');
            fprintf(fileID, '%s Max Area: %s\n', ref_im_x, '');
            fprintf(fileID, '%s Mean Intensity: %s\n', ref_im_x, '');
            fprintf(fileID, '%s Min Intensity: %s\n', ref_im_x, '');
            fprintf(fileID, '%s Max Intensity: %s\n', ref_im_x, '');
            fprintf(fileID, '%s Skewness: %s\n', ref_im_x, '');
            fprintf(fileID, '%s Kurtosis: %s\n', ref_im_x, '');
            fclose(fileID);


            continue

        end

        %% Get y projection Data
        if exist(ref_im_y, 'file') == 2

            im_og_y = imread(ref_im_y);

            im_y = im_og_y;
```

```
im_y = im2gray(im_y);
level1 = graythresh(im_y);
disp(["LEVEL 1: " level1]);
im_y = imbinarize(im_y,level1); % Otsu threshold


im_y = imclose(im_y, strel('disk', 10)); % close small gaps
im_y = bwareaopen(im_y, 50); % delete if fewer than X pixels
im_y = imfill(im_y,'holes'); % fill in holes
im_y = bwareaopen(im_y, 50); % delete if fewer than X pixels

imgOtsuThreshold = im_y;

% Compute the area of the binary mask
binaryMaskArea = sum(imgOtsuThreshold(:))*1.1;

% Compute the area of a circle
circleDiameter = max(size(im_y));
circleArea = pi * (circleDiameter / 2)^2;

% Check if the binary mask area is larger than the circle area
if binaryMaskArea > circleArea
    % If so, apply Otsu's thresholding again to the thresholded image
    level2 = graythresh(im2gray(im_og_y));
    disp(["LEVEL 2: " level2]);
    imgOtsuThreshold2 = imbinarize(im2gray(im_og_y), level2);
    imgOtsuThreshold2 = bwareaopen(imgOtsuThreshold2, 50);
    imgOtsuThreshold2 = imclose(imgOtsuThreshold2, strel('disk', 50));
    imgOtsuThreshold2 = imfill(imgOtsuThreshold2,'holes');
    imgOtsuThreshold2 = bwareaopen(imgOtsuThreshold2, 50);
else
    imgOtsuThreshold2 = imgOtsuThreshold;
end

imgOtsuThreshold = imgOtsuThreshold2;

% Compute the area of the binary mask
binaryMaskArea = sum(imgOtsuThreshold(:))*1.1;

% Compute the area of a circle
circleDiameter = max(size(im_y));
circleArea = pi * (circleDiameter / 2)^2;

if binaryMaskArea > circleArea
    % If so, apply Otsu's thresholding again to the thresholded image
    maskedImg = im2gray(im_og_y);
    maskedImg(~imgOtsuThreshold) = 0;

    level3 = graythresh(maskedImg);
    disp(["LEVEL 3: " level3]);
    imgOtsuThreshold2 = imbinarize(maskedImg, level3);
    imgOtsuThreshold2 = bwareaopen(imgOtsuThreshold2, 100);
    imgOtsuThreshold2 = imclose(imgOtsuThreshold2, strel('disk', 50));
    imgOtsuThreshold2 = imfill(imgOtsuThreshold2,'holes');
    imgOtsuThreshold2 = bwareaopen(imgOtsuThreshold2, 500);
else
    imgOtsuThreshold2 = imgOtsuThreshold;
end

figure('Position',[0 50 200 100]);
fig = gcf; % Get the current figure handle
fig.Position(3:4) = 2 * fig.Position(3:4);
subplot(1,2,1), imshow(im_y), title('Original Threshold');
subplot(1,2,2), imshow(imgOtsuThreshold2), title('Final Thresholded Image');
pause(1)

im_y = imgOtsuThreshold2;

figure('Position',[0 50 200 100]);
fig = gcf; % Get the current figure handle
fig.Position(3:4) = 2 * fig.Position(3:4);
subplot(1,2,1), imshow(im_og_y), title('Original Image');
subplot(1,2,2), imshow(im_y), title('Final Thresholded Image');
pause(1)
```

```
            ims = conv2(double(im_y), ones(7,7),'same');
            imbw = ims>6;

            props =
regionprops(imbw,'Area','PixelIdxList','MajorAxisLength','MinorAxisLength');
            if isempty(props)
                disp("Nothing segmented... Skipping");

                fileID = fopen([fullFileName '.txt'], 'a');
                fprintf(fileID, '%s Diameter (um): %s\n', ref_im_y, '');
                fprintf(fileID, '%s Major Axis (um): %s\n', ref_im_y, '');
                fprintf(fileID, '%s Minor Axis (um): %s\n', ref_im_y, '');
                fprintf(fileID, '%s Max Area: %s\n', ref_im_y, '');
                fprintf(fileID, '%s Mean Intensity: %s\n', ref_im_y, '');
                fprintf(fileID, '%s Min Intensity: %s\n', ref_im_y, '');
                fprintf(fileID, '%s Max Intensity: %s\n', ref_im_y, '');
                fprintf(fileID, '%s Skewness: %s\n', ref_im_y, '');
                fprintf(fileID, '%s Kurtosis: %s\n', ref_im_y, '');
                fclose(fileID);

                continue;
            end

            [~,indexOfMax] = max([props.Area]);
            approximateRadius =  props(indexOfMax).MajorAxisLength/2;

            largestBlobIndexes  = props(indexOfMax).PixelIdxList;
            bw = false(size(im_y));
            bw(largestBlobIndexes) = 1;
            bw = imfill(bw,'holes');

            % Get properties of mask
            s = regionprops(bw, 'Area', 'Centroid', 'MajorAxisLength', 'MinorAxisLength',
'Perimeter');
            maxArea = max([s.Area]);
            idxMaxArea = find([s.Area] == maxArea);
            radius = max([s.MajorAxisLength])/2;

            majorAxis = s(idxMaxArea).MajorAxisLength;
            minorAxis = s(idxMaxArea).MinorAxisLength;

            masked_img = im2uint8(double(im2gray(im_og_y))/255 .* bw);
            masked_img_colour = im2uint8(double(im_og_y)/255 .* bw);
            flattened_img = reshape(masked_img, [], 1);
            flattened_img = flattened_img(flattened_img ~= 0);
            skew_val = skewness(flattened_img);
            kurt_val = kurtosis(flattened_img);

            % use grayscale image to get properties
            s = regionprops(bw, masked_img,'Area', 'MeanIntensity', 'MinIntensity',
'MaxIntensity', 'PixelValues');
            maxArea = max([s.Area]);
            idxMaxArea = find([s.Area] == maxArea);

            meanIntensity = s(idxMaxArea).MeanIntensity;
            minIntensity = s(idxMaxArea).MinIntensity;
            maxIntensity = s(idxMaxArea).MaxIntensity;
            pixelValues = s(idxMaxArea).PixelValues;
            pixelValuesScaled = rescale(pixelValues);
            entropyMax = entropy(pixelValuesScaled);

            pad_size = [round(size(im_y, 1)/5) round(size(im_y, 2)/5)];
            pad_value = 0;
            bw = padarray(bw, pad_size, pad_value, 'both');

            im_og_y = padarray(im_og_y, pad_size, pad_value, 'both');

            % Save image
            cd(tifpath);
            imwrite(masked_img_colour, [fullFileName ref_im(1:end-4) '_y_proj_masked.tif'])

            scaledHeight_y = minorAxis*ZScaling;

            % Save metadata to .txt file
            fileID = fopen([fullFileName '.txt'], 'a');
```

```
            fprintf(fileID, '%s Diameter (um): %f\n', ref_im_y, majorAxis*ZScaling);
            fprintf(fileID, '%s Major Axis (um): %f\n', ref_im_y, majorAxis*ZScaling);
            fprintf(fileID, '%s Minor Axis (um): %f\n', ref_im_y, scaledHeight_y);
            fprintf(fileID, '%s Max Area: %f\n', ref_im_y, scaledArea);
            fprintf(fileID, '%s Mean Intensity: %f\n', ref_im_y, meanIntensity);
            fprintf(fileID, '%s Min Intensity: %d\n', ref_im_y, minIntensity);
            fprintf(fileID, '%s Max Intensity: %d\n', ref_im_y, maxIntensity);
            fprintf(fileID, '%s Skewness: %f\n', ref_im_y, skew_val);
            fprintf(fileID, '%s Kurtosis: %f\n', ref_im_y, kurt_val);
            fclose(fileID);

            meanHeight(2,chan) = scaledHeight_y;

            close all;
        else

            fileID = fopen([fullFileName '.txt'], 'a');
            fprintf(fileID, '%s Diameter (um): %s\n', ref_im_y, '');
            fprintf(fileID, '%s Major Axis (um): %s\n', ref_im_y, '');
            fprintf(fileID, '%s Minor Axis (um): %s\n', ref_im_y, '');
            fprintf(fileID, '%s Max Area: %f\n', ref_im_y, '');
            fprintf(fileID, '%s Mean Intensity: %s\n', ref_im_y, '');
            fprintf(fileID, '%s Min Intensity: %s\n', ref_im_y, '');
            fprintf(fileID, '%s Max Intensity: %s\n', ref_im_y, '');
            fprintf(fileID, '%s Skewness: %s\n', ref_im_y, '');
            fprintf(fileID, '%s Kurtosis: %s\n', ref_im_y, '');
            fclose(fileID);


            continue
        end
    end

    %% Get mean and SD

    meanDiameter = nonzeros(meanDiameter);
    meanEntropy = nonzeros(meanEntropy);
    meanOvalness = nonzeros(meanOvalness);
    meanArea = nonzeros(meanArea);
    meanSkew = nonzeros(meanSkew);
    meanKurt = nonzeros(meanKurt);
    meanHeight = nonzeros(meanHeight');
    meanHeight = meanHeight';

    avg_Entropy = mean(meanEntropy);
    sd_Entropy = std(meanEntropy);
    avg_Ovalness = mean(meanOvalness);
    sd_Ovalness = std(meanOvalness);
    avg_Area = mean(meanArea);
    sd_Area = std(meanArea);
    avg_diams = mean(meanDiameter);
    sd_diams = std(meanDiameter);
    avg_Skew = mean(meanSkew);
    sd_Skew = std(meanSkew);
    avg_Kurt = mean(meanKurt);
    sd_Kurt = std(meanKurt);
    avg_height = mean(meanHeight);
    sd_height = std(meanHeight);

    fileID = fopen([fullFileName '.txt'], 'a');
    fprintf(fileID, 'Average Diameter: %f\nSD of Diameters: %f\n', avg_diams, sd_diams);
    fprintf(fileID, 'Average Area: %f\nSD of Area: %f\n', avg_Area, sd_Area);
    fprintf(fileID, 'Average Ovalness: %f\nSD of Ovalness: %f\n', avg_Ovalness, sd_Ovalness);
    fprintf(fileID, 'Average Entropy: %f\nSD of Entropy: %f\n', avg_Entropy, sd_Entropy);
    fprintf(fileID, 'Average Skew: %f\nSD of Skew: %f\n', avg_Skew, sd_Skew);
    fprintf(fileID, 'Average Kurtosis: %f\nSD of Kurtosis: %f\n', avg_Kurt, sd_Kurt);
    fprintf(fileID, 'Average Height (Z-stack): %f\nSD of Height: %f\n', avg_height,
sd_height);
    fclose(fileID);

  else
      disp('file size too small...');
  end
end
disp('DONE!!! YAY!!!');
```

Python script to convert .czi files to .tif projection images.

```
import os
import numpy as np
import matplotlib.pyplot as plt
from skimage.io import imread, imsave
from skimage.transform import rescale
from skimage.color import rgb2gray
from skimage.util import img_as_ubyte
from skimage.transform import resize
from skimage import exposure
import czifile
from pathlib import Path
import tkinter as tk
from tkinter import filedialog
import cv2
import psutil
from skimage.transform import downscale_local_mean


def extract_image_data(file_path):
    print(f"Extracting image data from {file_path}")
    with czifile.CziFile(file_path) as czi:
        metadata = czi.metadata(raw=False)
        voxel_sizes = metadata['ImageDocument']['Metadata']['Scaling']['Items']['Distance']

        print("CZI axes:", czi.axes)
        print("Metadata channels:",
metadata['ImageDocument']['Metadata']['Information']['Image']['SizeC'])

        D = {}
        D['uscale'] = [voxel_sizes[i]['Value'] * 10e5 for i in range(3)]
        D['noc'] = int(metadata['ImageDocument']['Metadata']['Information']['Image']['SizeC'])
        print('Number of colors: ', D['noc'])

        D['color'] =
[metadata['ImageDocument']['Metadata']['DisplaySetting']['Channels']['Channel'][i]['Color']
for i
                       in range(D['noc'])]

        for i in range(D['noc']):
            D['color'][i] = D['color'][i][3:]
            if not isinstance(D['color'][i], str):
                raise ValueError(f"Expected a string, but got {type(D['color'][i]).__name__}")
            colour = D['color'][i]
            D['color'][i] = tuple(int(colour[i:i + 2], 16) for i in (0, 2, 4))

        # Read image data
        print("Reading image data...")
        image = czi.asarray()
        print("Original image shape:", image.shape)

        # Check available memory
        available_memory = psutil.virtual_memory().available
        image_memory = image.nbytes

        if image_memory > available_memory * 0.7:  # If image would use more than 50% of
available memory
            # Calculate downscaling factor
            downscale_factor = int(np.ceil(np.sqrt(image_memory / (available_memory * 0.5))))
            print(f"Downscaling image by factor of {downscale_factor}")

            # Downscale the image
            downscaled_shape = tuple(s // downscale_factor if i > 3 else s for i, s in
enumerate(image.shape))
            D['volume'] = np.zeros(downscaled_shape, dtype=np.float32)

            for i in range(D['noc']):
                D['volume'][0, 0, 0, i] = downscale_local_mean(image[0, 0, 0, i],
                                                               (1, downscale_factor,
downscale_factor, 1))

            # Adjust scale
```

```
            D['uscale'] = [s * downscale_factor for s in D['uscale']]
        else:
            D['volume'] = image.astype(np.float32)  # Use float32 instead of float64 to save
memory

        print("Final image shape:", D['volume'].shape)

        D['volume'] = normal(D['volume'])

        # Calculate maximum intensity projection for each channel
        print("Calculating maximum intensity projection...")
        D['mip'] = [np.max(D['volume'][0, 0, 0, i], axis=0) for i in range(D['noc'])]
        D['nmip'] = [normal(D['mip'][i]) for i in range(D['noc'])]

        # Calculate projections along x and y axes for each channel
        print("Calculating projections along x and y axes...")
        D['mip_x'] = [np.max(D['volume'][0, 0, 0, i], axis=1) for i in range(D['noc'])]
        D['mip_y'] = [np.max(D['volume'][0, 0, 0, i], axis=2) for i in range(D['noc'])]

        # Normalize projections for each channel
        print("Normalizing projections...")
        D['nmip_x'] = [normal(D['mip_x'][i]) for i in range(D['noc'])]
        D['nmip_y'] = [normal(D['mip_y'][i]) for i in range(D['noc'])]

        # Create 3D projection for each channel
        print("Creating 3D projection...")
        D['nmipxyz'] = [projector(D['nmip'][i], D['nmip_x'][i], D['nmip_y'][i], D['uscale'])
for i in range(D['noc'])]

    return D


def render_images(D, file_path):
    print(f"Rendering images and saving to {file_path}")

    colour_merge = np.zeros((int(D['nmipxyz'][0].shape[0]), int(D['nmipxyz'][0].shape[1]), 3))
    colour_panel = np.zeros((int(D['nmipxyz'][0].shape[0])*2, int(D['nmipxyz'][0].shape[1])*2,
3))
    height, width, _ = colour_panel.shape
    half_height, half_width = height // 2, width // 2

    # Define the four panel positions
    panel_positions = [
        (slice(0, half_height), slice(0, half_width)),  # Top left
        (slice(0, half_height), slice(half_width, width)),  # Top right
        (slice(half_height, height), slice(0, half_width)),  # Bottom left
        (slice(half_height, height), slice(half_width, width))  # Bottom right
    ]

    # Create image for each channel
    for j in range(D['noc']):
        # Colorize image
        colour_projection = colouriser(D['nmipxyz'][j], D['color'][j])
        colour_x_projection = colouriser(D['nmip_x'][j], D['color'][j])
        colour_y_projection = colouriser(D['nmip_y'][j], D['color'][j])

        colour_merge += colour_projection

        if j < len(panel_positions):  # Only add to panel if it's one of the first 4 channels
            colour_panel[panel_positions[j]] = colour_projection

        channel = ','.join(map(str, [int(c / 255) for c in D['color'][j]]))

        # Normalize image
        normalised_projection = colour_projection / np.max(colour_projection)
        normalised_x_projection = colour_x_projection / np.max(colour_x_projection)
        normalised_y_projection = colour_y_projection / np.max(colour_y_projection)

        new_dir = file_path.parent / ('__' + file_path.stem + '__1')
        os.makedirs(new_dir, exist_ok=True)

        new_file_path = new_dir / (f"__[{channel}]" + file_path.suffix)
        imsave(new_file_path, img_as_ubyte(normalised_projection))
        new_file_path = new_dir / (f"__[{channel}]__x_projection" + file_path.suffix)
        imsave(new_file_path, img_as_ubyte(normalised_x_projection))
```

```
            new_file_path = new_dir / (f"__[{channel}]__y_projection" + file_path.suffix)
            imsave(new_file_path, img_as_ubyte(normalised_y_projection))

            print(f"SAVED channel {channel}!")

    colour_merge = colour_merge / np.max(colour_merge)  # Scale the values so the maximum is
at 1

    # create merge and panel
    new_file_path = new_dir / (file_path.stem + f"__merge" + file_path.suffix)
    imsave(new_file_path, img_as_ubyte(colour_merge))

    if D['noc'] < len(panel_positions):
        colour_panel[panel_positions[D['noc']]] = colour_merge

    new_file_path = new_dir / (file_path.stem + f"__panel" + file_path.suffix)
    imsave(new_file_path, img_as_ubyte(colour_panel))


def estimate_optimal_gamma(image):
    # Calculate the mean pixel intensity
    mean_intensity = np.mean(image)
    # Estimate gamma using a simple heuristic (you can customize this further)
    gamma = 1.0 / np.sqrt(mean_intensity)

    return gamma


def histogram_stretch(image, low_percentile=1, high_percentile=99):
    """
    Stretch the histogram of the image to enhance contrast.

    :param image: Input image
    :param low_percentile: Low percentile to clip
    :param high_percentile: High percentile to clip
    :return: Contrast enhanced image
    """
    low, high = np.percentile(image, (low_percentile, high_percentile))
    return exposure.rescale_intensity(image, in_range=(low, high))

def colouriser(n, color):
    n_stretched = histogram_stretch(n)

    N = np.zeros((n_stretched.shape[0], n_stretched.shape[1], 3))
    color = [c / 255.0 for c in color]
    for i in range(len(color)):
        N[:, :, i] = np.squeeze(n_stretched) * color[i]

    N = N / np.max(N)

    return N

def projector(n1, n2, n3, uscale):
    scale_factor = uscale[2]/uscale[1]

    # Initialize N
    N = np.zeros((n1.shape[0] + n2.shape[0], n1.shape[1] + n3.shape[0]))

    # Assign values to N
    N[0:n1.shape[0], 0:n1.shape[1]] = n1[:, :, 0]
    N[n1.shape[0]:(n1.shape[0] + n2.shape[0]), 0:n2.shape[1]] = n2[:, :, 0]
    N[0:n1.shape[0], n1.shape[1]:(n1.shape[1] + n3.shape[1])] = n3.T[0, :, :]

    return N


def normal(n):
    n = n.astype(np.float32)  # Use float32 instead of float64
    n = n - np.nanmin(n)
    N = n / np.nanmax(n)
    return N

# Open file dialog to select directory
root = tk.Tk()
root.withdraw()  # Hide the main window
```

```
dir_path = filedialog.askdirectory()  # Open the file dialog
print(f"Selected directory: {dir_path}")

# Get list of .czi files
file_list = list(Path(dir_path).rglob('*.czi'))
print(f"Found {len(file_list)} .czi files")

# Process each file
for file_path in file_list:
    print(f"Processing file: {file_path}")
    # Extract image data
    D = extract_image_data(file_path)

    # Render images
    render_images(D, file_path.with_suffix('.tif'))

print("Done! YAY!!!")
```